Mechanisms of chloride modulated activity in the C-domain of Angiotensin-Converting Enzyme

Christopher John Yates

Thesis presented for the Degree of

Doctor of Philosophy

in the Division of Medical Biochemistry
University of Cape Town

April 2012

Supervisor: Professor E. D. Sturrock

Declaration

I, Christopher John Yates, declare that this thesis is my own, unaided work (except where acknowledgements indicate otherwise). Neither the whole work not part thereof has been, is being, or is to be submitted for any degree or examination at any other university.

I empower the University of Cape Town to reproduce for the purpose of research either the whole or any part of the contents of this thesis, in any manner whatsoever.

Signature of candidate:_____

Signed on the _____ day of _____, 2012.

Abstract

The somatic isoform of angiotensin-converting enzyme (sACE), a key regulator of blood pressure and electrolyte fluid homeostasis, primarily cleaves the hypertension-associated angiotensin-I (AngI) and bradykinin peptides, as well as a number of other physiologically relevant peptides *in vitro*. sACE consists of two homologous and catalytically active N- and C- domains which display marked differences in substrate specificities and chloride activation. To investigate these potential mechanisms, a series of single amino acid substitution mutants (based on analysis of aligned C- and N-domain 3D structures) were generated in a soluble, minimally glycosylated C-domain construct. Evaluation of these constructs was done using AngI and the short synthetic substrates hippuryl-L-histidyl-L-leucine (HHL) and Z-phenylalanyl-L-histidyl-L-leucine (Z-FHL) under differing chloride concentrations. An isothermal titration calorimetry-based assay was developed to determine the effect of chloride concentration on enzyme thermodynamic and kinetic parameters. Chloride binding in the chloride 1 pocket of tACE was found to affect positioning of K511 and potentially alter the conformation of the active site. This would alter C-terminal substrate interactions, which were suggested to affect chloride 2 pocket ion affinity by coordinating Y520 and affect peptide bond rotation and hence substrate interactions. The analysis of the chloride 2 pocket R522Q and R522K mutations revealed a key R522-Y523 Pi-cation interaction that is stabilized via chloride coordination of R522. Substrate interactions in the S2 sub-site were shown to affect positioning of this complex as well as chloride affinity in the chloride 2 pocket. The E403-K118 salt bridge in tACE was shown to stabilize the hinge-bending region and reduce chloride affinity by constraining the chloride 2 pocket, an interaction which is destabilized via substrate interactions within the S2 pocket which results in tighter chloride binding. This work showed that substrate composition to the C-terminal side of the scissile bond, as well as interactions of larger substrates in the S2 sub-site, moderate chloride affinity in the chloride 2 pocket of the ACE C-domain, providing a rationale for the substrate selective nature of chloride dependence in ACE and how this varies between the N- and C- domains.

Acknowledgements

This thesis would have been an intolerable affair were it not for those who selflessly devoted their time, experience and love in nudging me over the finish line. To each of you who have made an impact on me in your own way, I extend to you my undying gratitude:

To my supervisor, Prof Edward D. Sturrock, your faith in my ability to overcome challenges which others would run screaming from is phenomenal. You have given me an environment in which I could push myself as far as could be, yet provided direction and forced me to think critically about every aspect of my work. For your patience, timely encouragements when times were tough, disarmingly cheesy jokes and contribution to my personal development, I am extremely grateful.

To Sylva Schwager, thank you for being a constant, solid presence in what has been a fun, yet challenging, period of my life. Your tireless encouragement and willing ear in time of need was always welcome and your never-ending enthusiasm for science is amazing.

To Dr Trudi O'Neill, thank you for getting me off to a good start. As my M.Sc co-supervisor you were fantastic and really instilled in me a good scientific grounding, especially when I started getting too enthusiastic and not doing the basics.

To Dr Dave Woolley, thank you for always being willing to listen to my endless prattling regarding ITC minutiae, and for keeping the machine going during the last few months of work, without your support this thesis would look very different.

My peers and colleagues (past and present) within the Zinc-Metalloprotease Group: Dr Pierre Redelinghuys, Dr Ross Douglas, Nailah Conrad, Dr Ayesha Parker, Dr Tony Chang, Dr Jean Watermeyer, Dr Adele Thomas, Dr Colin Anthony, Itai Chitapi, Dr Kerry Gordon, Dr Riyad Domingo, Dr Aloysius Nchinda, Dr Dawn Webber, Kate Larmuth, Henry Kambafwile, Raymond Moholisa and the random honours students each year, I would like to thank you for your helpful technical assistance, advice, friendship, moral support, Gatsby days,

conspiratorial procrastination, endless jokes, endless food and for making the lab a great place to be, you are all fantastic and it has been a blast.

To all my friends, either in other labs or outside of UCT, thank you for being the best bunch of people I know, your friendship means the world to me. To my past and present UCT crew, especially Gemma, Jo, Caryn, Rachel, Liam, Olivia, Kate, Michael, Kate, Rachel, Paola, Linus, and Dave, be it regular coffees, squash, dominating DC++, boozing it up at the MAC or just shooting the breeze, you are all fantastic and I couldn't have made it through without your comradery. To all my friends outside of UCT, I know I've been scarce, but thanks for always being there, I value your friendship more than you know.

To my absolutely amazing parents, John and Rosemary, you have always been behind everything I do and there is no way I can possibly put into words how much that means to me. Your support, patience, understanding and regular financial support when funding was bad has been above and beyond and I thank you for giving me the opportunity to achieve and do what I needed to do. To my sisters: Megan, you know how this feels and the encouragement and support you have given means a whole lot. Dominique, thanks for all you've done for your poor student brother all these years, you have been amazing and always there for me in times of need and crisis. You are the most amazing family.

To my darling girlfriend Yolandi, your unwavering love and strength in getting me through what has been one of the toughest experiences of my life has been more than I could ever ask of a person. When I was down, you made sure I got back up; when I lost focus, you gave me wine, when I got tired, you fed me; we laughed, we cried, we lived, we loved. I look forward to many years giving you the same support in spreading your wings and flying.

The South African National Research Foundation, the German Academic Exchange Service, the Ernst and Ethel Erikson Trust, the CapeBiotech Trust and the University of Cape Town for funding this work.

Abbreviations

°C	degree Celsius
ΔH_{app}	apparent molar enthalpy
ΔH_{int}	intrinsic molar enthalpy change of the reaction
ΔH_{ion}	change in enthalpy associated with ionisation of buffer
ΔG	Gibbs free energy
ΔΔG	change in Gibbs free energy change on addition of chloride
ΔΔH	change in molar enthalpy change on addition of chloride
ΔTΔS	change in temperature dependent entropy change on addition of chloride
µcal	micro-calorie
µl	micro-litre
µM	micro-molar
Å	angstrom
ACE	angiotensin-converting enzyme
ACE2	angiotensin-converting enzyme 2
ACN	acetonitrile
AcSDKP	N-acetyl-Ser-Asp-Lys-Pro
Ang I	angiotensin I
Ang II	angiotensin II
Ang III	angiotensin III
Ang(1-7)	angiotensin(1-7)
AT_1	angiotensin II type I receptor
AT_2	angiotensin II type II receptor
AT_4	angiotensin type IV receptor
B_1	kinin type I receptor
BK	bradykinin
Bp	base-pair
CHO-K1	Chinese hamster ovary K1
$CONH_2$	amidated C-termini
CPA	carboxypeptidase A
CPD	carboxypeptidase D
dH_2O	de-ionised H2O
DMEM	Dulbecco's modified eagle's medium
DMSO	dimethyl sulphoxide
DNA	deoxyribonucleic acid
E. coli	Escherichia coli
EDTA	ethylenediaminetetraacetic acid
FAPGG	furylacryloyl-Phe-Gly-Gly
FCS	fetal calf serum
FRET	fluorescence resonance energy transfer
GnRH	gonadotropin-releasing hormone
HEPES	*N*-2-hydroxyethylpiperazine-*N*'-2-ethanesulphonic Acid
HHL	hippuryl-His-Leu
HL	His-L-Leu-L
HPLC	high-performance liquid chromatography
ITC	Isothermal Titration Calorimetry

KKS	kallikrein-kinin system
kDa	kilo-dalton
K_i	inhibition constant
k_{cat}	catalytic constant
$K_{d,app}$	apparent dissociation constant for chloride binding
K_d	dissociation constant for inhibitor binding
K_m	Michaelis constant
LB	Luria-Bertani
lis-W	lisinopril derivative with a P2' Trp substituent
mg	milli-gram
min	minute
ml	milli-litre
mM	milli-molar
n	stoichiometry of binding
n_H	proton transfer stoichiometry
nM	nano-molar
PBS	phosphate-buffered saline
PCR	polymerase chain reaction
PMSF	phenylmethylsulphonyl fluoride
PDB	protein data bank (http://www.rcsb.org/pdb)
RAS	renin-angiotensin system
RE	restriction endonuclease site
RXPA380	C-domain-specific phosphinic inhibitor
RXP407	N-domain-specific phosphinic inhibitor
FR1	the BamHI-Eco47III fragment of the tACEg13sol cDNA
FR2	the Eco47III-SphI fragment of the tACEg13sol cDNA
FR3	the SphI-NheI fragment of the tACEg13sol cDNA
FR4	the NheI-NotI fragment of the tACEg13sol cDNA
FR1,2,3	the BamHI-NheI fragment of the tACEg13sol cDNA
sACE	somatic angiotensin-converting enzyme
SA_{min}	specific activity at 0mM NaCl
SA_{max}	specific activity at NaCl saturation
SDS-PAGE	sodium dodecylsulphate polyacrylamide gel electrophoresis
sec	second
S_i	initial substrate concentration prior to addition of enzyme
S_0	initial substrate concentration after addition of enzyme
TΔS	temperature associated entropy
tACE	testis angiotensin-converting enzyme
TAPSO	3-[*N*-Tris(hydroxymethyl)methylamino]-2-hydroxypropanesulfonic acid
TBE	Tris-borate/EDTA buffer
TES	*N*-[tris(hydroxymethyl)methyl]-2-aminoethanesulfonic acid
TFA	trifluoroacetic acid
TM	transmembrane region
Tris	2-Amino-2-hydroxymethyl-propane-1,3-diol
V_{max}	maximum velocity
Z-FHL	Z-Phe-His-Leu

Table of Contents

List of Figures

List of Tables

Chapter 1: Review of the Literature

1.1 Biochemistry of ACE

Angiotensin I-converting enzyme (ACE, EC 3.4.15.1) has been categorized as a member of the M2 gluzincin family of zinc metallopeptidases and functions primarily as a dipeptidyl carboxypeptidase, catalyzing the hydrolysis of carboxy-terminal dipeptides from a wide range of functional peptides (reviewed by Ehlers & Riordan, 1989; Eriksson et al., 2002; Turner & Hooper, 2002).

1.1.1 Physical Properties

ACE consists of two isoforms, somatic ACE (sACE) and testis ACE (tACE) (Figure 1.1) (Ehlers et al., 1989; Soubrier et al., 1988). Somatic ACE is encoded by a single 21 kilobase gene on chromosome 17q23 consisting of 26 exons, with exon 13 spliced out, that is translated into a 1306 residue protein of 140-170 kDa in weight (Howard et al., 1990; Hubert et al., 1991; Wei et al., 1991a). Contained within this primary structure starting at the N-terminus is a 1230-residue ectodomain; a 36-residue juxtamembrane region, a 17-residue hydrophobic transmembrane anchoring region and a C-terminal 30-residue long cytoplasmic region (Wei et al., 1991a; Soubrier et al., 1988). The large ectodomain contains two domains of high homology (60% over two 357 residues stretches)(see Figure 1.2), the N-domain and the C-domain, each of which contains the conserved HEXXH zinc-binding-motif indicative of the active sites of many Zn-metalloproteases, and are presumed to have come about as the result of a gene duplication event (Soubrier et al., 1988). Somatic ACE is expressed in a wide variety of tissues, including vascular endothelium, renal proximal tubule epithelium, intestinal epithelium, macrophages and brain (Takada et al., 1984; Chai et al., 1987; Sibony et al., 1993; McKinley et al., 2003).

tACE, the smaller isoform of ACE that is only expressed in the adult testis, arises from transcription of the same gene, but more specifically from a tissue-specific promoter within intron 12, with exons 13 through 26 transcribed (Hubert et al., 1991). The mature tACE is a 701-residue protein that is identical to the C-terminal domain of sACE, except for a unique leader peptide distinct from that used by sACE and a 36-residue serine and threonine rich N-terminal region (Ehlers et al., 1989; Ehlers et al., 1992). This 36-residue N-terminus region is heavily *O*-glycosylated and, in studies where this region has been removed, has been shown to have no effect on catalytic activity of tACE (Ehlers et al., 1992).

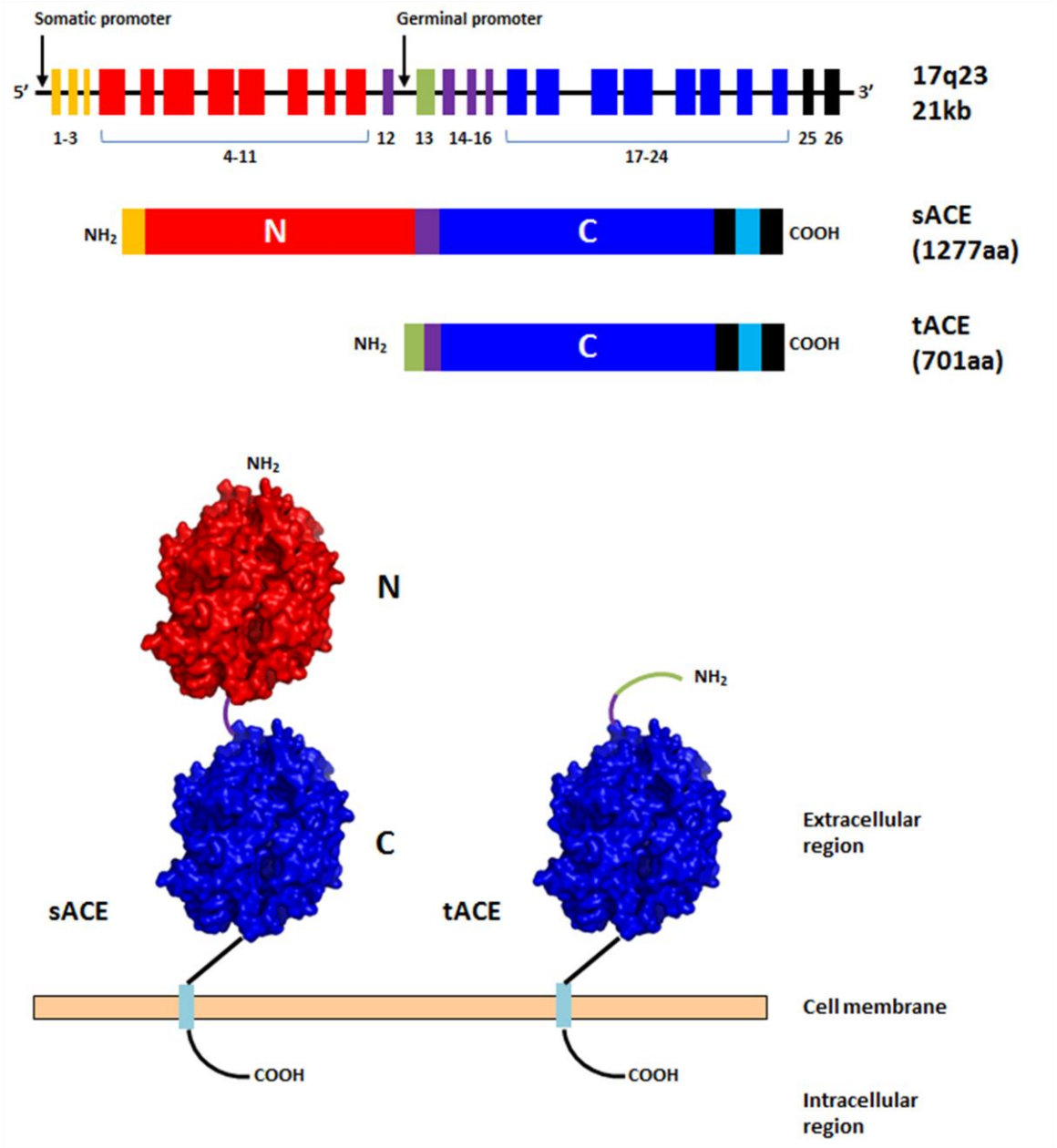

Figure 1.1 Diagrammatic representation of ACE gene organisation and products. The ACE gene is composed of 26 exons, with two separate promoters (somatic & germinal) producing two isoforms: sACE contains an N-domain (red) and C-domain (dark blue), and tACE contains just the C-domain region as well the 36-amino acid region transcribed by exon 13 (light green) which is spliced out in sACE expression. Both isoforms are anchored to the cell membrane by a transmembrane region (light blue).

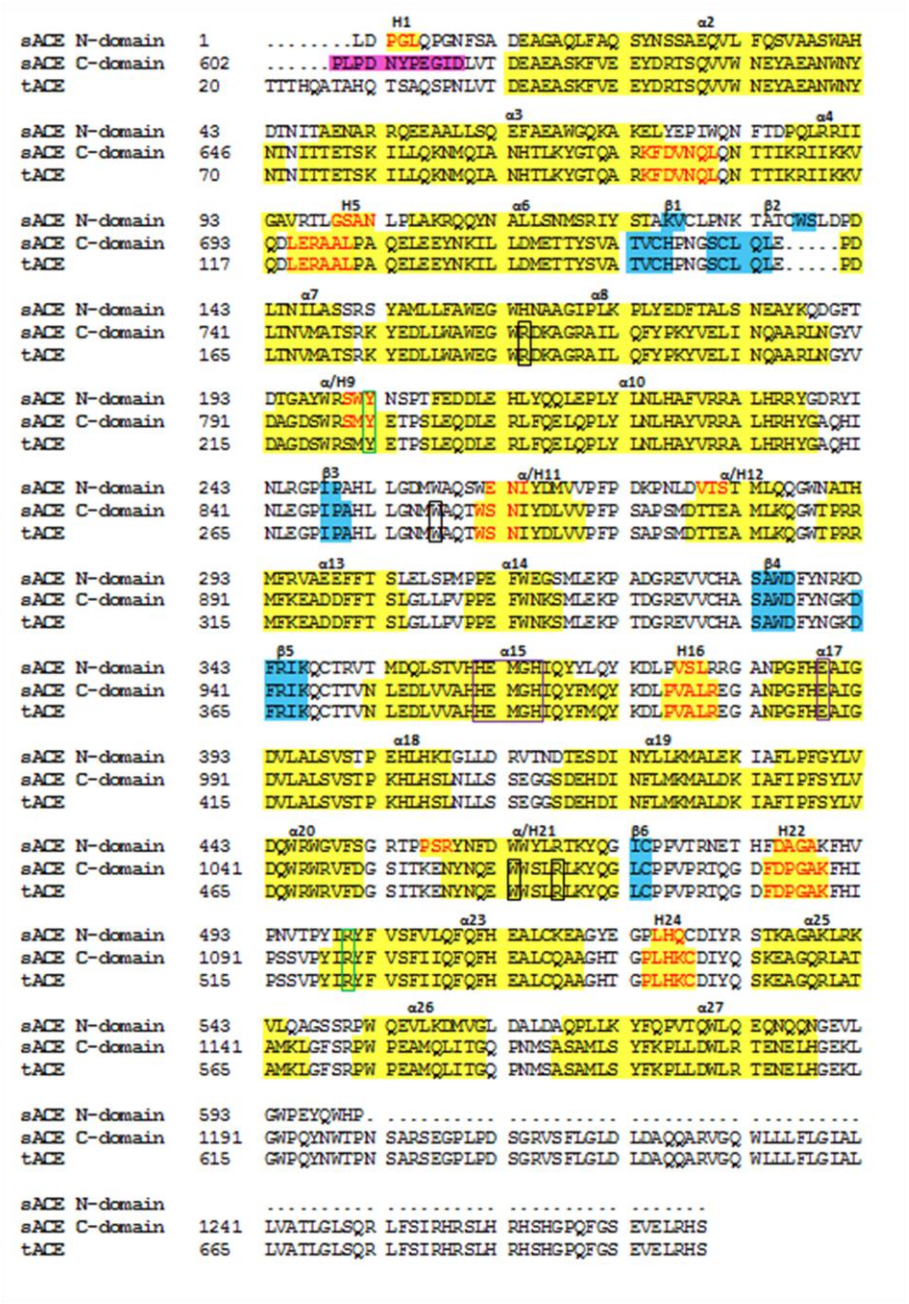

Figure 1.2 Protein sequence alignment of sACE N- and C-domains, and tACE. (adapted from Acharya et al, 2003; Natesh et al, 2003; Corradi et al, 2006). Residue numbering is according to that reported by Soubrier et al., (1988) and Ehlers et al., (1989). Helices (α or 310) and strands are numbered sequentially, with α-helices highlighted in yellow, B strands highlighted in blue and 3_{10} helices shown in red letters. The zinc-binding ligands and HEMGH motif are boxed in purple, chloride 1 pocket binding residues are boxed in black and chloride 2 pocket binding residues are boxed in green. The linker region is shown in pink.

The ectodomains of tACE and sACE are released from the cell surface (Ehlers et al., 1991; Wei et al., 1991a) by an as yet unidentified secretase that cleaves the Arg-Ser bond (Arg620 – tACE and Arg1203 –sACE) in the juxtamembrane region (Ehlers et al., 1996; Woodman et al., 2000).

Human sACE contains 17 potential *N*-glycosylation sites, with 7 located in the C-domain (tACE) and 10 within the N-domain (Yu et al., 1997; O'Neill et al., 2008). Of the seven potential sites in tACE, six were found to be glycosylated, with 3 always glycosylated and 3 partially glycosylated (Yu et al., 1997), with four of these sites clustered towards the N-terminal region of tACE, and the unglycosylated site located close to the transmembrane region. The N-domain was found to have a higher degree of glycosylation with 8 of the 10 sites being found to be glycosylated (Yu et al., 1997; Anthony et al., 2010). Glycosylation has been shown to be important for folding, localization and stability of glycoproteins (Hammond et al., 1994; Helenius & Aebi, 2004), which has been shown to be relevant to ACE as expression in bacteria, which lack eukaryote glycosylation machinery, or expression in the presence of the glycosylation inhibitor tunicamycin result in inactive protein (Sadhukan & Sen, 1996). Further, it has been shown that the N-domain is far more thermally stable than the C-domain (tACE) (Voronov et al., 2002; O'Neill et al., 2008), which can be attributed to their glycosylation patterns.

The variation between the domains is not limited to glycosylation patterns. Given that the C- and N- domains of ACE are the product of a gene duplication event, their 60% shared sequence identity (Figure 1.2) is expected, however they differ in a number of key ways. Firstly, they have different substrate specificities (Wei et al., 1991b). Furthermore, the C-domain has been found to have a higher chloride requirement for hydrolysis than the N-domain, a trend which is dependent on the nature of substrate (Wei et al., 1991b; Wei et al., 1992).

1.1.2 Domain Structure

The 3-dimensional structure of tACE has been determined in complex with a number of potent ACE inhibitors, including lisinopril (PDB code 1o36; Figure 1.3A) (Natesh et al., 2003), captopril and enalaprilat (Natesh et al., 2004), and the highly C-domain selective RXPA380 (PDB code 2oc2) (Corradi et al., 2007). The tACE protein used in the crystallization and that

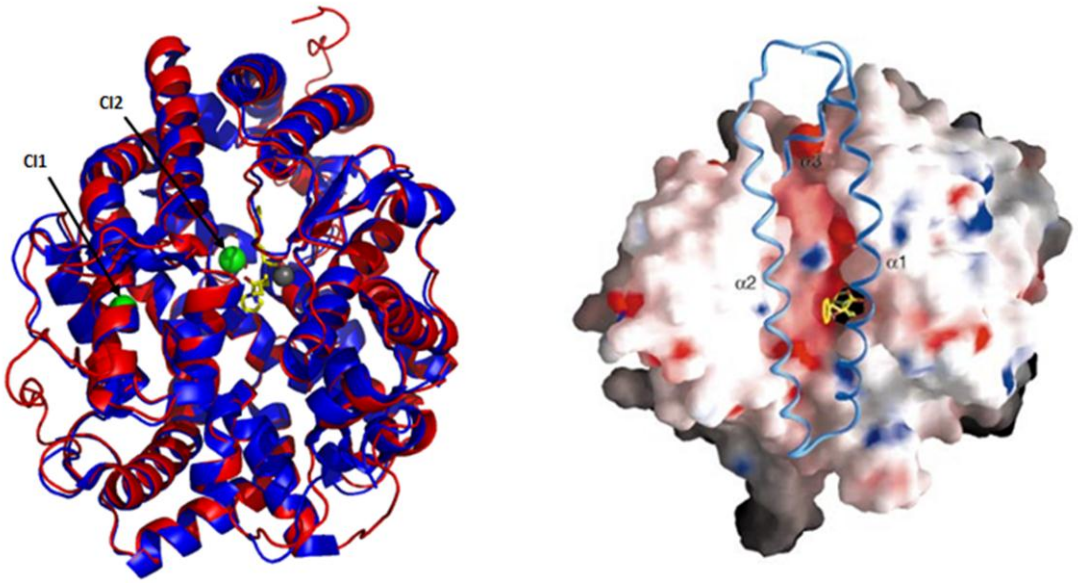

Figure 1.3 Three-dimensional N- and C- domain structures. A) Aligned structures of tACE-Lisinopril (PDB:1o86) in blue and N-domain-Lisinopril (PDB:2c6n) in red. Lisinopril is shown bound in the active site (yellow sticks), with the active site zinc (grey sphere) and chloride ions (green spheres) within either chloride 1 or chloride 2 pockets indicated. Chloride ion in Cl1 pocket not present in the N-domain structure. Image was created using PyMOL 0.99 (DeLano Scientific, Palo Alto, CA, U.S.A). B) Molecular surface representation (negative and positive potentials in red and blue, respectively) of tACE-Lisinopril (PDB:1o86) showing the active-site groove (taken from Natesh et al, 2003). The molecular surface has been sliced for clarity and the buried lisinopril molecule is shown in yellow. Helices α1, a2 and a3 forming the lid are shown.

yielded the data for the structural determination differed slightly from the wild-type form of tACE in that the unique 36 amino acids that constituted its N-terminus had been removed, essentially rendering it identical to the C-domain of sACE (Natesh et al., 2003). The overall shape that tACE (residues 37-625) assumes is ellipsoid, and can be divided into two subdomains with a central channel that descends for approximately 30Å into the molecule (Natesh et al., 2003). The structure of tACE assumes a largely helical conformation, with helices α13, α14, α15, α17 and strand β4 forming the boundaries of the aforementioned central groove (Natesh et al., 2003). There are three N-terminal α-helices (α1, α2, α3), all containing several charged residues, that cover this cavity containing the active site thereby accounting for tACE's inability to hydrolyse large, folded polypeptides (Figure 1.3B) (Natesh et al., 2003). The N- and C-termini of the tACE ectodomain are defined by the Asp40 residue (α1) and the Gly615 residue, respectively, evidenced in the structure but further

substantiated by mutagenic studies (Chubb et al., 2002; Natesh et al., 2003). The structure also contains two internally bound chloride ions, each within a distinct binding pocket, which will be discussed later with regard to the main focus of this study (Natesh et al., 2003).

The crystal structure for the N-domain has been reported in complex with lisinopril (PDB code 2c6n; Figure 1.3A) (Corradi et al., 2006) and the highly N-domain selective inhibitor RXP407 (PDB code 3nxq) (Anthony et al., 2010). The structures display a high degree of similarity in the overall topology and location of the zinc binding motif in the active site (Corradi et al., 2006). A major point of variation when compared to the C-domain (tACE) is that only one chloride ion is bound to the N-domain to the two of tACE, a feature that will be discussed further.

1.1.3 Active Site and catalytic mechanism

The active site for both domains is contained within the large central groove, with the signature HEXXH zinc-binding motif residing on the α15 helix (Natesh et al., 2003; Corradi et al., 2006). Access to this active site is severely limited, with a small pore in the N-terminal chamber or an occluded slot in the C-terminal chamber providing the only theoretical access and suggests that a degree of flexibility in the domain movements is required for admittance of substrate (Watermeyer et al., 2006; Corradi et al., 2006). H383, E411 and H387 in the C-domain (tACE numbering) and H361, E389 and H365 in N-domain, all part of the signature HEXXH motif for each domain, are seen to coordinate the highly ordered catalytic zinc ion (Natesh et al., 2003; Corradi et al., 2006). The catalytic mechanism has been suggested based on comparison with work done on the structurally analogous zinc-metalloprotease, thermolysin, and is proposed to occur via a general-base mechanism whereby a nucleophilic water molecule or hydroxide ion attacks the carbonyl carbon of the scissile bond (Figure 1.4) (Matthews, 1988; Sturrock et al., 2004). The nucleophilicity of the water molecule may be enhanced by polarization between the positive zinc and the negative carboxylate of E143 (which corresponds to E384 in tACE and E362 in N-domain), caused by substrate interactions displacing the zinc-bound watet al.,er toward E143, and may account for the different catalytic efficiencies for different substrates (Sturrock et al., 2004). The nucleophilic attack results in tetrahedral penta-co-ordinated carbonyl carbon intermediate, which breaks down to yield the hydrolysis products. Mutagenic work has

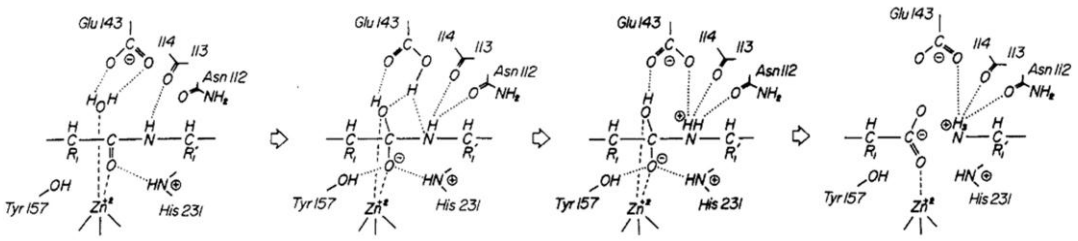

Figure 1.4 The proposed mechanism of thermolysin substrate hydrolysis (taken from Matthews, 1988).

confirmed the critical nature of the two zinc coordinating His residues (383 & 387 in tACE; 361 & 365 in N-domain) and the Glu (E384 in tACE; 262 in N-domain), where substitution renders the domains inactive (Wei et al., 1991b; Wei et al., 1992) Further mutagenic work by Fernandez et al (2001) has implicated H513 (tACE) as being involved in stabilizing the transition-state intermediate, supported by the fact that it's identity is conserved in the N-domain. Additionally, K511 and Y520 in tACE (K489 and Y498 in N-domain) have been suggested to also play a role in stabilizing the transition-state intermediate by coordinating the C-terminal carboxylate of the substrate (Natesh et al., 2003).

Lisinopril interacts with the active sites of both domains in an extended, highly-ordered, conformation that is shared when the two lisinopril-bound structures are superimposed, as well as retaining a number of conserved binding residues conformations (Natesh et al., 2003; Corradi et al., 2006). To describe interactions of substrates and inhibitors with the active sites of the ACE domains, the Schechter & Berger nomenclature model (Schechter and Berger, 1967) is routinely adopted. Residues on the N-terminal side of the scissile bond (or zinc binding group for inhibitors) are designated P_1-P_2-P_3-...-P_n, continuing outwards towards the N-terminus, while residues on the C-terminal side are assigned P_1'-P_2'-P_3'-...-P_n'. The sidechains for each of the residues of the peptide/inhibitor interact with a series of sub-site pockets lining the active site which are designated with the corresponding S_n-...-S_2-S_1-S_1'-S_2'-...-S_n nomenclature. Using a similar nomenclature, both ACE active sites can be described as having four sub-sites, S2, S1, S1' and S2', where the C-terminal dipeptide that is cleaved from the substrate (P1' and P2') interact with the S1' and S2' sub-pockets.

1.1.4 Chloride binding sites

Two chloride ions are found buried in the structure of tACE, separated by a distance of 20.3Å (Natesh et al., 2003). The first chloride (Cl1) 20.7Å away from the zinc, is bound by four ligands, namely Arg186, Trp485, Arg489 and water, and is encapsulated by a hydrophobic shell of four tryptophans (Natesh et al., 2003). The N-domain crystal structures show no chloride bound in this pocket, with the only difference in residue composition in the pocket being H164 which corresponds to R186 in tACE (Corradi et al., 2006). The second chloride ion (Cl2) is located much closer to the zinc at 10.4Å and is coordinated by Arg522, Y224 (R500 and Y202 in N-domain) and a water molecule (Natesh et al., 2003). Mutagenic work has highlighted Arg1098 (R522 in C-domain, R500 in N-domain) as having a crucial role in the chloride dependent activity of the C-domain (tACE) of ACE (Liu et al., 2001), which will be discussed further in section 1.3.

1.2 Physiological importance of ACE

1.2.1 Renin-Angiotensin and kallikrein-kinin systems

The Renin-Angiotensin System (RAS) (Figure 1.5) is a complex enzymatic pathway that plays a critical role in blood pressure regulation and generates a number of bio-active peptides which control fluid and electrolyte homeostasis, hormone secretion as well as behavioural and cognitive responses (Inagami, 1994; Savaskan, 2005). ACE has long been established as having an important role in the RAS, with ACE inhibitors being a major component of the medical treatment of hypertension. Apart from ACE, the other key enzyme in controlling the RAS is renin, an enzyme produced from an inactive precursor in the liver in response to stress, decreased sodium levels or effective plasma volumes (Goldblatt et al., 1934; Houssay. and Fasciolo, 1937; Page and Helmer, 1940). Active renin circulates in the blood where it releases the N-terminal decapeptide angiotensin I (Ang1) from the glycoprotein angiotensinogen, which is also produced in the liver (Inagama, 1994). ACE primarily cleaves AngI to the potent vasoconstricting octapeptide angiotensin II (AngII) by removal of the C-terminal His-Leu (Skeggs et al., 1954; Skeggs et al., 1956). AngII mediates its effects via either the angiotensin II type I (AT_1) receptor or the angiotensin II type II (AT_2) receptor which exhibit opposing outcomes (Gasparo et al., 1995). Stimulation of the AT_1 receptor leads to vasoconstriction, release of aldosterone from the adrenal cortex which leads to

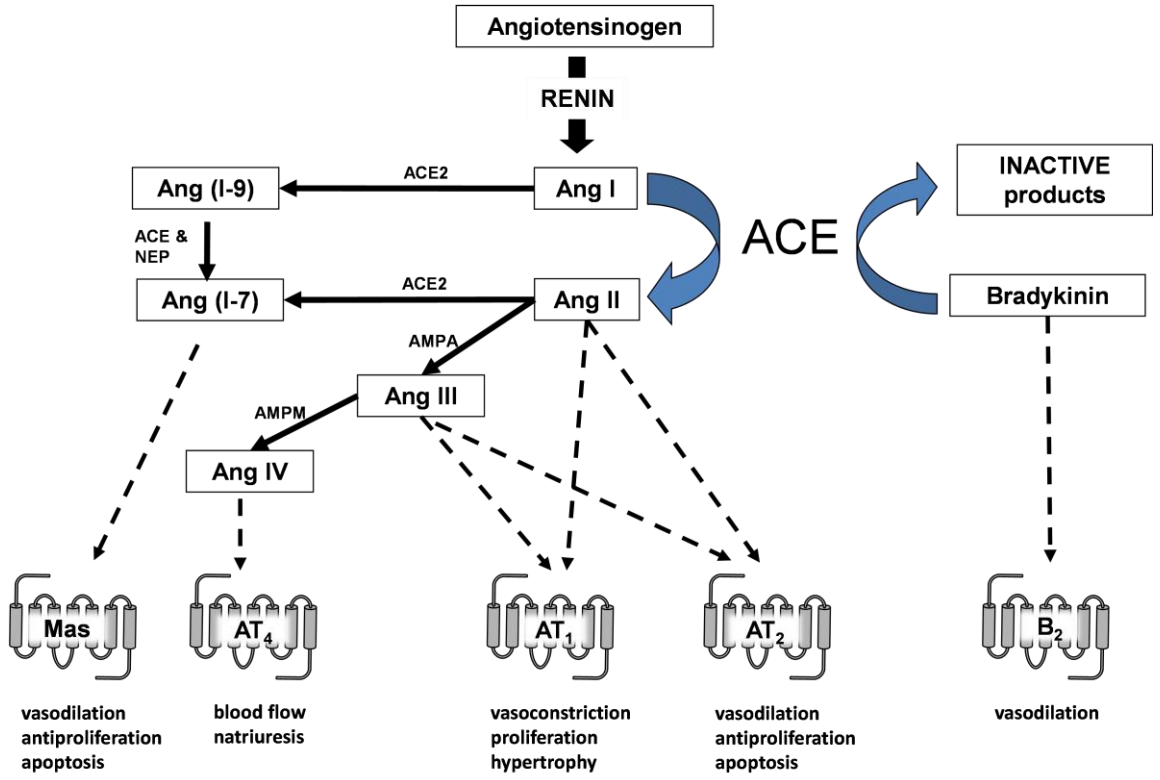

Figure 1.5 Role of ACE in the Renin-Angiotensin System. (adapted from Acharya et al., 2003; Fyhrquist and Saijonmaa, 2008). Solid lines indicate conversion of a peptide to a product, while broken arrows indicate action of a hormone on a receptor. Enzymes involved: Angiotensin converting enzyme (ACE); Angiotensin converting enzyme 2 (ACE2);Neutral endopeptidase (NEP); aminopeptidase A (AMPA); aminopeptidase M (AMPM); BK receptor (B2).

sodium retention and water readsorption, sympathetic activation and cell growth proliferation (Timmermans et al., 1992; Timmermans et al., 1993). Conversely, the effects of AT_2 stimulation result in vasodilation, growth and proliferation inhibition, differentiation and apoptosis, although this receptor is only highly expressed during foetal development and is vastly reduced after birth (Horiuchi, 1996; Csikós et al., 1998; Lazard et al., 1994; Shanmugam & Sandberg, 1996).

Whilst the central angiotensinogen-AngI-AngII pathway is core to the RAS, a number of other bioactive angiotensin peptide forms exist, which contribute to the complexity (Figure 1.5). The ACE homologue, ACE2, cleaves both AngI and AngII into angiotensin(1-9) and angiotensin(1-7) respectively, where ACE (as well as neural endopeptidase) also converts the inactive angiotensin(1-9) peptide into the vasodilatory angiotensin(1-7) although

cleavage of AngII to Ang(1-9) is the predominant route (Donoghue et al., 2000; Turner et al., 2002). Angiotensin (1-7) mediates its effects via the Mas G-protein coupled receptor (Santos et al., 2003), which is interestingly increased in the context of an activated RAS (Nakamoto et al., 1995; Iyer et al., 2000; Nakamura et al., 2003). Angiotensin III (AngII) is generated by the action of aminopeptidase A on AngII, and stimulates the AT1 and AT2 receptors in a similar manner to AngII (Wright and Harding, 1997; Ardaillou and Chansel, 1997). Of importance is the aminopetidase M-mediated conversion of AngIII to angiotensin IV, which binds to the AT4 receptor (Swanson et al., 1992; Albiston et al., 2001) and is linked to renal and cerebral blood flow, neuronal development and memory formation & retention (Wright and Harding, 1997). The critical role of the RAS is demonstrated by transgenic mice models, where knockout of angiotensinogen (Kim et al., 1995), renin (Yanai et al., 2000), ACE (Krege et al., 1995; Esther et al., 1996) and AT1 receptor (Ito et al., 1995; Chen et al., 1997; Tsuchida et al., 1998; Oliverio et al., 1998) all resulted in significant reductions in blood pressure when compared to wildtype controls.

Additionally, there is significant interplay between the RAS and the kallikrein-kinin system (KKS). The vasodilatory peptide bradykinin (BK) is produced by the action of plasma kallikrein on the high molecular weight glycoprotein precursor kininogen (Bhoola et al., 1992). Tissue kallikrein can also cleave this kininogen, as well as a second low molecular weight kininogen, into kallidin. The kinin type II (B2) receptor is the primary target of these kinin peptides, which results in vasodilation, although the kinin type I (B1) receptor (which is upregulated during tissue damage) can also be triggered by products of kinin-carboxypeptidase activity (des-Arg9-bradykinin and des-Arg10-kallidin) (Regoli et al., 1989). ACE has been shown to inactivate the vasodilatory BK into inactive products (Erdos & Yang, 1967; Yang et al., 1970; Yang et al., 1971) via sequential C-terminal didpeptidyl degradation at the Pro7-Phe8 and Phe5-Ser6 scissile bonds (Baudin, 2002). Further interaction between the systems is seen where kallikreins have been shown to activate pro-renin (Sealey et al., 1979) and can generate AngII directly from angiotensinogen (Yamaguchi et al., 1991; Sasaguri et al., 1995). The latter ability to generate non-renin-mediated AngII may be quite important as recent work by Guimaraes et al (2011) show that AngII interacts with ACE to trigger calcium signalling, potentially via a physical interaction with the AT1 receptor.

1.2.2 Non-BP regulating roles for ACE hydrolysis activity

A study by Shen et al (2007) generated transgenic mice that overexpressed ACE in macrophages by switching control of the ACE locus to the macrophage specific c-fms promoter. Challenge of these mice using an aggressive mouse melanoma cell line showed that they were remarkably resistant to tumour growth and resulted in increased interleukin-12 and nitric oxide. The same transgenic mice were challenged with Listeria and methicillin-resistant *Staphylococcus aureus* and shown to have 50-fold lower levels of bacterial load with similar increases in nitric oxide (Okwan-Duodu et al., 2010). This enhanced inflammatory response with ACE overexpression is attributed to ACE being involved in processing the C-terminus of antigenic peptides for presentation by MHC Class I molecules thus enhancing the efficiency of antigen-specific CD8+ T cell priming (Shen et al., 2008).

ACE was first linked to Alzheimer's disease using genetic studies where the I allele of and insertion (I)/deletion(D) polymorphism in intron 16 of ACE, which leads to reduced ACE plasma levels, was associated with an increased risk for disease progression, whereas the D allele that produced increased ACE plasma levels was associated with protection (Rigat et al., 1990; Kehoe et al., 1999; Elkin et al., 2004; Lehmann et al., 2005). ACE has been shown to degrade amyloid β peptides, which are responsible for plaque formation, both *in vitro* (Hemming & Selkoe, 2005; Oba et al., 2005) and *in vivo* where it has been suggested that ACE conversion of amyloid-β peptide 1-42 to amyloid-β peptide 1-40 preventing plaque formation (Zou et al., 2007). ACE inhibitors have been shown to enhance cognitive function in mouse models (Yamada et al., 2010) suggesting ACE hydrolysis generates plaque forming products of amyloid-β peptide; however, there remains contention as to the exact cleavage sites and domain contributions (Hu et al., 2001; Oba et al., 2005; Zou et al., 2007). Further complicating the picture is the fact that angiotensin receptor blockers (ARB's) also prevent amyloid-β associated cognitive impairment (Takeda et al., 2009), which suggests that the brain RAS, of which ACE is a key part, is also playing a role. The exact role of ACE in this remains contentious and is under active investigation in our laboratory.

N-acetyl-seryl-aspartyl-lysyl-proline (AcSDKP) is a widely expressed peptide that is a natural inhibitor of pluripotent hematopoietic stem cell proliferation (Lenfant et al., 1989; Bonnet et al., 1993), elicits anti-fibrotic effects by suppressing the differentiation of human cardiac fibroblasts into myofibroblasts (Rasoul et al., 2004; Peng et al., 2010), and has been linked

to promotion of angiogenesis *in vivo* and *in vitro* (Wang et al., 2004). Critically, AcSDKP is hydrolysed almost exclusively by ACE (Hanesworth et al., 1993), with ACE inhibition *in vivo* showing reduced levels of peptide (Azizi et al., 1996; Azizi et al., 1997). This highlights the critical role ACE plays in modulating levels of this critical peptide.

Testis ACE (tACE), an isoform of ACE which is expressed exclusively in the germinal sperm cells has been shown to be critical in fertility. Male mice with tACE knocked out produce normal numbers of sperm with normal motility, yet reproduce poorly (Krege et al., 1995; Esther et al., 1996; Hagaman et al., 1998). Fuchs et al (2005) showed work to indicate that dicarboxypeptidase activity, and not just the presence of tACE, is crucial for male fertility, although this remains an unconfirmed finding pending independent verification.

ACE has also been shown to possess endopeptidase activity, hydrolyzing substrates that are amidated at the carboxyl terminus (reviewed by Eriksson et al., 2002). Substrates implicated as targets of ACE endopeptidase activity include the neuropeptides substance P and cholecystokinin, as well as the gonadotropin releasing hormone (GnRH), which is blocked at both the N- and C- termini yet can be cleaved into several di-and tri-peptides (Skidgel & Erdos 1985; Skidgel et al., 1987; Jaspard et al., 1993). The physiological roles for these peptides are unclear, however, substance P has been found to co-localise in specific areas of the brain (Defendini et al., 1983; Matsas et al., 1984; Strittmatter et al., 1984; Oblin et al., 1988; Barnes et al., 1988).

1.2.3 Domain selective ACE hydrolysis

As has been discussed, ACE is primarily involved in the RAS where it converts AngI to AngII, as well as hydrolysing angiotensin(1-9) and (1-7) to angiotensin (1-7) and (1-5), respectively. It also hydrolyzes bradykinin, a component of the KKS, to the inactive bradykinin (1-7). Outside of this primary function though, ACE has also been implicated in a number of other physiological roles and shown to hydrolyze a number of highly diverse substrates (Figure 1.6). ACE also possesses endopeptidase activity, hydrolyzing substrates that are amidated at the carboxyl terminus (Eriksson et al., 2002). Substrates implicated as targets of ACE endopeptidase activity include the neuropeptides substance P and cholecystokinin, as well as the gonadotropin releasing hormone (GnRH), which is blocked at both the N- and C-

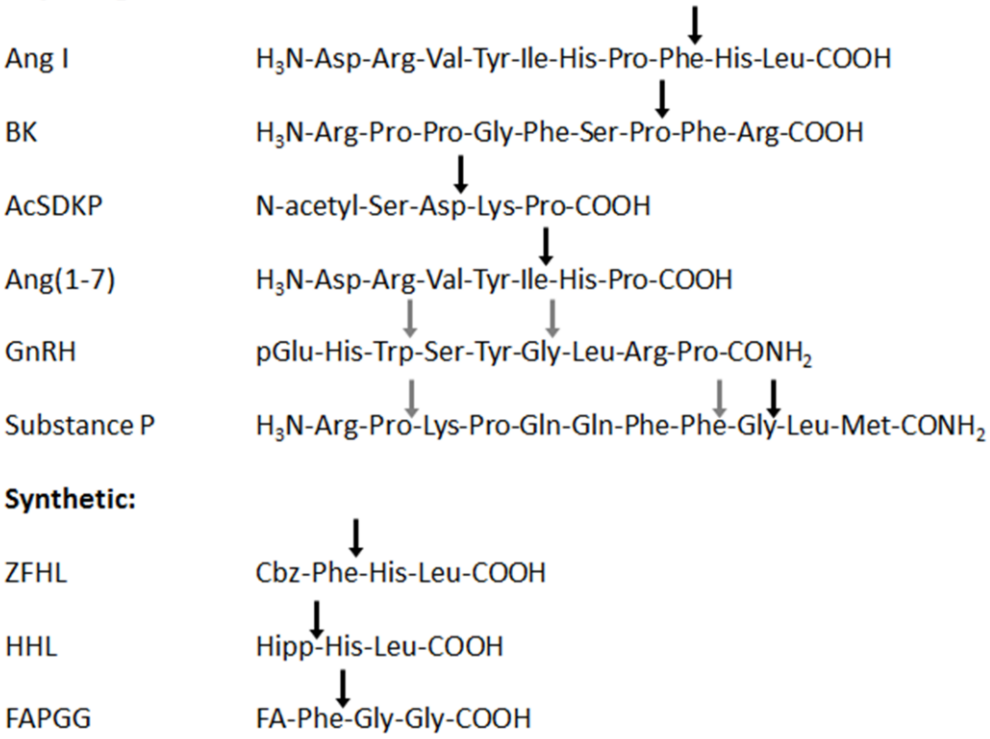

Figure 1.6 Physiological and synthetic substrates of ACE. Peptide bond cleavage position is indicated by an arrow which is black for dipeptidyl carboxypeptidase activity and grey for endopeptidase activity. Pyroglutamic acid (pGlu); amidated C-termini (CONH2); Carboxybenzyl (Cbz); Hippuric acid (Hipp); Furylacryloyl (FA).

termini yet can be cleaved into several di-and tripeptides (Eriksson et al., 2002; Skidgel & Erdos 1985).

Of great importance when looking at ACE substrates is the fact that there are two catalytically active domains in sACE, both highly homologous, yet different enough to display varying substrate specificities (discussed below) and chloride dependence (Wei et al., 1991b; Wei et al., 1992) for each of the large plethora of ACE substrates.

Both the C and N domains have equal binding affinity for AngI, yet the C-domain hydrolyses this substrate more efficiently both *in vitro* (Wei et al., 1991b) and *in vivo* (Fuchs et al., 2008). Interestingly, when the domains are expressed separately, the N-domain exhibits 2-3 fold higher activity than the C-domain (Liu et al., 2001), which indicates a role for domain cooperativity in the context of sACE (Binevski et al., 2003). The C-domain for AngI has a

higher dependence on chloride than the N-domain (Wei et al., 1991b; Liu et al., 2001). This chloride dependence trend is not seen only with AngI, but also for many other domain-selective substrates although the trend varies for each. For instance, BK is cleaved with equal efficiency by both domains and exhibits no significant difference in chloride requirement between domains (Jaspard et al., 1993).

This domain variability extends to most other ACE substrates, physiological or synthetic. The N-domain preferentially cleaves AcSDKP by 50-fold over the C-domain *in vitro* (Rousseau et al., 1995), with the C-domain having a 6-fold higher requirement for chloride (Rousseau-Plasse et al., 1996). The domain selectivity was confirmed *in vivo* by using the highly N-domain specific inhibitor RXP407 which resulted in 6-fold higher AcSDKP levels in mice (Junot et al., 2001). The N-domain also presents a higher catalytic rate over C-domain for LHRH (GnRH) (Ehlers and Riordan, 1991, Jaspard et al., 1993) as well as Ang(1-7) (Deddish et al., 1994), although Rice et al (2004) found that the specificity was similar between domains. Conversely, like AngI, substance P is hydrolysed faster by the C-domain in a chloride dependent manner (Jaspard et al., 1993).

ACE activity has long been characterized using synthetic analogue substrates derived from physiological peptides. Hippuryl-His-Leu (HHL) and Z-Phe-His-Leu (Z-FHL) are both analogues of AngI, yet show very different domain preferences and chloride dependent profiles. Like AngI, HHL is preferentially cleaved by the C-domain in a chloride dependent (Friedland &

Silverstein, 1976). However, whilst the N-domain shows no difference in chloride affinity between AngI and HHL, the C-domain has a 40-fold higher requirement for chloride with HHL than AngI (Wei et al., 1991b). Conversely, Z-FHL has been shown to be hydrolysed at fairly similar rates for both domains (Danilov et al., 1994), with the Phe in the P1 position suggested to mediate this difference (Michaud et al., 1997). Z-FHL has been shown to be chloride dependent in the C-domain (Moiseeva et al., 2005), however there is no comparative evidence in the literature for the N-domain in this regard. Furylacryloyl-Phe-Gly-Gly (FAPGG) is another synthetic peptide which is cleaved in a chloride dependent manner to yield the Gly-Gly dipeptide, however no domain bias has been shown as it has only been assessed with sACE (Holmquist et al., 1979; Beneteau et al., 1986; Baudin, 2002).

Thus, the large discrepancies in chloride dependence and domain preference for the different substrates is well described, but poorly understood.

1.2.4 Physiological relevance of chloride dependence

It has long been established in the literature that ACE activity is dependent on chloride, with the degree of dependence being substrate specific (Shapiro et al., 1983). As already mentioned, ACE's most established physiological role is in the RAS. It is situated mainly on the surface of endothelial tissue, an environment where blood plasma chloride levels rarely fluctuate from the 100mM average, sufficient chloride for ACE to be considered fully active in angiotensin I hydrolysis (Shapiro et al., 1983). However, ACE is not found solely in vascular endothelial tissue and has been found in other non-vascular tissues where the chloride levels can vary quite substantially.

For instance, the dipeptidyl carboxypeptidase activity of tACE has been implicated in being essential for male fertility, where male mice with enzymatically inactive tACE produce normal, motile sperm yet have poor reproductive efficiency, suggesting tACE expression on the sperm cells is involved (Fuchs et al., 2005). Whilst the exact substrate for tACE in this context is unknown, the chloride concentration in the semen environment varies from 31.6mM (Jeyendran et al., 1989) to 45mM (Rosecrans et al., 1987), which might be significant if a substrate has a high requirement for chloride.

Another tissue region with variable chloride concentrations is in the brain, where the tissue specific brain RAS mediates, apart from normal RAS physiological function, a role in memory and learning thought to be via the angiotensin IV/AT_4 receptor interaction (reviewed by Wright & Harding, 2004). Outside of RAS function, ACE has been shown to hydrolyse several neuropeptides such as enkephalin, substance P, dynorphin and neurotensin (Skidgel & Erdos, 2004; van den Buuse et al., 2005). Chloride plays a major role in the repolarization of depolarized cells (Hille 1992; Inoue et al. 2005), most notably where the transmembrane distribution of chloride anions determines the direction of the chloride flux through the γ-aminobutyric acid (GABA) and glycine receptors, thus moderating signalling in neurons (De Koninck, 2007; Kroeger et al., 2010). In evaluating the $GABA_A$ receptor-mediated response in different layers of the rat hippocampus, Kroeger et al (2010) found large fluctuations in extracellular chloride concentrations, which ranged from ~20mM up to ~260mM in

response to stimulation. Whilst ACE is not expressed in the hippocampus (Strittmatter et al., 1984), this does suggest that there could be similarly large fluctuations in chloride levels in other regions of the brain where ACE does function. Indeed, altered chloride homeostasis is implicated in a number of neurological disorders, and has been suggested as a means by which the microglia can modulate neuronal excitability (reviewed by De Koninck, 2007). ACE has been implicated in regulation of dopamine turnover (Jenkins et al., 1997), which has been linked to sensorimotor gating and schizophrenic pathology (van den Buuse, 2005). The exact mechanisms for this role are unknown, but it is modulated by captopril, suggesting that ACE hydrolysis might be involved and where the chloride dependent nature of ACE substrates may be a relevant factor.

ACE has also been detected intracellularly in kidney mesangial cells, where it is upregulated by high glucose stimulation and has been suggested to modulate AngII levels along with chymase (Andrade et al., 1998; Cristovam et al., 2008). In the context of chloride dependence, the chloride concentration intracellularly is ~5mM (Lodish, 1999) which would have an impact on ACE catalytic efficiency. Further to this is the effect that other factors, such as pH, have on chloride dependent activity, factors that are not necessarily constant in local environments (Shapiro et al., 1983). This has implications for localized ACE activity, not only with tissue RAS systems, but more likely with other non-RAS substrates and suggests that particular substrates can be selectively hydrolysed under certain local *in vivo* conditions, leaving other substrates relatively untouched (Shapiro et al., 1983).

Variance in chloride activity is also seen in inhibitor binding. The difference in affinities for the ACE inhibitors trandolaprilat, enalaprilat, and lisinopril between the N- and C-domains is greater at high chloride concentration (300 mM), whereas for captopril, the difference is larger at low chloride concentration (20mM) (Wei et al., 1992). The variability in chloride mediated enhancement of inhibitor affinity may have potential applications in design of inhibitors targeting tissue specific ACE activity. Indeed, a full delineation of the exact structural and mechanistic aspects of ACE chloride dependence for each domain may play a role in development of domain selective inhibitors.

1.3 Chloride dependent substrate hydrolysis

The exact mechanisms of chloride dependence in ACE and the relation to substrate composition is poorly understood. Some mutagenic and structural work has been done to contribute to understanding this phenomenon and is summarised in the following sections.

1.3.1 Chloride 1 pocket

The chloride 1 pocket of tACE (C-domain) has been suggested to be involved in C-terminal stabilisation of substrates (Guy et al 2003, Natesh et al 2003, Sturrock et al 2004). The crystal structure of the N-domain of ACE shows no chloride bound in this pocket, where the only residue difference is a H164 in place of the chloride coordinating R186 in tACE (Figure 1.7) (Corradi et al., 2006). Tzakos et al (2003) propose that it acts as a synergistic anion promoting high affinity substrate binding. They suggest that when Cl1 isn't bound, K511 (K489 of N-domain), a residue important in stabilization of the C-terminal carboxylate of lisinopril, could form amino-aromatic interactions with three tryptophans at positions 279, 485 & 486 (257, 463 & 464 of N-domain) that form part of the Cl1 pocket. When Cl1 is bound, it is coordinated by W279 in tACE (W257 of N-domain) which may disrupt these interactions allowing the aforementioned lysine to stabilize the C-terminal carboxylate of the substrate (Tzakos et al., 2003). Rushworth et al (2008) found that mutation of R186, W279 and R489 (the other chloride coordinating residue) to Glu, Ala and Glu respectively resulted in a marked decrease in chloride dependence in tACE for all mutants. This was the first evidence that indicated that this pocket had an effect on activity. A kinetic assessment by Moiseeva et al (2005) suggested that binding of chloride in this pocket in tACE had an inhibitory role at high chloride concentrations. They proposed that, in the absence of chloride, D507 would form a salt-bridge with K511, and with chloride binding the D507 would switch to form a salt-bridge with R501 and allow K511 to swing into the active site and participate in stabilization of the carboxylate of the substrate. Liu et al (2001) evaluated the chloride dependent profiles for a number of tetrapeptides that differed in their P1' and P2' residue identities, yet the P2 and P1 residues were identical (an acetylated Ala and a Phe) across all peptides. What was very clear was that the nature of the P' dipeptide structure greatly affected chloride dependence (Liu et al., 2001). However, a lack of structural data and knowledge of the presence of a chloride 1 pocket prevented any further

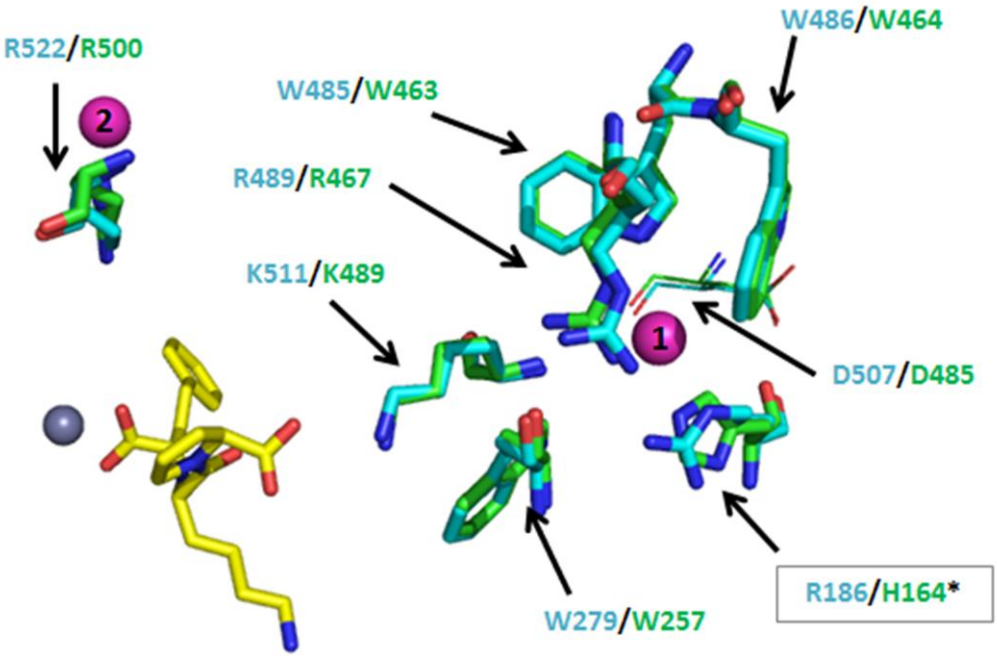

Figure 1.7 Residues comprising the chloride 1 pocket of ACE. Representative stick overlay of tACE-Lisinopril (PDB:1o86) in blue and N-domain-Lisinopril (PDB:2c6n) in green showing residues comprising the chloride 1 pocket as well as C-terminal stabilizing lysine (K511/K489). Residue labels are shown in the same colour for each domain, with residues differing between domains indicated by a grey box. Lisinopril is shown bound in the active site (yellow sticks), with the active site zinc (grey sphere) and chloride ions (numbered purple spheres) indicated. The position of the chloride 2 pocket is indicated via R522/R500 being adjacent to one of the chloride ions. Images were created using PyMOL 0.99 (DeLano Scientific, Palo Alto, CA, U.S.A).

interpretation of this data. The mutagenic work of Rushworth et al (2008) and the evidence that interactions of substrate within the S1' and S2' pockets, which share residues with the chloride 1 pocket, showed effects on chloride dependence indicates that chloride binding at this site in tACE is relevant to catalysis.

1.3.2 Chloride 2 pocket

The crystal structure of tACE has given us the exact positions of all residues in proximity to the chloride ions and active site (Figure 1.8); however, the exact mechanism has not proved easy to unravel. As mentioned, Arg522 in tACE (Arg1098 in sACE) has already been implicated in playing a crucial role in chloride dependence with AngI as substrate (Liu et al., 2001). When the arginine at position 522 was mutated to a glutamine, a residue with a

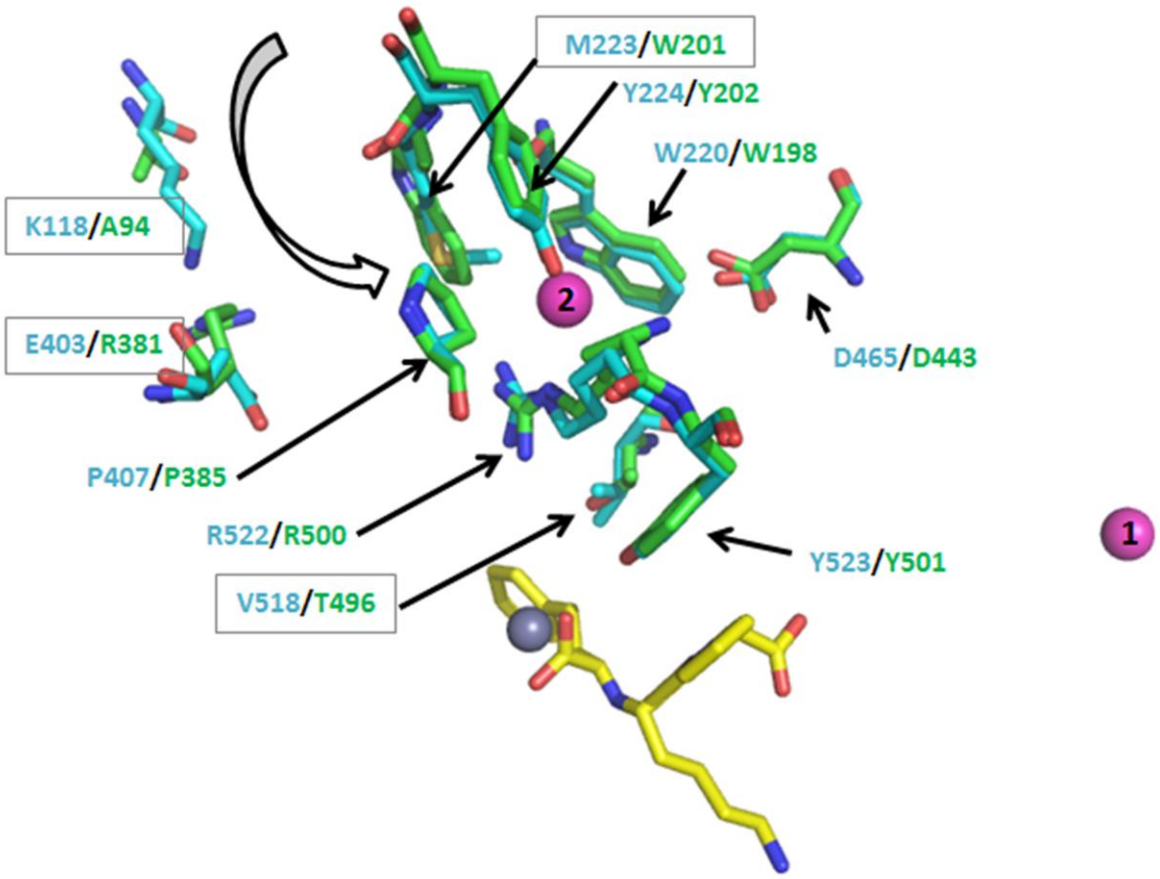

Figure 1.8 Residues comprising the chloride 2 pocket of ACE. Representative stick overlay of tACE-Lisinopril (PDB:1o86) in blue and N-domain-Lisinopril (PDB:2c6n) in green showing residues comprising the chloride 2 pocket as well as well as E403/R381 which is situated in the S2 active site sub-site pocket. Residue labels are shown in the same colour for each domain, with residues differing between domains indicated by a grey box. Path of proposed chloride channel mediating access to the chloride 2 pocket is indicated by the curved arrow. Lisinopril is shown bound in the active site (yellow sticks), with the active site zinc (grey sphere) and chloride ions (numbered purple spheres) indicated. Images were created using PyMOL 0.99 (DeLano Scientific, Palo Alto, CA. U.S.A).

smaller side chain that lacks a positive charge, there was a resultant loss of chloride dependent activation (Liu et al., 2001; Rushworth et al., 2008). When the same arginine was replaced with a lysine, also a basic residue, chloride dependence was largely restored although it had an approximately 100-fold decrease in chloride binding affinity (Liu et al., 2001). Activation experiments using other monovalent halides of varying radii, such as bromine, iodine and fluorine, on the Arg1098 to Lys substitution mutant suggests that the spatial geometry of anion-liganding residues within the binding site is of importance (Liu et

al., 2001). Tzakos et al (2003) have suggested that R522 may act as a carrier of Y523, which is proposed to stabilize the tetrahedral transition-state intermediate of the substrate. R522 would form a salt bridge with D465 in the absence of chloride, where chloride binding would disrupt this salt-bridge, R522 would coordinate the chloride ion and allow Y523 to swing into the active site (Figure 1.8). The chloride 2 pocket shows some variation between the domains, where M223 corresponds to W201 and V518 corresponds to T496 in the C and N-domains, respectively (Natesh et al., 2003; Corradi et al., 2006). Conversion of V518 to a Thr in tACE has been shown to have reductions in both activity with a small fluorogenic peptide and affinity of the inhibitors RXP407 and RXPA380 (Kroger et al., 2009). This is ascribed to its location in the S1 pocket where it presumably disrupts substrate/inhibitor interactions (Kroger et al., 2009), however whether this has any effect on chloride dependence is not clear.

1.3.3 Chloride channel

In exploring possible mechanisms of chloride dependence in ACE, Tzakos et al (2003) proposed the presence of a "chloride channel" mediating access of chloride to the chloride 2 pocket, which was based on structural comparison with *Salmonella enterica* serovar *typhimurium* CLC Chloride channels described by Dutzler et al (2002). It was proposed that E403 (tACE numbering) forms a potent salt-bridge with R522 in the absence of chloride, and that chloride binding would disrupt this interaction, coordinate R522 and allow Y523 to swing into the active site (Figure 1.8) (Tzakos et al 2003). Furthermore, K118 residue was proposed to enhance the R522-E403 salt bridge by also forming a salt bridge with E403. Mutation of the residues that corresponded to K118 in other ACE homologues, K154 in rabbit testicular ACE (Sen et al., 1993), and K694 of rabbit lung ACE (Chen et al., 1990), reduced chloride sensitivity, thus highlighting its potentially critical role. That Tzakos suggested that R522 formed salt-bridges with both E403 and D465 in the absence of chloride, a seemingly unlikely occurrence given their spatial proximity, is indicative of the lack of clarity on the mechanisms involved (Figure 1.8). Mutagenic structure-function studies are required to ascertain the exact role that each of these residues, or combination of residues, plays on the chloride dependent activity of ACE.

Hypothesis

Substrate composition and interactions within the active site are critical in modulating the chloride dependent response via structural disruption/facilitation of specific interactions governed by a few key residues.

Aims and objectives of this study

All ACE substrates, either physiological or synthetic, show varying degrees of chloride dependence, which indicates that substrate composition is important. Variability in the substrate P' composition was shown to affect chloride binding (Liu et al., 2001). Furthermore, the S' sub-pockets are also affected by mutations in the chloride 1 pocket (Rushworth et al., 2008). The chloride coordinating R522 in tACE has been shown to be catalytically important (Liu et al., 2001), and theoretical work has provided insights into possible mechanistic interactions of R522 (Tzakos et al., 2003), however no adequate experimental evidence has been produced in their support. Tzakos et al (2003) also proposed a "chloride gated channel" mediated by E403 in the S2 sub-pocket, which would block access of chloride to the chloride 2 pocket in the C-domain alone. The aim of this study was to probe how substrate interactions in the prime and non-prime sides of the active site contribution to the chloride mechanism(s) of tACE and how key residues moderate these effects. This would be done using a combination of structural, kinetic and thermodynamic approaches.

The following objectives have been identified:

1. Design, expression and purification of key Chloride 1 and 2 pocket mutants in which tACE (C domain) residues were either converted to their corresponding N-domain residues, or converted to specific residues if conserved between domains.
2. Assessment of mutant constructs using chloride titrations with HHL and Z-FHL to determine whether chloride binding is altered.
3. Establishment of an Isothermal Titration Calorimetric method for the determination of ACE kinetic constants.

4. Kinetic characterisation of constructs using angiotensin I and two of its analogues, Z-FHL and HHL to determine whether substrate interactions in the S2 pocket contribute to a chloride gating mechanism.
5. To determine the contributions of key residues in both chloride pockets to the kinetic and thermodynamic parameters of HHL, Z-FHL and angiotensin I hydrolysis in the presence and absence of chloride.
6. Generate a structural rationale for the chloride dependence mechanisms based on substrate composition.

Chapter 2: Cloning and Mutagenesis of tACE Constructs

2.1 Introduction

In order to investigate the role that certain residues play in modulating the chloride – dependent profile of the C-domain of ACE (as described in Chapter 1), a number of tACE mutants were constructed. The rationale for these mutations was based on a number of points, namely:

A) R186 within the C-domain chloride 1 binding pocket corresponds to a histidine in the N-domain, where no chloride binding is observed, hence mutating the R186 to a histidine would provide insight into the role of this pocket.

B) The chloride 2 pocket contains certain residues that were postulated by Tzakos et al. (2003) as playing a role in chloride binding (M223 and V518), which were converted to their corresponding variable N-domain counterparts (Trp and Thr, respectively). The mechanistically important R522 and potentially important D465 in the C-domain, which are conserved in the N-domain (R500 and D443), were converted to residues that would change the chemical functionality of the side-chain in order to probe their effects.

C) E403 was suggested to act as an ionic gate to a proposed chloride channel in the chloride 2 pocket in the C-domain, and was converted to an Arg, which is the corresponding residue in the N-domain.

Therefore, the objectives of this section of work were:

1. Sub-cloning of the minimally glycosylated tACEΔ36g13 coding DNA region, lacking the 36 amino acid N-terminal *O*-glycosylated region and retaining only the 1st and 3rd (of 7) N-glycosylation sites, into the pcDNA 3.1(+) mammalian expression vector.

2. To engineer a double stop codon to ensure termination of translation at S625, just short of the natural cleavage site of tACE which is after R627, and hence generate a soluble tACE construct.

3. To generate a suitable intermediary shuttle construct using pBluescript SK(+) and containing only the first 3 of 4 tACE1,3 cDNA fragments to facilitate the assembly of fragments into the pcDNA_ tACEΔ36g13sol expression vector.

4. Using site-directed mutagenesis to generate the mutations hypothesized to affect chloride activation within the appropriate gene fragments (Fig 2.1), each contained within the pGEM11Zf+ shuttle vector.

5. To subclone these mutated fragments, directly for fragment 4 or via the intermediary shuttle construct for fragments 2 & 3, into the pcDNA_tACEΔ36g13sol expression vector for subsequent transfection and expression.

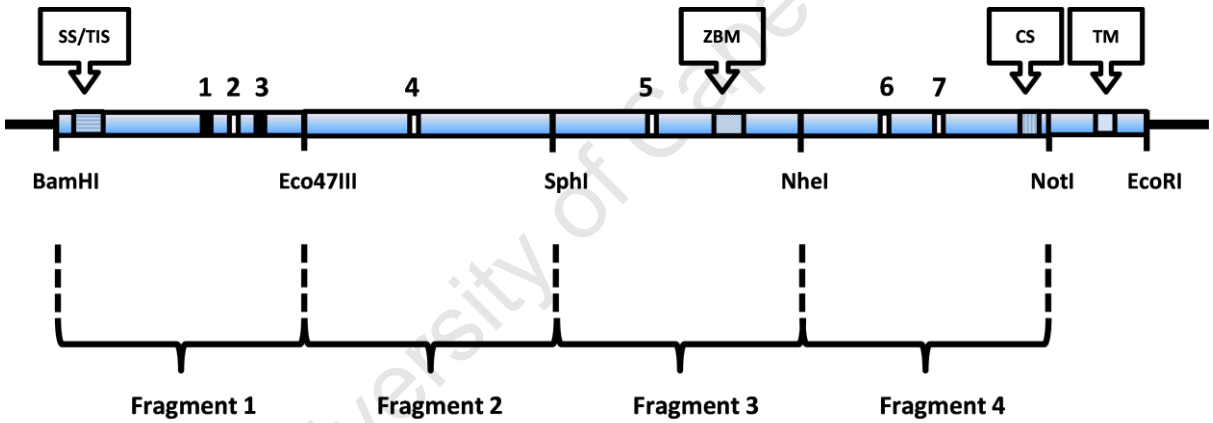

Figure 2.1 Schematic representation of the tACEg1,3 cDNA organisation. The relevant coding region for the soluble tACEg1,3 construct is contained between *BamHI* and *NotI*, with the region between *NotI* and *EcoRI* containing the transmembrane anchor (TM; block containing zigzag stripes) as well as the natural stop codon. For subsequent sub-cloning and mutagenesis purposes the cDNA between *BamHI* and *NotI* is separated into 4 fragments, using the restriction endonuclease sites indicated, each contained with the pGEM11Zf+ cloning vector (constructed as part of Dr Kerry Gordon's M.Sc thesis). The region encoding the zinc-binding motif (ZBM) is indicated by diagonal stripes, with the signal sequence/transcription initiation site (SS/TIS) and cleavage site (CS) indicated by horizontal and vertical stripes, respectively. The potential N-linked glycosylation sites are indicated by the numbered blocks (1-6), with number 7 being a potentially O-linked glycosolation site, with the two minimally required sites that are still intact (solid black) and the remainder having been knocked out (solid white).

2.2 Methods & Experimental Approach

2.2.1 Chemicals

All restriction endonucleases used (*Bam*HI, *Sph*I, *Eco47*III, *Nhe*I, *Not*I, *Sca*I, *Asc*I, *Ppu*MI, *Bse*RI, *Dra*III, *Eco*NI), as well as their buffers, were acquired from either Roche, New England BioLabs or Fermentas. Both *E.coli* strains (XL1-Blue and JM110) used for sub-cloning work, as well as the pBluescript SKII+, were purchased from Stratagene. Promega supplied the Pfu polymerase with buffer, Polymerase chain reaction (PCR) nucleotide mix, $MgCl_2$, *Dpn*I restriction endonuclease with buffer, pGEM11Zf+ DNA vector and Wizard SV Gel Purification System. The T4 DNA Ligase with ligation buffer were supplied by Fermentas, with InVitrogen being the source of the pcDNA3.1(+) mammalian expression vector. Fermentas supplied the Fermentas GeneRuler™ DNA Ladder Mix (100-10,000 bp). QIAGEN were the source of the Midi-Prep Plasmid Purification Kit. All DNA primer synthesis was performed by Inqaba Biotech, who also performed some of the DNA sequencing, with the remainder done in-house by the Division of Human Genetics, Faculty of Health Sciences, UCT.

2.2.2 Methods

2.2.2.1 Site-directed mutagenesis

Site-directed mutagenesis was performed using the DpnI method, with the protocol having been adapted from Papworth et al (1996). The DpnI method involves using primers that overlay and extend either side of the nucleotide bases that are to be mutated (Figure 2.2). These primers are almost exactly complementary to each other, only differing in those bases that need to be changed, and therefore bind to both strands of the target sequence that is contained within a plasmid vector. Primer extension using a high fidelity DNA polymerase with 3' to 5' exonuclease activity generates a nicked daughter strand containing the desired mutation. Undesired exponential amplification of the daughter strand is avoided as any primers that bind do so at the 3'-end and the nick prevents primer extension in the other

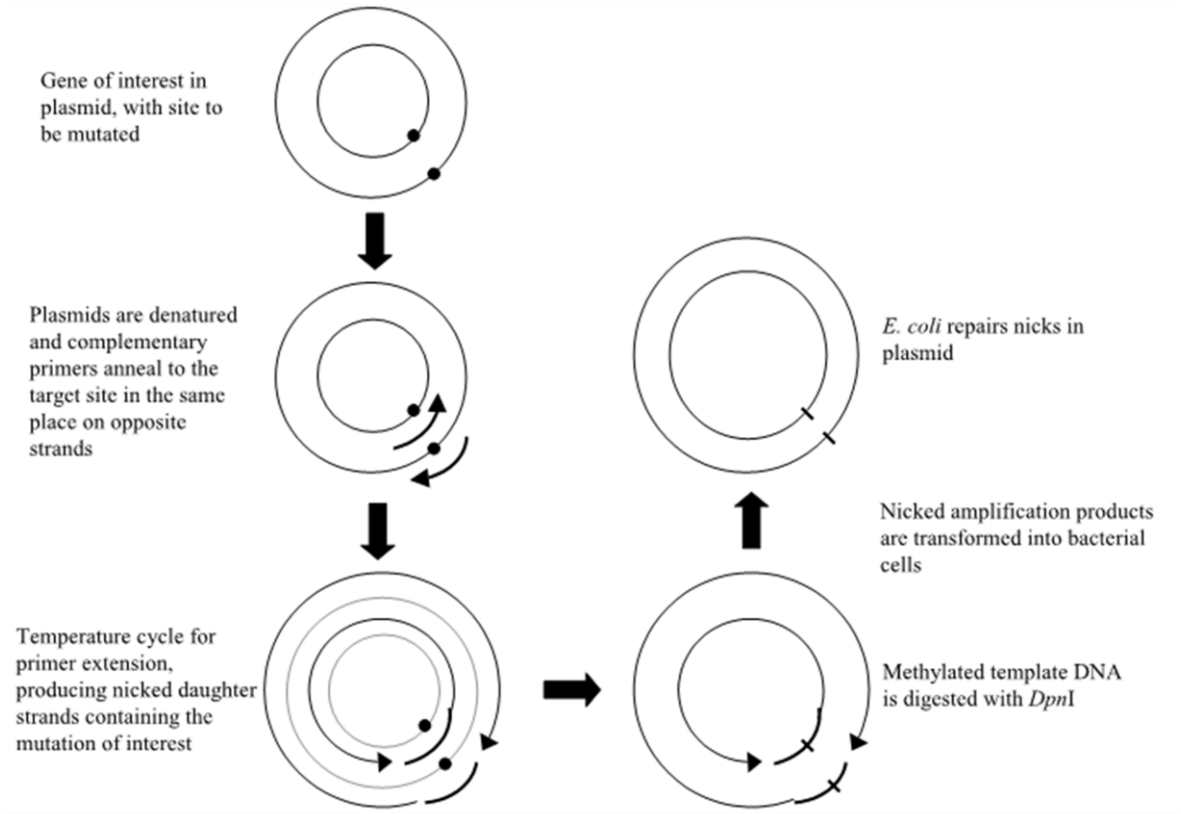

Figure 2.2 Schematic of the DpnI site-directed mutagenesis methodology. (Taken from Papworth et al., 1996)

direction. The primers, template DNA, free nucleotides and DNA polymerase are subjected to a number of thermocycles (of template separation, primer annealing and primer extension) resulting in a mixed population of original template and daughter strands. Exposure of this mixture to DpnI restriction endonuclease digestion, which is specific for methylated DNA, results in only the original template DNA being degraded, hence selecting for the unmethylated, mutated DNA amplicons. Transformation of this DNA into *E.coli* results in repair of the nicked strands and facilitates amplification of the DNA for screening purposes.

The thermocycling amplification mixture was made up as follows: 5µl 10x polymerase buffer, 4-12µl of 25mM $MgCl_2$, 2µl of 10mM PCR nucleotide mix, 1µl 10µM (+)sense primer, 1µl 10µM (-) sense primer, 10µl of 10ng/µl pCDNA3.1(+) template DNA, 2 units Pfu polymerase and made up

to a total volume of 50µl with sterile dH_2O. A negative control containing no template DNA was included to discount any spurious amplification. An initial incubation of 5 minutes at 94°C was done to activate the polymerase and ensure complete template separation, which was followed by 16 cycles of 94°C for 30 seconds, 55°C for 30 seconds and 75°C for 12 minutes, followed by an extra 20 minutes at 75°C and storage at 4°C. 3µl of each reaction mixture were then visualised using agarose gel electrophoresis. The reaction mixtures were then incubated with 5-10 units of DpnI for 2-3 hours at 37°C, thereafter 10µl of digested reaction mixture were transformed into competent *E.coli* Xl1 Blue cells for screening purposes.

2.2.2.2 Vector/Insert Ligations

Plasmid DNA used for ligations were taken from stock samples that were purified using a QIAGEN MidiPrep Kit according manufacturer's instructions. Double restriction digestion of said DNA was performed and separated by agarose gel electrophoresis; the bands of interest were then excised and purified using the Promega Wizard® SV Gel and Clean-Up System as per manufacturer's instructions. Two microliters of each digested, purified fragment was visualized via agarose gel electrophoresis, along with DNA of known concentration, in order to establish relative concentrations of vector and insert fragments. The ligation reaction mixture contained DNA concentrations at a vector to insert molar ratio of 3:1, along with 2µl 10x ligation buffer, 1 unit T4 Ligase and made up to a total volume of 20µl with sterile dH_2O. A positive control (containing single digested purified plasmid) and a negative control (containing just the purified vector fragment and no insert) were included with each ligation to validate the efficacy of either the ligation or bacterial transformation reaction. Ligation mixtures and controls were incubated in the absence of light and at room temperature overnight, with 10µl of each transformed into competent *E.coli* XL1 Blue cells.

2.2.3 Site-directed mutagenesis

Site-directed mutagenesis was used for two purposes: 1) to introduce double stop-codons just before the natural cleavage site in order to generate a soluble construct; and 2) to introduce the desired chloride pocket mutations into tACEg13. The target sequences were located within

various tACEg13 fragments contained within pGEMZ11f+ (constructs generated by Dr K. Gordon). These fragments of the coding region were used to facilitate bi-directional sequencing data and avoid introducing any deleterious mutations into the coding region of tACEg13. Appropriate primers were designed for sequencing reactions (Table 2.1).

The target DNA for the stop-codon primers was in pGEM_FR4, which contained Fragment 4 (FR4) of the tACEg13 coding region (flanked by the restriction endonucleases *NheI* and *NotI*) within the pGEM11Zf+ vector (see Fig. 2.3). Site directed mutagenesis was performed

Table 2.1. Primer design for site-directed mutagenesis. Complementary primers were designed containing the mutation of interest as well as silent mutations to introduce restriction endonuclease sites that facilitated screening. Sequences shown are that of the forward primers (5'-3') along with the corresponding wildtype sequence for comparison. The altered amino acid codon letters are enlarged, with those letters that have been altered in bold and the recognition sequence for the screening restriction endonuclease underlined. The location of the primer target DNA is indicated in the far right column.

Mutation	RE	Sequence		Location
R186H	AscI	Primer	GGAGGGCTGG**CAT**GACAAGGCGGGGCGCGCCATCCTCC	
		Wildtype	GGAGGGCTGGCGAGACAAGGCGGGGAGAGCCATCCTCC	Fragment 2
M223W	PpuMI	Primer	CGTGGAGGTCC**T**GGTACGAGACACC	
		Wildtype	CGTGGAGGTCTATGTACGAGACACC	Fragment 2
E403R	BseRI	Primer	GTGGCCTTG**AG**GAGGGGTGCCAACCCCG	
		Wildtype	GTGGCCTTGGAGAGGGGTGCCAACCCCG	Fragment 3
D465T	DraIII	Primer	GCTACCTCGTC**ACT**CAGTGGCGCTGG	
		Wildtype	GCTACCTCGTCGATCAGTGGCGCTGG	Fragment 4
V518T	EcoNI	Primer	CCACATTCCTTCTAGC**AC**GCCCTACATCAGGTACTTCG	
		Wildtype	CCACATTCCTTCTAGCGTGCCTTACATCAGGTACTTCG	Fragment 4
R522K	ScaI	Primer	GCGTGCCTTACATCA**AG**TACTTCGTCAGCTTC	
		Wildtype	GCGTGCCTTACATCAGGTACTTCGTCAGCTTC	Fragment 4
R522Q	ScaI	Primer	GCGTGCCTTACATC**CA**GTACTTCGTCAGCTTC	
		Wildtype	GCGTGCCTTACATCAGGTACTTCGTCAGCTTC	Fragment 4
FR4-Stop	PpuMI	Primer	GGACGCCGAACTCC**TGA**CGC**TGA**GAAGGACCCCTCC	
		Wildtype	GGACGCCGAACTCCGCTCGCTCAGAAGGACCCCTCC	Fragment 4

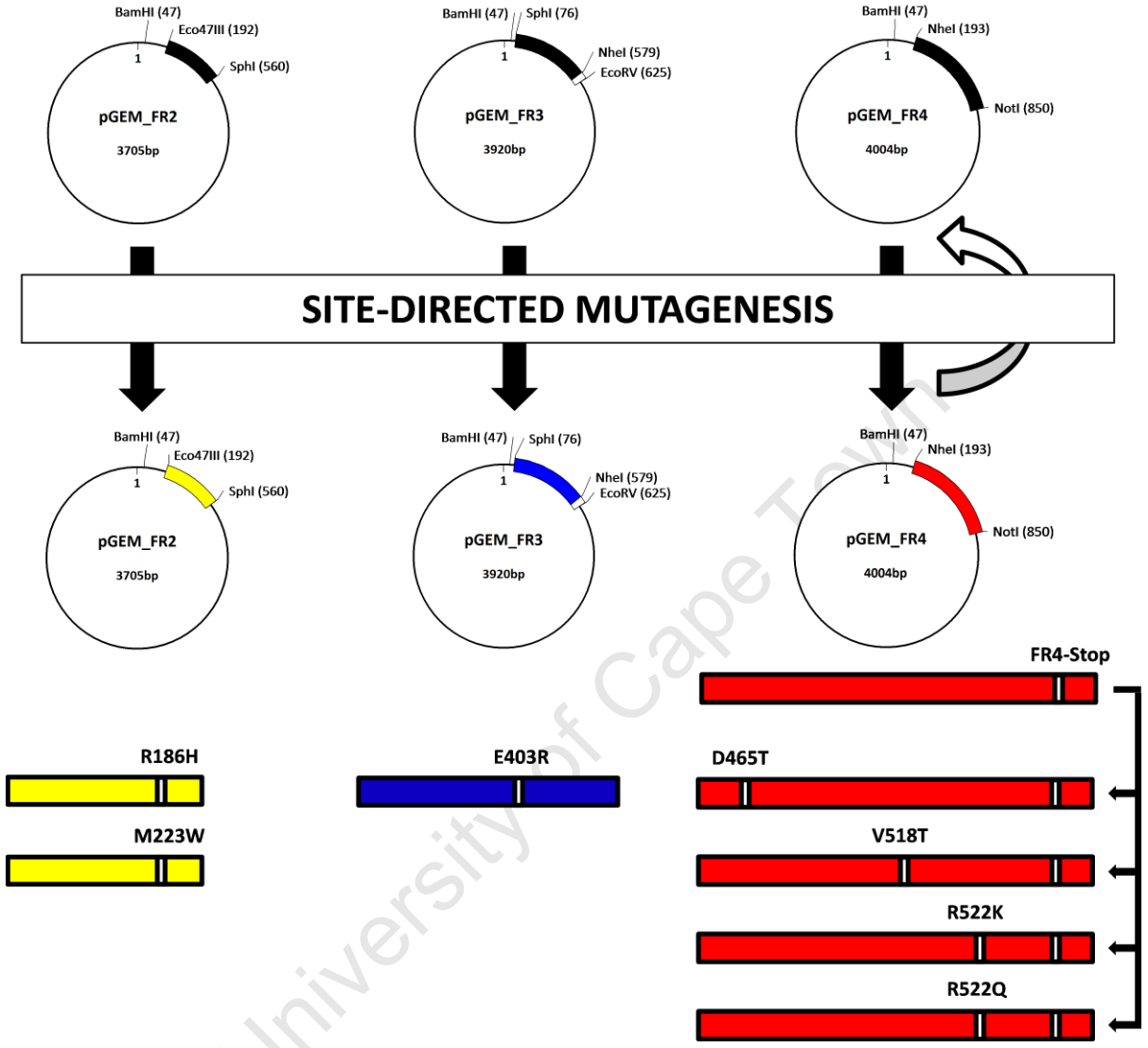

Figure 2.3: Schematic overview of the mutagenesis approach. The three tACEg13 cDNA fragments (FR2,FR3 & FR4; solid black elements) that contained primer target sequences were contained within the pGEMZ11f+ vector and are indicated by the plasmid vector maps at the top (pGEM_FR2, pGEM_FR3 and pGEM_FR4). Plasmids were subjected to site-directed mutagenesis as described in 2.2.3 using corresponding primers (Table 2.1), screened using restriction endonuclease digestion and correct sequence for positive clones confirmed via DNA sequencing. Plasmid maps containing correct and confirmed codon changes are indicated by the vector elements of varying colour (Fragment 2 is yellow, Fragment 3 is blue and Fragment 4 is red). Below each plasmid map are linear vector elements to indicate the number and identity of the mutations introduced into each fragment. Fragment 4 was subject to an initial mutagenesis cycle where stop codons were introduced immediately after the natural cleavage site, with this serving as the template for the remaining mutagenic reactions for Fragment 4.

(described in Appendix) and the plasmid products were transformed into competent *E.coli* XL1 Blue cells (Appendix), clones selected and grown up so that mini-preparations of plasmid DNA could be performed (Appendix). Mutations were screened via restriction digestion using *Ppu*MI, the site introduced by the mutagenesis, and the FR4 insert sequenced using p13 forward and reverse primers that bind sequences flanking the pGEM11Zf+ multiple cloning site. The resultant construct was named pGEM_FR4-Stop.

The same approach was followed for the introduction of the chloride pocket mutations using the primers shown in Table 2.1 and is summarised in Figure 2.3. For all mutations within FR4, the pGEM_FR4-Stop construct was used as the template so that the stop codon would be present in all subsequent constructs. Fragment 2 and 3 mutations were generated in unaltered templates. Mutations were named using conventional nomenclature and single-letter amino acid codes, with the amino acid identity first, followed by numbers indicating its position along the protein backbone and ending with the identity of the amino acid it is to be mutated to.

2.2.4 Generation of soluble tACEg13 construct within pcDNA 3.1+

The pLEN_tACEg13 construct was previously prepared in our laboratory (Gordon et al., 2003). This minimally glycosylated form of tACE was chosen as it is readily crystallisable for X-ray structure determination. The relevant tACEg13 coding cDNA was excised from pLEN_tACEg13 via double digestion with *Bam*HI/*Not*I and ligated into pcDNA 3.1+ which had also been *Bam*HI/*Not*I digested to yield an open vector (Fig 2.4 A, see 2.2.2.2 for methods used). The resultant construct of tACEg13 in pcDNA 3.1+ is referred to as pcDNA_tACEg13.

Further to the incorporation of the tACEg13 coding region into pcDNA3.1+, it was decided to make the construct soluble by introducing a termination sequence (stop-codon). The reasoning was two-fold: firstly, a soluble construct would not need to be cleaved from the cell surface, and, being extruded directly into the growth medium, would thus lead to higher yields in the purification process; secondly, by ensuring termination after Ser625 (which is 2 residues short of the natural cleavage after Arg627) a more compact form of tACEg13, without the disordered stalk region, would help facilitate crystallization of the construct(s).

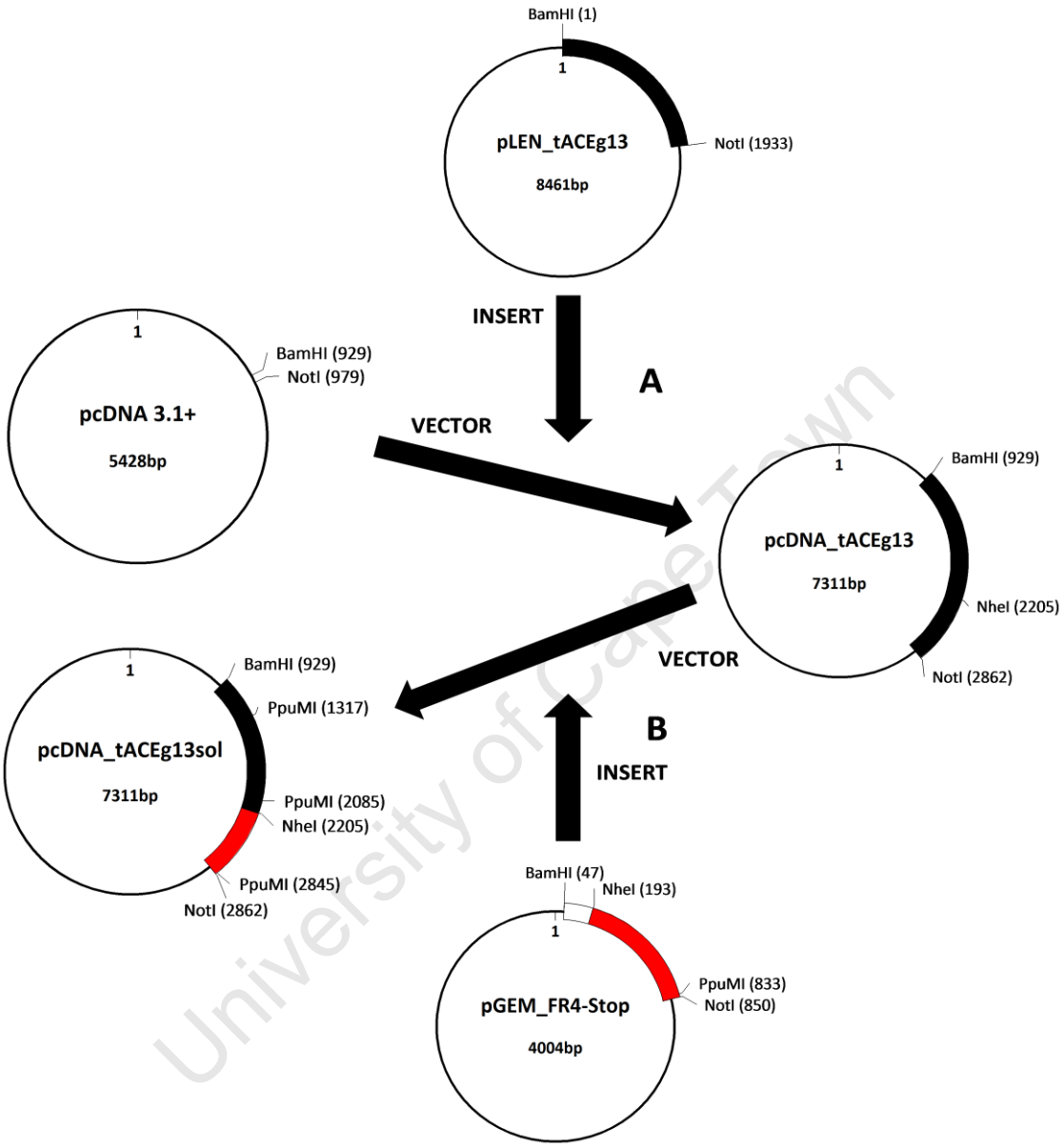

Figure 2.4: Generation of soluble tACEg13 in pcDNA 3.1+. A) The tACEg13 cDNA was excised from pLEN_tACEg13 via double digestion with *Bam*HI/*Not*I. This was ligated into pcDNA 3.1+ which had been digested with *Bam*HI and *Not*I to yield an open vector. The resultant construct of tACEg13 in pcDNA 3.1+ is referred to as pcDNA_tACEg13. B) Fragment 4 containing the inserted stop codons was excised from pGEM_FR4-Stop via double digestion with *NheI/NotI*. This was ligated into pcDNA_tACEg13 which had its Fragment 4 removed, also via *NheI/NotI* digestion, to yield a soluble tACEg13 construct termed tACEg13sol.

Fragment 4 containing the inserted stop codons (generated in 2.2.3.1) was excised from pGEM_FR4-Stop via double digestion with *Nhe*I/*Not*I. This was ligated into pcDNA_tACEg13, which had also had its Fragment 4 removed via *Nhe*I/*Not*I digestion (Fig 2.4 B). The resultant construct is pcDNA_tACEg13 containing engineered stop codons and is referred to as pcDNA_tACEg13sol.

2.2.5 Construction of pBS_FR1,2,3 shuttle vector

It was necessary to generate an intermediary shuttle vector for the cloning of Fragments 2 and 3 (FR2 and FR3) into pcDNA_tACEg13sol. Whilst FR4 can be subcloned directly into pcDNA_tACEg13sol (as already described in 2.2.4), the restriction endonuclease sites that flank both FR2 and FR3 prevent direct sub-cloning. The *Sph*I restriction site that separates FR2 and FR3 cuts a number of times in pcDNA and would hence prevent either fragment from being directly subcloned. Additionally, the *Eco47*III restriction site separating FR1 and FR2 is also present in FR4 and would also prevent any sub-cloning of FR2 into the tACEg13sol coding region. This restriction enzyme sequon is not present in the wildtype sequence and was engineered as part of the removal of the sixth N-linked glycosylation site during construction of the tACEg13 minimally glycoylated isoform (part of M.Sc work of Dr Kerry Gordon). This necessitated the construction of an intermediary shuttle vector containing the tACEg13sol coding DNA region between *Bam*HI and *Nhe*I (FR1, FR2 and FR3) and excluding that between *Nhe*I and *Not*I (FR4). Thus, it was necessary to generate an additional intermediary shuttle vector for the cloning of Fragments 2 and 3 (FR2 and FR3) into pcDNA_tACEg13sol. pBluescript SKII+ was chosen, as it lacked any *Eco47*III or *Sph*I sites and contained the necessary restriction endonuclease sites in the MCS for the construction of a suitable intermediary shuttle vector, which is described below.

The tACEg13sol coding region was subcloned from pcDNA_tACEg13sol into pBluescript SKII+ via *BamHI/NotI* double digestion (see Fig 2.5 A). The ligation mix was transformed into

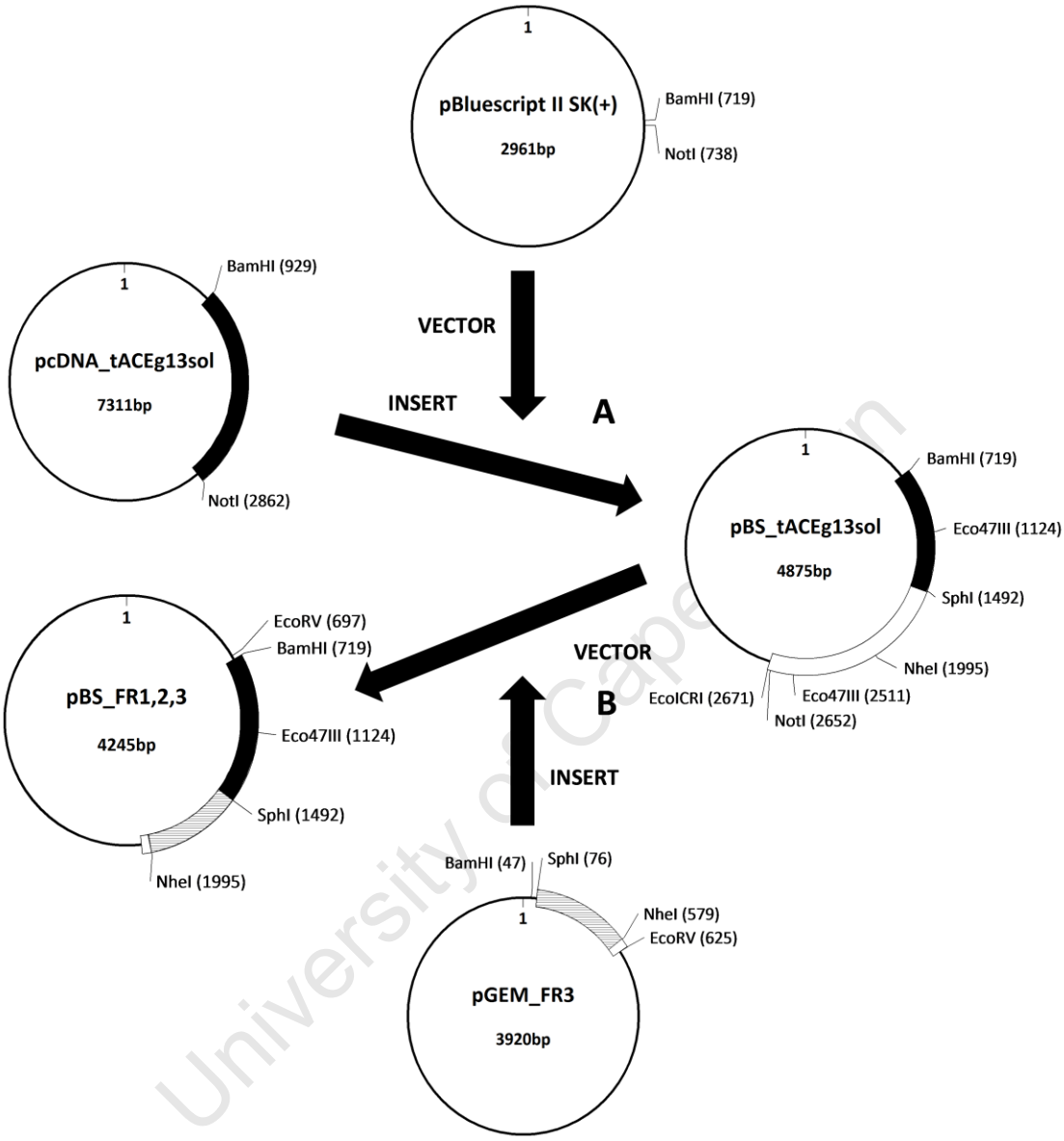

Figure 2.5 Construction of pBS_FR1,2,3 subcloning intermediary A) The tACEg13sol gene was excised from pcDNA_tACEg13sol via double digestion with *Bam*HI/*Not*I. This was ligated into pBluescript II SK(+) which had been *Bam*HI/*Not*I digested to yield an open vector. The resultant construct of tACEg13sol in pBluescript II SK(+) is referred to as pBS_tACEg13sol. **B)** Double digestion of pBS_tACEg13sol with *Sph*I & *Eco*ICRI allowed removal of Fragments 3 & 4. pGEM_FR3 was double digested with *Sph*I *& Eco*RV to yield Fragment 3 and a small portion of non-coding DNA (shown as white element between *Nhe*I and *Eco*RV sites), which was ligated into the pBS_tACEg13sol minus Fragments 3&4 vector to yield pBS_FR1,2,3.

competent *E.coli,* grown under antibiotic selective media for plasmid mini-preparation. The mini-preparations were screened via double digestion with *Bam*HI*/Not*I, along with pcDNA_tACEg13sol as a size control.

The next step was to remove FR4 (and hence the extra *Eco47*III site) and generate a construct containing FR1, FR2 and FR3 only. pGEM_FR3 contained an extra stretch of base pairs after the 3' end of the FR3 coding region, which was introduced in its construction (M.Sc work of Dr Kerry Gordon). This stretch of sequence contained an *Eco*RV restriction site, digestion of which produces a blunt end. Similarly, pBS_tACEg13sol contains a blunt cutting *Eco*ICRI restriction site outside the 3' end of the tACEg13sol coding region and within the pBluescript sequence. The pBS_tACEg13sol vector was prepared by double digestion with *Sph*I*/Eco*ICRI allowing the removal of FR3 and FR4, along with a small portion of pBluescript sequence, leaving a free *Sph*I sticky end, along with the *Eco*ICRI blunt end. FR3 was excised from pGEM_FR3 using *Sph*I*/Eco*RV, and ligated into the prepared pBS_tACEg13sol vector (see Fig 2.5B). This generated the pBS_FR1,2,3 construct. The blunt end ligation of the *Eco*RV and *Eco*ICRI ends resulted in destruction of the recognition sequon for both restriction endonucleases. This was not of significance as the *Nhe*I site flanking FR3 that was required for later sub-cloning steps remained intact.

2.2.6 Sub-cloning of mutated Fragment 2 and Fragment 3 into pBS_FR1,2,3

Mutants M223W and R186H, located on FR2, were subcloned into pBS_FR1,2,3 (Figure 2.6) using the *Eco*47III and *Sph*I restriction sites. This produced pBS_FR1,2,3_R186H and pBS_FR1,2,3_M223W. In a very similar manner to the sub-cloning of FR2 into pBS_FR1,2,3, FR3 that has the E403R mutation introduced via site-directed mutagenesis was also subcloned from pGEM_FR3_E403R into the pBS_FR1,2,3 shuttle construct using the *Sph*I & *Nhe*I restriction endonucleases. This produced pBS_FR1,2,3_E403R which was pBS_FR1,2,3 with a mutation introduced into FR3 (indicated by an *).

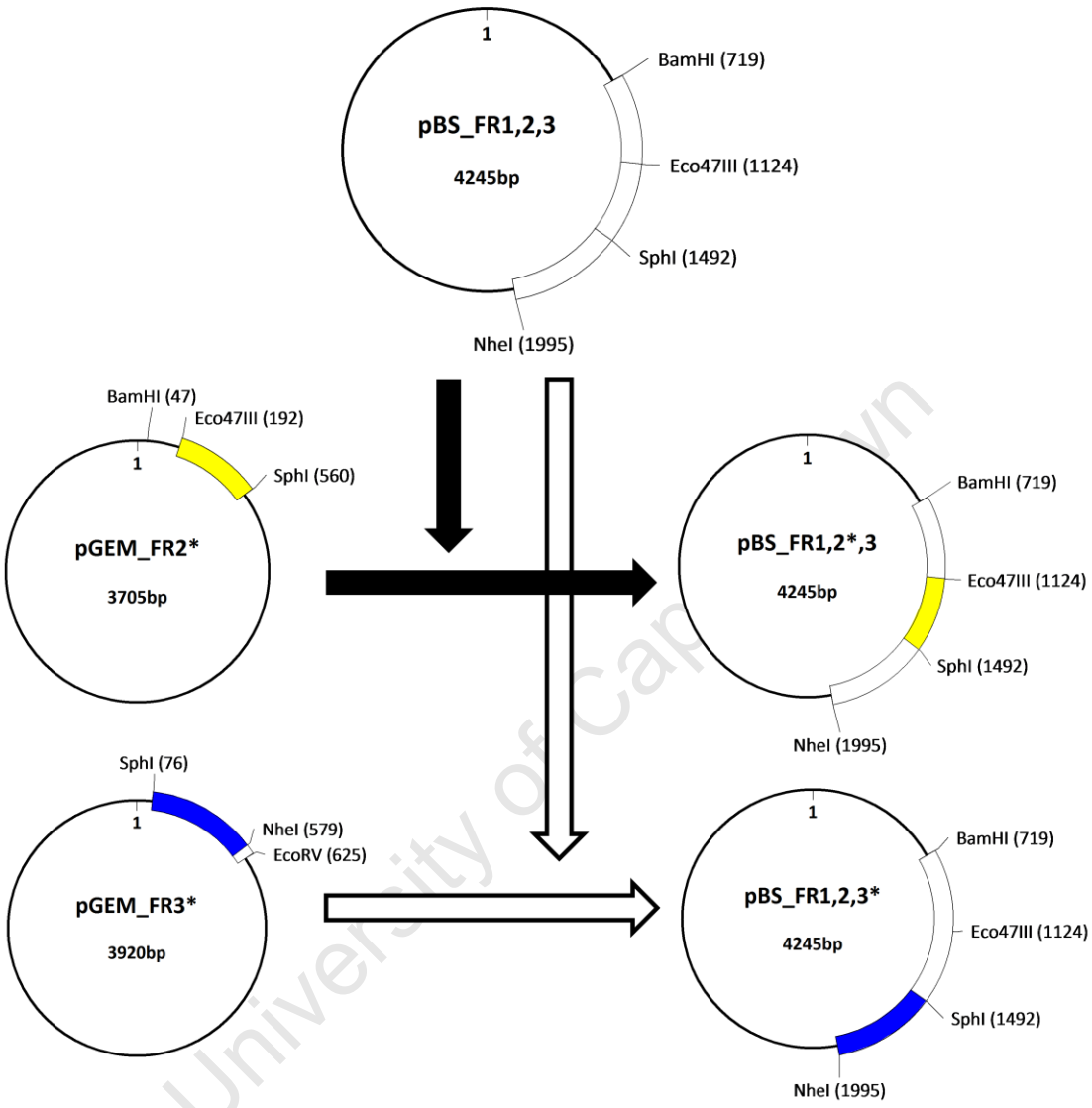

Figure 2.6 Subcloning of mutated Fragment 2 and Fragment 3 into pBS_FR1,2,3. Black arrows indicate the sub-cloning of the 368bp FR2 containing a mutation (yellow) from pGEM_FR2* into pBS_FR1,2,3 which has had its Fragment 2 removed via *Eco47III/SphI* digestion. This produces pBS_FR1,2*,3. White arrows indicate the sub-cloning of the 503bp Fragment 3 containing a mutation (blue) from pGEM_FR3* into pBS_FR1,2,3 which has had its Fragment 3 removed via *SphI/NheI* digestion. This produces pBS_FR1,2,3*. The presence of an * after the fragment number in the naming of a plasmid indicates that that fragment has had a mutation introduced.

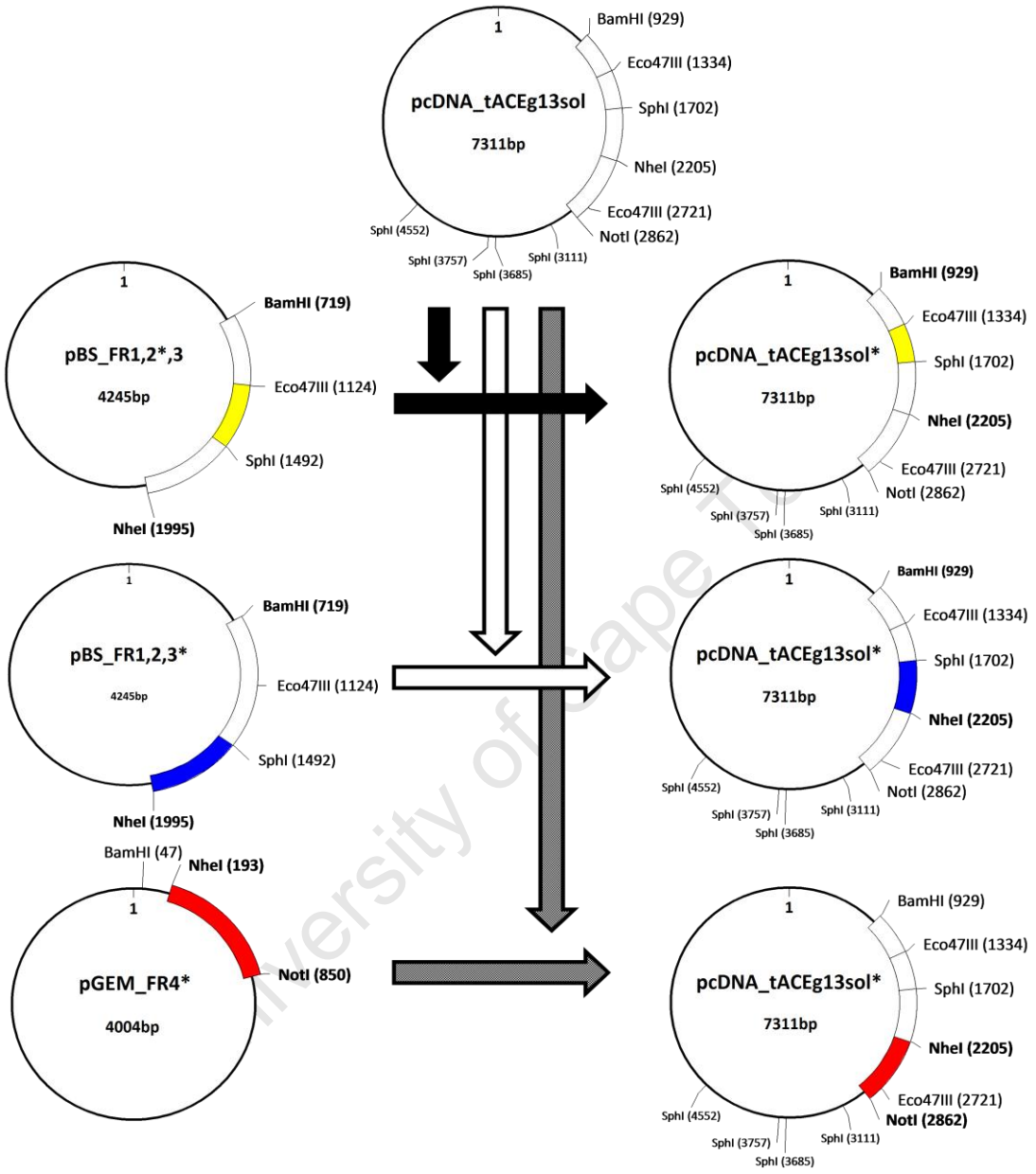

Figure 2.7: Subcloning of mutation-containing fragments into pcDNA_tACEg13sol. Black arrows indicate sub-cloning of the 1276bp FR_1,2*,3 fragment containing FR2* (yellow) from pBS_FR1,2*,3 into pcDNA_tACEg13sol which has had its FR1,2,3 removed via *BamHI/NheI* digestion. This produces pcDNA_tACEg13sol*. White arrows indicate the sub-cloning of the 1276bp FR_1,2,3* fragment containing FR3* (blue) from pBS_FR1,2,3* into pcDNA_tACEg13sol which has had its FR1,2,3 removed via *BamHI/NheI* digestion. Chequered arrows indicate the sub-cloning of the 657bp FR4 (red) from pGEM_FR4 into pcDNA_tACEg13sol which has had its FR4 removed via *NheI/NotI* digestion.

2.2.7 Generation of pcDNA_tACEg13sol mutant expression constructs

The previous section described the sub-cloning of the mutated fragments FR2 and FR3 into pBS_FR1,2,3. The next step involved introducing these mutations into pcDNA_tACEg13sol, which is illustrated in Figure 2.7. Here, all three fragments (FR1, 2 and 3, with either FR2 or FR3 containing a mutation) were removed from pBS_FR1,2,3 via *Bam*HI/*Nhe*I double digestion. Similarly, the corresponding stretch of DNA (FR1,2 & 3) was removed from pcDNA_tACEg13sol, also via *Bam*HI/*Nhe*I double digestion, and the FR1,2,3* was inserted in its place using a ligation reaction. This generated a full pcDNA_tACEg13sol expression vector, with mutations in either FR2 or FR3 depending upon which route had been followed via the pBS_FR1,2,3 intermediary shuttle vector. Unlike the sub-cloning of FR2 and FR3, which required the additional step of sub-cloning into an intermediary vector, the sub-cloning of FR4 was done directly from pGEM_FR4* straight into pcDNA_tACEg13sol. Site-directed mutagenesis was used to introduce desired chloride pocket mutations into FR4 contained within pGEM_FR4-Stop (see 2.2.3). Double digestion using *Nhe*I and *Not*I yielded FR4 containing the mutation of choice. This was inserted using a ligation reaction into pcDNA_tACEg13sol, which had also been *Nhe*I/*Not*I digested, to give a full pcDNA_tACEg13sol construct with a desired mutation within the FR4 region (see Figure 2.7).

2.3 Results & Discussion

2.3.1 Site-Directed Mutagenesis of tACEg13sol Fragments

Site-directed mutagenesis was performed using primers and corresponding tACEg13sol cDNA fragments contained within pGEM11Zf+, as described in 2.2.3. The *DpnI* digested PCR products for each reaction were transformed into *E.coli*, selected, and mini preparations of the plasmid DNA screened using appropriate restriction endonucleases that recognised the restriction sites introduced via the mutagenic process. Positive clones were selected for each mutagenic reaction and exact DNA composition was confirmed via nucleotide sequencing. A summary of all the mutations generated is given in Table 2.2.

Table 2.2: Site-Directed Mutagenesis of tACEg13sol Fragments. Table shows the location of the mutations with respect to potential role, name of mutation, residue in tACE that is being mutated along with its numerical position , identity of amino acid if it is being converted to its corresponding N-domain residue, and the identity of the residue if that mutation is completely novel (i.e same in both domains). All mutations were generated using methodology described in 2.2.5 and Appendix

Location	Mutant Name	tACE (C-domain)	N-domain	Non-domain mutation
Chloride 1 Pocket	R186H	Arg 186	His	
S2 Pocket (Chloride Channel)	E403R	Glu 403	Arg	
Chloride 2 Pocket	M223W	Met 223	Trp	
	D465T	Asp 465		Thr
	V518T	Val 518	Thr	
	R522K	Arg 522		Lys
	R522Q	Arg 522		Glu

2.3.2 Generation of soluble tACEg13 construct within pcDNA 3.1+

The coding region of tACEg13 was removed from pLEN_tACEg13 via *Bam*HI/*Not*I restriction digestion and inserted into the expression vector pcDNA 3.1+ (outlined in 2.2.2, Appendix), and positive constructs were identified using restriction endonuclease digestions. The stop codons were introduced into pGEM_FR4 (as described in 2.2.3) and sequencing confirmed the presence of both stop-codons, as well as the *Ppu*MI restriction site used for screening purposes (data not shown). The sub-cloning of FR4-Stop into pcDNA_tACEg13 (described in 2.2.4) generated the pcDNA_tACEg13sol construct. Restriction digestion was used to confirm identity and integrity of the construct (Figure 2.8). Digestion of pcDNA_tACEg13 with *Ppu*MI yields a very faint band of 768bp: the faintness of the band is due to the presence of overlapping *dcm*

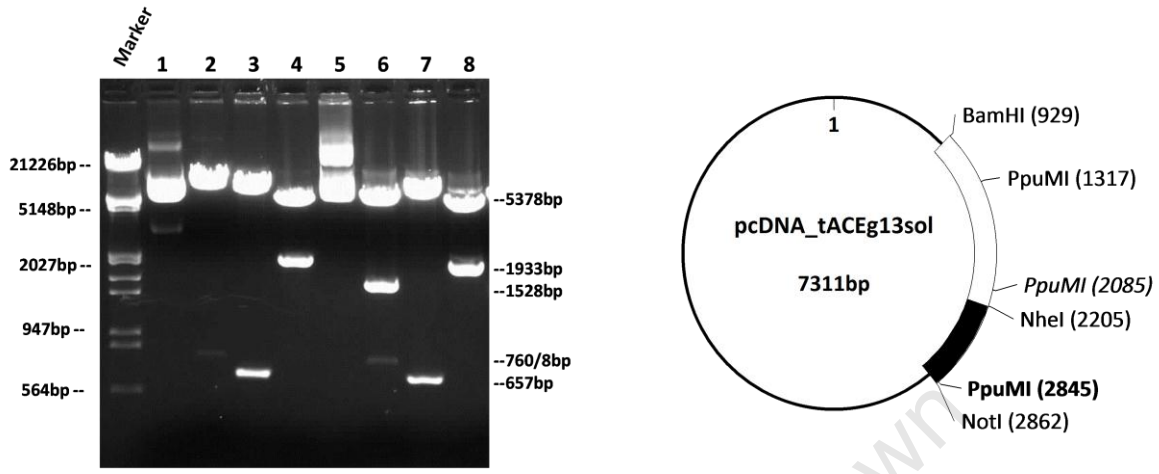

Figure 2.8 Generation of soluble tACEg13 construct within pcDNA 3.1+. Representative 10% agarose gel showing restriction digestion screening comparison between pcDNA_tACEg13 and pcDNA_tACEg13sol: pcDNA_tACEg13 (lane 1) and pcDNA_tACEg13sol (lane 5) undigested; pcDNA_tACEg13 (lane 2) and pcDNA_tACEg13sol (lane 6) *Ppu*MI digested; pcDNA_tACEg13 (lane 3) and pcDNA_tACEg13sol (lane 7) *Nhe*I/*Not*I digested; pcDNA_tACEg13 (lane 4) and pcDNA_tACEg13sol (lane 8) *Bam*HI/*Not*I digested. Lambda DNA digested with *Eco*RI and *Hind*III was used as a molecular marker.

methylation at one of the *Ppu*MI recognition sites (centred at 2085 on the vector diagram), to which *Ppu*MI is sensitive and cleavage is reduced to about 10% of normal. The presence of another *Ppu*MI restriction site (at position 2845) along with the stop codons in pcDNA_tACEg13sol results in a 1528bp band appearing with *Ppu*MI digestion. The inefficiency of the 2085 *Ppu*MI site results in the 760bp and 768bp doublet being considerably less intense than the 1528bp band they are produced from. Restriction digestion of both pcDNA_tACEg13 and pcDNA_tACEg13sol with *Nhe*I/*Not*I (sub-cloning enzymes) yields identical 657bp bands (FR4), and digestion with *Bam*HI/*Not*I yielding 5378bp and 1933bp bands for both. This serves to show that all sizing between the constructs is the same and the only difference being the presence of the added *Ppu*MI site introduced with the stop codons. pcDNA_tACEg13sol represents the final expression vector and nucleotide sequencing of the entire coding region confirmed that everything was correct.

2.3.3 Construction of pBS_FR1,2,3 sub-cloning intermediary

The coding region of tACEg13sol was removed from pcDNA_tACEg13sol via *BamHI/NotI* restriction digestion and inserted into the cloning vector pBluescript II SK(+) (outlined in 2.2.5), and positive constructs were identified using restriction endonuclease digestions. Figure 2.9A shows a confirmatory restriction digestion of the final selected clone: restriction digestion using *BamHI* gives an approximately 4875bp band, which corresponds to the predicted size of the construct. Double digestion with *BamHI/NotI* gives expected band sizes of 2942bp and 1933bp, corresponding to vector and coding region, respectively. Double digestion with *BamHI/NheI* gives expected band sizes of 3599bp and 1276bp, corresponding to vector plus FR4 and the FR1,2,3 region respectively, serving as further evidence that the construct size is correct. Digestion with *PpuMI* gives a very similar banding pattern to that seen in Figure 2.8, with a more intense 1528bp band and the faint 760/768bp doublet arising from within the tACEg13sol coding region.

The generation of pBS_FR1,2,3 required the removal of FR4 from pBS_tACEg13sol via the cloning strategy described in section 2.2.5. Restriction digestion was used to confirm identity and integrity of the pBS_FR1,2,3 construct in comparison to pBS_tACEg13sol (Figure 2.9B). Linearization of both constructs using *Bam*HI gave a 4245bp band for pBS_FR1,2,3 compared to the slightly larger 4875bp band for pBS_tACEg13sol. Linearization doesn't allow for clear differentiation of such large bands, so double digestion using *Bam*HI*/Nhe*I was employed to remove FR1,2,3 from both constructs. As expected, the 1276bp band (FR1,2,3) is identical for both, yet the size of the remaining vector fragments are 3599bp and 2969bp for pBS_tACEg13sol and pBS_FR1,2,3 respectively. This indicates that the section of DNA between *Nhe*I and *Eco*ICRI containing FR4 has been removed (outlined in 2.2.5). To further confirm that this region is no longer there, double digestion using *Nhe*I*/Not*I showed the 657bp FR4 being removed from pBS_tACEg13sol (giving 3588bp band), but only linearization of pBS_FR1,2,3 due to the lack of a *Not*I site that would be there if FR4 were. The cloning strategy that employed blunt end ligation destroyed both *Eco*RV and *Eco*ICRI sites that were used, hence they could not be used for screening purposes.

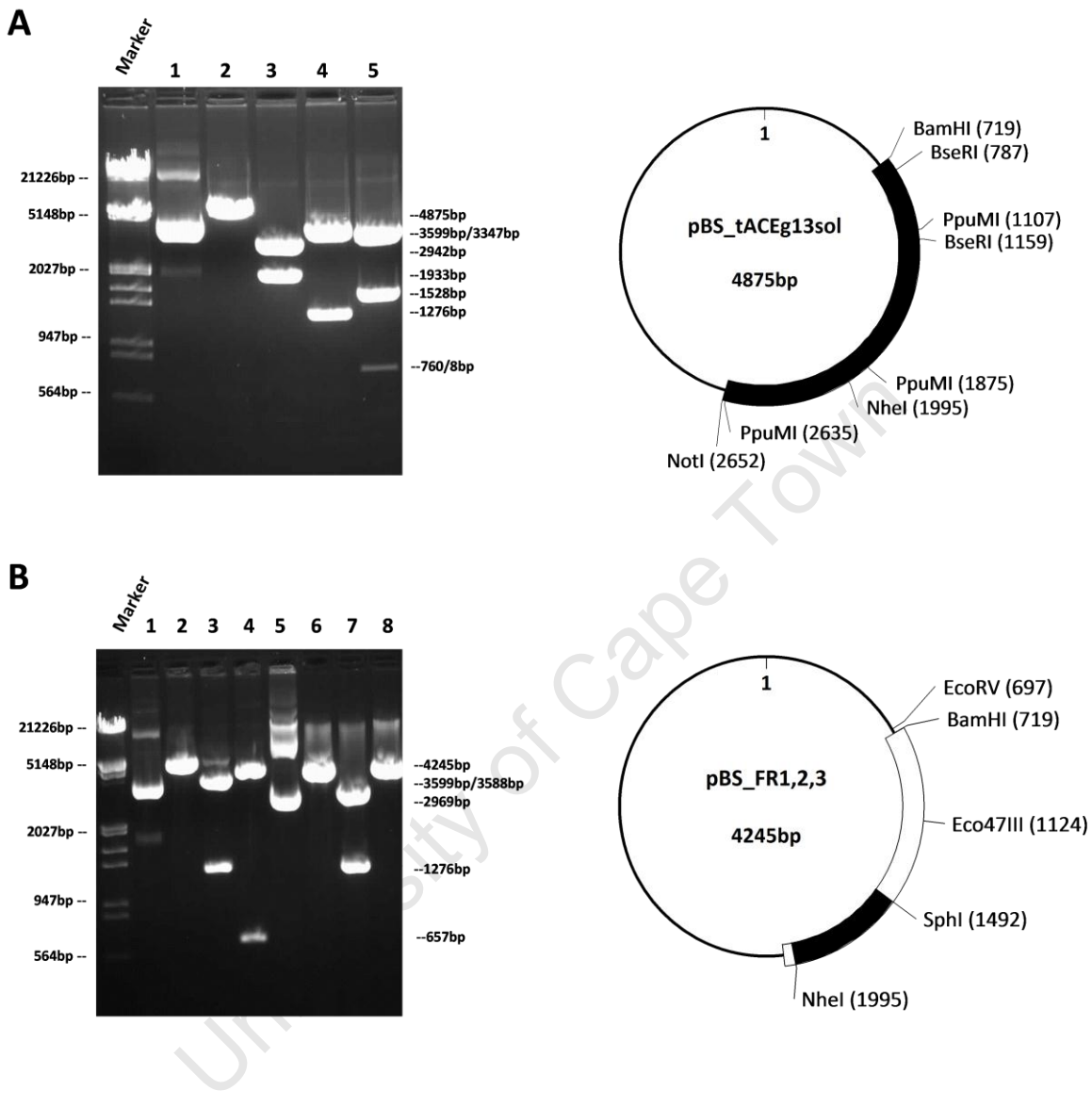

Figure 2.9 Generation of pBS_FR1,2,3. **A**) Sub-cloning of tACEg13sol into pBluescript II SK(+): Representative gel showing restriction digestions for pBS_tACEg13sol: undigested DNA (lane 1); *Bam*HI digested (lane 2), *Bam*HI/*Not*I digested (lane 3), *Bam*HI/*Nhe*I digested (lane 4) and *Ppu*MI digested (lane 5). Lambda DNA digested with *Eco*RI and *Hind*III was used as a molecular marker. **B**) Removal of FR4 from pBS_tACEg13sol: Representative gel showing restriction digestion screening comparison between pBS_tACEg13sol and pBS_FR1,2,3: pBS_tACEg13sol (lane 1) and pBS_FR1,2,3 (lane5) undigested; pBS_tACEg13sol (lane 2) and pBS_FR1,2,3 (lane 6) *Bam*HI digested; pBS_tACEg13sol (lane 3) and pBS_FR1,2,3 (lane 7) *Bam*HI/*Nhe*I digested; pBS_tACEg13sol (lane 4) and pBS_FR1,2,3 (lane 8) *Nhe*I/*Not*I digested. Lambda DNA digested with *Eco*RI and *Hind*III was used as a molecular marker.

2.3.4 Sub-cloning of mutated Fragment 2 and Fragment 3 into pBS_FR1,2,3

The two mutations that were generated in pGEM_FR2 were R186H and M223W, which yielded pGEM_FR2_R186H and pGEM_FR2_M223W. As outlined in 2.2.6, FR2_R186H and FR2_M223W were subcloned into pBS_FR1,2,3 via *SphI/Eco47III* digestion. Comparative digestions of pBS_FR1,2,3 with pBS_FR1,2,3_R186H & pBS_FR1,2,3_M223W (Figure 2.10) show that *SphI/Eco47III* digestion of all three constructs yields a 368bp band, indicating that the subcloned FR2_R186H and FR2_M223W are of identical size to the FR2 removed from pBS_FR1,2,3. Digestion of pBS_FR1,2,3_R186H with *BamHI* and the *AscI* site introduced with the mutation yields a 598bp fragment, where similar digestion of pBS_FR1,2,3 is only linearised, hence confirming that FR2_R186H was indeed subcloned into pBS_FR1,2,3. Similarly, *PpuMI* digestion was used to compare pBS_FR1,2,3 with pBS_FR1,2,3_M223W. pBS_FR1,2,3 yields a very faint 768bp band, which is due the presence of overlapping Dcm methylation at one of the two *PpuMI* sites (position 1107 on the pBS_FR1,2,3_M223W plasmid map) which results in less than 10% cleavage. A third *PpuMI* site is introduced with FR2_M223W, which results in the 768bp band being cleaved into 466bp and 302bp bands. The varying intensity between the 466bp and 302bp bands further highlights the sensitivity of the one PpuMI site to Dcm methylation. The issue was alleviated in subsequent cloning steps by transforming the constructs into a methylation negative *E.coli* strain such as JM110.

For the same reasons as described for FR2, FR3 also needed to be subcloned into the pBS_FR1,2,3 shuttle vector (outlined in 2.2.6). The only mutation introduced into FR3 was E403R, which yielded the pGEM_FR3_E403R construct. FR3_E403R was subcloned into pBS_FR1,2,3 using *Nhe*I and *Sph*I restriction digestion. Comparative digestions of pBS_FR1,2,3 with pBS_FR1,2,3_E403R (Figure 2.10) show that *Sph*I/*Nhe*I digestion yields identical 503bp bands, confirming the correct FR3 size. Digestion using *Bse*RI produces a 372bp band in pBS_FR1,2,3, whereas introduction of another *Bse*RI site in FR3 of pBS_FR1,2,3_E403R results in the appearance of an 806bp band. This confirmed that the FR3_E403R fragment was subcloned successfully into pBS_FR1,2,3.

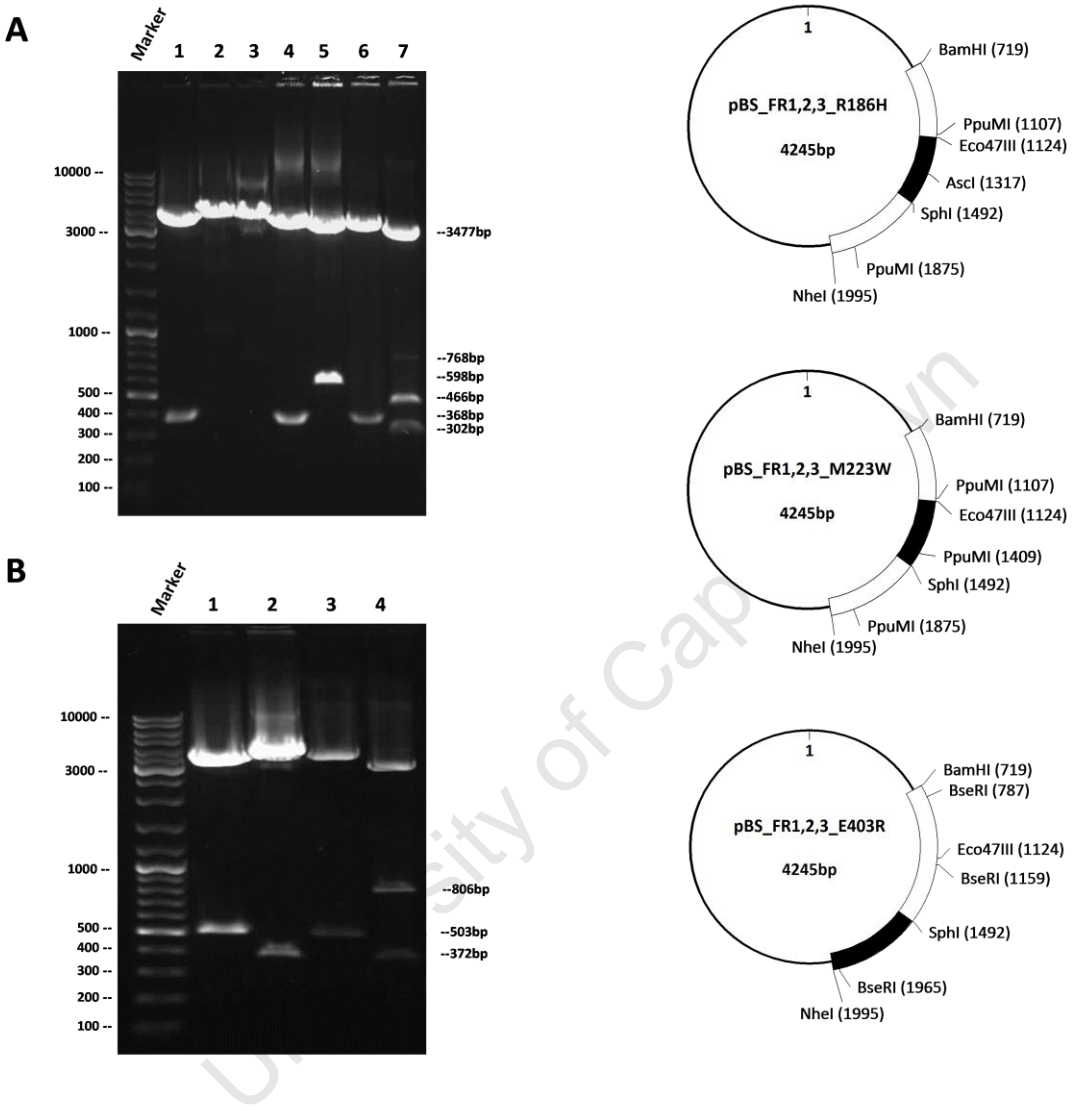

Figure 2.10 Subcloning of mutated Fragment 2 and Fragment 3 into pBS_FR1,2,3 **A**) Sub-cloning of Fragment 2 constructs into pBS_FR1,2,3: Representative gel showing restriction digestion screening comparison between pBS_FR1,2,3, pBS_FR1,2,3_R186H & pBS_FR1,2,3_M223W: pBS_FR1,2,3 (lane 1), pBS_FR1,2,3_R186H (lane 4) & pBS_FR1,2,3_M223W (lane 6) are digested with *Eco47*III/*Sph*I; pBS_FR1,2,3 (lane 2) and pBS_FR1,2,3_R186H (lane 5) are digested with *Bam*HI/*Asc*I; pBS_FR1,2,3 (lane3) and pBS_FR1,2,3_M223W (lane 7) are digested with PpuMI. Fermentas O'Generuler DNA Ladder was used as a molecular marker. **B**) Sub-cloning of Fragment 3 constructs into pBS_FR1,2,3: Representative gel showing restriction digestion screening comparison between pBS_FR1,2,3& pBS_FR1,2,3_E403R: pBS_FR1,2,3 (lane 1) & pBS_FR1,2,3_E403R (lane 3) are digested with *Sph*I/*Nhe*I; pBS_FR1,2,3 (lane 2) & pBS_FR1,2,3_E403R (lane 4) are digested with BseRI. Fermentas O'Generuler DNA Ladder was used as a molecular marker.

2.3.5 Generation of pcDNA_tACEg13sol mutant expression constructs

Once it had been confirmed that the mutation containing FR2 and FR3 had been successfully subcloned into FR1,2,3 (Section 2.3.4), the next step (as outlined in 2.2.7) was to subclone all three fragments (FR1,2 & 3) from each of these individual mutation-containing pBS_FR1,2,3 constructs into pcDNA_tACEg13sol. Comparative digestions of pcDNA_tACEg13sol with the R186H, M223W and E403R mutation containing pcDNA_tACEg13sol constructs (Figure 2.11) shows that *Bam*HI*/Nhe*I digestion of all constructs yields a 1276bp band, confirming the identical size of the FR1,2,3 between all constructs. To confirm presence of mutations, restriction digestion using screening enzymes is also shown. Digestion of pcDNA_tACEg13sol _R186H with *Bam*HI and *Asc*I (introduced with the mutation) yields a 598bp fragment, where similar digestion of pcDNA_tACEg13sol is only linearised, hence confirming that R186H mutation is present. In the digestion with *Ppu*MI, the pcDNA_tACEg13sol and pcDNA_tACEg13sol_M223W plasmid DNA was prepared from transformations of methylation negative *E.coli* JM110 cells, which alleviated the issue of reduced cleavage with one of the *Ppu*MI sites alluded to in 2.3.3 and 2.3.4. This digestion of pcDNA_tACEg13sol produces a bright 760bp/768bp doublet, with a faint 1528bp band visible due to incomplete cleavage. The additional *Ppu*MI site associated with the M223W mutation in pcDNA_tACEg13sol_M223W causes the cleavage of the 768bp band into two smaller 466 and 302bp bands. pcDNA_tACEg13sol digestion with *Bse*RI yields 2564bp and 372bp bands, with the additional *BseRI* site associated with the E403R mutation in pcDNA_tACEg13sol_E403R causing the 2564bp band to be split into 1758 and 806bp bands. These gels serve to confirm the successful generation of pcDNA_tACEg13sol_R186H, pcDNA_tACEg13sol_M223W and pcDNA_tACEg13sol_E403R. Unlike the FR2 and FR3 segments that need to be subcloned via pBS_FR1,2,3, FR4 could be subcloned straight into pcDNA_tACEg13sol via *Nhe*I*/Not*I (outlined in 2.2.8). Five separate mutations were generated in FR4 (see 2.3.1; Table 2.2) to yield pGEM_FR4_D465T, pGEM_FR4_V518T, pGEM_FR4_R522K pGEM_FR4_R522Q, pGEM_FR4_VR-TK. The FR4 from each of these was excised and subcloned into pcDNA_tACEg13sol using

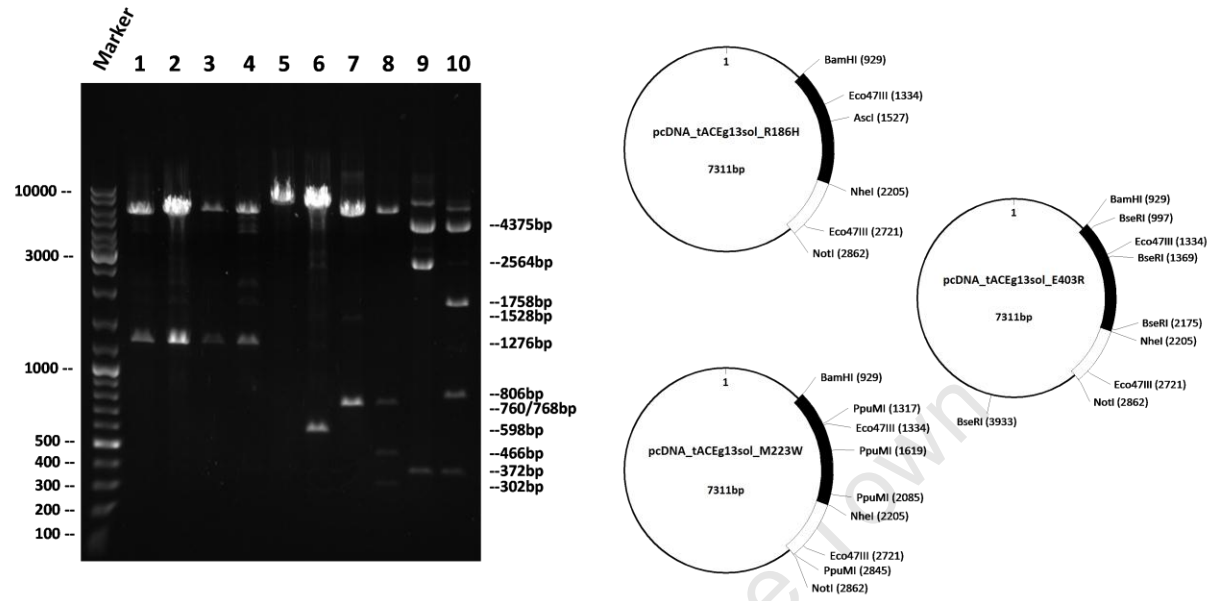

Figure 2.11 Sub-cloning of Fragment 1,2,3 containing mutations into pcDNA_tACEg13sol. Representative gel showing restriction digestion screening comparison between pcDNA_tACEg13sol and the pcDNA_tACEg13sol constructs containing the R186H, M223W and E403R mutations: pcDNA_tACEg13sol (lane 1), pcDNA_tACEg13sol_R186H (lane 2), pcDNA_tACEg13sol_M223W (lane 3) and pcDNA_tACEg13sol_E403R (lane 4) were digested using *Bam*HI/*Nhe*I; pcDNA_tACEg13sol (lane 5) and pcDNA_tACEg13sol_R186H (lane 6) digested using *Bam*HI/*Asc*I; pcDNA_tACEg13sol (lane 7) and pcDNA_tACEg13sol_M223W (lane 8) digested using *Ppu*MI; pcDNA_tACEg13sol (lane 9) and pcDNA_tACEg13sol_E403R (lane 10) digested using *Bse*RI. Fermentas O'Generuler DNA Ladder was used as a molecular marker.

*Nhe*I/*Not*I restriction digestion. Comparative restriction digestion of pcDNA_tACEg13sol and the D465T, V518T, R522K, R522Q and VR-TK containing pcDNA_tACEg13sol (Figure 2.12 A) shows that *Nhe*I/*Not*I digestion of all constructs yields a 657bp band, confirming the identical size of FR4 between all constructs. Figure 2.12 B gives comparative restriction digestions using screening restriction enzymes for each mutation. Digestion of pcDNA_tACEg13sol and pcDNA_tACEg13sol_D465T with *Dra*III resulted in a large 2005bp band for pcDNA_tACEg13sol, with the additional site associated with the D465T mutation cleaving that into 1060bp and 945bp bands in pcDNA_tACEg13sol_D465T. Digestion of pcDNA_tACEg13sol and

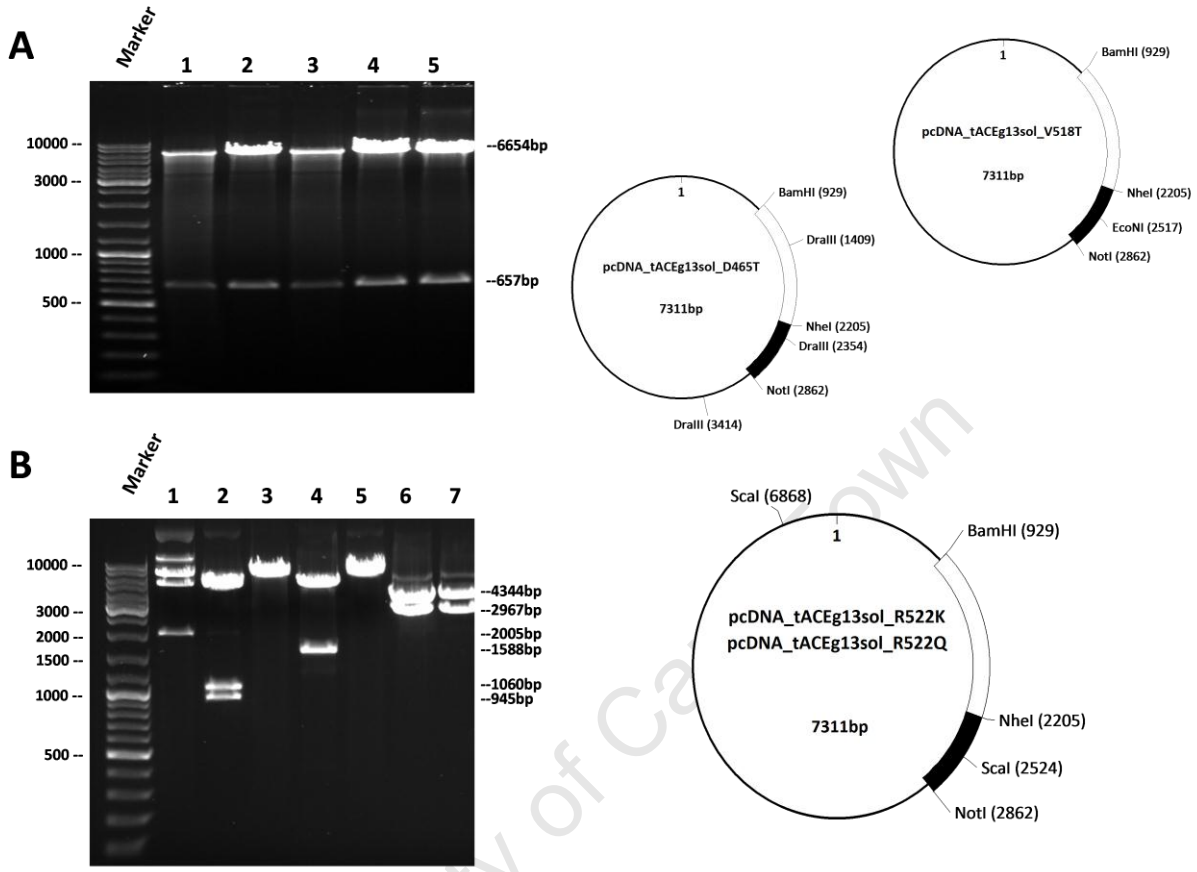

Figure 2.12 Sub-cloning of Fragment 4 constructs into pcDNA_tACEg13sol. Representative gel showing restriction digestion screening comparison between pcDNA_tACEg13sol and the pcDNA_tACEg13sol constructs containing the D465T, V518T, R522K, R522Q, VR-TK mutations: **A**) pcDNA_tACEg13sol (lane 1), pcDNA_tACEg13sol_D465T (lane 2), pcDNA_tACEg13sol_V518T (lane 3), pcDNA_tACEg13sol_R522K (lane 4), pcDNA_tACEg13sol_R522Q (lane 5) and pcDNA_tACEg13sol_VR-TK (lane 6) digested with *Nhe*I/*Not*I. **B**) pcDNA_tACEg13sol (lane 1) and pcDNA_tACEg13sol_D465T (lane 2) digested with *Dra*III; pcDNA_tACEg13sol (lane 3) and pcDNA_tACEg13sol_V518T (lane 4) digested with *Bam*HI/*Eco*NI; pcDNA_tACEg13sol (lane 5), pcDNA_tACEg13sol_R522K (lane 6), pcDNA_tACEg13sol_R522Q (lane 7) and pcDNA_tACEg13sol_VR-TK (lane 8) digested with *Sca*I. Fermentas O'Generuler DNA Ladder was used as a molecular marker.

pcDNA_tACEg13sol_V518T with *Bam*HI and *Eco*NI resulted in a 1588bp band dropping out due to the presence of the *Eco*NI site associated with the V518T mutation, with pcDNA_tACEg13sol just being linearised. The R522K, R522Q and VR-TK mutations all introduced a *Sca*I restriction

site, hence *Sca*I digestion of pcDNA_tACEg13sol constructs containing these mutations produced 4244bp and 2967bp bands, whereby without these mutations the construct is merely linearised due to the lone *Sca*I site in the pcDNA 3.1+ vector sequence. These gels serve to confirm the successful generation of pcDNA_tACEg13sol_ D465T, pcDNA_tACEg13sol_V518T, pcDNA_tACEg13sol_R522K, pcDNA_tACEg13sol_R522Q and pcDNA_tACEg13sol_VR-TK.

2.4 Summary

In summary, the tACEg13 cDNA was successfully established in the pcDNA 3.1(+) expression vector, which had the *Nhe*I-restriction endonuclease site removed from the multiple cloning site to facilitate a more efficient cloning strategy. Stop-codons were engineered into the gene to make the protein product soluble in order to improve potential yields and promote crystallization efforts, resulting in the pcDNA_tACEg13sol expression vector. An intermediary shuttle vector was constructed by cloning the tACEg13sol gene into pBluescript II SK(+) and then removing the fourth gene fragment (FR4), which contained RE sites that would interfere with cloning, resulting in pBS_FR1,2,3. Site-directed mutagenesis was employed to alter target nucleotide sequences within gene fragments (FR2, FR3 & FR4) contained within the pGEM11Zf+ cloning vectors and the sequences checked by nucleotide sequencing. These mutated fragments were then subcloned into pcDNA_tACEg13sol via either direct sub-cloning (for FR4 mutants) or sub-cloning into pBS_FR1,2,3 first and then sub-cloning that FR1-3 into pcDNA_tACEg13sol (for FR2 and FR3 mutants). All final mutated pcDNA_tACEg13sol constructs were checked extensively via restriction endonuclease digestion and prepared for transfection into mammalian cells for expression.

The cassette approach described here, where multiple cDNA fragments are mutated separately then substituted into the final expression vector, provides an efficient means for generating multiple single amino acid mutant constructs in the structure-function investigation into ACE function.

Chapter 3: Expression, Purification and Evaluation of tACE Constructs

3.1 Introduction

A variety of mutated forms of tACEg13sol were generated (described in Chapter 2) where specific residues in and around the chloride binding pockets were substituted in order to investigate specific aspects of chloride dependence. These constructs were stably transfected into Chinese hamster ovary (CHO) cells that do not express any endogenous ACE. Mutant protein was expressed, purified and characterised in terms of enzymatic activity. Initial characterization was done by assessing the chloride titrated activity of the mutant constructs using the synthetic substrate hippuryl-L-histidyl-L-leucine (HHL), which displays a highly chloride-dependent profile, and Z-phenylalanyl-L-histidyl-L-leucine (Z-FHL) which has a profile similar to the physiologically relevant peptide angiotensin I.

Objectives:

1. Transfect plasmids containing tACEg13sol mutant encoding cDNA into CHO cells and establish high expressing clones for each.
2. Purify tACEg13sol mutants using Sepharose-lisinopril affinity chromatography.
3. Evaluate whether mutations have affected chloride dependence profile of HHL and Z-FHL using chloride titrations.

3.2 Experimental Approach

3.2.1 Chemicals

Dulbecco's modified eagle's medium (DMEM) and Ham's F12 were obtained from Sigma, with Fetal calf serum (FCS), tissue culture flasks and trypsin supplied by Gibco. N-2-hydroxyethylpiperazine-N'-2-ethanesulphonic Acid (HEPES), genetecin G418, HHL, HL, Z-FHL and o-phthaldialdehyde, were purchased from Sigma. CHO-K1 cells were obtained from American Type Culture Collection (ATCC® CCL-61). The Profection Mammalian Transfection System was purchased from Promega, with NaCl, Boric acid and $ZnSO_4$ from Merck and Lisinopril from Zeneca Pharmaceuticals.

3.2.2 Transfection of tACEg13sol constructs

pcDNA_tACEg13sol mutant constructs were transfected using the ProFection® Mammalian Transfection System into CHO-K1 cells, which contain no endogenous ACE expression. The

growth media used to culture the cells consisted of 45% DMEM, 45% HAMS, 10% foetal calf serum (heat inactivated at 56°C for 30 min) and 20mM HEPES (pH 7.5), with growth conditions being 5% CO_2 at 37°C, 80% relative humidity. A CHO-K1 stock solution (500µl of cells frozen in a solution of 10% DMSO in foetal calf serum) were inoculated into 10 ml of culture medium and grown until confluent. Cells were then seeded into 10 cm^3 culture dishes at a concentration that would result in 30-60% confluency after overnight incubation. Three hours prior to transfection, the cells were washed with 1x phosphate buffered saline (PBS) and incubated further with fresh growth medium. A 500µl solution of 10-20µg of plasmid DNA and 248mM $CaCl_2$ was added to 2X HEPES-buffered saline [25mM HEPES, 25mM NaCl, 5mM $MgCl_2$, 0.5mM dithiothreitol, pH 7.9] whilst air was bubbled through, which formed a DNA-$CaPO_4$ precipitate after incubation for 30min at room temperature. The precipitate was then added to cells in a dropwise manner, swirled and incubated for 4h at 37°C in 5% CO_2. The cells were subsequently shocked by addition of a 15% glycerol in 1X PBS [137mM NaCl, 2.7mM KCl, 4.3mM $Na_2HPO_4.7H_2O$, pH 7.3] solution for 2min at room temperature. The cells were washed twice with 1X PBS and incubated overnight in fresh culture medium. After 24h, cells were switched to media containing 0.8mg/ml G418 (Sigma), with daily media changes until individual colonies were observed on the plates. Individual colonies were transferred to 12-well plates using sterile swabs dipped in trypsin-EDTA [0.13M NaCl, 10mM $Na_2HPO_4.2H_2O$, 2.7mM KCl, 1.5mM KH_2PO_4, 0.5% (w/v) trypsin, 0.1% (w/v) EDTA, pH 7.4]. Remaining cells (mixed stock) were trypsinized and reseeded. Highest expression clonal lines were screened for ACE expression by assessing ACE activity in the medium using substrates HHL and Z-FHL.

3.2.3 HHL and Z-FHL Assays

Hippuryl-L-histidyl-L-leucine (HHL) and Z-Phenylalanyl-L-histidyl-L-leucine (Z-FHL) are both cleaved by ACE, which results in an L-histidine-L-leucine (HL) product. The free histidyl moiety of HL can form a fluorescent adduct with O-pthaldialdehyde, which is measured spectrofluorometrically ($\lambda_{excitation}$ = 360 nm; $\lambda_{emission}$ = 485 nm) (Friedland and Silverstein, 1976). Medium or purified sample (10 µl of appropriate dilution adjusted to keep fluorescent readings in a specific determinable range) was incubated at 37°C for 15 minutes with 30µl of substrate in assay buffer; either HHL (5.6 mM, 0.05 M HEPES buffer, pH 7.5,

0.3 M NaCl, 10 µM $ZnSO_4$) or Z-FHL (1 mM in 0.1 M KPO_4 buffer, pH 8.3, 0.1 M NaCl, 10 µM $ZnSO_4$), with the reaction subsequently stopped by the addition of 170 µl of 0.28 M NaOH. Fourteen microlitres of 20 mg/ml O-pthaldialdehyde was added, incubated at room temperature for 10 minutes to allow the formation of fluorescent adducts, and the reaction then stopped with the addition of 26µl of 3N HCl. The entire reaction was performed in a 96-well plate, with the 250µl final volume read using a Varian Eclipse Fluorescence Spectrophotometer. An HL standard curve (0-20 nmol HL) was generated to convert fluorescent units into milliunits (mU) ACE activity, where 1 unit is defined as 1 nmole of HL produced per minute per millilitre ($.min^{-1}.mL^{-1}$) at 37°C in assay buffer.

3.2.4 Isolation and Purification of tACEg13sol Constructs

The tACEg13sol clonal cell lines generated in 3.2.2 were grown using 10% FCS growth medium and ultimately seeded into T175 cm^2 flasks, where they were grown to 90-100% confluency. Growth medium was then replaced with expression medium, consisting of 50 % DMEM, 50 % Ham's F12, 20 mM HEPES supplemented with 2 % FCS (heat-inactivated for a further 15 min at 70°C), and harvested every 3 days for between 5 and 7 cycles. Harvested medium was centrifuged for 2 minutes to remove any cellular debris, pooled and stored at -20°C until needed for purification.

Purification of tACEg13sol constructs was achieved via affinity chromatography, where the thawed expression medium harvests were passed over a Sepharose-28-lisinopril affinity column (Ehlers et al., 1991). The 10ml column was then washed overnight by passing approximately 400-600ml of wash buffer (20 mM HEPES, pH 7.5, 0.5 M NaCl) to reduce non-specific binding, followed by elution using 50 mM Borate buffer (pH 9.5). The elution of protein was monitored by UV absorption (280nm). Fractions were assayed for ACE activity using substrate HHL. The fractions with ACE activity were pooled and dialysed in 4 x 2L of dialysis buffer (5mM HEPES (pH 7.5), 0.1 mM PMSF) at 4°C over a period of 48 hours. Protein was then removed from dialysis and applied to multiple centrifugation steps using 4ml Amicon Ultra-4 centrifugal filter tubes (30 kDa MWCO), where it was concentrated to between 6 and 15µM and concomitantly equilibrated to appropriate storage conditions (50mM HEPES pH 7.5, 10µM $ZnSO_4$). Concentrations (C) were calculated based on the Beer-Lambert equation $A = \varepsilon Cl$. The extinction coefficient (ε) was calculated using the formula

established by Gill & Von Hippel (1989) and found to be 137122 $M^{-1}cm^{-1}$ for tACEg13sol and all mutants except M223W (142662 $M^{-1}cm^{-1}$), with N-domain D629 being 161142 $M^{-1}cm^{-1}$. Absorbance (A) of the samples was measured at 280 nm, and the pathlength (l) of the cell was 1 cm.

3.2.5 Chloride Titrations

Chloride titrations were performed using HHL and *Z*-FHL solutions containing varying amounts of NaCl (0-1M). The protocol for the assay was as described in 3.2.3, the only difference being that for both substrates the buffer used was TAPSO (pH 7.5) at 50mM, which was used in order to maintain consistency with the ITC experimental approach (described in Chapters 4 and 5) that necessitated the use of this buffer. Enzyme sample (20µl of appropriate dilutions) containing no NaCl was combined with 20µl of substrate containing a given NaCl concentration, the final NaCl concentration is diluted by a factor of 0.5 (hence range of 0-0.5M). Milliunits (mU) of ACE activity were calculated as described in 3.2.3, divided by the total number of micrograms (µg) in the reaction volume, and thus expressed as specific activity ($mU.\mu g^{-1}$). Substrate concentrations used were ≥5x Km and the total percentage hydrolysis in each reaction was kept below 20% in order to approximate first order rates (k_{cat}/K_M). The measure of chloride binding ($K_{d,app}$) was calculated from activation plots of specific activity versus the logarithm of chloride concentration, with the resultant curves analyzed via non-linear regression using a sigmoidal dose-response curve with the formula:

$$Y = \frac{(SA_{max} - SA_{min})}{1 + 10^{LogEC50-X}}$$

where SA_{min} is the specific activity in the absence of NaCl, SA_{max} is the maximum specific activity upon titration with chloride, X is the logarithm of chloride concentration, Y is the response (specific activity) and EC50 is is the X value when the response is halfway between SA_{max} and SA_{min}.

3.2.6 Molecular Docking

The short synthetic tri-peptides HHL and *Z*-FHL were docked into the tACE-RXPA380 crystal structure (PDB code 2oc2) using the Accelrys Discovery Studio© Molecular Simulation program. The tACE-RXPA380 crystal structure was used as RXPA380 is a similar size to *Z*-FHL and occupies a similar binding site. The HHL and *Z*-FHL molecules were built and minimized

into the defined active site using CDOCKER simulation tool. Poses were visually evaluated based on proximity (<2.5Å) and orientation of: A) the scissile peptide carbonyl group (displayed in the geminal diol form) to the active site zinc, and B) the C-terminal carboxylate to Lys511, a likely interaction given that this residue interacts with the lisinopril c-terminal carboxylate (Natesh et al 2003). The pose that best fit these criteria and had the highest CDOCKER score was chosen.

3.3 Results & Discussion

3.3.1 Protein Expression and Purification

All constructs were expressed in CHO cells, purified using Sepharose-lisinopril affinity chromatography and qualitatively assessed for purity and to determine the molecular weight using SDS-PAGE. As can be seen in Figure 3.1, bands for all tACEg13sol constructs migrated with a mobility that correlated to a molecular weight of 70 kDa, which is in

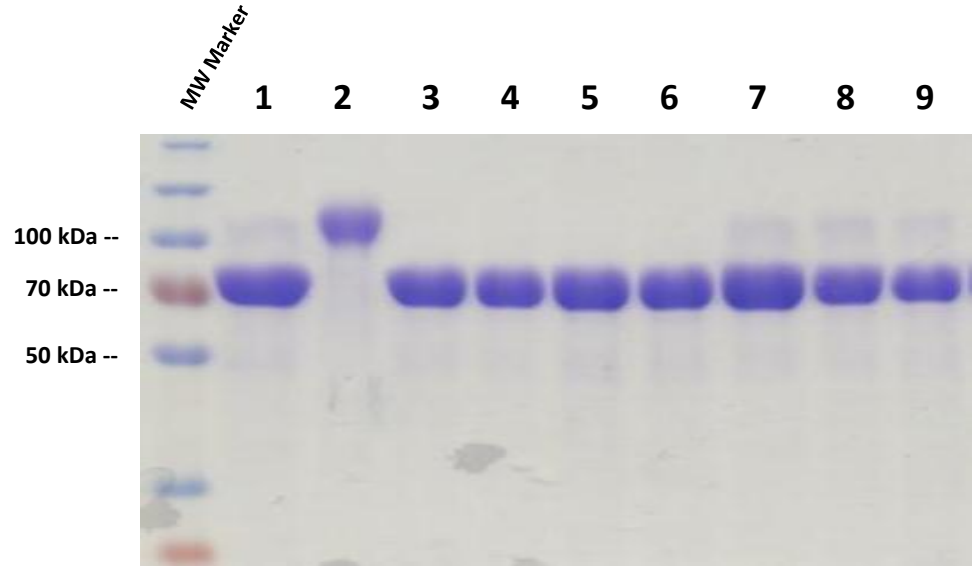

Protein Yield ($mg.L^{-1}$ medium)	5.6	1.2	6.0	1.9	8.8	7.7	7.7	2.5	4.9

Figure 3.1 Representative SDS-PAGE (10 %) indicating purity of all tACEg13sol mutants. Lanes 1, tACEg13sol; 2, N-domain D629; 3, R186H; 4, M223W; 5,E403R; 6, D465T; 7, V518T; 8, R522Q; 9, R522K. Lanes were loaded with approximately 10 µg of protein. Arrow indicates the size of the tACEg13sol constructs (~70 kDa) with the N-domain D629 being larger at ~100kDa. Protein yields for each construct are indicated below the gel image.

agreement with the predicted molecular weight and previously published literature (Gordon et al., 2003). The N-domain construct had a molecular weight of 100 kDa as described previously (Anthony et al., 2010) and migrated as a broad band due to heterogeneity of the glycosylation. The tACEg13sol proteins are minimally glycosylated and do not have such heterogeneity, migrating as sharper bands on SDS-PAGE. Absorbance of each construct was measured at OD280 and the protein concentration calculated (as described in 3.2.4). This allowed calculation of total protein yields for each construct (Figure 3.1), with yields which compare very favourably with previously reported yields for tACE. All proteins were active to varying degrees with both HHL and Z-FHL, allowing for further characterisation.

3.3.2 Chloride Titrated Activity of tACEg13sol mutants

In order to assess whether the mutations introduced have had an effect on the chloride dependence profile, the chloride titrated activity with both HHL and *Z*-FHL for each construct was performed (Table 3.1). The $K_{d,app}$ for chloride binding, along with the minimum and maximum specific activities (SA_{min} & SA_{max}) allow for preliminary evaluation of the mutants.

3.3.2.1 Chloride 1 pocket

Investigation of the chloride 1 pocket is of interest as the crystal structure of the N-domain, unlike that of the C-domain, showed that a chloride ion was not present (Corradi et al., 2006). It has been suggested that chloride binding in this pocket in the C-domain plays an activation role via the structural orientation of Lys511, a residue that stabilizes the C-terminal carboxylate group of lisinopril (Tzakos et al., 2003; Sturrock., 2001; Natesh et al., 2003). However, Moiseeva et al (2005) suggest the pocket plays an inhibitory role and proposed a mechanism whereby, in the absence of chloride, Asp507 switches from forming a salt bridge with Lys511 to forming one with Arg501 in the enzyme-substrate complex. Disruption of the Asp507-Arg501 salt bridge by chloride binding would disrupt the orientation of Lys511 and negatively affect catalysis. All the residues discussed regarding this particular pocket are shown in Figure 3.2A. However, very little functional work concerning this proposal has been performed and the only mutagenic work done to date

Table 3.1 Effect of NaCl on the hydrolysis of HHL and Z-FHL synthetic peptides by ACE constructs. All values were obtained from chloride titrated activity assays (described in 3.2.5). Units for SA_{min} and SA_{max} are $mU.\mu g^{-1}$ and $K_{d,app}$ are in mM. Data shown represent the average of two independent determinations, each in triplicate. The ~ indicates that accurate estimations of $K_{d,app}$ and SA_{max} could not be obtained as the chloride concentration range was insufficient for saturation to occur. SA_{max} for these values is activity at 500mM and 50mM NaCl for HHL and Z-FHL respectively.

Construct	HHL				Z-FHL			
	$K_{d,app}$ (mM)	SA_{min} (mU/µg)	SA_{max} (mU/µg)	SA_{min} % of SA_{max}	$K_{d,app}$ (mM)	SA_{min} (mU/µg)	SA_{max} (mU/µg)	SA_{min} % of SA_{max}
tACEg13sol	46.92	2.09	83.15	2.5	1.81	93.46	339.26	27.5
N-domain	0.16	10.54	24.20	43.5	0.75	36.54	206.72	17.6
R186H	76.90	3.65	113.30	3.2	2.14	130.26	467.20	27.8
M223W	44.64	2.76	27.91	9.9	2.07	17.55	194.66	9.0
E403R	2.66	6.34	99.80	6.3	0.25	214.48	398.46	53.8
D465T	12.72	0.36	46.59	0.8	2.83	2.10	110.74	1.8
V518T	47.47	6.53	116.26	5.6	5.54	40.16	667.23	6.0
R522Q*	~417.8	4.58	~11.21	40.8	~231.90	161.87	~217.97	74.3
R522K*	~339.7	4.07	~10.03	40.5	~104.56	97.19	~193.18	50.3
R381E (N-domain)	4.73	0.47	10.15	4.6	11.37	1.11	88.00	1.2

was by Rushworth et al., (2008). These authors found that the R186Q mutation reduced chloride dependence with AngI as well as overall level of activity in presence of NaCl. Two other mutations in the chloride 1 pocket had similar effects, suggesting the overall structure (not just one interaction) of the pocket may be important.

The initial assessment of the tACEg13sol_R186H (hence referred to as R186H) was done using short synthetic peptides HHL and Z-FHL and showed different effects. The $K_{d,app}$ for R186H compared to tACEg13sol was increased by only 18% for Z-FHL, yet showed a 64%

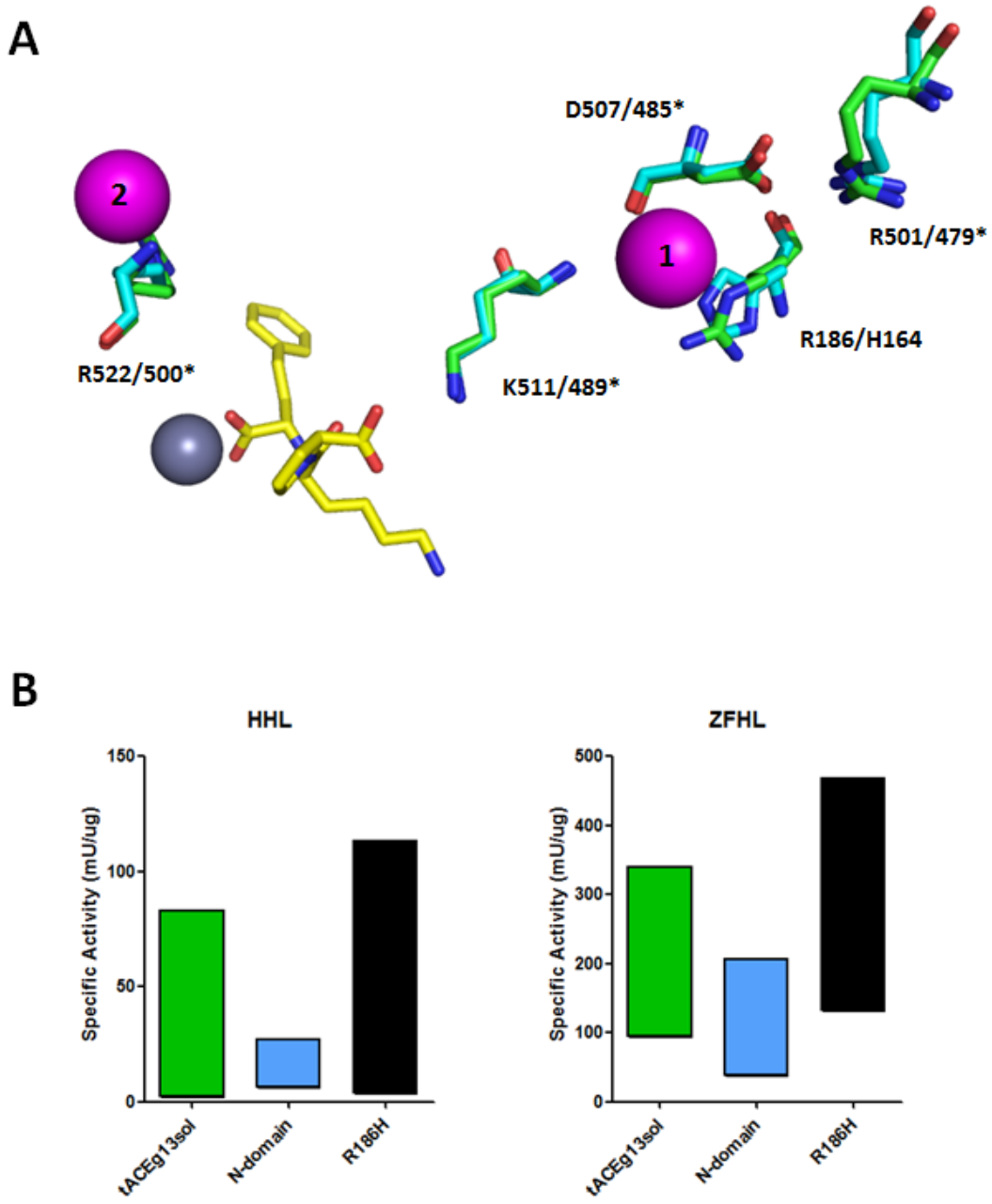

Figure 3.2 Chloride 1 pocket of ACE. A) Stick representation showing C-domain (PDB code 1o86) aligned to the N-domain structure (PDB code 2c6n), with residues at each position shown in green and light blue respectively. Residue position and identity are shown below each, with the tACE numbering prior to that of the N-domain and the asterisk indicating that the residue identity is unchanged. The critical active site zinc ion is shown as a grey sphere, with the chloride ions shown as purple spheres and numbered according to the pocket they're in (pocket 1 or 2). The lisinopril (yellow) that was co-crystallised with tACE is shown in the active site coordinating the zinc ion. Images were created using PyMOL 0.99 (DeLano Scientific, Palo Alto, CA, USA). **B)** Low-High Bar graphs for the specific activity of tACEg13sol, N-domain D629 and tACEg13sol_R186H with HHL and Z-FHL substrates. The bottom of each bar corresponds to the SA_{min}, with the top corresponding to SA_{max} (data reproduced from table 3.1). Graphs were generated in Graphpad Prism 5 software.

increase for HHL. Given that the main mechanistic role of chloride binding is observed in the chloride 2 pocket (Liu et al., 2001) where disruption of the coordinating Arg522 resulted in orders of magnitude increases in $K_{d,app}$, these shifts in $K_{d,app}$ are relatively small. Along with the distal location of the chloride 2 pocket, this indicates that these shifts can be attributed to minor structural shifts.

For HHL hydrolysis at 0mM NaCl there appears to be no significant difference in activity between tACEg13sol, N-domain and R186H. However, upon titration with chloride the maximal activity of R186H increased by 36% over tACEg13sol, as opposed to reducing to the lower N-domain level (fig 3.2B). A similar trend is seen for Z-FHL hydrolysis between tACEg13sol and R186H, differing in that the SA_{min} for tACEg13sol, N-domain and R186H exceeds the SA_{max} for HHL hydrolysis. This trend is the opposite of that observed by Rushworth et al (2008) where they found that the R186Q mutation reduced chloride dependence with AngI as well as overall level of activity in presence of NaCl. Two potential explanations can be put forward: The first being that this difference is a result of the different mutations, where Rushworth et al (2008) converted the R186 to a glutamine and in the current study it was converted to the corresponding N-domain histidine. Both mutations would presumably abrogate or disrupt coordination of chloride in this pocket of tACE and the difference in overall activity would presumably be a result of other differences between the two domains. However, there is the possibility that the His in R186H may still coordinate chloride, performing a similar role, hence the lack of considerable variation in activity. This would then point to the lack of a chloride observed in the N-domain structure as either an anomaly or that chloride cannot access the pocket. A further possibility may be that the His may substitute for the chloride-coordinated Arg, via interactions with other residues in the pocket, and thereby maintain the shape and dynamics of the pocket and thus rendering chloride unnecessary.

The second explanation hinges on the greater length of the angiotensin I decapeptide over the shorter HHL and Z-FHL tripeptides. There is evidence for a hinge bending mechanism of tACE based on its structural similarity to ACE2 (Watermeyer et al., 2006). Furthermore, if the chloride 1 pocket is involved in stabilizing one conformation over another, disruption of chloride coordination in the C-domain may affect either substrate binding, substrate access or both. Thus, the larger angiotensin I peptide might be blocked from accessing the active

site, yet the smaller peptides would have better access and, with the structural shift be better hydrolysed. However, the N-domain crystal structure showed no chloride bound in this pocket (Corradi et al., 2006) and is hence not critical for activity. Also, the N-domain has been shown to be more thermally stable than the C-domain (Anthony et al., 2010) discounting the idea that chloride binding in the chloride 1 pocket plays a stabilising role. This suggests that the pocket elicits similar structural effects in the two domains yet does so via different interactions, as the R186H mutation does not convert C-domain activity to more N-domain like activity. These assertions are all based on specific activity data reported here and by Rushworth et al (2008) and more definitive kinetic and structural data is needed to fully delineate the effects this pocket has on tACE activity. More in-depth analysis regarding the roles of these residues is performed in chapter 5.

3.3.2.2 Chloride Channel

The presence of a channel that allowed access of chloride ions from the external milieu into the chloride 2 pocket of each ACE domain was proposed by Tzakos et al (2003). They identified E403 in the C-domain as potentially acting as an ionic gate, blocking the channel via interaction with R522 and hence needing to be dislodged before chloride ions can access the chloride 2 pocket. As shown in Figure 3.3A, this channel filled with a network of five hydrogen-bonded water molecules (764, 767, 720, 1124, 1150) is conserved in both the native and lisinopril-bound tACE crystal structures. The K118 residue forms a salt bridge with E403 in the native structure of tACE, but not in the lisinopril-bound structure (Tzakos et al., 2003). That this residue corresponds to an alanine (A94) in the N-domain suggests this may be of relevance due to the loss of interaction in the N-domain. Central to this hypothesis is that the corresponding residue to E403 in the N-domain (R381) has the opposite charge and would presumably not block the channel. This represents a potentially major cause of the variation in the chloride dependence profiles between the two domains.

With the change from a Glu to an Arg in tACEg13sol_E403R mutant (hence referred to as E403R), 18- and 7-fold reductions in the $K_{d,app}$ values were obtained with HHL and Z-FHL chloride titrations, respectively (Table 3.1). This supports the idea that E403 is gating chloride access and that an Arg in that position alleviates this. To provide further evidence

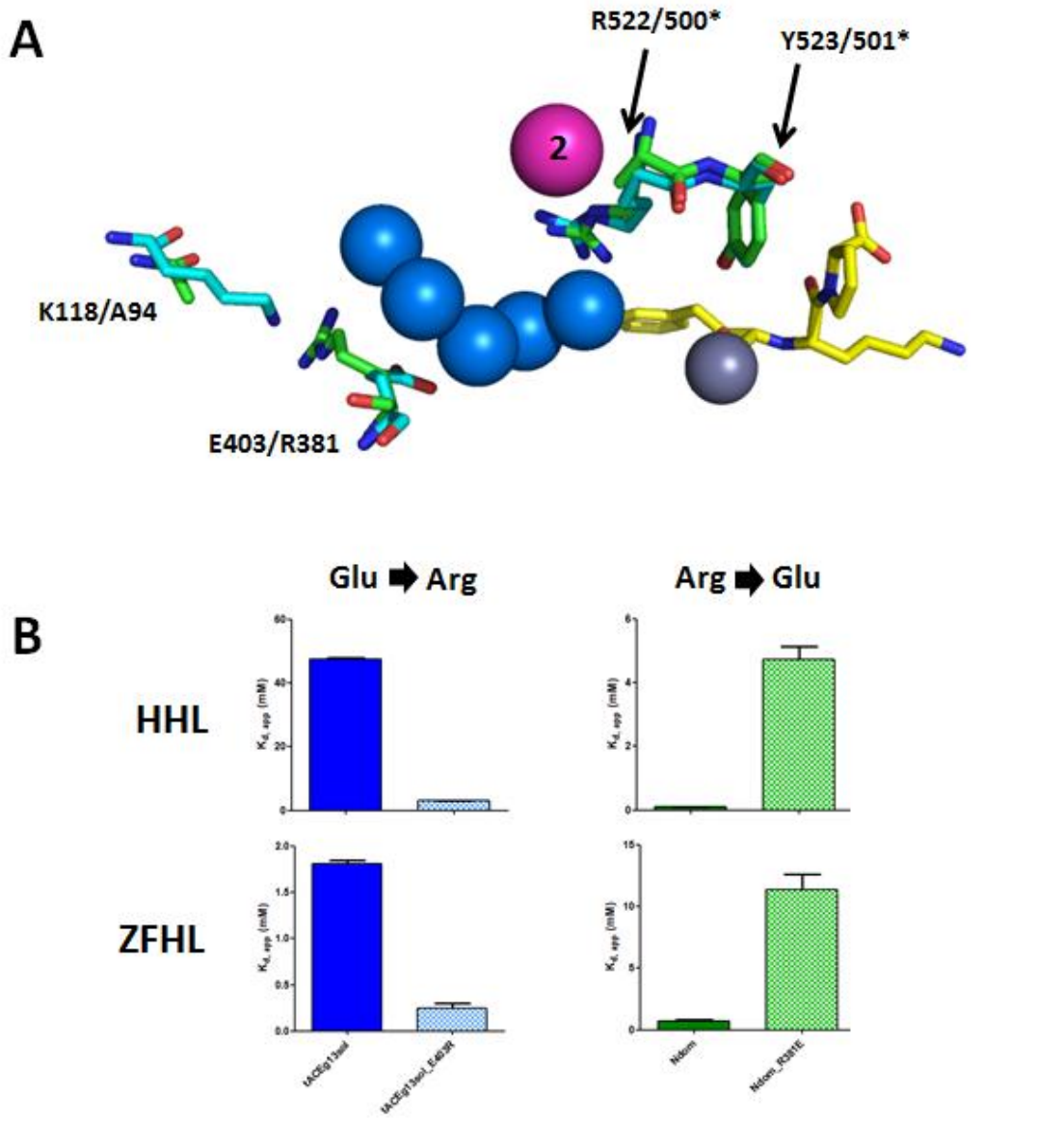

Figure 3.3 Chloride channel of ACE. A) Stick representation showing tACE (PDB code 1o86) aligned to the N-domain structure (PDB code 2c6n), with residues at each position shown in green and light blue respectively. Residue position and identity are shown below each, with the tACE numbering prior to that of the N-domain and the asterisk indicating that the residue identity is unchanged. The critical active site zinc ion is shown as a grey sphere, the chloride ion within Chloride pocket 2 shown as a numbered purple sphere and the hydrogen bond-linked waters that indicate the path of the proposed channel (described by Tzakos et al., 2003) shown as blue spheres. The lisinopril (yellow) that was co-crystallised with tACE is shown in the active site coordinating the zinc ion. Images were created using PyMOL 0.99 (DeLano Scientific, Palo Alto, CA, USA). **B)** Bar graphs comparing the $K_{d,app}$ values of tACEg13sol versus tACEg13sol_E403R (dark and light blue respectively) and N-domain D629 versus N-domain_R381E (dark and light green respectively) with both HHL and Z-FHL substrates (indicated on the left of the graphs). The residue identity at the 403 and 381 positions are indicated above the bars. Data were reproduced from table 3.1 (with standard error between two means included, which are not shown in table 3.1), with graphs generated in Graphpad Prism 5 software.

that this effect is robust and reciprocal, a purified sample of N-domain_R381E mutant (where Arg381 has been converted to a Glu in the N-domain) was analysed. As can be seen by the $K_{d,app}$ values in Table 3.1, the reverse is seen with 29- and 15-fold increases for HHL and Z-FHL titrations, respectively, clearly showing a reciprocal trend in both domains. This represents the first clear evidence of a gating mechanism in the ACE C-domain.

The degree of activation by chloride (%SA_{max}) is represented by the increase in activity between SA_{min}, which is activity without NaCl, and the SA_{max}, which is the maximum activity obtained upon chloride titration. The %SA_{max} for both HHL and Z-FHL with the E403R mutation increased 2-fold over tACEg13sol (Table 3.1). This is as a result more of an increase in SA_{min} than in SA_{max}, which had minor increases. Interestingly, this trend is more pronounced in the Arg to Glu reversion between N-domain and R381E, where the %SA_{max} decreased by 10- and 15-fold for HHL and Z-FHL, respectively. This effect was made more pronounced due to a more than 50% decrease in SA_{max} with both substrates. This data is in accordance with the hypothesis put forward by Tzakos et al (2003) that E403 might form a salt bridge with R522 in the absence of chloride. An Arg in this position would lack this salt bridge allowing for greater flexibility of the R522, which would allow Y523 to swing into the active site and thereby increase catalysis in the absence of chloride.

Further insights can be gained by looking at the chloride titration curves for these four constructs (Figure 3.4A). After initial activation of E403R and N-domain using HHL as substrate, there is a decrease in activity as the chloride concentration increases. In contrast, both R381E and to a greater extent tACEg13sol show slower activation consistent with higher $K_{d,app}$ values, but plateau at high chloride concentration. A similar trend is only seen with the substrate Z-FHL for E403R, but it must be pointed out that the reduction in activity at high chloride concentration is seen for tACEg13sol and N-domain with Z-FHL in phosphate buffer (data not shown), but could not be ascertained here as Z-FHL was not soluble at high NaCl concentrations in the buffer used (TAPSO). Moiseeva et al (2005) attributed this phenomenon of activity reduction at high chloride concentration to an inhibitory role for chloride binding in the chloride 1 pocket based on kinetic modelling. What is evident from the above analysis here is that an Arg in the 403/381 position appears to exaggerate this effect. This position is greater than 25Å from the chloride 1 pocket, hence structural

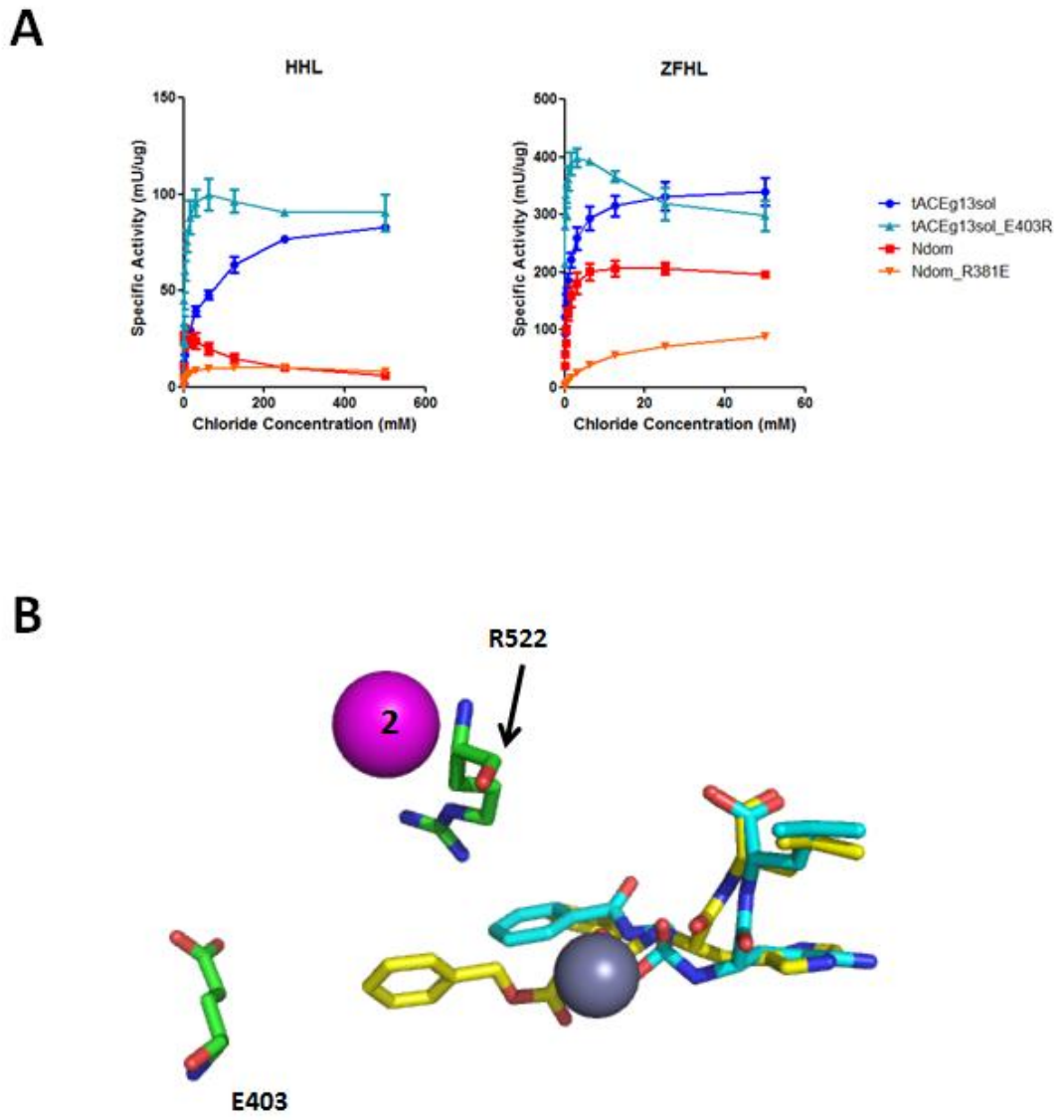

Figure 3.4 Chloride channel of ACE. A) Chloride titrated specific activity of tACEg13sol (dark blue), tACEg13sol_E403R (light blue), N-domain D629 (red) and N-domain_R381E (orange) with HHL and Z-FHL substrates. Each data point is the average of two independent determinations, each in triplicate, with error bars showing the standard error between averages. Graphs were generated in Graphpad Prism 5 software. **B)** Stick representation of overlayed HHL (blue carbon atoms) and Z-FHL (yellow carbon atoms) docked into the tACE-RXPA380 crystal structure (Corradi et al., 2007; PDB code 2oc2) using the Accelrys Discovery Studio© Molecular Simulation program (described in 3.2.6). tACE residues are shown in green, with position and identity shown below each, the critical active site zinc ion is shown as a grey sphere, the chloride ion within Chloride 2 pocket shown as a numbered purple sphere.

perturbation could to be transmitted by influencing the proposed hinging of the subdomains of tACE (Watermeyer et al., 2008), although how this would occur is unclear.

A more likely scenario is that the effect is mediated by interactions with the substrate. Comparing HHL and Z-FHL and their potential interactions with ACE (Figure 3.4B), the hippuryl group of HHL only partially protrudes into the S2 pocket (where 403/381 is situated), whereas the Cbz group of Z-FHL is larger and occupies more of the S2 sub-site. The shorter E403 sidechain in tACEg13sol is less likely to have any interactions with HHL, and this is supported by the high $K_{d,app}$ value where the "gate" would be fully closed. This gating is presumably disrupted with Z-FHL hydrolysis in tACEg13sol, hence the $K_{d,app}$ value being in a similar range to that of the N-domain hydrolysis of Z-FHL. This gives credence to the idea that substrate interaction in the S2 pocket may play a role in mediating chloride access to the S2 pocket and opens up the possibility that substrate interactions may facilitate chloride 2 pocket binding.

3.3.2.3 Chloride 2 pocket

Mutagenic work by Liu et al (2001) identified the R522 (R1098 in somatic ACE) as being the critical residue in the coordination of the chloride ion, a fact that was confirmed in the crystal structures of both domains (Natesh et al., 2003; Corradi et al., 2006). Despite this, the exact mechanisms of chloride activation remain poorly understood. Tzakos et al (2003) have proposed a mechanism for the C-domain (tACE) where the R522 forms a salt bridge with D465 in the absence of NaCl. Tyr523 is suggested to play a role in the stabilisation of the enzyme-substrate transition-state and is right next to R522 on the protein backbone (Sturrock et al., 2004). It is suggested that the R522-D465 salt bridge would keep Y523 oriented away from the active site, and disruption of this interaction by chloride entering the pocket and coordinating R522 would push Y523 further into the active site, facilitating catalysis. These residues are highly conserved in the N-domain, suggesting the overall mechanism is shared between the two domains. The mutation of R522 to a glutamine or a lysine was originally described by Liu et al (2001) and evaluated for its effect on angiotensin I hydrolysis. They reported a complete abolition of chloride dependence with the glutamine mutation and a considerable increase in the $K_{d,app}$ for lysine, indicating that the charge and sidechain length is critical for coordination. These mutations were repeated in tACEg13sol in order to further evaluate their role with HHL and Z-FHL, and to provide context for the evaluation of the other mutations in the chloride 2 pocket (Figure 3.5).

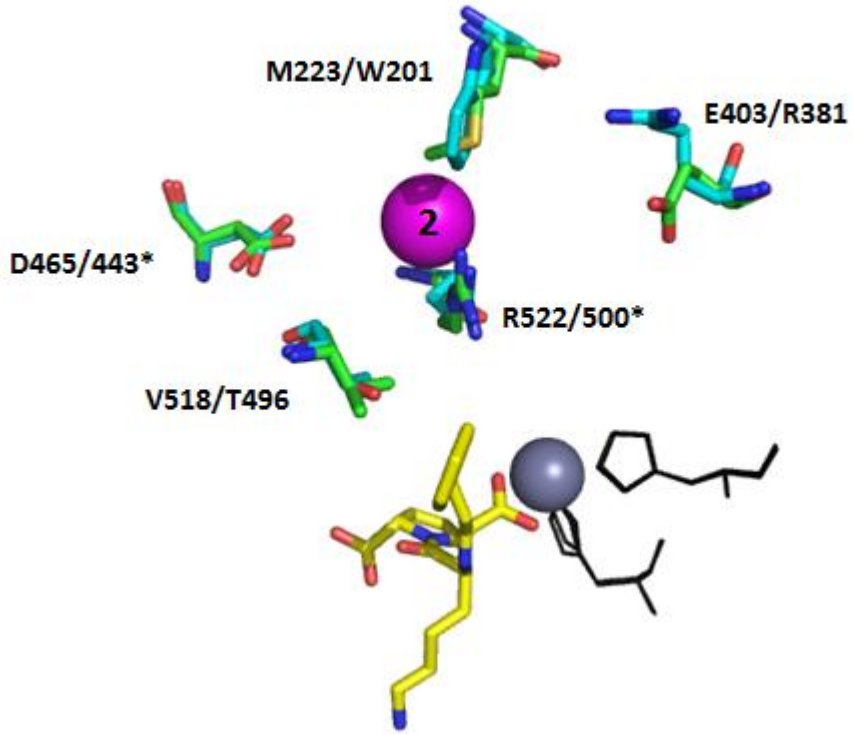

Figure 3.5 Chloride 2 pocket of ACE. Stick representation showing tACE (PDB code 1o86) aligned to the N-domain crystal structure (PDB code 2c6n), with residues in the chloride 2 pocket shown in green and light blue, respectively. Residue position and identity are shown below each, with the tACE numbering prior to that of the N-domain and the asterisk indicating that the residue identity is unchanged. The critical active site zinc ion is shown as a grey sphere, with the chloride ion in pocket 2 shown as a purple sphere. The lisinopril (yellow) that was co-crystallised with tACE is shown in the active site coordinating the zinc ion, with the 2 zinc coordinating histidines (H383 and H387) shown as black lines. Images were created using PyMOL 0.99 (DeLano Scientific, Palo Alto, CA, USA).

As can be seen in Table 3.1, the $K_{d,app}$ values for R522Q and R522K are considerably higher than that for tACEg13sol with both HHL and *Z*-FHL, with the estimated values for R522Q being higher than those for R522K. This is consistent with the data reported by Liu et al (2001) and supports the hypothesis that coordination is largely abolished by Gln in this position and greatly reduced by Lys. The $\%SA_{max}$ values for both are also higher than tACEg13sol, indicating reduced activation upon chloride addition. Interestingly the SA_{min} value for R522K with Z-FHL is very similar to tACEg13sol, yet for R522Q it is about 2-fold

higher. An explanation may be that the Lys in R522K may still be able to form a salt bridge with D465, unlike a Gln substitution, keeping it in a similar conformation as tACEg13sol. This would result in greater flexibility and an increased likelihood for Y523 to move towards the active site and increase catalysis. This differs with HHL where both R522K and R522Q have only slightly higher SA_{min} levels than tACEg13sol. Also of note is that the $\%SA_{max}$ for R522Q with *Z*-FHL is higher than that with HHL, and at 74% is very much in line with the values described for angiotensin I (Liu et al., 2001). This suggests that R522K may be more rotationally restricted than R522Q (presumably due to a salt bridge with D465), potentially explaining the difference between the two mutations.

In order to determine whether D465 participates in a salt bridge with R522, a tACEg13sol_D465T mutant (referred to as D465T) was generated, where the polar acidic D465 (conserved as D443 in N-domain) was converted to the smaller polar uncharged threonine in order to prevent salt bridge formation. What is immediately apparent is that the $K_{d,app}$ with HHL for D465T is 4-fold lower than tACEg13sol, yet for Z-FHL, the $K_{d,app}$ is only marginally higher than both tACEg13sol and N-domain. That an appreciable change in $K_{d,app}$ is seen with one substrate versus the other would indicate that D465 is not mechanistically important. Further variation between HHL and Z-FHL is seen with the $\%SA_{max}$ values for D465T which are about 4-fold and 15-fold lower than tACEg13sol respectively, which is due to the combined lowering of SA_{min} and SA_{max} values to varying degrees (Table 3.1). The D465 residue is situated on the opposite side of the chloride pocket to the active site, which precludes direct interactions with substrate (Figure 3.5). The variability in $\%SA_{max}$ values seen for D465T between HHL and Z-FHL may be due to the mutation somehow inducing a structural alteration of either the chloride 2 pocket or the active site sub-site structure. This would indicate a structural role for D465 over the proposed mechanistic role suggested by Tzakos et al (2003).

The tACEg13sol_M223W and tACEg13sol_V518T mutations were constructed based on the fact that the residues lined the chloride 2 pocket and were variable between the C- and N-domains. The $K_{d,app}$ values for both HHL and Z-FHL with these mutations showed no change and indicates that these residues have little effect on chloride binding.

Some minor effects on overall activity were observed suggesting other interactions may be affected. M223W showed reductions in both SA_{min} and SA_{max} for both HHL and Z-FHL with its effects presumably due to the bulky tryptophan residue results in a differential interaction affecting the overall structure of the chloride 2 pocket. Indeed, the SA_{max} values for both HHL and Z-FHL with M223W more closely resemble those of the N-domain and this may represent a determinant in the variation in overall levels of activity between the two domains.

For V518T, the SA_{max} values are seen to be marginally elevated for both HHL yet more pronounced for Z-FHL relative to those of tACEg13sol. The Val to Thr mutation changes the nature of the side-chain from hydrophobic to polar uncharged without any major change in size, yet this has a large effect on Z-FHL hydrolysis. The V518 residue borders the chloride 2 pocket and active site S_1 binding pocket, and molecular minimisation studies show that it is in close proximity to the Z-FHL Phe in the P1 position. Presumably, the Thr mutation removes a hydrophobic interaction between the V518 and substrate Phe, resulting in increased catalysis in the presence of chloride.

Where the R522K and R522Q mutations showed significant effects on chloride dependence and activation, the M223W, D465T and V518T mutations effects were relatively minor, indicating they were not mechanistically relevant but may be the result of minor structural effects.

3.4 Summary

All active-site mutant proteins were successfully transfected, expressed and purified. Constructs were analysed using chloride titrated activity with substrates HHL, which has been shown to be C-domain selective and more chloride dependent than N-domain, and Z-FHL, which is less domain selective and has a similar chloride binding profile between both domains. The R186H mutation in the chloride 1 pocket showed increases in overall activity and $K_{d,app}$ values for both substrates, suggesting that the effect of replacing the aliphatic chain and guanidinium group of Arg with a an imidazole may be more structural than mechanistic. The E403R and R381E mutations provided clear evidence for a gating mechanism mediating chloride access to the chloride 2 pocket. Moreover, chloride titration

suggested that substrate interaction in the S2 pocket may disrupt this gating mechanism, providing a potential explanation for the differences in chloride dependence with different substrates. The D465T mutation showed some effect on activity and chloride binding, yet this was variable between HHL and Z-FHL indicating that its role is unlikely to be mechanistic and more likely a structural. The R522Q and R522K showed similar profiles for HHL and Z-FHL to that described by Liu et al (2001) using angiotensin I, with the difference between the mutations with the different substrates highlighting the role of substrate interactions. The M223W and V518T mutants did not show major deviations from wildtype, particularly in their $K_{d,app}$ values, and hence it is presumed they would not be mechanistically important. Taken together, most mutations in the relevant chloride pockets were shown to affect activation to varying degrees, yet only those varying in their $K_{d,app}$ values and hence having relevance to the chloride dependence mechanism warrant further investigation.

Chapter 4: Isothermal Titration Calorimetry as a method for determining ACE kinetics

4.1 Introduction

Evaluation of ACE enzyme kinetic constants has traditionally been limited to a few specific methods of detection, dependent on the nature of the substrate used. For enzyme kinetic measurements to be made, it is required that there be some observable event associated with the transformation of substrate into product. For ACE kinetics all the methods described in the literature employ some way of evaluating product concentrations and are based on the pseudo-first order method originally described by Michaelis & Menten (1913), which is used predominately in enzyme kinetic evaluation throughout the literature.

The physiological substrates, such as angiotensin I and bradykinin, have predominantly had product formation determined by High Performance Liquid Chromatography (HPLC) (Rice et al., 2004; Liu et al., 2001; Jaspard et al., 1993; Wei et al., 1991b). Whilst HPLC has proved suitable over the years, it is limited in its capacity for extensive and efficient kinetic evaluation of multiple constructs.

Monitoring of reaction progression of smaller synthetic peptides has usually been done either via HPLC, spectrophotometrically, or, as described by Friedlander & Silverstein (1976), fluorometrically via a coupled derivitization step for HHL and Z-FHL. More recently, the advent of Fluorescence Resonance Energy Transfer (FRET) technology has allowed for the synthesis of modified peptides that fluoresce upon cleavage, making kinetic evaluation more efficient. While FRET is suitable for shorter peptides, and has been applied to evaluating the kinetics of the tetrapeptide substrate AcSDKP (Araujo et al., 1999, Araujo et al., 2000), the technology is not applicable to the larger physiological peptides such as angiotensin I and bradykinin. The use of FRET also has the disadvantage that the substrate needs to be covalently modified via the addition of fluorescence acceptor and donor groups, which is not always ideal when looking at specific enzyme/substrate interactions. In recent years, the use of Isothermal Titration Calorimetry (ITC) to evaluate enzyme kinetics has started to become more widespread and presents an option in kinetics evaluation of ACE activity towards a wide range of substrates.

ITC is a powerful, well-established technique for the thermodynamic determination of equilibrium binding/association reactions. A single titration experiment directly measures not only the enthalpic change (ΔH_b) for a given reversible interaction, but can also yield both

the equilibrium binding constant (K_b) and stoichiometry of binding (n) (Wiseman et al., 1989; Ladbury, 1995; Haq et al., 2000/1). The broad applicability of this technique, where no specific assay development is required, and the commercial availability of high-sensitivity ITC equipment, has led to a dramatic increase in publications utilizing ITC to investigate molecular interactions over the last decade (Haq, 2005 Microcal application notes).

Apart from its more extensive application towards reversible association interactions, ITC has also been evaluated and successfully applied to the observation of enzyme kinetic reactions (Spink & Wadso, 1976; Watt, 1990; Morin & Freire, 1991; Williams & Toone, 1993; Lonhienne et al., 2000; Todd et al., 2001). ITC serves as a direct and observable means of monitoring an enzyme catalysed reaction, as the heat absorbed or released by an enzyme reaction as it proceeds over time (thermal power) is directly proportional to the rate of the reaction (Todd et al., 2001). The primary method for obtaining enzyme rate parameters is where multiple injections of substrate are made into the reaction cell containing low enzyme concentration, resulting in multiple steady-state rate determinations in a single reaction volume. The alternative, less commonly used method involves a single injection of substrate (at concentrations greater than K_m) into enzyme (or vice versa) followed by continuous rate measurements as substrate conversion to product runs to completion. Both of these methods yield rate data as a function of substrate concentration, which is readily analysed via non-linear regression using the integrated form of the Michaelis-Menten equation or a derivative thereof.

The two previous methods described represent two different strategies in determining Michaelis-Menten kinetics. The Multiple Injection Method represents a steady-state system where initial rates are determined at varying substrate concentrations, a method used widely for enzymes that obey the traditional Michaelis–Menten mechanism. The Single Injection Method represents a non-steady-state system where substrate depletion is tracked over time, with rate and substrate concentrations calculated, plotted and fitted to the Michaelis-Menten equation. The drawback of both of these methods is that they do not directly measure the initial rates, but use the determination of product formation or substrate depletion to approximate initial rates and hence calculate the Michaelis constant (K_m) and catalytic rate (k_{cat}) using the Michaelis-Menten equation (Golicnik 2010). Schnell & Maini (2000, 2003) suggested that there are significant constraints on the conditions under

which the measurement of initial rates are valid and can be applied to the Michaelis-Menten equation, questioning the accuracy of this approach. In this regard, any errors in the determination of rates can have a compounding effect on the calculation of K_m and k_{cat}, and hence a larger effect on k_{cat}/K_m.

The initial rate of a reaction can be (as is routinely done in the literature) determined using a progress curve, which is a plot of product formation over time. The initial rate is calculated using linear regression from the origin through the initial 10% of the curve (Eisenthal, 1992). Indeed, this method has been applied to ITC by Stockbridge & Wolfenden (2009, 2011). However, using this linear approach has drawbacks, the most notable being that the initial part of the curve may not be completely linear around or below K_m (Golicnik 2010). This not only makes linear fitting prone to error, but places severe limitations on usable substrate concentrations. Furthermore, this method provides no way of devolving k_{cat}/K_m into the separate k_{cat} and K_m constants in a single experiment, and would require separate determination of either for all constants to be unveiled. Fortunately, in recent years progress has been made in developing non-linear regression analysis methods to fully utilize the progress curve in determining Michaelis-Menten constants (Schnell & Mendoza 1997; Goudar et al., 1999; Goudar et al., 2004; summarized by Golicnik, 2010). These attempts had always been hampered due to the computational complexity involved in solving the Lambert W function, an integral component of the formulae. Only recently, with the advent of commercial non-linear regression software (such as Excel, Prism, SigmaPlot) could progress curve data be fitted to explicit formulae containing this function. This approach was pioneered by Duggleby (2001), and has since been refined by Golicnik (2010, 2011), who presents a robust formulation in the analysis of progress curve data. Combining this approach with the method of ITC data transformation put forward by Stockbridge & Wolfenden (2009) provides a viable approach to determine Michaelis-Menten kinetic parameters with a high throughput for potentially any substrate.

The aim of the work presented here was to evaluate the feasibility of applying the ITC-based enzyme kinetic methods to the study of ACE using a short synthetic peptide (HHL) and a larger physiological peptide (Angiotensin I). The work presented many challenges and highlighted the limitations of the above methodology in evaluating a more complex enzyme system. It also provided valuable insights into the mechanisms of ACE hydrolysis that would

not have been identified by alternate methods. Furthermore, we present a robust methodology that circumvents many of the limitations of the common methods and allows for accurate and reproducible determination of enzyme reaction rate constants.

Objectives:

1. Determine whether the hydrolysis reactions between tACEg13sol and its substrates HHL and angiotensin I produce detectable changes in thermal power and ascertain the role buffer choice plays in this.
2. Evaluate the suitability of the Multiple and Single Injection Methods for the study of tACEg13sol enzyme kinetics.
3. Determine whether the use of Progress curves and the non-linear regression analysis of these curves correlate with either method in objective 2.
4. Evaluate the effect that different buffers have on the kinetic parameters of tACEg13sol hydrolysis of HHL and Angiotensin I
5. Determine the optimal assay approach for the study of chloride dependence mutants generated in Chapter 3.

4.2 Methods and Experimental Approach

4.2.1 Chemicals and Equipment

All ITC experiments were performed using an iTC_{200} microcalorimeter purchased from MicroCal LLC (GE Healthcare), with raw data either extracted for custom calculations using Microsoft Excel or analysed using Origin 7 software with proprietary MicroCal analysis module. All enzyme samples used were purified as described in Chapter 3. HHL, HL, angiotensin I, angiotensin II, HEPES, TES and TAPSO were obtained from Sigma. TRIS, NaCl, KH_2PO_4 and K_2HPO_4 were obtained from Merck. Sephadex® G-10 Medium was obtained from Sigma-Aldrich. Custom data manipulation and calculations were performed in Microsoft Excel and non-linear regression analysis done using Graphpad Prism 5 software.

4.2.2 Sample Preparation

Preparation of enzyme and substrate samples needs to be done to ensure that there is minimal mismatch in buffer concentrations as this can have a negative effect on data quality. Enzyme samples were equilibrated by dialysing 3- times against 500ml of reaction buffer (50-100mM buffer, pH 7.5; 10uM $ZnSO_4$; either 0mM, 20mM or 300mM NaCl). Substrate was prepared by either dissolution directly into dialysate, to desired concentration (for HHL), or by equilibrating against a 1ml G10 Sephadex desalting column (for Angiotensin I). The purchased angiotensin I powder contained appreciable amounts of Trifluoroacetate (TFA), which, when dissolved directly in dialysate, resulted in significant decrease in signal-to-noise ratio. Angiotensin I was dissolved in dialysate at high concentration then passed through a 1ml G10 column (equilibrated with dialysate in order to reduce TFA concentrations) under gravity. 200µl fractions were collected and tyrosine absorbance measured at 275nm to determine peptide containing fractions. These were pooled and the final concentration determined spectrophotometrically via absorbance at 275nm, using the empirically calculated extinction coefficient of 1280 $M^{-1}.cm^{-1}$.

4.2.3 Calorimetric Assays

Calorimetric assays were performed using an iTC_{200} microcalorimeter, which consists of a sample cell and a reference cell (filled with either dH_2O or reaction buffer) held at constant temperature. An automated stirring syringe is inserted into the sample cell and serves as the configurable titration vehicle, as well as a means of ensuring rapid mixing of reaction volume. Reaction cells (0.2027 mL) were filled with degassed solutions and equilibrated at the indicated temperatures, with stirring speed being 500 rpm. The exact power-compensation mechanisms of the instrument are summarized by Todd et al., (2001). Addition of either substrate, inhibitor or enzyme to the sample cell through the stirred injection syringe initiates the reaction, which, if exothermic will result in a negative deflection in observed thermal power or, if endothermic, will give a positive deflection in observed thermal power (Todd et al., 2001). Reaction rates are determined by measuring this change in instrumental thermal power.

4.2.4 Calorimetric Rate Equations

The following descriptions of the theoretical underpinnings for measuring enzyme kinetic rates have been described extensively in the literature (Morin & Freire, 1991; Williams &

Toone, 1993; Todd & Gomez, 2001). An enzyme-catalysed reaction is driven by a thermodynamically favourable decrease in free energy (ΔG), which is the combination of its entropy (ΔS) and enthalpy (ΔH), and is summarised in the formula:

$$\Delta G = \Delta H - T\Delta S \quad [1]$$

The enthalpic component (ΔH) represents the amount of heat absorbed or released by the reaction. Thus, measuring the rate of heat generation associated with the conversion of substrate to product gives a measure of the reaction rate.

In order for reaction rates to be determined, the apparent molar enthalpy (ΔH_{app}) needs to be determined experimentally. This is done by allowing a given reaction to run to completion with thermal power returning to the original baseline. Integration of the area under this curve (minus the heat of dilution obtained via control experiments) gives the experimental ΔH_{app} :

$$\Delta H_{app} = \frac{1}{[S]_{Total} * V} * \int_{t=0}^{t=\infty} \frac{dQ(t)}{dt} \quad [2]$$

Here $[S]_{Total}$ is the total substrate concentration, V is the volume of the reaction cell (µL) and dQ/dt represents the thermal power output of the calorimeter as a function of time (µcal/s). This experimentally determined ΔH_{app} is the amount of heat associated with the conversion of n moles of substrate, and it's relation to product formation is given by the following

$$Q = n.\Delta H_{app} = [P]_{Total}.V.\Delta H_{app} \quad [3]$$

where V is the reaction cell volume, $[P]_{Total}$ is the molar concentration of product generated. It can be seen from Equation 3 that measuring the thermal power as substrate is catalysed by enzyme, gives a measure of reaction rate:

$$Power = \frac{dQ}{dt} = \frac{d[P]}{dt}.V.\Delta H_{app} \quad [4]$$

where d[P]/dt is the rate of product formation. Rearranging, we get:

$$\text{Rate} = \frac{d[P]}{dt} = \frac{1}{V.\Delta H_{app}} \cdot \frac{dQ}{dt} \quad [5]$$

There are two methods by which assays can be performed using the titration calorimeter and where this rate equation can be applied in the determination of Michaelis-Menten kinetic constants.

4.2.4.1 Multiple Injection Method (Pseudo-First Order kinetics)

Here, multiple injections of substrate solution are injected from the syringe into the reaction cell containing enzyme solution. Time is allowed subsequent to each injection for heat of dilution to dissipate and for the instrument to equilibrate to a new power level due to the increased substrate concentration. This change in power level after each injection corresponds to the heat released/absorbed by the reaction at that concentration of substrate. The aim here is to ensure that no more than 5% of substrate is depleted prior to the next injection so as to ensure that steady-state conditions are maintained. This is done by having as low an enzyme concentration as possible (whilst maintaining adequate signal) and having as short a time between injections as possible, so that excessive substrate depletion is avoided. Thus, at each injection point the rate and substrate concentration is determined: the change in thermal power (dQ/dt) is converted to a rate value using formula 5 and the experimentally determined ΔH_{app}, and the substrate concentration is calculated with adjustments for dilution into the reaction cell taken into account. Data are plotted as Rate vs [S] and fitted to the Michaelis-Menten equation

$$\text{Rate} = \frac{k_{cat} \cdot [E_{tot}] \cdot [S]_t}{K_M + [S]} \quad [6]$$

using non-linear regression analysis (see Figure 4.2 B), where k_{cat} is the catalytic rate constant for substrate decomposition, K_M is the Michaelis constant, $[E]_{tot}$ is the total enzyme concentration, and $[S]_t$ is the instantaneous concentration of substrate.

4.2.4.2 Single Injection Method (Continuous Kinetics)

An alternate assay strategy for determining kinetic rate constants involves continuous rate measurements following a single injection of substrate into enzyme contained within the reaction cell, or vice versa, so long as the substrate concentration in the reaction cell is greater than 5X K_M. Immediately after injection, substrate concentration is at a maximum which results in a large shift in instrumental thermal power away from established baseline (either exothermic or endothermic). Here, the thermal power remains constant because the reaction is occurring at maximal velocity (V_{max}). As substrate is depleted, the rate decreases and the instrumental thermal power returns to the initial baseline, the point at which substrate has been completely depleted. At any specific time point, the rate is determined from the thermal power (using equation 5) and the remaining substrate concentration from the integral of the heat evolved using:

$$[S]_t = [S]_{Total} - [P]_t = [S]_{Total} - \frac{\int_{t=0}^{t} \frac{dQ(t)}{dt}}{\Delta H_{app} \cdot V} \quad [7]$$

The rate plotted as a function of the substrate concentration generates a continuous kinetic curve which can be fitted to equation 6 via non-linear regression analysis to yield kinetic parameters. All of these calculations are done automatically in an Origin 7 software add-on supplied with the iTC200 instrument. Rate and substrate concentration values were removed and analysed using non-linear regression analysis in GraphPad Prism 5, which allowed for greater flexibility of data manipulation and variety in fitting functions.

4.2.5 Progress Curve Kinetics

Similar to the Single Injection Method (4.2.4.2), the assay setup for the titration calorimeter involves a single injection of substrate into enzyme, or enzyme into substrate, and the continuous monitoring of thermal power as substrate is catalysed to completion. Stockbridge & Wolfenden (2009) describe a means of converting this thermal power into a reaction curve of product formed over time. Given that heat released or absorbed by the enzyme reaction is directly proportional to the amount of substrate hydrolysed, the amount of product formed over time can be calculated and a progress curve generated. Integration of the total area under the curve represents the total heat turned over in catalysing all of

the substrate. Integrating the area between substrate injection (t=0) and each time point (t), and then dividing by the total integrated area, gives a percentage of the product formed at time (t). Multiplying this fraction at each time point by the total substrate concentration at t=0 (S_0) relates it to molar concentration. The formula describing this relationship is

$$P(t)=[S]_0 . \frac{\int_0^t \frac{dQ(t)}{dt}}{\int_0^\infty \frac{dQ(t)}{dt}}$$

[8]

with the resultant progress curve being a plot of P(t) (product formed) versus t (time).

Where this methodology deviates from that of Stockbridge & Wolfenden (2009) is in the starting concentration used, where they use amounts approximately 5-10X below K_M. The reasoning for this was that, because they were using the linear approximation method to calculate initial rates (alluded to in 4.1), more of the progress curve represented initial rate, hence allowing for a more accurate estimation. However, the non-linear regression analysis functions put forward by Golicnik (2010, 2011) are not bound by these constraints, which allowed for the use of initial substrate concentrations above or below K_M allowing greater flexibility in experimental design.

Progress curves were generated and analysed according to functions described by Golicnik (2010). The temporal closed-form solution of the Michaelis-Menten equation used is given by

$$[S]_t=K_m . W\left\{\frac{[S]_0}{K_m} . \exp\left(\frac{[S]_0-V_M . t}{K_m}\right)\right\}$$

[9]

where W is the Lambert W (x) function (Corless et al., 1996). Golicnik (2010) evaluated a number of approximations of W and found one version that produced an acceptably low amount of systemic error when applied to formula 9 in evaluating progress curves

$$W(x) \approx (1 + \epsilon).ln\left\{\frac{6\,.x}{5\,.\ln\left[\left(\frac{12}{5}\right).\left(\frac{x}{\ln\left(1+\left(\frac{12}{5}\right).x\right)}\right)\right]}\right\} - \epsilon\,.ln\left\{\frac{2\,.x}{\ln(1+2\,.x)}\right\}$$

[10]

where ε = 0.4586887. Progress curves were generated in Microsoft Excel using Equation 8 and analysed using the combined Equations 9 & 10, which were written into Graphpad Prism 5 software according to instructions provided by Golicnik (2010) Supplementary Data.

4.2.6 ITC binding curves

Samples were prepared as per 4.2.1 and experiments performed at 20°C as described in 4.2.3, with enzyme in the reaction cell and inhibitor (lisinopril) in the syringe. Concentrations of enzyme used were in the range of 6-15µM, whilst concentrations of lisinopril in the syringe (60-150 µM) were maintained at approximately 10-12X the enzyme concentration for each experiment in order to ensure the correct range for lisinopril (which has an established 1:1 binding stoichiometry). All experiments in this chapter were performed in either Tris buffer (100mM) or TAPSO (50mM), both at pH 7.5, and either 0mM, 20mM or 300mM NaCl. The enzyme solution in the cell was titrated via a series of 24 consecutive 1.5µL injections with 240 second intervals. Dilution heat experiments were initially performed (as per MicroCal experimental procedures), but were found to produce negligible heat effects and were thus deemed unnecessary. Integration of the raw thermogram peaks using Equation 2 (described in 4.2.4, with inhibitor concentration being substituted for substrate concentration in this case) yields the final ΔH_{app} for each injection, which is then plotted against the molar ratio after each injection. These binding isotherms were subjected to non-linear regression fitting using the following equation:

$$Q = \frac{n[E]_{tot}\Delta H_{app}V_0}{2}\left[1 + \frac{I_t}{n[E]_{tot}} + \frac{1}{nK[E]_{tot}} - \sqrt{\left(1 + \frac{I_t}{n[E]_{tot}} + \frac{1}{nK[E]_{tot}}\right)^2 - \frac{4I_t}{n[E]_{tot}}}\right]$$

[11]

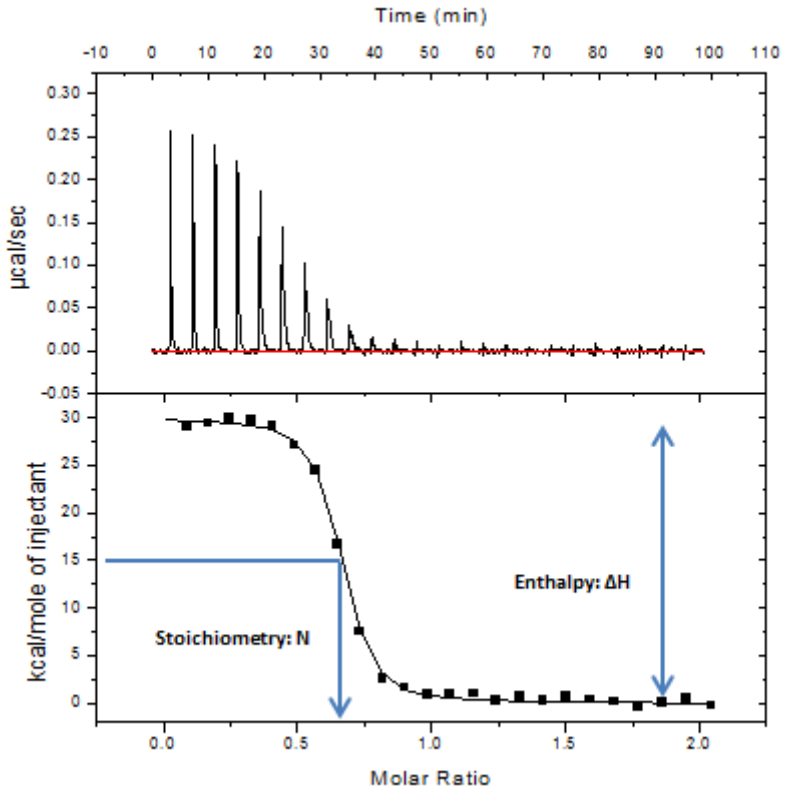

Figure 4.1 Raw vs Transformed data for calorimetric titration of tACEg13sol with lisinopril. Upper panel shows the raw calorimetric output of 24 consecutive injections of lisinopril into the reaction cell containing tACEg13sol. Lower panel shows the integrated heat (black squares) evolved per mole of lisinopril upon binding as a function of the molar ratio. The solid line through the points represents the line of best fit after nonlinear regression analysis using Equation 11 in Origin 7. Enthalpy of the reaction (ΔH) is the maximum heat evolved by the binding reaction and is indicated by the amplitude of the sigmoidal curve (double arrow). The stoichiometry of binding, N, is equal to the fraction of active protein and corresponds to the molar ratio at the inflection point of the curve where a ratio of 1.0 corresponds to 100% occupancy of binding sites (Schon & Velazquez-Campoy, 2005).

where Q is the total heat evolved, n is the number of binding sites, V_0 is the total cell volume, $[E]_{tot}$ is the total enzyme concentration in V_0, ΔH_{app} is the change in enthalpy upon binding, I_t is the total concentration of inhibitor and K is the binding constant. Experimental data was analysed using Origin7 software with iTC_{200} analysis module (MicroCal).

4.2.7 HPLC of angiotensin I hydrolysis products

HPLC was performed using a Sephadex® C18 Jupiter column. Reaction samples were removed from the reaction cell after ITC ΔH_{app} determination, where hydrolysis had run to

completion, and kept @ 4°C. Sample was separated by HPLC over a 0-75% ACN gradient in 0.1% TFA. Sample runs were compared to pure substrate and products (Angiotensin II and L-Histidyl-L-Leucine (HL)) in order to confirm peak identity. Absorbance was read at λ = 215nm to detect peptide bond absorbance and λ = 275nm to detect the absorbance of the tyrosine contained within Angiotensin I and Angiotensin II, but not HL.

4.3 Results & Discussion

4.3.1 Determination of Molar Enthalpy of Reaction

Given that no prior work has been published for enzyme hydrolysis reactions for ACE using ITC, it was necessary to do an initial assessment of the molar enthalpies of reaction (ΔH_{app}) in different buffers. This was done primarily to determine whether the total heats evolved were high enough for further study. A secondary aspect is that the ΔH_{app} can vary if the reaction involves the uptake or release of protons from the surrounding aqueous environment (Eftink et al., 1981). The ΔH_{app} is made up of the intrinsic molar enthalpy of the reaction (ΔH_{int}) and an enthalpy of ionisation of the buffer (ΔH_{ion}) dependent on the number of protons taken up or released (n_H), as described by the formula $\Delta H_{app} = \Delta H_{int} + n_H.\Delta H_{ion}$ (Haq 2005). Whilst the proposed mechanism of action for ACE catalysis (Sturrock et al., 2001; Matthews, 1988) doesn't specifically indicate a mechanistic proton transfer, there is no clear evidence for or against and we sought to verify this.

In order to address these goals, we determined the ΔH_{app} (as described in 4.2.4 using equation 2, see Figure 4.2) for tACEg13sol with two substrates (HHL and Angiotensin I) using a variety of buffers. A linear plot of ΔH_{app} versus the ΔH_{ion} for each buffer (Figure 4.3A) gives the n_H (slope of the linear fit) and the ΔH_{int} (y-intercept at x=0). As can be seen, there does appear to be a variation in ΔH_{app} with varying ΔH_{ion} for both substrates assessed. The positive ΔH_{int} values for both reactions indicates an endothermically driven process, where breaking of the peptide bond contributes 2-5 kcal/mol to the energy of stabilisation in the protein. The difference in ΔH_{int} between the two substrates is about 1 $kcal.mol^{-1}$ and is probably due to a greater number of interactions of the larger decapeptide Angiotensin I over the short tripeptide HHL, which gives off more heat (exothermic) and is hence more negative. The negative slope of the lines for both indicates

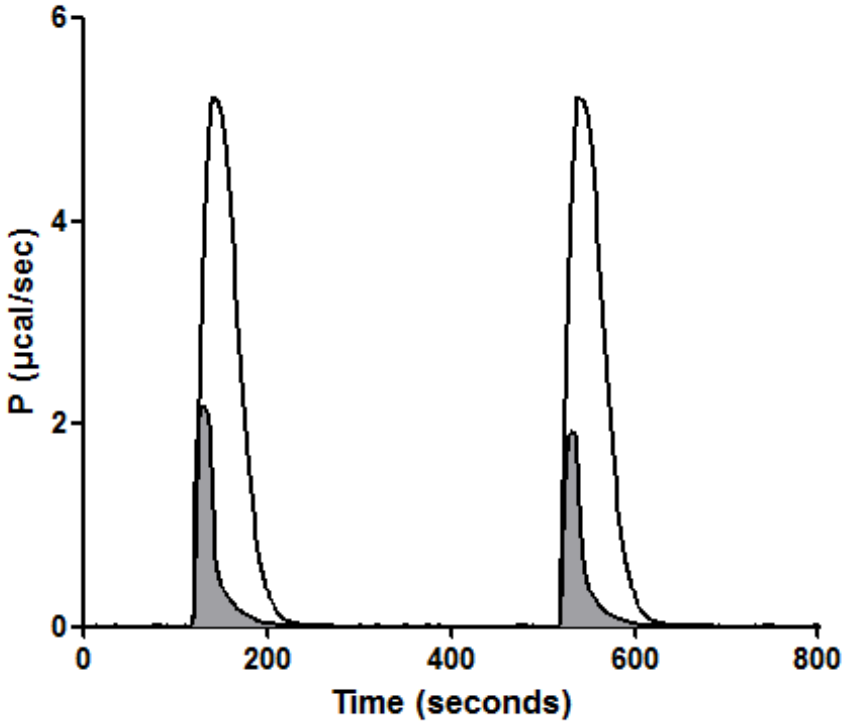

Figure 4.2 Representative data for the determination of apparent molar enthalpy (ΔH_{app}). Raw calorimetric output (solid black line) with thermal power P (µcal/sec) on the Y-axis and Time (sec) on the X-axis. Two separate experiments are performed as described in 4.2.4 with the resultant peaks overlayed: 1) The larger peaks (white fill) are the result of injecting substrate into an enzyme solution of high concentration and allowing all substrate to be hydrolysed, with integration and calculation of molar enthalpy resulting in $\Delta H_{observed}$. 2) The smaller peaks (grey fill) are the result of injecting substrate into buffer containing no enzyme, which accounts for the enthalpy associated with dilution of the substrate, with integration and calculation of molar enthalpy resulting in $\Delta H_{dilution}$. The ΔH_{app} is determined by subtracting the $\Delta H_{dilution}$ from the $\Delta H_{observed}$. The method is described in detail by Todd et al (2001).

that protons are released during the hydrolysis reaction (Todd et al., 2001; Bianconi, 2003). A discrepancy in this data is that the n_H values of -0.37 for both substrates are not integers, where a value of 1 would represent a single proton exchange. If the mechanism of ACE hydrolysis is assumed to be the same as that proposed by Matthews (1988), then the proton release must be attributed to some other mechanism. One suggestion would be that, upon hydrolysis, a subset of one or more charged amino acids may change their protonation state. The imidazole groups of histidines are known to be sensitive to their microenvironments, and with a pKa value near 6 may be responsible. What is evident is that this is consistent between substrates and should presumably be attributable to the

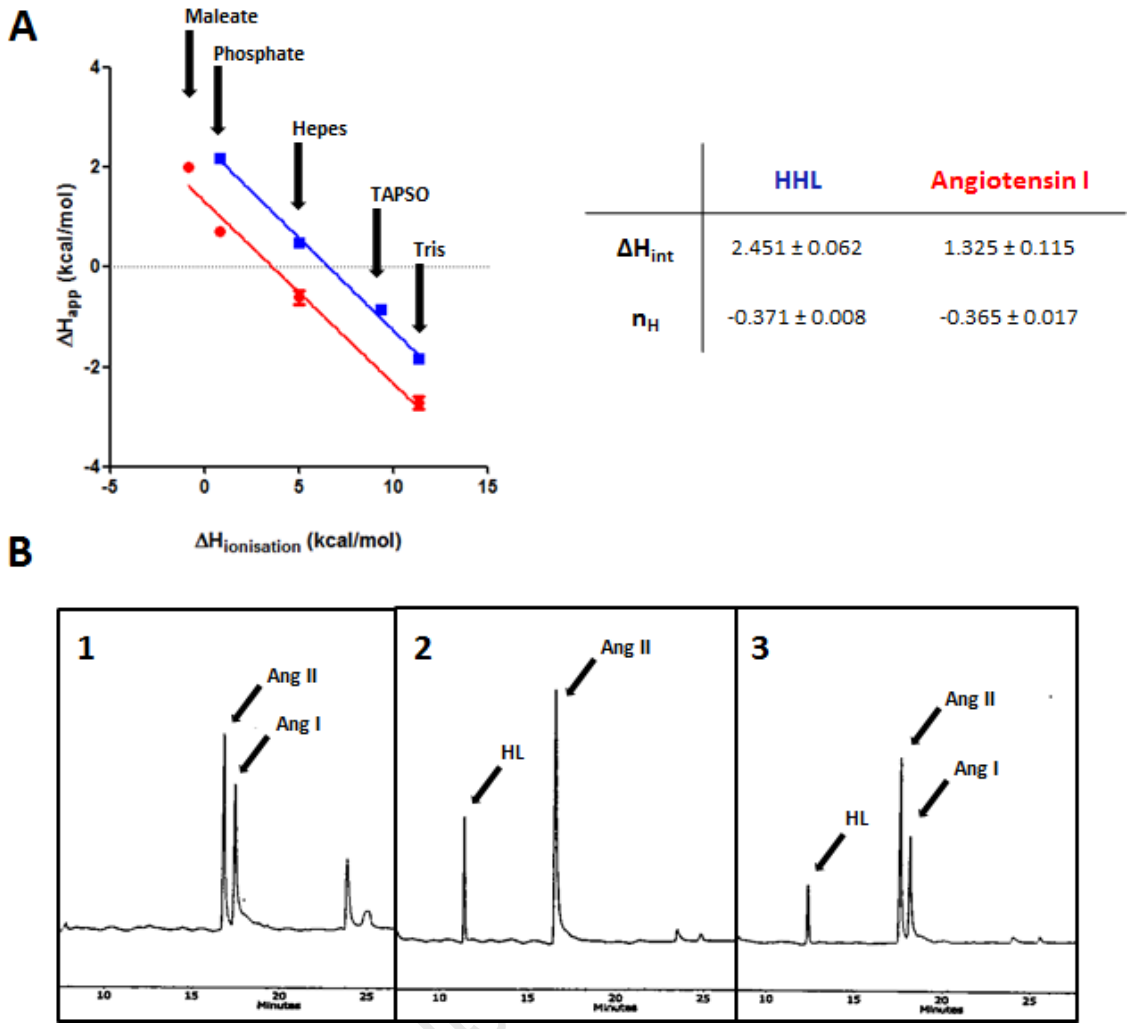

Figure 4.3 Determination of reaction molar enthalpies. A) The molar enthalpies of reaction (ΔH_{app}) for tACEg13sol with HHL and Angiotensin I were determined as described in 4.2.4 (Eqn 2). Samples were prepared as described in 4.2.1. Successive injections (between 6 and 12µl in volume) of either HHL (10mM) or Angiotensin I (1-1.5mM) into the reaction cell with concentrations of tACEg13sol between 0.8 and 1.2µM were performed. All reactions were at 37°C, in 100mM of buffer (pH 7.5), 10uM $ZnSO_4$ with either 20mM NaCl (for AngI) or 300mM NaCl (for HHL). Buffers include phosphate (ΔH_{ion} =1.22 kcal/mol), Maleate (ΔH_{ion} = -0.86 kcal/mol), Hepes (ΔH_{ion} = 4.89kcal/mol), TAPSO (ΔH_{ion} = 9.37 kcal/mol), and Tris (ΔH_{ion} = 11.37 kcal/mol). The ΔH_{ion} values for these buffers were taken from Goldberg et al (2002). The graph shows a plot of the determined ΔH_{app} values against their ΔH_{ion} energies for each buffer, analysed via linear regression with those values for AngI in red and those for HHL in blue. The ΔH_{int} for each substrate corresponds to the Y-intercept of the linear fit, with the slope reflecting n_H and these values tabulated alongside the graph. **B)** Samples were subjected to HPLC as described in 4.2.7. Panel 1 shows the raw data for a control of pure samples of Angiotensin I and Angiotensin II, which were combined, and ran at 17.16' and 16.5' respectively. Panel 2 shows the raw data for an Angiotensin I hydrolysis sample which was removed from the ITC reaction cell after ΔH_{app} determination. Angiotensin II and HL, the products of Angiotensin I cleavage, are seen running at 16.5' and `11' respectively. Panel 3 shows the raw data for the same hydrolysis product shown in panel 2 but spiked with Angiotensin I. Here, we see peaks at ~11', 16.5' and 17.16', corresponding to HL, Angiotensin II and Angiotensin I, respectively.

general catalytic mechanism. Whilst this data provides some interesting leads, the primary goal was to assess which buffer system, if ΔH_{app} was variable, would evolve the largest heat and hence be suitable for further investigation of ACE catalysis. For this purpose Tris buffer was chosen, as it gave the largest signal with AngI and, whilst not the largest for HHL, was sufficiently large so that we could maintain consistency and use it for both substrates.

As an added measure to ensure that the ΔH_{app} values were accurate, immediately after the thermal signal had returned to baseline, representative samples were removed from reaction cells and subjected to HPLC in order to assess whether the reaction had gone to completion (Figure 4.3B). Panel 2 shows that there is no Angiotensin I present, with only the products of cleavage (Angiotensin II and the HL dipeptide) visible. Appropriate controls were performed (Panels 1 and 3) to verify that the peaks observed were identified correctly. This served to confirm that the reactions were running to completion and that the ΔH_{app} values determined were representative of the reaction being studied.

4.3.2 Multiple Injection Method

This experimental approach (outlined in 4.2.4.1) was first described by Todd et al., (2001) and is the most widely used method in the literature for the determination of the Michaelis-Menten constants K_m and k_{cat}. Like the pseudo-first order method described by Michaelis & Menten (1913), determination of the initial reaction rates at varying substrate concentrations allows for calculation of these constants via non-linear regression analysis. Where it differs from normal experimental setups is that the whole experiment happens in one reaction volume and substrate concentration is increased by consecutive injections into a cell containing low amount of enzyme.

Initially this method was evaluated for its feasibility in determining the rate constants for tACEg13sol using Angiotensin I and HHL (representative data in Figure 4.4). In assessing this, it is important for the reaction to produce sufficient change in thermal power (dQ/dt) and it was advised that the thermal power at V_{max} should be no lower than 0.2µcal/sec [personal correspondence Dr Luminita Damian (MicroCal, GE Healthcare)]. This was in order to maintain a signal-to-noise ratio greater than 100:1 and stay within the instruments detection limits. As can be seen in Figure 4.5A, where the thermal power (dQ/dt) obtained for a reaction between tACEg13sol (70nM) and HHL is plotted against the substrate

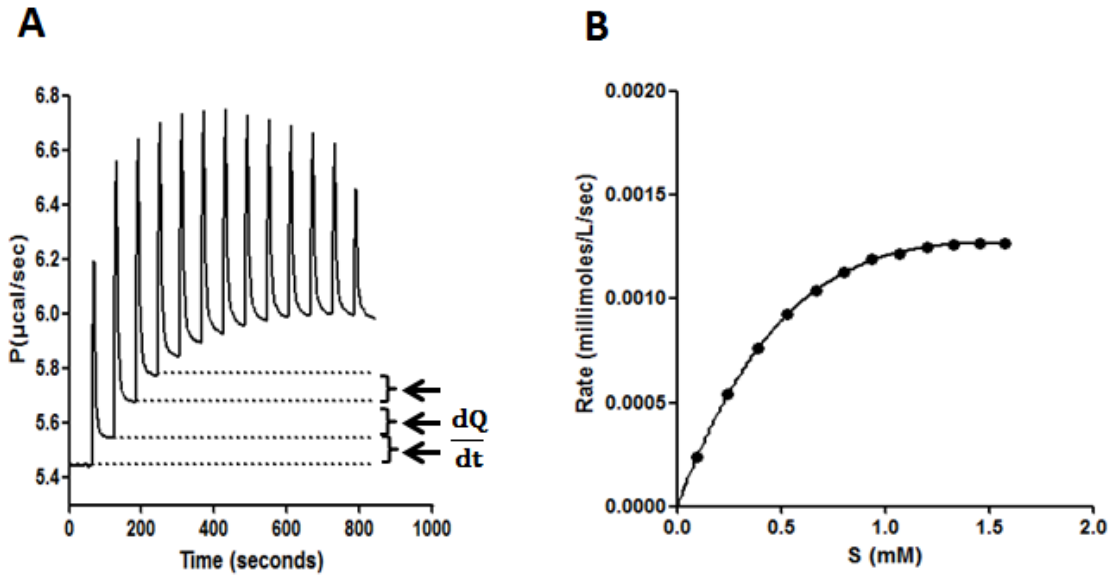

Figure 4.4 Representative data for the Multiple Injection Method. Methodology is described in 4.2.4.1. **A)** Raw calorimetric ouput (solid black line) with thermal power P (ucal/sec) on the Y-axis and Time (sec) on the X-axis. Extrapolation of baseline re-equilibration prior to subsequent injection (dotted lines) shows the change in baseline thermal power as a function of time (dQ/dt). Peaks represent dilution heats associated with injection of substrate into enzyme. **B)** The resultant rate versus substrate data (solid black circles), which were calculated from raw data, is fitted to the Michaelis-Menten formula using non-linear regression analysis (solid black line).

concentration (S), this requirement was achieved. Conversion of the thermal power to the rate of product formation (using equation 5) and fitting to the Michaelis-Menten equation via non-linear regression gave rate constants very similar to those obtained in our laboratory using a fluorescence-based assay (data not shown). However, when the same approach was attempted with a similar concentration of tACEg13sol (90nM) using Angiotensin I as the substrate, the thermal power never exceeded the 0.2µcal/sec minimum cut-off (Figure 4.5B). The expected k_{cat} for this reaction was around 10-34 $.s^{-1}$ (Rice et al., 2004; Rousseau-Plasse, 1996), which is fairly comparable to other proteases described by Todd et al., (2001). Given that the V_{max}, and hence thermal power change, is enzyme concentration dependent, we looked to determine whether V_{max} could be increased without breaking pseudo-first order requirements. As evident in Figure 4.7B, using higher enzyme concentrations did not result in a proportional increase in V_{max}, suggesting that substrate hydrolysis exceeded 5% at greater than 90nM of enzyme. The ΔH_{app} values for HHL and AngI in Tris buffer differ by only ~1 kcal/mol (see 4.3.1), yet the k_{cat} values are approximately 10-

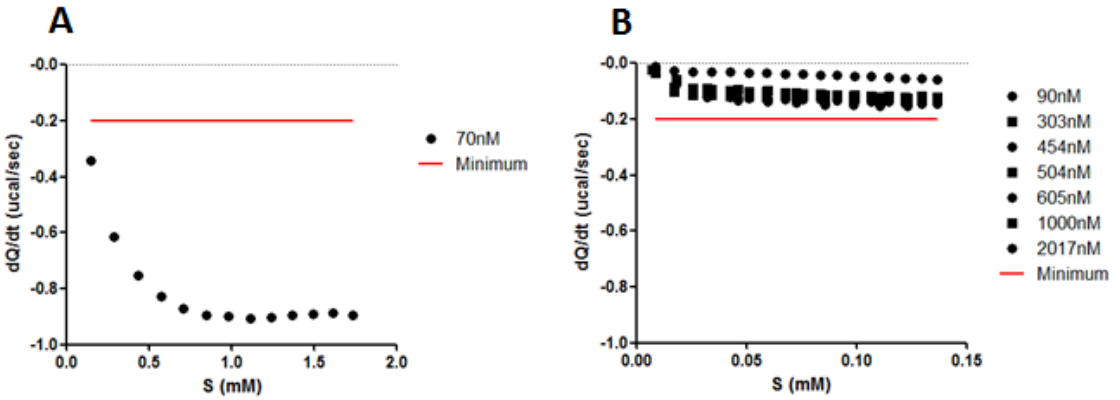

Figure 4.5 Thermal power limitations for Angiotensin I using the Multiple Injection Method. The change in raw thermal power (dQ/dt) associated with the change in substrate concentration (S) after each injection are shown for the reaction between tACEg13sol and HHL (A) and AngI (B) in 20mM NaCl, 100mM Tris(Acetate) buffer (pH 7.5), 10uM $ZnSO_4$. Varying concentrations of tACEg13sol were used and are indicated by the key on the right of each graph. The straight line corresponding to 0.2 µcal/sec indicates the minimum thermal change required for a greater than 100:1 signal-to-noise ratio.

fold higher for HHL (based on values for both as reported by Wei et al., 1991b) suggesting that the difference in molar enthalpies of reaction is not the problem. It appears that the magnitude of the ΔH_{app} values for HHL and AngI in Tris buffer (-1.83 and -2.62 kcal/mol respectively) puts a lower limit on the determinable k_{cat} values. This is indirectly supported by review of the literature, where very few reactions reported have ΔH_{app} values less than 7-10 kcal/mol, which is considerably higher than those for tACEg13sol. This suggests that this is a fundamental limit of this method and, given that activity is expected to drop considerably when these reactions are performed in the absence of chloride (Liu et al., 2001, Wei et al., 1991b), it is clearly not viable for further study of tACEg13sol reactions.

4.3.3 Single Injection Method

The Single Injection Method was then assessed for its feasibility in determining tACEg13sol kinetics using HHL and AngI. Krokeide et al (2007) reported the use of this method for a chitinase hydrolysis reaction with a ΔH_{app} (-0.55 kcal/mol), which is lower than that of AngI with tACEg13sol in Tris buffer, and a comparable k_{cat} (40.9 $.sec^{-1}$). Given that this method (described in 4.2.4.2, representative data shown in Figure 4.6) continuously monitors substrate depletion, and doesn't rely on pseudo-first order conditions where total substrate hydrolysis needs to be kept below 5% at each point, the thermal power change at V_{max}

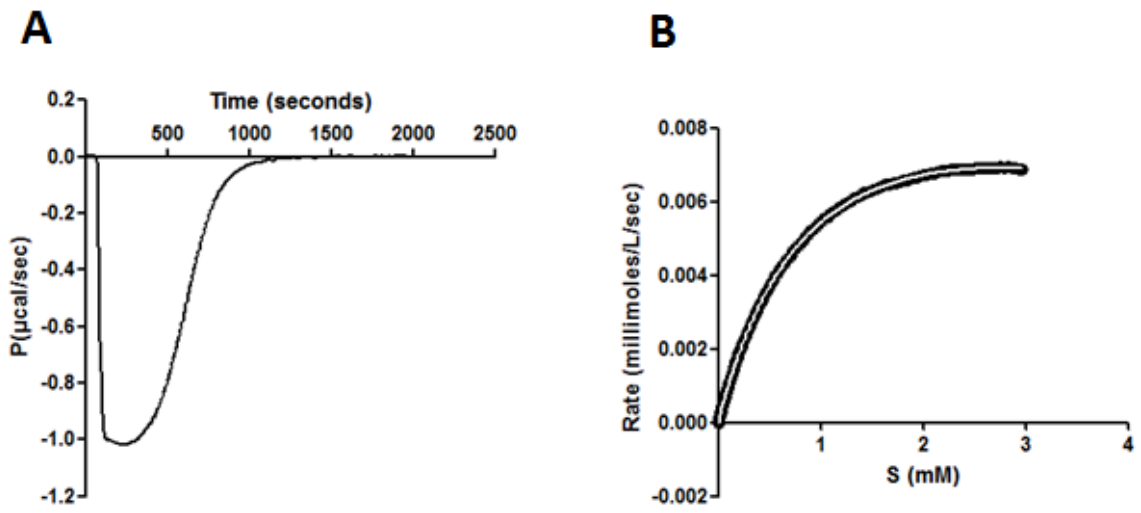

Figure 4.6 Representative data for the Single Injection Method. Methodology is described in 4.2.4.2. **A)** Continuous raw calorimetric output (solid black line) with thermal power P (ucal/sec) on the Y-axis and Time (sec) on the X-axis. **B)** The resultant rate versus substrate data (continuous thick black line), which was calculated from raw data, is fitted to the Michaelis-Menten formula using non-linear regression analysis (thin white line line, which is aligned exactly to the rate data).

should be proportionally higher for the same enzyme concentration. One of the parameters when designing these experiments is the initial substrate concentration (S_i) that is loaded into the reaction cell (where S_0 is the substrate concentration at t=0 which is adjusted for dilution by enzyme addition; in all cases S_0 is 5-10% lower than S_i). The S_i concentration needs to be in the range of 5-10X K_m so that a steady state can be established at V_{max} before excessive hydrolysis takes place. Based on values reported by Gordon et al (2003) for the identical construct, the expected K_m for this reaction should be around 2.7mM. A consideration here is the fact that HHL is not very soluble above 5mM and it was established that the highest soluble concentration was 10mM, lower than the 13.5mM necessary for the S_i to be above 5X K_m. High substrate concentrations resulted in substrate inhibition using the Multiple Injection Method (data not shown), a trend reported in the literature (Baudin et al., 1999). Thus, a range of S_i concentrations was explored in order to determine whether this variable plays a factor in the resultant kinetic constants. Figure 4.7A shows the raw calorimetric traces of the complete hydrolysis of four different HHL S_i concentrations with the same concentration of tACEg13sol. As expected, the time taken for complete hydrolysis

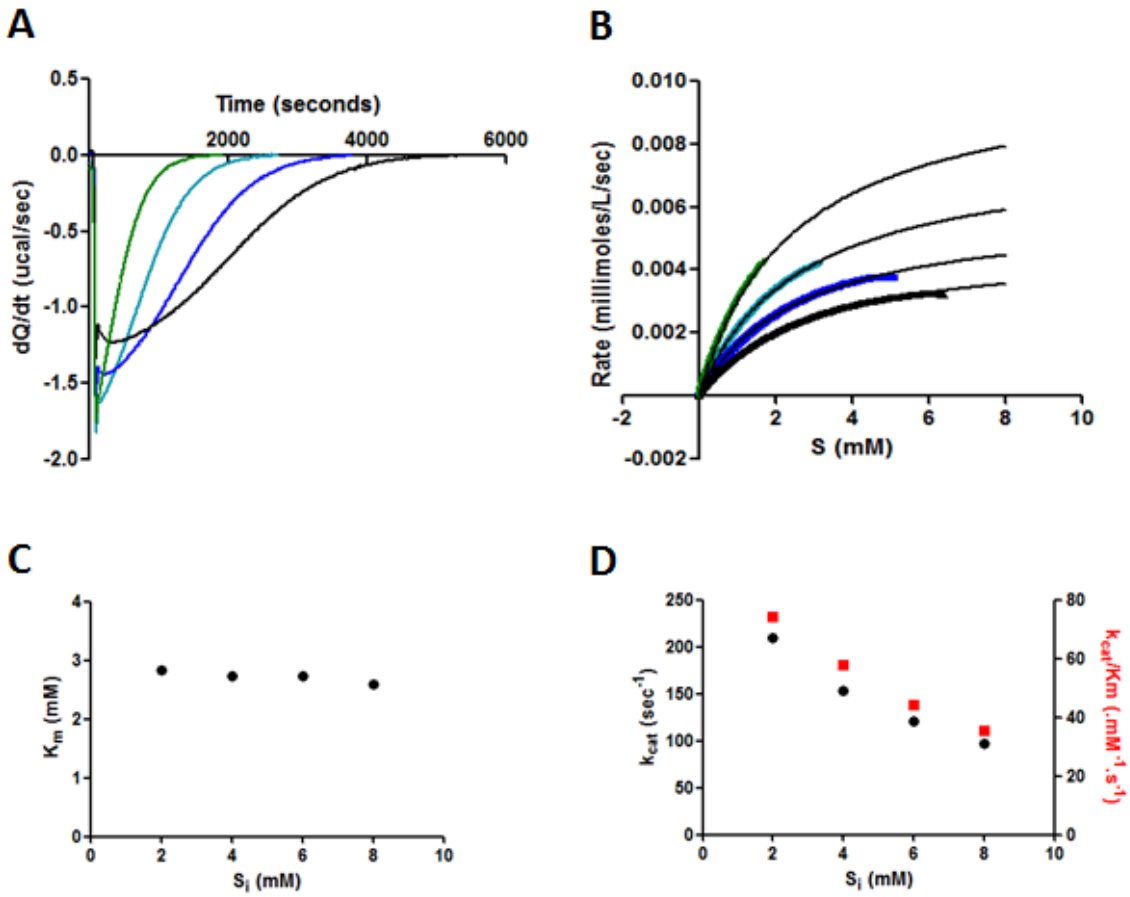

Figure 4.7 Effect of starting substrate concentration (S_i) on HHL hydrolysis using the Single Injection Method. Representative examples of the reaction between tACEg13sol and HHL in 300mM NaCl, 100mM Tris(Acetate) buffer (pH 7.5), 10uM $ZnSO_4$. Enzyme concentration was kept constant (52nM) between all runs. Units are all indicated on each axis. **A)** The change in raw thermal power (dQ/dt) associated with the change in substrate concentration (S) over time as it is hydrolysed after a single injection of 52nM tACEg13sol into the reaction cell containing HHL. Four different initial substrate concentrations (S_i) are shown; 2mM HHL (green), 4mM HHL (light blue), 6mM HHL (dark blue) and 8mM HHL (black). **B)** Raw thermal power was converted to enzyme turnover (as described in 4.2.4.2) and fitted to Equation 6 using non-linear regression analysis. The rate data for the four different S_i concentrations are in the same colours as in A, with the non-linear regression fits (solid black lines) for each was extended to highlight the variation between the fits. All fits had R^2 values greater than 0.999. **C)** The resultant K_m values of the non-linear regression in B, plotted against the initial substrate concentration (S_i) on the X-axis. **D)** The resultant k_{cat} (black circles; left hand Y-axis) and k_{cat}/K_m (red squares; right hand Y-axis) values of the non-linear regression in B, plotted against the initial substrate concentration (S_i) on the X-axis.

to occur increased proportionally with increased S_i concentration, with the magnitude of the thermal peak (which is proportion to rate) only decreasing slightly with increased S_i concentration. These curves were converted to rates (using the method in 4.2.4.2) and

fitted via non-linear regression analysis to the Michaelis-Menten equation (equation 6) (Figure 4.7B). None of the rate data produced clearly plateauing curves that could be confidently fitted to the Michaelis-Menten equation without extrapolation of V_{max}. However, given that the data is continuous and represents hundreds of data points, this extrapolation can be assumed to be fairly accurate for the higher S_i concentrations but decreasingly so for the lower the concentration used (i.e. 2mM and 4mM). With this in mind, we can also see that V_{max} decreased proportionally with increased S_i concentration, a clear demonstration of substrate inhibition. Indeed, plotting the resultant Michaelis-Menten constants (K_m, k_{cat}, k_{cat}/K_m) against the S_i concentration used for each determination (Figure 4.7C & D) further bears out this point. It is clear that the K_m, which is consistent with published values (Gordon et al., 2003) doesn't change that much over the S_i range, yet the k_{cat} and hence k_{cat}/K_m does, further supporting the substrate inhibition model. It is also clear that the k_{cat} and k_{cat}/K_m calculated using the lower S_i concentrations are far more in line with those reported by Gordon et al (k_{cat}=170±25 $.s^{-1}$ and k_{cat}/K_m=63 $.mM^{-1}.s^{-1}$), suggesting that the lower the S_i used, the more representative the data is of the actual rate constants. The problem with that is that the lower the S_i concentration used, the more extrapolation of the curve fit is required and therefore, the confidence in reported constants is lowered.

A similar evaluation of the angiotensin I reaction was done in order to ascertain whether a similar effect would be observed. The range of S_i concentrations used was based on the reported K_m values of 47±1.5mM at 20mM NaCl (Liu et al., 2001) and 55.6±6.4mM at 100mM NaCl (Rice et al., 2004), thus an angiotensin I range of approximately 5-20 X K_m (200-1000µM) was used. Figure 4.8A shows the raw calorimetric traces of the complete hydrolysis of five different angiotensin I S_i concentrations with the same concentration of tACEg13sol. The raw data differed from that of HHL in that there was an increase in both peak height and time taken to total hydrolysis with increasing S_i concentration. What is also not entirely evident from the raw calorimetric traces is that the total reaction heat (characterised by the height of the peaks in 4.8A) at the lower S_i concentrations (200-300µM) are bordering on the lower detection limits of the instrument. It is recommended that the height at V_{max} should be no less than 0.2µcal/sec and ideally not much less than 0.5µcal/sec (personal correspondence with Dr Luminita Damian - MicroCal). The only way to potentially increase the peak heights is to use a higher enzyme concentration. This was

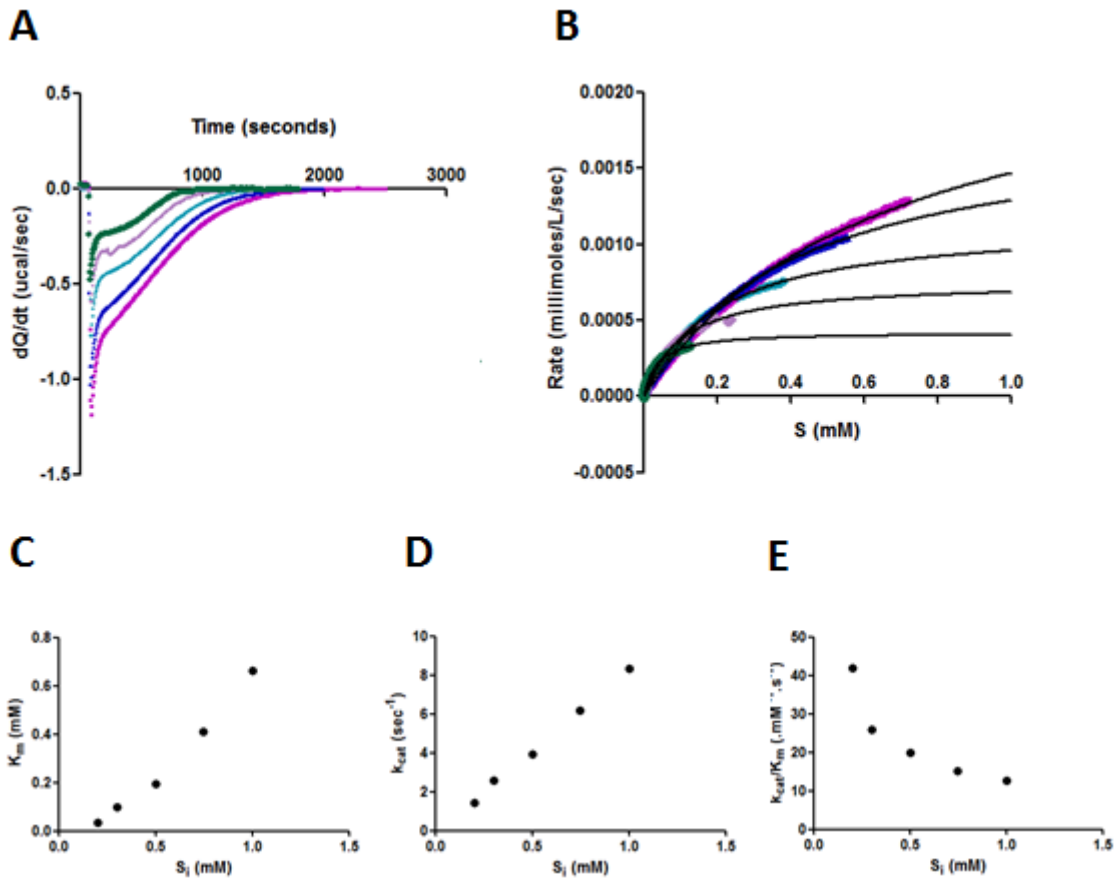

Figure 4.8 Effect of starting substrate concentration (S_i) on Angiotensin I hydrolysis using the Single Injection Method. Representative examples of the reaction between tACEg13sol and Angiotensin I in 20mM NaCl, 100mM Tris(Acetate) buffer (pH 7.5), 10uM $ZnSO_4$. Enzyme concentration was kept constant (293nM) between all runs. Units are all indicated on each axis. **A)** The change in raw thermal power (dQ/dt) associated with the change in substrate concentration (S) over time as it is hydrolysed after a single injection of tACEg13sol into the reaction cell containing AngiotensinI. Five different initial substrate concentrations (S_i) are shown; 200µM (green), 300µM (violet), 500µM (light blue), 750µM (dark blue) and 1000µM (purple). **B)** Raw thermal power was converted to enzyme turnover (as described in 4.2.4.2) and fitted to Equation 6 using non-linear regression analysis. The rate data for the four different S_i concentrations are in the same colours as in A, with the non-linear regression fits (solid black lines) for each extended to highlight the variation between the fits. All fits had R^2 values greater than 0.995. The resultant K_m **(C)**, k_{cat} **(D)**, and k_{cat}/K_m values **(E)** of the non-linear regression analysis are shown in B, plotted against the initial substrate concentration (S_i) on the X-axes.

explored (data not shown) with higher concentrations resulted in faster hydrolysis and reduced steady-state plateau at V_{max}, an important consideration in the analysis of the subsequent rate data. We thus had to use the lowest concentration (293nM) that produced heat change at V_{max} greater than 0.2µcal/sec. The conversion of these raw traces to rate values (using method in 4.2.4.2) and non-linear regression analysis to the Michaelis-Menten

equation (equation 6) is shown in Figure 4.8B. Here, it is seen that not only is V_{max} increasing with increased S_i, but so is the K_m. Similarly to the HHL data, steady-state plateaus at V_{max} were not obtained, and could not be obtained using higher S_i concentrations. The resultant Michaelis-Menten constants were plotted against the S_i concentration used for each determination (Figure 4.8C, D & E) confirming the concentration dependent increase in both k_{cat} and K_m, which results in a sharply decreasing k_{cat}/K_m. The increase in K_m with increased S_i concentration is consistent with product inhibition, which has been shown for ACE (Shapiro & Riordan, 1984) and specifically with Angiotensin I as substrate and Angiotensin II as competitive inhibitor using rabbit lung ACE (Tsai & Peach, 1976). Karim et al (2005) proposed a method of accounting for the effect of product accumulation on the kinetic rate constants based on the Single Injection Method. By plotting the K_m values against the S_i concentration (as has been done in Figure 4.8C), they showed a linear increase in K_m with increased S_i concentration, which they subjected to linear regression analysis to obtain the positive Y-intercept and calculate an apparent K_m. However, as can be seen in Figure 4.8C, a linear least-squares fit to the data would not yield a positive Y-intercept. A cornerstone of this approach is that the k_{cat} remains constant across all S_i concentrations, which is not the case here (see Figure 4.8D).

Further illustration that product inhibition is playing a role is shown in the separate determination of ΔH_{app}, which is required for the conversion of raw assay data to rate data. Figure 4.9A shows the raw data for multiple injections of Angiotensin I into a cell containing tACEg13sol (with a control for heat of dilution), with Figure 4.9B showing the calculated ΔH_{app} for the hydrolysis of each injection of Angiotensin I. A product concentration dependent endothermic (more positive) shift in the ΔH_{app} was observed, an effect that can be attributed to product inhibition (Todd et al., 2001). Cai et al., (2001) looked at employing this product inhibition effect as a probe to measure the kinetic parameters of a reaction, thus this approach was investigated to determine applicability. The approach required a separate determination of the K_i (K_d of binding) for the product(s) (either His-Leu or Angiotensin II), which was attempted using the ITC binding approach (described in 4.2.6) in line with their methodology. ITC has been used to determine binding of a dipeptide (Asp-Phe) to somatic ACE (Andujar-Sanchez et al., 2007) with a Kd of ~110µM using up to 10µM enzyme. However, binding enthalpies for His-Leu at concentrations up to 8µM tACEg13sol

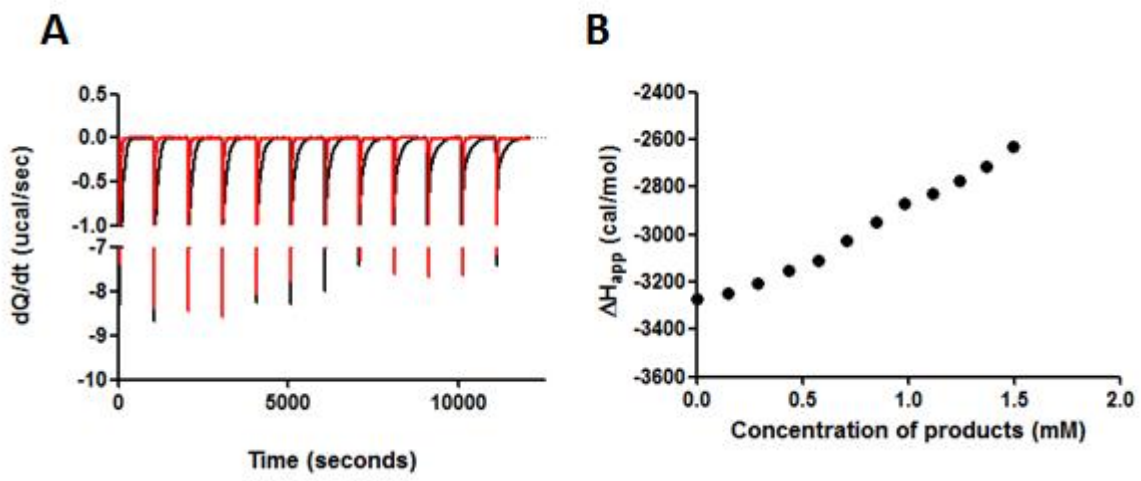

Figure 4.9 Enthalpic contribution of product accumulation from Angiotensin I hydrolysis. A) Raw calorimetric output of 12 injections (each 3µL in volume) of 10mM Angiotensin I into the reaction cell containing either 802nM tACEg13sol (black line) or buffer containing no enzyme (red line). Sufficient time (1000 seconds) was allowed between each injection for the hydrolysis reaction to run to completion. Reactions were performed in 20mM NaCl, 100mM Tris(Acetate) buffer (pH 7.5), 10uM $ZnSO_4$ using the method described in 4.2.4 (Figure 4.1). **B)** Molar enthalpies for each injection were calculated (using equation 2) and the ΔH_{app} determined by subtracting the $\Delta H_{dilution}$ from the $\Delta H_{observed}$ (see Figure 4.1). These are plotted against the total product concentration, which, for each injection, is equal to the cumulative substrate concentration injected preceding that injection. This is the case given that all substrate prior to each injection has been completely hydrolysed and represents the cumulative product concentration.

in the reaction cell could not be ascertained (data not shown). Whilst binding of Angiotensin II could be determined, the enthalpies were very low, resulting in very erratic, unreliable data (not shown). The enthalpies for these reactions could have been improved by the use of higher tACEg13sol concentrations; however, the amounts required for the effect to be appreciable would have been wholly impractical given the limited scalability of the mammalian expression system used. Taking into account the fact that reliable K_d values could not be obtained for both Angiotensin II and His-Leu, and that the model presented by Cai et al., (2001) assumes product inhibition only and does not factor in the potential disparate effects of two products, this approach was found to be unsuitable.

Given that Angiotensin I hydrolysis results in two products (Angiotensin II and His-Leu), the effect these individual components have on Angiotensin I hydrolysis kinetics was investigated. Assays were performed as before using 300µM Angiotensin I in the reaction

cell and 293nM tACEg13sol introduced via a single injection. In order to ascertain the effects of the reaction products, the substrate mixture in the cell contained 300µM Angiotensin I mixed with either 400µM Angiotensin II or 400µM His-Leu. As can be seen in the raw calorimetric traces in Figure 4.10A and the subsequent Michaelis-Menten fitted rate data (Figure 4.10B), the effects are notably different for the two products. The experiments were repeated using varying concentrations of products (not shown) and found to be concentration dependent. The presence of 400µM Angiotensin II had the effect of increasing the K_m by two-fold with no increase in k_{cat} (data not shown), suggesting its inhibitory effect is purely competitive in nature. By contrast, the presence of 400µM His-Leu caused a threefold increase in both k_{cat} and K_m. The most likely explanation is that His-Leu binds to tACEg13sol and modulates the activity. Michaud et al (1997) report a K_i (using ACE C-domain) for His-Leu of 150 and 170µM using Hipp-His-Leu and Hip-Ala-Pro as substrates respectively. This suggests that the increased K_m, which would be associated with competitive inhibition, is balanced by the observed rise in k_{cat}, with the overall k_{cat}/K_m values being approximately equal. The fact that enthalpic heat of binding was not detected with His-Leu alone, as mentioned before, indicates that its effect is more than likely non-competitive and allosteric in nature. It's quite possible that HL requires substrate binding to occur before it can bind, possibly in the active site groove which is quite large. Evidence for dual binding in the active site is reported by Ortiz-Salmerón et al (1998) who show that two molecules of captopril, a potent ACE inhibitor, bind highly entropically to each monomer of ACE, with the second molecule presumably binding within the active site, supporting the idea that His-Leu could bind along with the substrate.

Due to the fact that product accumulation is playing such a prominent role, it can't be discounted that the early part of the curve is being skewed, hence affecting the non-linear regression and accounting for the increased k_{cat} and K_m values. To negate this effect, a method originally described by Lonhienne et al (2000) to independently determine k_{cat} without fitting to the Michaelis-Menten equation was used. This involved multiple injections of small volumes of tACEg13sol into the reaction cell containing saturating levels of Angiotensin I (see Figure 4.10C), with the enthalpic change (hence rate) proportional to V_{max}. This allowed multiple determinations of k_{cat} for two saturating conditions (500µM and 1 mM), which are shown in comparison with the data obtained

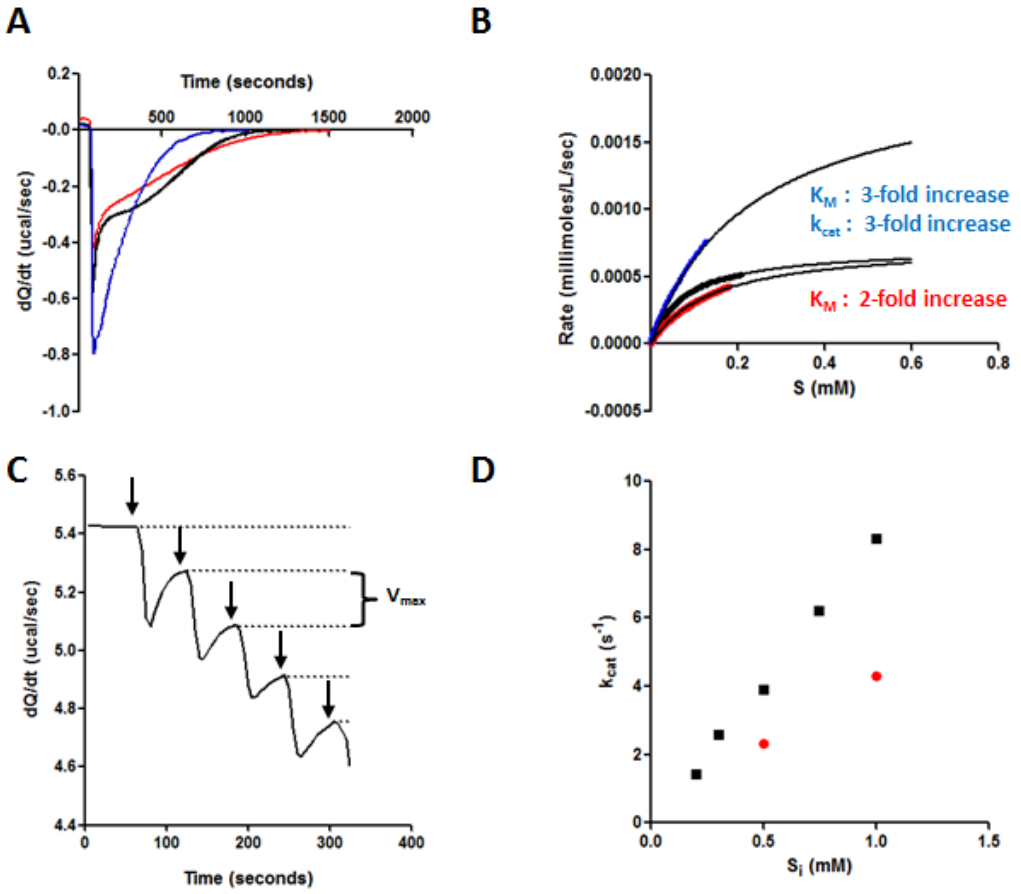

Figure 4.10 Effect of product formation and substrate concentration on kinetic parameters of Angiotensin I hydrolysis. Representative examples of the reaction between tACEg13sol and Angiotensin I in 20mM NaCl, 100mM Tris(Acetate) buffer (pH 7.5), 10uM $ZnSO_4$. **A)** The change in raw thermal power (dQ/dt) associated with the change in substrate concentration (S) over time, as it is hydrolysed after a single injection of tACEg13sol (293nM) into the reaction cell containing 300µM AngiotensinI (black), 300µM AngiotensinI + 400µM Angiotensin II (red) and 300µM AngiotensinI + 400µM HL (blue). **B)** Raw thermal power was converted to enzyme turnover (as described in 4.2.4.2) and fitted to Equation 6 using non-linear regression analysis. The rate data for the four different S_i concentrations are in the same colours as in A, with the non-linear regression fits (solid black lines) for each extended to highlight the variation between the fits. All fits had R^2 values greater than 0.995. Annotations in red (Angiotensin II) or blue (HL) indicate the effect of the presence of product on the kinetic constants K_m and k_{cat}. **C)** The change in raw thermal power (dQ/dt) upon multiple consecutive injections (indicated by arrows) of equal amounts of tACEg13sol into a saturating amount of Angiotensin I (method described by Lonhienne et al., 2000). Under these conditions, a steady state is reached prior to the subsequent injection, with the thermal change being proportional to V_{max} (indicated by dotted lines). Conversion of the thermal change to a rate value (using equation 5) and division by the enzyme concentration at each point yields multiple k_{cat} determinations in a single experiment. **D)** Comparison of the k_{cat} data determined using Single Injection Method (black squares; taken from 4.X D) and from two separate determinations of kcat at 500µM and 1000µM Angiotensin I (red dots) using method descibed in (C). Each red dot is the average of six injections from a single experiment, with standard deviation (not shown) below 5% for both.

via normal non-linear regression (Figure 4.10D). What is clear is that the S_i concentration dependent increase in k_{cat} is still occurring, though not quite to the same degree, suggesting that the substrate is playing a role in this effect. Angiotensin I is quite a large peptide and in very high concentrations (>1mM) was found to be quite viscous. High viscosity is generally associated with having a negative effect on k_{cat} by interfering with catalytically important structural changes in the enzyme (Gavish & Werber, 1979). Given that the k_{cat} increases, it can only be surmised that the effect is of a more stabilising nature which would promote catalysis. What is clear is that product accumulation and high substrate concentrations adversely affect determination of kinetic rate constants for Angiotensin I using S_i concentrations greater than 200µM with this methodology, making it unfeasible.

4.3.4 Progress Curve Analysis

Rather than look for a way to account for the confounding effects at high S_i concentrations, the use of progress curves was investigated as a means of utilizing lower substrate concentrations. As discussed in section 4.1, the application of a non-linear regression analysis proposed by Golicnik (2010) to progress curves generated using a method adapted from that described by Stockbridge & Wolfenden (2009) provided a viable alternative (representative data shown in Figure 4.11). Duggleby (2001) suggested that, for continuous kinetics assays, an appropriate starting substrate concentration (S_i) would be about 2-3X K_m. However, Golicnik (2010) showed using simulations that the non-linear regression analysis (using the combined equations 9 & 10) of a progress curve generated with a S_i concentration equal to K_m would produce accurate constants with a very low degree of error. In follow up work, Golicnik (2011c) showed, using the same analysis, with data obtained from the literature, that using a S_i concentration as low as half that of the K_m would still produce accurate constants with a very low standard deviation. Thus, this approach was compared to the normal Single Injection Method.

Figure 4.12A shows progress curves for HHL generated from the same raw calorimetric data as that used for the Single Injection Method (shown in 4.8A), as well as an additional experiment performed with a S_i concentration of 1mM HHL (raw data not shown). The K_m values are in strong agreement with those generated using the Single Injection Method over a wide range of S_i concentrations (Figure 4.12B). An S_i concentration for HHL as low as 1mM, which is about 0.4 X below K_m, produced K_m values consistent with the higher S_i

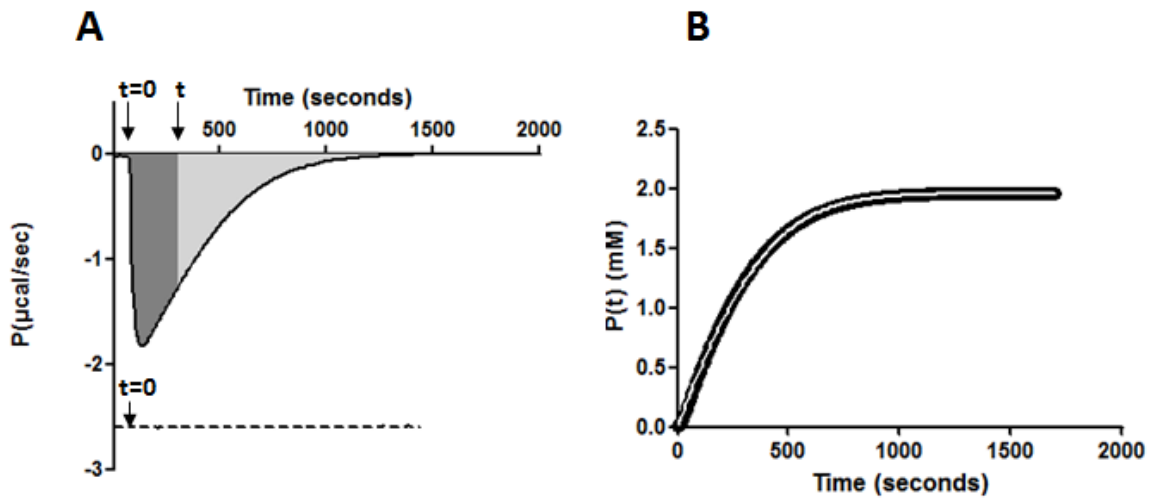

Figure 4.11 Representative data for the Progress Curve Method. Methodology is described in 4.2.5 **A)** Continuous raw calorimetric output (solid black line) of a single injection of enzyme into the reaction cell containing substrate, with thermal power P (ucal/sec) on the Y-axis and Time (sec) on the X-axis. Total integrated area is shown in light grey shaded area and the integrated area between t=0 and t is shown in dark grey. The dotted line represents the raw calorimetric output of a control experiment where the same amount of enzyme is injected into the reaction cell containing only buffer. Figure adapted from Stockbridge & Wolfenden (2009). **B)** The resultant reaction progress curve (thick black line), which was calculated from raw experimental data using equation 8, is fitted to the temporal closed form of the Michaelis-Menten equation (equations 9 & 10) using non-linear regression analysis (thin white line).

concentrations, showing that the analysis is consistent at such low S_i concentrations. The high consistency with the Single Injection Method is also observed with the k_{cat} values (Figure 4.12C), which also translates to the k_{cat}/K_m values shown in Figure 4.12D. There is some variation for the k_{cat}/K_m values at low Si concentrations, a phenomenon more likely attributed to the fact that the Single Injection Method rate data does not reach a plateau and hence k_{cat} is based on an extrapolation. In contrast, the progress curves at all S_i concentrations are complete, providing a higher degree of confidence in the constants obtained. Thus, the Progress Curve method has been shown to be highly comparable to the Single Injection Method for HHL, and, more importantly, allows the use of S_i concentrations below K_m which would then vastly reduce influence of substrate inhibition in determining accurate rate constants.

The same approach was then followed in order to see if the S_i concentration could be lowered for Angiotensin I. In 4.3.3 it was ascertained that the Single Injection Method was

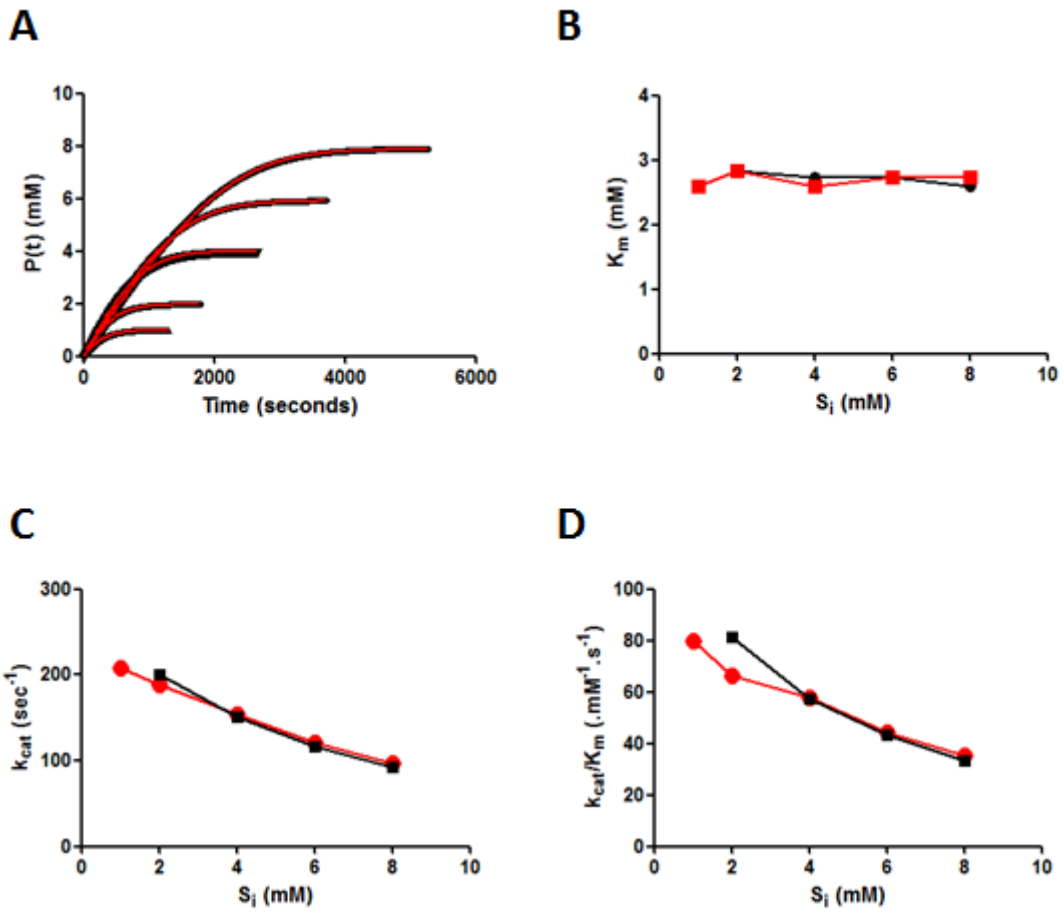

Figure 4.12 Comparison of Single Injection Method and Progress Curve Method for HHL kinetics. Representative examples of the reaction between tACEg13sol and HHL in 300mM NaCl, 100mM Tris(Acetate) buffer (pH 7.5), 10uM $ZnSO_4$. Units are all indicated on each axis. A) Progress curve (thick black lines) for a range of HHL S_i concentrations (8, 6, 4, 2, 1mM) calculated from raw data using equation 8 and fitted to equation 9 & 10 using non-linear regression analysis (thin red lines) as described in 4.2.5. The raw data used was identical to that for the Single Injection Method. R^2 values for all fits were greater than 0.998. The resultant K_m values (B), k_{cat} values (C), and k_{cat}/K_m values (D) of the non-linear regression analysis in A (all red dots), plotted against the initial substrate concentration (S_i) on the X-axes. For comparison, the corresponding values calculated from the same raw data using the Single Injection Method (identical to Figure 4.7). Each data point represents a single experiment.

not viable below 200µM due to the combination of low enthalpies associated with low S_i concentration and the need to keep enzyme concentration low so that as close to steady-state V_{max} could be achieved. Figure 4.13A shows fitted progress curves from assays done using Angiotensin I S_i concentrations ranging from 128-183µM, approximately 2-3X K_m as suggested by Duggleby (2001), using a higher enzyme concentration to increase the maximum enthalpy (raw data not shown). The maximum peak height of the lowest

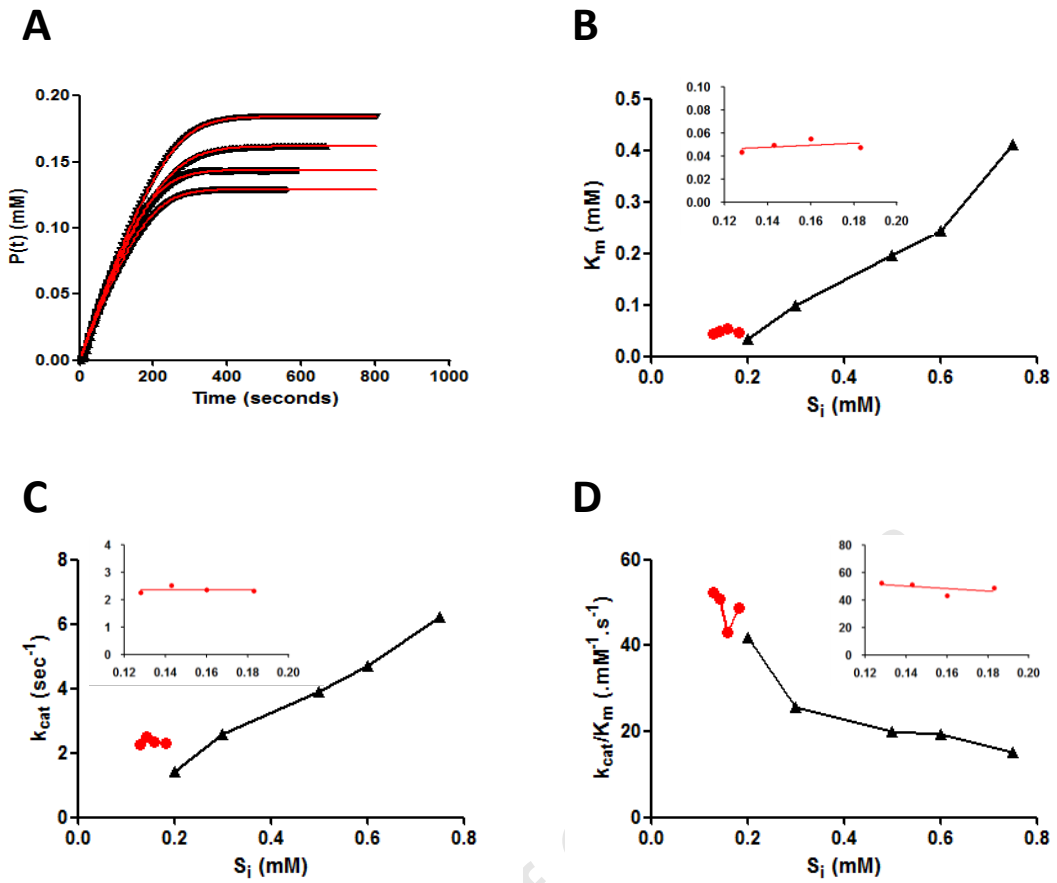

Figure 4.13 Comparison of Single Injection Method and Progress Curve Method for Angiotensin I kinetics. Representative examples of the reaction between tACEg13sol and Angiotensin I in 20mM NaCl, 100mM Tris(Acetate) buffer (pH 7.5), 10uM $ZnSO_4$. Units are all indicated on each axis. **A)** Progress curve (thick black lines) for a range of Angiotensin I S_i concentrations (128µM, 143µM,160µM,183µM) using constant tACEg13sol concentration (434nM) calculated from raw data using equation 8 and fitted to equation 9 & 10 using non-linear regression analysis (thin red lines) as described in 4.2.5. The raw data used was identical to that for the Single Injection Method. The resultant K_m values **(B)**, k_{cat} values **(C)**, and k_{cat}/K_m values **(D)** of the non-linear regression analysis in A (all red dots), plotted against the initial substrate concentration (S_i) on the X-axes. For comparison, values calculated using the Single Injection Method (identical to Figure 4.8) are shown (black triangles). Each data point represents a single experiment. Insets show only progress curve data points subjected to linear regression analysis to show there is no significant slope.

concentration (128µM) was greater than 0.4µcal/sec, double the minimum requirement of 0.2µcal/sec. Using a S_i concentration lower than 128µM proved to be unviable, as the low enthalpies encountered caused the data to become irreproducible. The K_m values obtained in this range show that the trend from the Single Injection Method data is continued into the lower S_i concentrations (Figure 4.13B). The inset shows that the progress curve K_m data

is fairly consistently level, a trend observed repeatedly using other ACE constructs (data not shown), and agrees very well with the reported values of 47±1.5 at 20mM NaCl (Liu et al., 2001) and 55.6±6.4 at 100mM NaCl (Rice et al., 2004). Similarly in Figure 4.13C, the trend from Single Injection Method data to Progress curve k_{cat} values is fairly consistent as the S_i concentration decreases. Only the K_m at 200µM deviates from the trend, which can be accounted for as poor data, as this has been established as the lower detection limit for the Single Injection Method. As with the K_m data inset (Figure 4.13B), the progress curve data in the S_i range used is consistent. However, the expected k_{cat} for this reaction was around 10-34 $.s^{-1}$ (Rice et al., 2004; Rousseau-Plasse, 1996), somewhat higher than the ~$2.s^{-1}$ observed here (Figure 4.13C). Figure 4.13D shows the same comparison of k_{cat}/K_m values obtained between the two techniques with the same trends observed. These k_{cat}/K_m values (calculated from the k_{cat}) are generally lower than those reported in the literature, which range from $180.mM^{-1}.s^{-1}$ (Rice et al., 2004) up to ~$1900.mM^{-1}.s^{-1}$ (Rousseau-Plasse et al., 1996; Liu et al., 2001). A possible explanation for this inconsistency with the literature is that the active enzyme concentration was not determined which would be a factor that would affect the calculation of k_{cat}. A report by Schulleck & Wilson (1989) determined that the Tris, phosphate and borate buffers inhibited ACE activity, unlike HEPES that had no effect on enzymatic activity. They also reported a K_m of 0.21mM for HHL in HEPES (at 37°C, pH 7.0 and 100mM KCl), which is an order of magnitude lower than was obtained for HHL using Tris buffer (see Figure 4.12B). This value is contrary to those obtained for the more widely used phosphate buffer, that correlate well with the values reported here using Tris buffer, which suggested that the buffer was playing a role in modulating the kinetic constants obtained. Further to this, reports in the literature regarding assays of Angiotensin I hydrolysis by ACE routinely use HEPES as the buffer system, where thus far only Tris due has been investigated based on the fact that it contributes significantly to the overall enthalpy. This would go some way to explain why the k_{cat} for Angiotensin I hydrolysis (see Figure 4.13C) is considerably lower than the reported values which were obtained in HEPES buffer.

4.3.5 Effects of Buffer on ACE Activity

We investigated the effect of a variety of buffers on the kinetic constants obtained for the hydrolysis of HHL by tACEg13sol. Buffers were chosen primarily based on their effective

buffer range, which needed to encompass pH 7.5 to allow for comparable evaluation and exclude pH effects. The enthalpies of ionisation (ΔH_{ion}) of these buffers (significance is described in 4.3.1) needed to be close to either 0 or 10kcal/mol so as to maximise overall ΔH_{app} (see figure 4.3). Assays were performed as described in 4.2.5 using the Progress Curve method and multiple S_i concentrations, with the only variation (apart from minor enzyme concentration differences) being the buffer system used. As can be seen in Figure 4.14A, there is a distinct difference between the K_m values obtained for Tris (values reproduced from Figure 4.12) and phosphate (2.69±0.046 and 3.4±0.09 mM respectively), and the rest of the buffers, which ranged from 0.4 to 0.8mM. This supports the findings of Schulleck & Wilson (1989), with the K_m for HEPES, as well as Maleate, TES and TAPSO, being much closer to the 0.21mM quoted. The k_{cat} values at various S_i concentrations do not vary extensively between the buffers, with all buffers maintaining a similar degree of substrate inhibition suggesting it is not a buffer related effect (Figure 4.14B). It must be noted again that active enzyme concentration was not determined for these assays as it was investigatory in nature, so the k_{cat} values must be taken as guidelines only and may vary. This must be taken into account as well when looking at the k_{cat}/K_m values in Figure 4.14C, as minor variations in k_{cat} and K_m can translate into large variation in these values. One can only postulate as to the mechanism behind these effects, but it is unlikely to be due to ionic effects, as this has been explored by Liu et al (2001) and Schulleck & Wilson (1989) and found not to be significant. Upon examination of the structures of the buffers, a trend can be seen where Tris and phosphate physically occupy a very small volume in comparison to HEPES, TES, Maleate and TAPSO, suggesting that they may be infiltrating the interior of tACEg13sol. There is evidence for a large hinge-bending mechanism, based on crystallographic data and comparison with the ACE homolog ACE2 (Watermeyer et al., 2006). It is possible that the smaller buffers are potentially locking the enzyme in one of two or more specific conformations associated with the hinge motion and modulating activity somehow.

To investigate this buffer effect further the tACE activity at different chloride concentrations was determined using substrates HHL and angiotensin I. Whilst the logical choice of buffers to compare to Tris would be HEPES, its ionisation enthalpy (ΔH_{ion}) of 4.89kcal/mol resulted in the overall ΔH_{app} being too close to zero (see Figure 4.3), which made kinetic assays impossible (data not shown). TAPSO buffer was thus chosen on the basis of its high ΔH_{ion}

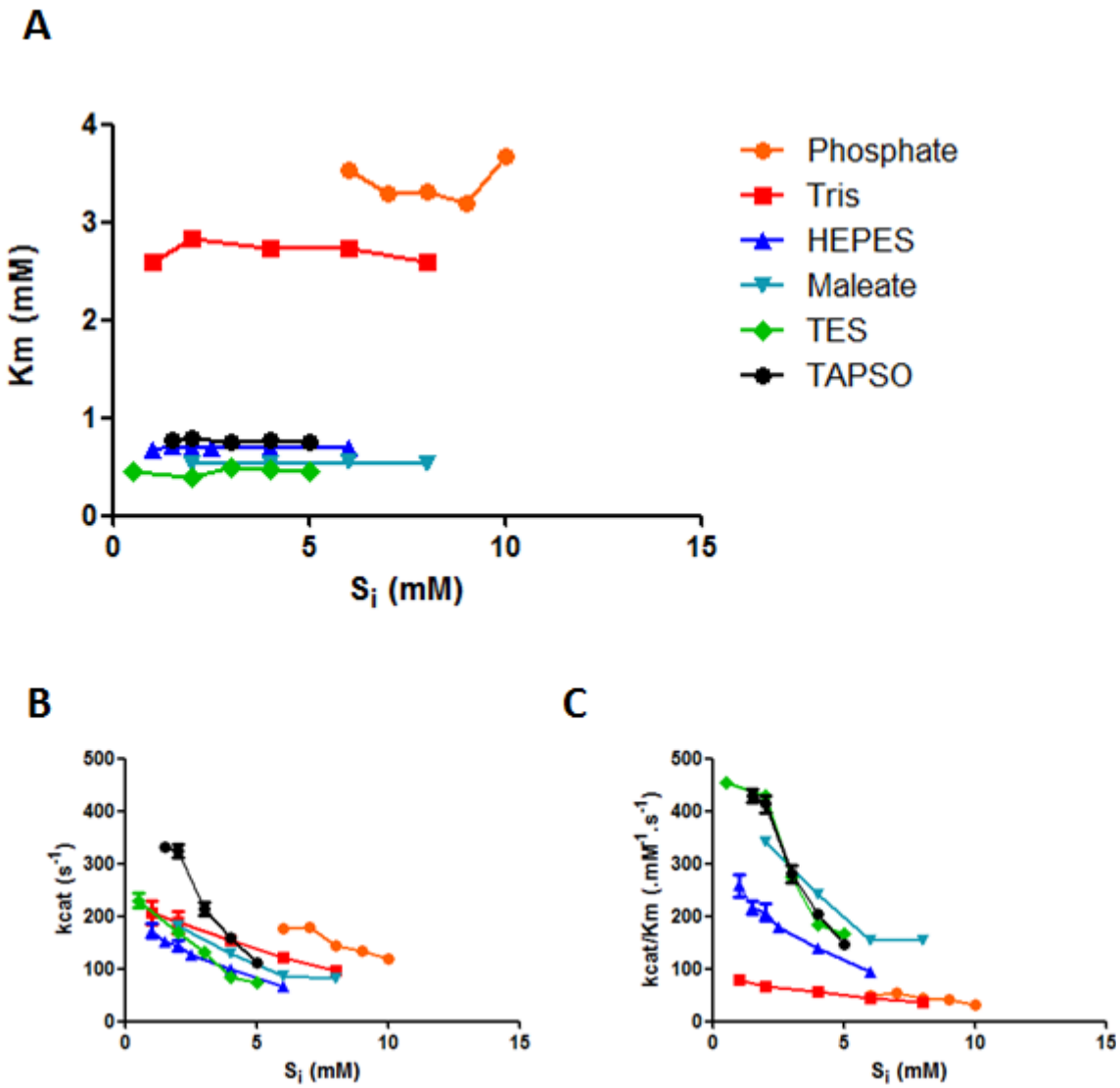

Figure 4.14 Effects of varying buffers on the kinetic constants of HHL hydrolysis by tACEg13sol. Representative examples of the reaction between tACEg13sol and HHL in a variety of buffers, all at pH 7.5, 300mM NaCl, 10uM $ZnSO_4$. Six different buffers (100mM phosphate, 100mM Tris, 50mM HEPES, 50mM Maleate, 50mM TES and 50mM TAPSO) were investigated with the key on the right indicating the colour for each. For each buffer condition, multiple single injection hydrolysis reactions were performed and analysed as described in 4.2.5 using progress curve approach, with enzyme concentrations kept constant (between 200 and 600nM) and multiple S_i concentrations were used. The resultant K_m values (A), k_{cat} values (B), and k_{cat}/K_m values (C) of the non-linear regression analysis are plotted against the initial substrate concentration (S_i) on the X-axes. Each data point represents a single experiment.

and the fact that its K_m for HHL aligned fairly closely with that of HEPES (see Figure 4.14A). Irrespective of purification method and storage conditions (which have been optimally determined in our lab), degradation of enzyme can occur when stored for long periods of

time, which lowers the concentration of active enzyme (Knight, 1995). Thus, lisinopril binding curves using ITC were performed for all enzyme samples in order to determine the active enzyme concentration (outlined in 4.2.6, data not shown), a factor that would provide confidence in the k_{cat} values determined.

The K_m, k_{cat} and k_{cat}/K_m values for HHL hydrolysis by tACEg13sol with either Tris or TAPSO are shown in Figure 4.15 A, B & C respectively. What is readily apparent is that increasing the chloride concentration with TAPSO results in a concentration dependent lowering of K_m for HHL, which is in contrast to what is observed with Tris. The k_{cat} values show an increase from 0mM to 20mM NaCl using Tris buffer, yet very little difference at the much higher 300mM NaCl. The same conditions for TAPSO by contrast, show a chloride dependent increase in k_{cat} up to 300mM NaCl. The same pattern extends to the k_{cat}/K_m values, with the increase in k_{cat}/K_m from 20mM to 300mM being only 1.22X with Tris, yet 12.5X for TAPSO. The greater increase in k_{cat}/K_m compared to what was observed with the tACE chloride titration curve is likely due to different substrate concentrations. This pattern for TAPSO confirms its greater chloride dependency and suggests that Tris is somehow disrupting the enzyme catalytic mechanism at high chloride levels. This supports the idea that the smaller Tris molecule is somehow locking ACE in a specific conformation.

The same buffer comparison was done for Angiotensin I hydrolysis, but only used 0mM and 20mM NaCl, which is the reported chloride concentration of maximal activity (Liu et al., 2001). The K_m, k_{cat} and k_{cat}/K_m values for hydrolysis by tACEg13sol with either Tris or TAPSO are shown in Figure 4.15 D, E & F, respectively. Whilst there is very little variation in the K_m, with Tris values unchanged between 0 and 20mM NaCl and TAPSO decreasing slightly, the major variation occurs with k_{cat}. There was very little variation at 0mM NaCl with Tris and TAPSO, however, at 20mM NaCl the TAPSO k_{cat} value was more than 2-fold that of Tris. This pattern carries through to the k_{cat}/K_m values for both buffers and further highlights the negative impact of Tris on tACEg13sol catalysis in the presence of chloride. The approximate 6-fold increase in k_{cat}/K_m values between 0 and 20mM NaCl using TAPSO is not as high as the 20-fold increase between the same chloride concentrations reported by both Wei et al (1991b) and Liu et al (2001) , who used an HPLC based methodology. This variation could be attributed to a combination of both detection technique and analysis methodology used. The important point is that Angiotensin I hydrolysis in TAPSO appears to

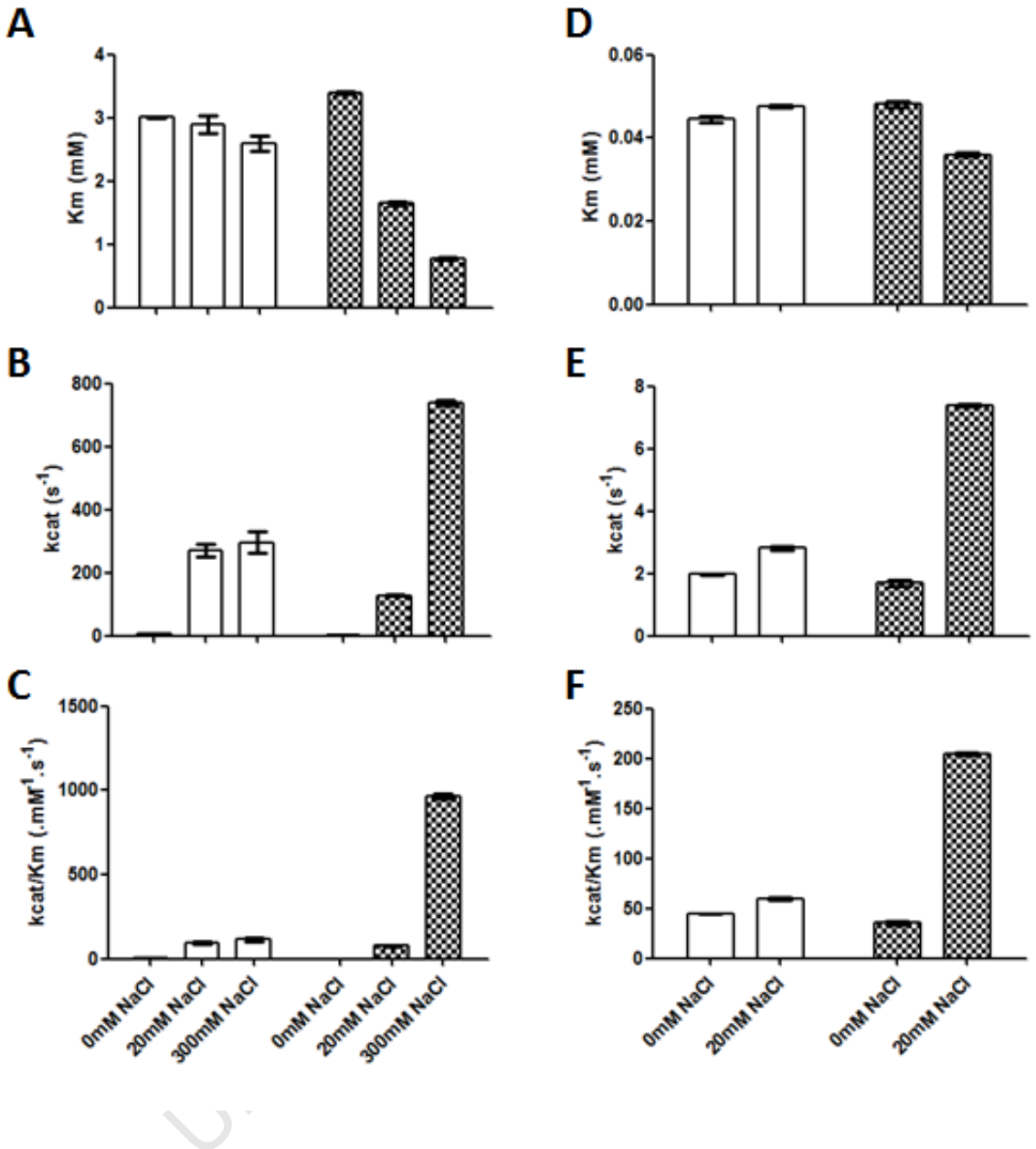

Figure 4.15 Comparison of Tris and TAPSO buffers in the hydrolysis of Angiotensin I and HHL at varying chloride concentrations. Progress curve approach (described in 4.2.5) was used to evaluate the kinetic parameters (K_m, k_{cat} & k_{cat}/K_m) for tACEg13sol hydrolysis of either HHL (A, B, C) or Angiotensin I (D, E, F) using either Tris (white bars) or TAPSO (chequered bars) at pH 7.5, 10uM $ZnSO_4$. Varying NaCl concentrations were used; 0mM, 20mM & 300mM for HHL and 0mM and 20mM for Angiotensin I. For HHL, S_i concentrations were all 1mM HHL and for Angiotensin I they were kept in the range of 120-180µM. Each bar represents a minimum of 3 repeats with the error bars indicating standard error. For each condition, ITC binding curves were performed on the enzyme sample using lisinopril (as described in 4.2.6, data not shown) in order to ascertain the stoichiometry of binding N (see Figure 4.5). The stoichiometry of binding acts as an active site titration and indicates the percentage of active enzyme in the sample. These values were used to adjust enzyme concentration and hence make k_{cat} determination more accurate.

have a chloride dependent profile more akin to that of HEPES than Tris. The effect that Tris is exhibiting appears to affect the chloride profile for both HHL and Angiotensin I, and given that investigation of chloride dependence is the primary focus of this study, it would be ill-advised to use this buffer. For the purposes of further study of tACEg13sol chloride mutants generated in Chapter 3, the evidence here indicates that the best approach would be to use TAPSO buffer with all substrates investigated.

4.4 Summary

The feasibility of using ITC to determine the kinetic rate constants for ACE hydrolysis was investigated using the short synthetic peptide HHL and the large physiological peptide Angiotensin I. It was shown that the hydrolysis reactions produced measurable enthalpies, which varied due to contributions of various buffers, with the use of Tris buffer giving the largest ΔH_{app} for Angiotensin I and one of the largest for HHL. Tris was employed as the buffer of choice in investigating the Multiple and Single Injection Methods. The Multiple Injection Method proved viable for HHL, but failed to produce adequate changes in enthalpy for Angiotensin I due to a combination of relatively low ΔH_{app}, low k_{cat} and a requirement for pseudo first-order conditions. The Single Injection Method produced viable enthalpies for both substrates, but was extremely sensitive to high substrate concentrations for HHL and accumulation of reaction products for Angiotensin I. The use of Progress Curves was explored in order to use lower starting substrate concentrations and thus avoid the problems associated with the Single Injection Method. This approach proved highly comparable and effective at S_i concentrations below K_m. Concerns over the kinetic constants obtained using Tris prompted evaluation of a range of buffers, the results of which showed that Tris negatively affects ACE hydrolysis. More specifically, this negative effect altered the chloride dependence profile for both substrates. It was shown that TAPSO buffer produced kinetic constants and chloride profiles far more consistent with those reported in the literature. It was concluded that the use of the ITC-based Progress Curve Method with S_i concentrations low enough to avoid substrate and product inhibition effects and using TAPSO as the buffer system is a viable, consistent and reproducible approach suitable to the study of chloride dependence in tACE.

Chapter 5: Investigation of Chloride Dependence Mechanisms using tACE Constructs

5.1 Introduction

Chapter 3 described the initial characterisation of a number of tACEg13sol mutants generated to probe the underpinnings of the chloride dependence observed in the C-domain of ACE. It was established that the chloride 1 pocket mutant R186H showed a small increase in $K_{d,app}$ from tACE, as well as an increase in overall activity, with HHL and Z-FHL substrates. Rushworth et al (2006) showed a decrease in activity for their R186Q mutant with angiotensin I, indicating that the Arg identity is important in chloride dependence in the C-domain. Further investigation of R186H was warranted using angiotensin I as substrate to assess the implications of having the bulkier aromatic His in that position and whether this contributes to variable chloride dependence between the domains.

A number of mutants in the chloride 2 pocket were generated with varying effects. The V518T and M223W C to N-domain mutants showed no change in $K_{d,app}$ for either HHL or Z-FHL, though there were some differences in overall activity. The D465T mutant showed some variation in $K_{d,app}$, however this was inconsistent with HHL being lower and Z-FHL being higher, with maximal activity also being lower with both substrates. The R552K and R522Q mutations had a similar effect with HHL and Z-FHL as that observed by Liu et al (2001) with AngI, with $K_{d,app}$ values for R522K and R522Q increasing considerably and activation considerably reduced. The relatively minor differences observed for V518T, M223W and D465T suggest they were not having significant roles in the chloride dependence mechanism, thus R522K and R522Q were chosen as the focus of further analysis as they showed the largest effects.

The E403R mutant was generated in order to probe the mechanism of the proposed chloride gating. This mutation had markedly reduced $K_{d,app}$ values for HHL and Z-FHL relative to tACE, as well as very similar levels of maximal activity but with reduced degree of activation. The effect on $K_{d,app}$ was shown to be reversible in the N-domain with the R381E mutation showing increased $K_{d,app}$ values, though not to the same extent. This was the first clear evidence that E403 was clearly modulating chloride binding, though the exact mechanism was unclear, and it was hypothesized that substrate interactions in the S2 sub-site might be modulating this interaction. Thus, it was felt that further evaluation was warranted to determine which residues E403 interacts with and whether substrate affects these interactions.

The following mutants, R186H, E403R, R522K and R522Q, were evaluated with HHL, Z-FHL and Angiotensin I under different salt conditions using three different approaches:

Firstly, molecular docking simulations of HHL and Z-FHL into both the C-and N-domains were performed. This was to complement work done by collaborators who have done complex simulations of Angiotensin I interacting with the C- and N-domains of ACE (unpublished). Having an idea of the potential interactions of these substrates allowed for informed conclusions to be made in relation to the kinetic analysis.

Secondly, the effect these mutations had on the kinetic constants of tACE in the presence or absence of chloride was assessed. In order to effectively characterise these mutants, a novel approach using ITC to determine the K_m, k_{cat} and K_{cat}/K_m was developed, which is described extensively in Chapter 4. This allowed the differentiation of whether the mutations are affecting binding (K_m) or the catalytic mechanism (k_{cat}), and their combined contribution to overall activity (K_{cat}/K_m). Of importance with this method is that it permits the precise evaluation of the kinetic parameters of all three substrates (HHL, Z-FHL and AngI) using the same technique.

Thirdly, the ITC-based technique developed in Chapter 4 permitted the evaluation of thermodynamic profiles of the reaction under different chloride conditions. This is the first thermodynamic analysis of chloride activation to be carried out, and provides a link between kinetic rate constants and structural interpretation associated with structural inspection and molecular docking simulations. Changes in K_m or k_{cat} associated with chloride binding could be associated with either enthalpic or entropic effects.

ITC is routinely used to evaluate the thermodynamic contributions of inhibitor binding, allowing experimental evaluation of structural changes in the lead optimization process (Velasquez Campoy et al., 2000; Velasquez Campoy et al., 2001; Ohtaka et al., 2003; Olsson et al., 2008). Whilst this approach is readily applied to binding experiments, it is rather uncommonly used for enzyme kinetics in the literature, due almost entirely to the fact that the vast majority of assay methods used do not provide a viable measure of enthalpy. Fortunately, the Progress Curve method described in 4.2.5 allows for the determination of the reaction enthalpy (ΔH_{app}) by virtue of the fact that the entire curve represents the complete hydrolysis of substrate. This allowed the change in true enthalpy of the reaction

(ΔH_{int}; referred to as ΔH), and subsequently the Gibbs free energy change (ΔG) and temperature dependant change in entropy (TΔS), to be calculated, which represent the thermodynamic parameters associated with the hydrolysis of substrates by tACE. Enthalpy and entropy both contribute to ΔG, with each having a different role. The enthalpic contribution (ΔH) is composed primarily of hydrogen bond formation, protonation events, van der Waals interactions and ionic interactions, and reflects the strength of the ligand-target interaction relative to those with solvent. When ΔH is negative, binding is enthalpically favoured which requires correct placement of hydrogen bond acceptor and donor groups at the binding interface. Entropically favourable binding is reflected by a positive TΔS (i.e. more negative – TΔS), with changes primarily due to any combination of increased hydrophobic interactions, increase in solvent entropy from burial of hydrophobic groups, release of water or ions upon binding, as well as minimal loss of conformational degrees of freedom. So, where lead optimization of inhibitors uses these parameters (calculated in a similar manner for a reversible binding reaction) to inform the effect of change (either inhibitor functional groups or specific residues in target protein), these measures were used to probe the mechanistic underpinnings of chloride dependent substrate hydrolysis.

In a comprehensive review of molecular interactions, Bissantz et al (2010) ascertain that, whilst tempting, speculation about the link between thermodynamics and geometry of protein-ligand complexes via crystal structure information should be treated with care. Any practically useful relationships between structure and calorimetrically determined components of free energy (entropy and enthalpy) have proven difficult to establish as both terms contain solute and solvent contributions (Bissantz et al., 2010). Experimental determination of these solvent effects have been attempted (Chervanak et al., 1994), but given that a number of assumptions were required, means that to date, only computer simulations can delineate these contributions (Gilson et al., 2007; Bissantz et al., 2010). Furthermore, detailed contributions of protonation and deprotonation steps, along with other enthalpic contributors, need to be fully understood (Klebe et al., 2001; Bissantz et al., 2010). In the context of drug lead optimisation, it has been shown that small structural changes can lead to significant shifts in relative ΔH and TΔS contributions, making structural conclusions tricky (Freire, 2008; Bissantz et al , 2010). On this note, the thermodynamic

data obtained with the ITC-based enzyme assay was applied with caution in the evaluation of chloride mutant proteins. It should be emphasized that full interrogation of all enthalpic or entropic contributions was not attempted, but instead the variation seen in either was used to qualitatively strengthen the interpretations of kinetic and structural data from the chloride dependence mutants.

In evaluating the tACE chloride mutants, the kinetic and thermodynamic data were evaluated and related to the crystal structure and molecular docking of substrates to provide a mechanism by which chloride dependence was related to substrate composition

Objectives:

1. Determine kinetic constants (K_m, k_{cat} and k_{cat}/K_m) using HHL, Z-FHL and Angiotensin I substrates for tACE mutants constructs under different chloride concentrations.
2. Calculate thermodynamic parameters (ΔG, ΔH and TΔS) associated with HHL, Z-FHL and angiotensin I hydrolysis under different chloride concentrations.
3. Perform molecular dynamic simulations to dock HHL and Z-FHL into the C and N domains of ACE and characterise potential binding interactions.

5.2 Experimental Approach

5.2.1 Chemicals & Equipment

Chemicals and equipment used are identical to those described in 4.2.1, with the exception being that only TAPSO buffer was used. Additionally, Z-FHL was purchased from Bachem.

5.2.2 Sample preparation

Preparation of enzymes, substrates and lisinopril samples was as described in 4.2.2, with Z-FHL prepared in an identical manner to HHL.

5.2.3 ITC Progress Curve Assays

Assays were performed at 37°C using the Progress Curve protocol described in 4.2.5. Buffer conditions for all substrates used (HHL, Z-FHL and Angiotensin I) consisted of 50mM TAPSO buffer (pH 7.5), 10µM $ZnSO_4$ and either 0, 20 or 300mM NaCl. Enzyme concentrations used varied between 2nM and 1000nM and were optimized for each assay to ensure substrate was not completely hydrolysed faster than 200 seconds (which lowered quality of data).

Assays were performed in triplicate as a minimum and all kinetic constants are reported as the mean of the three separate determinations along with standard error.

5.2.4 ITC Binding Curves

Assays were performed at 20°C using the protocol described in 4.2.6. Data was analysed using Origin 7 software provided, primarily to provide the stoichiometry value N to adjust total protein concentration to active protein concentration via the assay acting as an active site titration (see Figure 4.1). Binding assays were performed with every preparation of enzyme used in Progress Curve kinetic assays in order to improve the accuracy of the k_{cat} ($=V_{max}/[E]$) values obtained in those experiments.

5.2.5 Calculation of Thermodynamic parameters

The thermodynamic parameters (ΔG, ΔH, ΔS) were determined using the kinetic data (k_{cat}/K_m) and the raw data from each of those assays. The Gibbs free energy (ΔG) was calculated by the formula $\Delta G = -RT \ln(k_{cat}/K_m)$, with R being the gas constant (1.9858 $cal.K^{-1}.mol^{-1}$) and T being assay temperature (310 Kelvin). The apparent enthalpy (ΔH_{app}) was determined for each assay via integration of the area under the curve using formula 2 (see 4.2.4). To exclude the contribution of buffer to enthalpy the intrinsic enthalpy (ΔH_{int}) was calculated using the relationship $\Delta H_{app} = \Delta H_{int} + n_H.\Delta H_{ion}$ (ΔH_{ion} for TAPSO buffer = 9.378 kcal/mol; n_H = -0.37 for all substrates). Incorporation of ΔG and ΔH_{int} into $\Delta G = \Delta H_{int} - T\Delta S$ allows calculation of minus TΔS which is the entropy as a function of temperature. These values were calculated separately for each assay, which were done in triplicate as a minimum, with values shown as mean and standard error. The ΔG, ΔH, and ΔS values for lisinopril binding were calculated using Origin 7 with the iTC_{200} MicroCal Software Addon.

5.2.6 Docking of substrates into tACE active site

The short synthetic tri-peptides HHL and *Z*-FHL were docked into both the tACE-RXPA380 crystal structure (PDB code 2OC2) and the N-domain389-RXP407 crystal structure (PDB code 3NXQ) using the Accelrys Discovery Studio© Molecular Simulation program. These crystal structures for both domains were used as RXPA380 and RXP407 are larger than lisinopril and extend further into the non-prime binding site where *Z*-FHL is likely to interact. The HHL and *Z*-FHL molecules were built and minimized into the defined active site using CDOCKER simulation tool, which uses a CHARMm-based molecular dynamics (MD) scheme to dock

ligands into a receptor binding site. A minimum of ten poses were generated for each substrate in both tACE and N-domain structures. These poses were visually evaluated based on proximity (<2.5Å) and orientation of: A) the scissile peptide carbonyl group (displayed in the geminal-diol form) to the active site zinc, and B) the C-terminal carboxylate to Lys511, a likely interaction given that this residue interacts with the lisinopril C-terminal carboxylate (Natesh et al 2003). The pose that best fit these criteria and had the highest CDOCKER score was chosen.

5.3 Results & Discussion

Mutant tACEg13sol constructs showing greatest effect on chloride dependence and activation were characterised using HHL, Z-FHL and AngI under conditions of both 0mM and 20mM NaCl. Kinetic constants and thermodynamic parameters are displayed in Tables 5.1 and 5.2 respectively and are represented graphically in the following sections in context with the discussion.

5.3.1 Energetic Contributions in ACE binding and catalysis

In order to assess the effect of chloride concentration on the thermodynamics of substrate hydrolysis, first the thermodynamics of inhibitor binding and substrate hydrolysis had to first be compared at constant chloride concentrations. Once a comparative framework had been established, the thermodynamic parameters associated with substrate binding and catalysis in the presence and absence of chloride were evaluated to determine the effects of chloride binding on enthalpy and entropy values.

Figure 5.1A shows a representation of three different types of thermodynamic signatures that may be associated with drug binding, each having the identical ΔG and binding affinity, but differing in the relative contributions of ΔH and TΔS. Scheme A displays a favourable ΔH and an unfavourable TΔS, with ligands showing this profile typically have large degree of flexibility and high polarity, which could negatively affect membrane permeability in vivo. Conversely, Scheme B shows a favourable TΔS and an unfavourable ΔH, indicating that binding is driven by hydrophobic interactions. Scheme C, with its favourable ΔH and TΔS, is the most favourable thermodynamic profile for tight binding.

Table 5.1 Kinetic parameters for the cleavage of HHL, Z-FHL and Angiotensin I by ACE constructs. Cleavage of HHL, Z-FHL and Angiotensin I by tACE, N-domain and a number of tACE mutant constructs. Constants were determined using ITC assay as described in 5.2.3 at 0mM and 20mM NaCl (including 300mM for tACE with HHL) in 50mM TAPSO (pH 7.5) and 10µM $ZnSO_4$. Values are shown as the mean of three separate determinations of K_m, k_{cat} and k_{cat}/K_m along with standard error of the mean, with the units they are in displayed below respective headings.

Construct	Substrate	[NaCl]	K_m	k_{cat}	k_{cat}/K_m
		mM	*mM*	$.s^{-1}$	$.mM^{-1}.s^{-1}$
tACEg13sol	HHL	0	1.960 ± 0.020	3.26 ± 0.46	1.66 ± 0.24
		20	1.650 ± 0.030	127.00 ± 1.78	77.15 ± 1.03
		300	0.779 ± 0.008	606.00 ± 21.86	777.50 ± 28.11
	Z-FHL	0	0.580 ± 0.010	80.25 ± 1.20	140.00 ± 2.13
		20	0.120 ± 0.010	282.00 ± 11.16	2372.50 ± 93.67
	Angiotensin I	0	0.049 ± 0.001	1.70 ± 0.11	35.28 ± 2.11
		20	0.036 ± 0.001	7.38 ± 0.05	204.67 ± 1.21
N-domain	HHL	0	3.910 ± 0.060	14.15 ± 0.53	3.63 ± 0.14
		20	0.720 ± 0.020	38.84 ± 0.13	53.97 ± 0.15
	Z-FHL	0	1.360 ± 0.010	73.38 ± 0.62	54.10 ± 0.47
		20	0.520 ± 0.010	509.50 ± 15.61	991.25 ± 31.06
	Angiotensin I	0	0.520 ± 0.010	4.04 ± 0.06	36.23 ± 0.47
		20	0.077 ± 0.006	24.98 ± 1.59	325.40 ± 20.54
R186H	HHL	0	2.740 ± 0.030	2.09 ± 0.08	0.77 ± 0.03
		20	2.060 ± 0.020	122.00 ± 1.16	59.27 ± 0.62
	Z-FHL	0	1.000 ± 0.040	76.24 ± 2.94	76.44 ± 2.94
		20	0.150 ± 0.010	467.34 ± 36.45	3193.34 ± 247.68
	Angiotensin I	0	0.085 ± 0.003	1.52 ± 0.03	17.93 ± 0.29
		20	0.095 ± 0.003	7.83 ± 0.19	82.65 ± 2.02
E403R	HHL	0	4.360 ± 0.050	20.48 ± 0.43	4.70 ± 0.10
		20	1.540 ± 0.040	459.00 ± 24.12	298.67 ± 15.90
	Z-FHL	0	0.530 ± 0.010	159.34 ± 2.91	304.34 ± 5.21
		20	0.540 ± 0.010	929.34 ± 14.77	1736.67 ± 28.49
	Angiotensin I	0	0.069 ± 0.003	3.96 ± 0.28	57.46 ± 4.07
		20	0.061 ± 0.004	9.08 ± 0.41	123.00 ± 5.42
R522Q	HHL	0	2.820 ± 0.020	6.18 ± 0.17	2.20 ± 0.06
		20	1.680 ± 0.010	4.80 ± 0.18	2.87 ± 0.11
	Z-FHL	0	0.110 ± 0.010	92.24 ± 2.16	860.34 ± 20.01
		20	0.200 ± 0.010	124.67 ± 9.36	653.34 ± 47.73
	Angiotensin I	0	0.092 ± 0.003	12.98 ± 0.29	141.75 ± 3.20
		20	0.077 ± 0.003	13.75 ± 0.84	179.50 ± 11.14
R522K	HHL	0	3.720 ± 0.020	5.31 ± 0.19	1.43 ± 0.06
		20	2.250 ± 0.020	2.03 ± 0.05	0.91 ± 0.02
	Z-FHL	0	0.570 ± 0.010	126.00 ± 1.00	223.25 ± 1.94
		20	0.880 ± 0.020	193.50 ± 5.13	220.75 ± 5.97
	Angiotensin I	0	0.130 ± 0.002	0.83 ± 0.03	6.37 ± 0.21
		20	0.119 ± 0.002	3.79 ± 0.07	32.05 ± 0.53

Table 5.2 Thermodynamic parameters for the cleavage of HHL, Z-FHL and Angiotensin I by ACE constructs. Thermodynamic parameters associated with the cleavage of HHL, Z-FHL and Angiotensin I by tACE, N-domain and a number of tACE mutant constructs corresponding to the data from table 5.1. Values were determined as described in 5.2.5 at 0mM and 20mM NaCl (including 300mM for tACE with HHL). Values are shown as the mean of three separate determinations of ΔG, ΔH, -TΔS along with standard error of the mean.

Construct	Substrate	[NaCl]	ΔH_{int}	ΔG	-TΔS
		mM	*kcal.mol^{-1}*	*kcal.mol^{-1}*	*kcal.K^{-1}.mol^{-1}*
tACEg13sol	HHL	0	2.37 ± 0.07	-4.19 ± 0.01	-6.56 ± 0.07
		20	2.73 ± 0.03	-6.93 ± 0.01	-9.66 ± 0.03
		300	2.60 ± 0.01	-8.33 ± 0.01	-10.93 ± 0.01
	Z-FHL	0	2.27 ± 0.03	-7.30 ± 0.01	-9.57 ± 0.04
		20	2.70 ± 0.04	-9.06 ± 0.02	-11.80 ± 0.03
	Angiotensin I	0	2.16 ± 0.07	-6.44 ± 0.04	-8.60 ± 0.10
		20	2.19 ± 0.04	-7.53 ± 0.00	-9.72 ± 0.04
N-domain	HHL	0	2.48 ± 0.03	-5.04 ± 0.02	-7.52 ± 0.05
		20	2.59 ± 0.01	-6.93 ± 0.00	-9.52 ± 0.01
	Z-FHL	0	2.25 ± 0.01	-6.71 ± 0.01	-8.96 ± 0.01
		20	2.80 ± 0.06	-8.50 ± 0.02	-11.29 ± 0.08
	Angiotensin I	0	2.80 ± 0.06	-6.46 ± 0.01	-11.29 ± 0.08
		20	2.71 ± 0.10	-7.81 ± 0.05	-10.52 ± 0.10
R186H	HHL	0	2.25 ± 0.01	-3.75 ± 0.01	-6.00 ± 0.01
		20	2.72 ± 0.02	-6.77 ± 0.01	-9.49 ± 0.02
	Z-FHL	0	2.53 ± 0.06	-6.92 ± 0.02	-9.45 ± 0.08
		20	2.74 ± 0.08	-9.22 ± 0.05	-11.95 ± 0.07
	Angiotensin I	0	2.27 ± 0.04	-6.03 ± 0.01	-8.30 ± 0.03
		20	2.19 ± 0.01	-6.97 ± 0.02	-9.16 ± 0.02
E403R	HHL	0	2.62 ± 0.01	-5.21 ± 0.01	-7.82 ± 0.02
		20	2.93 ± 0.05	-7.76 ± 0.03	-10.69 ± 0.04
	Z-FHL	0	2.41 ± 0.03	-7.77 ± 0.01	-10.18 ± 0.04
		20	2.83 ± 0.10	-8.85 ± 0.01	-11.67 ± 0.11
	Angiotensin I	0	2.63 ± 0.05	-6.73 ± 0.05	-9.35 ± 0.10
		20	2.75 ± 0.11	-7.21 ± 0.03	-9.97 ± 0.10
R522Q	HHL	0	2.48 ± 0.03	-4.46 ± 0.02	-6.94 ± 0.05
		20	2.65 ± 0.16	-4.90 ± 0.02	-7.54 ± 0.18
	Z-FHL	0	2.38 ± 0.05	-8.41 ± 0.02	-10.79 ± 0.06
		20	2.51 ± 0.06	-8.24 ± 0.05	-10.75 ± 0.01
	Angiotensin I	0	2.28 ± 0.01	-7.30 ± 0.01	-9.59 ± 0.02
		20	2.36 ± 0.11	-7.45 ± 0.04	-9.80 ± 0.15
R522K	HHL	0	2.29 ± 0.05	-4.47 ± 0.02	-6.76 ± 0.07
		20	2.24 ± 0.04	-4.46 ± 0.01	-6.69 ± 0.04
	Z-FHL	0	2.22 ± 0.02	-7.58 ± 0.01	-9.81 ± 0.03
		20	2.78 ± 0.04	-7.58 ± 0.02	-10.36 ± 0.05
	Angiotensin I	0	2.21 ± 0.04	-5.39 ± 0.02	-7.24 ± 0.02
		20	1.85 ± 0.00	-6.39 ± 0.01	-8.60 ± 0.04

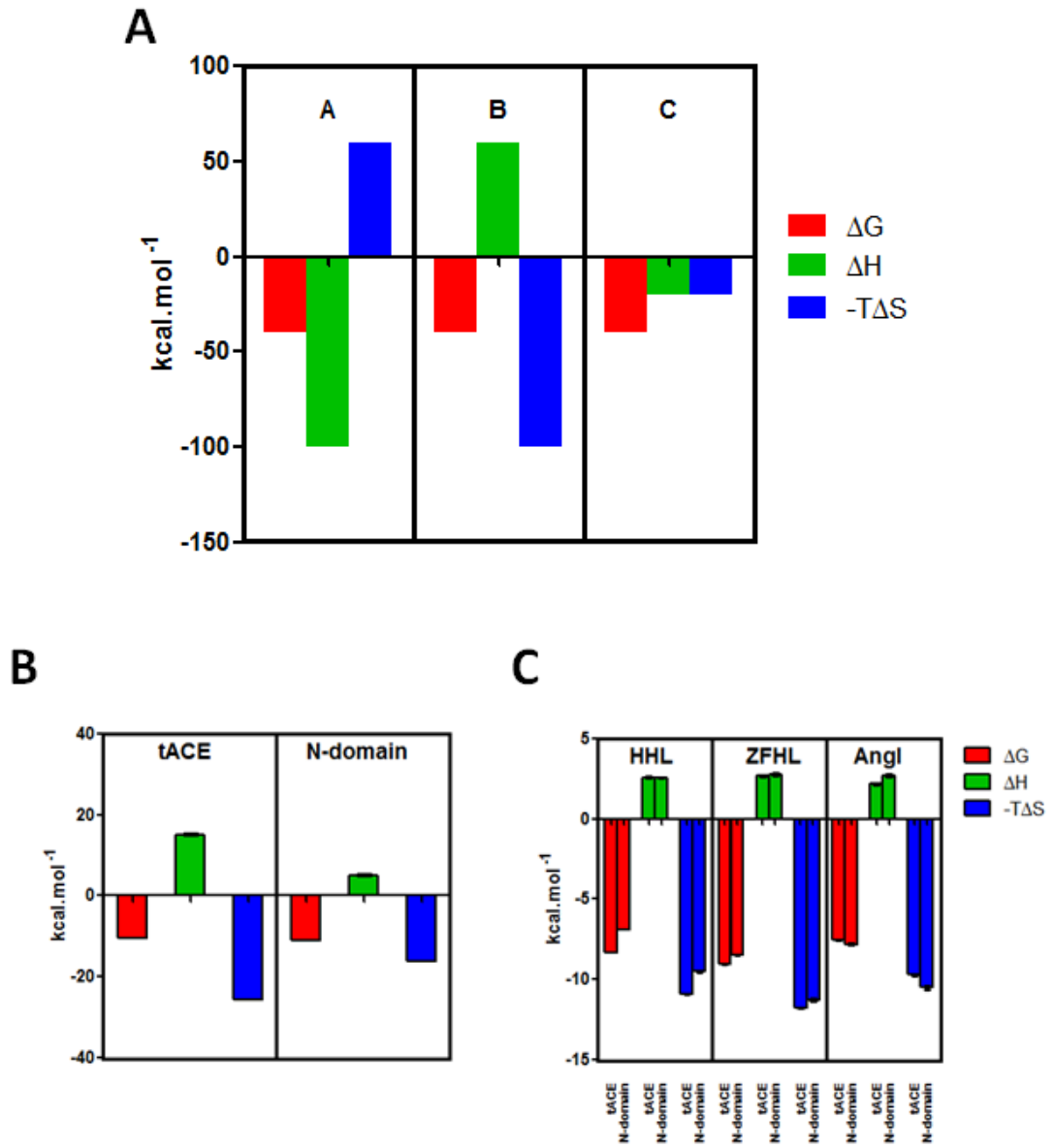

Figure 5.1 Thermodynamic signatures and energetic contributions. **A)** Representative schematic showing three different thermodynamic signatures. Scheme A: good hydrogen bonding and a conformational change. Scheme B: binding dominated by hydrophobic interactions. Scheme C: Favourable hydrogen bonding and hydrophobic interactions. Key on the right indicates designated colours for ΔG, ΔH, -TΔS. (Adapted from Freire (2004)) **B)** Thermodynamic signature for lisinopril binding to tACE and N-domain at 20mM NaCl (calculated as described in 5.2.5). **C)** Thermodynamic signature for the hydrolysis of HHL, Z-FHL and Angiotensin I by tACE and N-domain at 20mM NaCl, except for tACE with HHL which has maximal activity at 300mM NaCl (see table 5.2)

Figure 5.1B shows the thermodynamic profile for the potent ACE inhibitor lisinopril with both tACEg13sol and N-domain at 20mM NaCl. As is clearly evident, the profiles for both

domains matches that of Scheme B exactly, with unfavourable ΔH and favourable TΔS showing the interaction is dominated by hydrophobic interactions. The thermodynamic profiles shown here correlate strongly with those reported by Andujar-Sanchez et al (2007) who investigated lisinopril binding to somatic ACE. The relative binding of the tACE and N-domain (13.5 and 4.6 nM respectively) is not as C-domain specific as previously reported (Wei et al., 1992). However, this could be attributed to high C-values (917 and 1226 for tACE and N-domain respectively) which, as a measure of the accuracy of the K_d estimation, should ideally be between 50 & 500, yet not exceed 1000. Yet whilst the K_d estimations are on the lower limit of accurate detection, the calculated ΔG is largely unaffected, and, given that the determined ΔH values are quite accurate, there is a high degree of confidence in the overall thermodynamic profiles. Of interest, the N-domain shows markedly more favourable enthalpy than tACE, as well as less favourable entropy, suggesting a greater degree of specific interaction points at the binding interface.

The focus here though was not to evaluate inhibitor binding, but more to provide comparison with the thermodynamic parameters associated with substrate binding and catalysis. In Figure 5.1C, the enthalpic and entropic trend is maintained for the thermodynamic parameters calculated for HHL, Z-FHL and AngI hydrolysis at chloride concentration of maximum activity (values in Table 5.2). The ΔG values for Z-FHL for tACE and N-domain (-9.06 and -8.50 respectively) are far more favourable than those of either HHL or AngI by virtue of its considerably higher k_{cat}, and the fact that these substrates have higher K_m (HHL) and low k_{cat} (AngI) values, respectively. Furthermore, the enthalpy is very similar between the domains as well as between substrates for both domains. This suggests that the enthalpic contributions, and presumably any mechanisms, are highly similar between the domains. What is also evident for all substrates with both domains is the far larger contribution to ΔG by entropy (-TΔS) than enthalpy (ΔH), showing that binding is most likely driven by hydrophobic interactions, with desolvation of substrate and potentially structural changes being possible contributions.

In comparing the ΔH values between lisinopril and the three substrates, it can be seen that the values for lisinopril are considerably higher. This can be attributed to the large negative heat capacity change (ΔC_p) reported by Ortiz-Salmeron et al (1998) for captopril, and reiterated for lisinopril by Andujar-Sanchez et al (2007). A large negative ΔC_p would result in

considerably lower ΔH_{obs} values at higher temperatures for the buffer system, hence poorer signal and data, thus the lisinopril binding assays were performed at 20°C. Whilst the trend suggests that the ΔH_{obs} for lisinopril should be comparable to those for the various substrates, comparison of ΔH values between lisinopril and the three substrates cannot be done with the available data due to the different reaction temperatures used.

The large entropy contribution observed with lisinopril (and mirrored with HHL, Z-FHL and AngI) is indicative of the hydrophobic effect. Andujar-Sanchez et al (2007) used the approach of Spolar & Record (1994) to deconvolute the entropic change in order to discriminate between rigid body associations and those involving coupled conformational change. They found that a significant proportion of the entropy component could be attributed to conformational changes, which, along with the large ΔC_p indicates that binding is not a rigid body interaction. This suggests that there is a fair degree of conformational change upon binding and supports the proposed ACE hinge bending mechanism (Watermeyer et al., 2006). The closing of the active site would result in the association of numerous residues that would otherwise be bound to ordered solvent molecules when the protein is in an open conformation (Andujar-Sanchez et al., 2007). In considering the types of interactions involved and the associated bond energies (summarised in Table 5.3), the 2-5

Table 5.3 Enthalpic contribution associated with different types of bonding interactions. Values were taken from literature values reported in the right hand column.

Bond type	Bond energy	References
Peptide bond	2-5 kcal/mol	Dobry, 1952; Martin, 1998
Electrostatic/Salt bridge	3-5 kcal/mol	Anderson et al, 1990 Becktel et al, 1987
Hydrogen bond	1-3 kcal/mol	Larson et all, 1984; Emsley, 1980; Markovitch et al, 2007.
Van Der Waals forces	0.5-1 kcal/mol	Berg & Stryer, 2002.
Pi Aromatic bond	1.6-2.4 kcal/mol	Grover et al, 1987; Krause et al, 1991
Pi Cation	0.5-0.8 kcal/mol	Berry et al 2007
Hydrophobic Forces	5 kcal/mol per 100 $Å^2$ surface area	Pace , 1995; Pace et al ,1996

kcal/mol of energy heat that would be released by cleavage of the peptide bond could be counteracted by heat absorbed by a combination of other bond formations with the presumed structural change. This provides a possible explanation for the endothermic (positive enthalpy) nature of the reactions, although considerably more information would be needed to fully delineate the exact contributions. Thus, the enthalpy-entropy relationship is the same between inhibitor and substrate; hence it can readily be assumed that the structural mechanisms are shared between substrate hydrolysis and inhibitor binding.

5.3.2 Effect of chloride on energetic contributions

In evaluating the effect of chloride on the thermodynamic profile of tACE and N-domain, the thermodynamic parameters were determined in the presence or absence of chloride (Figure 5.2). There was a significant decrease in ΔG, hence lowered catalysis, in the absence of chloride for tACE and N-domain using AngI, HHL and Z-FHL. For all three substrates there were negligible changes in the ΔH values suggesting that increased activity in the presence of chloride is entropically driven. The fairly consistent ΔH with and without chloride between substrates suggests that the main interactions that form part of the catalytic mechanism are preserved, which is consistent with the observation that catalysis does occur in the absence of chloride. Moreover, it is likely that the mechanism does not involve majorly variable formation or breaking of bonds with the addition of chloride, which likely precludes the salt bridge breaking mechanisms proposed by Tzakos et al (2003).

In order to better evaluate the chloride dependent shifts in thermodynamic data, the changes in ΔG, ΔH and -TΔS (ΔΔG, ΔΔH and –TΔΔS) between 0mM NaCl and the concentration of maximal activity (300mM for HHL, 20mM NaCl for Z-FHL and AngI) were calculated for both domains (Figure 5.2C). For the C-domain the greatest change in ΔG is seen with HHL, with reduced change seen for Z-FHL and even less for AngI. These changes in free energy are almost completely entropy driven, as evidenced by the –TΔS values showing an almost identical trend. There is also almost no change in the enthalpy for AngI, with minor increases for HHL (0.236 kcal/mol) and Z-FHL approaching 0.5kcal/mol (0.475 kcal/mol). Given the magnitude of the bond energies shown in table 5.3, the cleavage of a peptide bond would presumably lead to a lowering of enthalpy by 2-5kcal/mol. However, it can be assumed that the conformational changes suggested by the negative –TΔΔS values

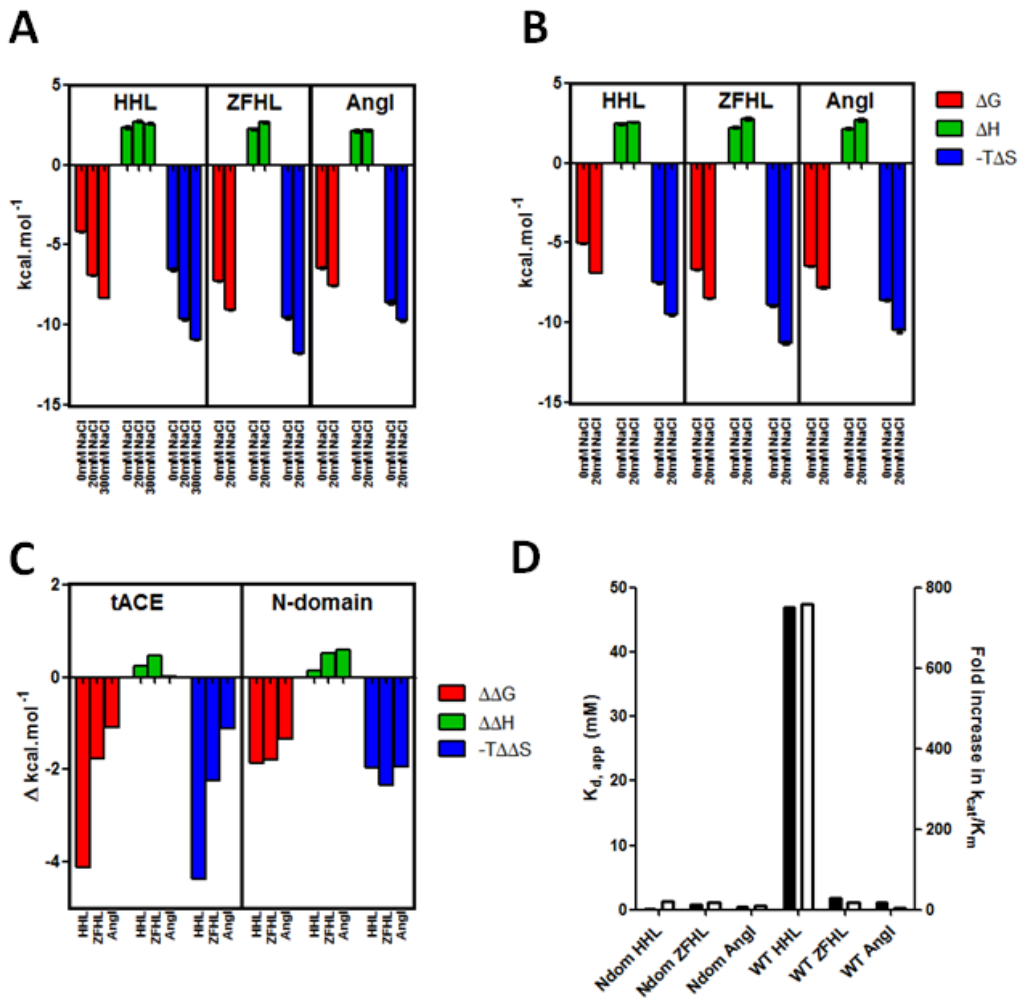

Figure 5.2 Effect of chloride concentration on thermodynamic parameters associated with ACE hydrolysis. Thermodynamic signature for the hydrolysis of HHL, Z-FHL and Angiotensin I at 0mM and 20mM NaCl by A) tACE and B) N-domain (values taken from table 5.2). The values for tACE with HHL at 300mM NaCl are included as this is the concentration of maximal activity and chloride saturation for this substrate and domain (whereas 20mM is the maximum for the other values). C) The ΔΔG, ΔΔH and –TΔΔS values for tACE and N-domain represent the difference in ΔG, ΔH, -TΔS between 0mM and 20mM (0mM and 300mM for HHL with tACE). D) Relative $K_{d,app}$ values (left Y-axis) and fold increase in k_{cat}/K_m from 0mM to maximal activity (right Y-axis) for tACE and N-domain with HHL, Z-FHL and AngI.

would result in the formation of sufficient interactions, presumably stabilising in nature, to counterbalance the effect of peptide bond cleavage and result in an overall slightly positive ΔΔH. The entropy linked increase in enthalpy would be a result of hydrophobic forces, either via desolvation of hydrophobic groups upon binding of substrate or via the formation of new bonds with a structural shift. By contrast, the corresponding ΔΔG, ΔΔH and –TΔΔS

values for the N-domain present far less variation between the different substrates. The ΔΔG and –TΔΔS for HHL are considerably less negative, whereas, in comparison, those for Z-FHL are relatively unchanged with the AngI values being slightly more negative than those for tACE. The larger entropic shift for AngI hydrolysis with the N-domain is driven by a ~0.5kcal/mol increase in the enthalpy, which could be a loss of specific interactions due to variability of interactions with AngI between the two domains. It could be expected, given the much larger size and presumably larger number of interactions, for there to be a greater degree of variability in the enthalpic component for AngI versus the two shorter peptides. However, if it is assumed that a fair degree of structural movement is occurring, presumably via the proposed hinge-bending mechanism (Watermeyer et al., 2006), it is possible that the larger peptide could be restricting this movement. This would balance the enthalpic component, as the bonds formed by AngI binding would compensate for those that would presumably form due to the structural shift. With this in mind, it could be surmised that the less variable entropic changes between substrates for the N-domain could be interpreted as the N-domain having a lesser degree of structural movement. That the largest variation between domains is seen with HHL would indicate that the difference in substrate composition, and hence interactions, compared to Z-FHL and AngI could be responsible for the observed shift. To highlight this variation, the $K_{d,app}$ values (from 3.3.2, table 3.1) were compared with the fold increase in k_{cat}/K_m between 0 mM NaCl and maximal activity (using values from table 5.1) for HHL, Z-FHL and AngI for both domains (Figure 5.2 D). The $K_{d,app}$ and fold increase in activity for tACE with HHL is considerably higher than with all the other substrates for either domain. This leads to two key questions: 1) How do the interactions of HHL with both domains lead to such variable degrees of chloride dependence and activation?; and 2) How do the interactions of Z-FHL and AngI differ to those of HHL in that their levels of activation and dependence are relatively similar between the two domains? These questions will be addressed in sections 5.3.4-5.3.7 in the evaluation of the tACE chloride mutants.

5.3.3 Molecular Docking

In order to evaluate potential interactions of the various substrates and provide context to the kinetic and thermodynamic data, molecular docking simulations for HHL and Z-FHL with both tACE and N-domain were performed. The interactions of HHL and Z-FHL with various

active site residues are shown in Tables 5.4 and 5.5 along with corresponding interactions for the molecular docking simulations of AngI which were kindly provided by Dr Georgios Spyroulias (University of Patras, Greece). It must be noted that the methodology employed for HHL and Z-FHL differs from that used for AngI. In the latter full global minimisations of both ligand and structure were performed, whereas HHL and Z-FHL ligands were docked into a rigid structure with local minimisations only. Furthermore, the docking program described here did not allow for evaluation of specific hydrophobic interactions (light blue squares), thus for comparison if these residues were within 4Å of either HHL or Z-FHL they are indicated in smaller italicised font.

The docking of HHL and Z-FHL into tACE (C-domain) showed interactions that correlate strongly with those of AngI, with the P2' Leu extending into the S2' pocket in all cases. Lys511, Tyr520 and Gln281 were shown to form either hydrogen bonds or salt bridges with the C-terminal carboxylate group of the peptide substrates, indicating good positioning of the peptide for presumed stabilization (Table 5.4; Figure 5.3 A & B). Similar interactions are observed in the tACE-Lisinopril crystal structure (Sturrock et al., 2004; Natesh et al., 2003), adding further confirmation that the C-terminal carboxylate groups of the docked substrates are correctly positioned.

The P1' His of all three substrates extends into the S1' pocket, although the relative orientation of the AngI imidazole ring does vary compared to that of HHL and Z-FHL. This is where some discrepancy in the interactions with Ala354 becomes noticeable. In Figure 5.3A, Ala354 hydrogen bonds directly with the imidazole nitrogen of the HHL histidine, whereas for Z-FHL this interaction is not present due to differential positioning of the His side-chain. Like HHL, Ala354 interacts with the P1' His of AngI, however this is not via the imidazole ring but rather via the peptide backbone amide (Figure 5.3B). As mentioned, Ala354 doesn't appear to bond directly to Z-FHL, however there is a compensatory interaction with Ala356 via the backbone amide of the P2 carboxybenzyl group. Ala356 doesn't form interactions with HHL as the hippuryl group is positioned in the opposite direction thus orienting the amide away from the alanine. The Ala356 to P2 amide hydrogen bond is not observed in the AngI simulation; however, the orientation more closely resembles that of Z-FHL suggesting the interaction may occur. Visual inspection and the variable interactions with

Table 5.4 Comparative molecular docking interactions for Angiotensin I, Z-FHL and HHL with tACE (C-domain). All interactions for Angiotensin I were provided by Dr Ravi Acharya (University of Bath, UK). HHL and Z-FHL were docked into the C -domain of ACE as described in 5.2.6 and interactions evaluated using Accelrys Discovery Studio software. Only interactions that occurred in >25% of valid poses are shown. Direct H-bonding interactions (X-H < 3.5 Å) are shown unaltered. Major hydrophobic interactions with non-polar residues: blue boxes. Pi-cation interactions between a hydrophobic residues and a charged cation group: blue shading. Salt bridge/ionic interactions have the residues underlined. Substrate C-terminal COO- stabilization interactions: yellow shading. Cl2 binding group/residues: grey shading. Residues within 3 Å of Z-FHL or HHL that are shown to interact with Angiotensin I are shown in smaller, italicized font).

		P8	P7	P6	P5	P4	P3	P2	P1	P1'	P2'
tACE	Ang I	Asp	Arg	Val	Tyr	Ile	His	Pro	Phe	His	Leu
		Thr92	Lys118	Lys118	Tyr360	Trp357	Glu403	Phe391	Glu411	Glu162	Gln281
		Lys118	Asp121	Trp59	Glu403		Cl2		Tyr523	His353	Lys511
		Asp121	Glu123	Pro407					Phe512	Ala354	Tyr520
		Glu123		Phe570					Val518		Val379
		Arg124									Val380
											Phe457
											Phe527
	Z-FHL							Cbz	Phe	His	Leu
								Ala356		Tyr523	Lys511
											Tyr520
											Gln281
								Phe391	*Phe512*	*Glu162*	*Phe457*
								Glu403	*Val518*	*His 353*	*His 513*
								Arg522		*Val380*	*Phe527*
	HHL								Hipp	His	Leu
									Arg522	Ala354	Lys511
											Tyr520
											Gln281
									Glu411	*Glu162*	*Phe457*
									Phe512	*Val380*	*His 513*
									Val518		*Phe527*

Ala354 and Ala356 between HHL, Z-FHL and AngI suggest that there is a fair degree of differential rotation around the bonds to either side of the scissile bond carbonyl (represented by gem-diol in HHL and Z-FHL). This, along with the observed shift in the orientation of the scissile bond carbonyl group relative to the catalytic zinc (which is clear for HHL vs Z-FHL, but less obvious for AngI due to lack of alignment), could account for the

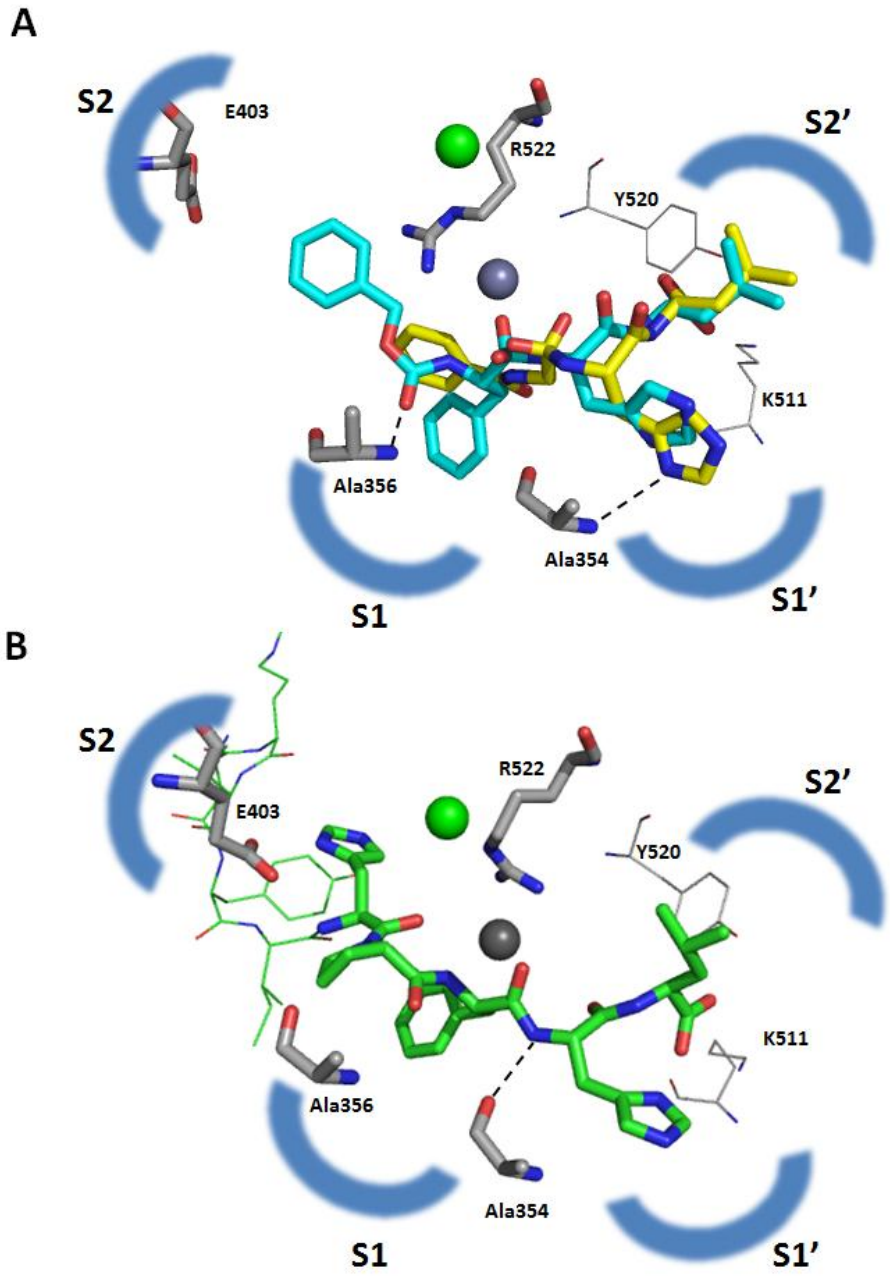

Figure 5.3 Stick representation of HHL, Z-FHL and AngI docked into the C-domain of ACE. A) Best representative overlaid poses for molecular docking of HHL and Z-FHL are shown in yellow and light blue sticks respectively; and B) Lowest energy conformation of AngI (sequence:DRVYIHPFHL) are shown as green sticks (HPFHL) and lines (DRVYI); both in the C-domain of ACE which has key residues displayed as grey sticks and lines of ACE. Active site zinc and chloride 2 pocket chloride ion are represented by the grey and green spheres respectively. Positions of the S2, S1, S1' and S2' sub-sites relative to substrates are indicated by faded blue half-circles. Hydrogen bonds are indicated by dashed black lines. Images were created using PyMOL 0.99 (DeLano Scientific, Palo Alto, CA, U.S.A).

variability in overall catalytic rate between substrates. Although this is unlikely to be the sole explanation, this could possibly explain the AngI maximal k_{cat} being almost 40-fold lower than that of Z-FHL, which itself has a 2-fold lower k_{cat} at maximal activity than HHL (Table 5.1). In support of this assertion, Tyr523 forms a hydrogen bond with the primary amine of the P1' His of Z-FHL, another differential interaction with that observed with AngI and HHL (table 5.1). Where Tyr523 interacts with the AngI P1 Phe side-chain, the Tyr523 doesn't appear to form a hydrogen bond with the HHL P1 hippuryl amide but is similarly positioned and within 3Å. It has been suggested that Tyr523 promotes formation of the tetrahedral gem-diolate intermediate (Sturrock et al., 2004; Hangauer et al., 1984) indicating its importance. Given that the hydroxyl group of Tyr523 is positioned within 3Å of the scissile bond amide for all docked structures, yet positioned differently, supports the idea that orientation of the peptide backbone has an effect on catalytic efficiency.

What did appear quite prevalently (~75% of poses) in the analysis was the presence of a potential Pi-cation interaction between the benzene ring of HHL hippurate and the positively charged Arg522, which is known to coordinate chloride (Liu et al., 2001; Natesh et al., 2003). This type of interaction was not assessed in the docking simulations done for AngI, so it is difficult to draw conclusions. However, the only part of AngI that could potentially form this interaction with R522 would be the P3 His and it is shown to hydrogen bond with E403, rendering Pi-cation interactions unlikely.

In assessing the docking of HHL and Z-FHL into the N-domain, somewhat different substrate binding interactions were observed (Table 5.5). The pattern of Z-FHL interactions with N-domain shows a very similar pattern to that of the C-domain, with some key differences. The N-domain Ala334, like Ala356 in C-domain, forms a hydrogen bond with the backbone amide of the P2 carboxybenzyl group of Z-FHL (Figure 5.4 A). In the N-domain, Ala334 also interacts with AngI, although this is hydrophobically via the P2 Pro, a trend not observed for C-domain where AngI was not shown to interact with the corresponding Ala356. Also in common for both Z-FHL and AngI are interactions with Tyr501, Lys489, Tyr498 & Gln259 (Tyr523, Lys511, Tyr520 & Gln281 in C-domain respectively). Where they differ is that Z-FHL in the N-domain showed interactions with either Ala332 (backbone amide) and Thr358 (imidazole nitrogen) which varied between poses and which were not observed in C-domain. Whilst interactions of Ala332 are observed for AngI in the N-domain, we do not see

Table 5.5 Comparative molecular docking interactions for Angiotensin I, Z-FHL and HHL with ACE N-domain. Methods, labels and descriptors are identical to those described in the legend for Table 5.4.

		P8	P7	P6	P5	P4	P3	P2	P1	P1'	P2'
N-domain	**Ang I**	**Asp**	**Arg**	**Val**	**Tyr**	**Ile**	**His**	**Pro**	**Phe**	**His**	**Leu**
		Arg90	Thr97	Trp201	Arg500	Leu32	Asp43	Ala334	Glu389	His331	Gln259
			Arg381	Pro385		Val36	Thr496		Tyr501	Ala332	His331
						Trp335	Arg500		Phe490	Glu362	Lys489
										His491	Tyr498
											Phe435
											Phe505
	Z-FHL							**Cbz**	**Phe**	**His**	**Leu**
								Ala334		Tyr501	Gln259
								Arg381		Thr358	Tyr498
										Ala332	Lys489
								Tyr369	*Phe490*	*His491*	*Phe435*
									Thr496	*His331*	*Phe505*
	HHL								**Hipp**	**His**	**Leu**
									Arg500	His331	Gln259
										Glu362	
									Phe490	*Phe435*	*Lys489*
									Arg381	*His491*	*Tyr498*
										Phe505	

Thr358 interactions. Another point of variation is in the orientation of the Cbz benzene group of Z-FHL in the N-domain which allows it to form a Pi-cation bond with R381, an interaction that could not occur in the C-domain given that there is a Glu in that position (E403).

Inspection of HHL interactions in the N-domain revealed the lack of Lys489 & Tyr498 (Lys511 & Tyr520 in C-domain respectively) interactions with the C-terminal carboxylate group of HHL, whereas both Z-FHL and AngI show clear interactions with these residues (table 5.4). Firstly, it must be pointed out that all three residues that could potentially coordinate the C-terminal carboxylate of HHL (Lys489, Tyr 498, Gln259) were less than 3Å away, with the maximum distance for hydrogen bonding to occur needing to be below 3Å. Secondly, for the molecular dynamic simulations for HHL docking into the N-domain, 40 poses (4X that of the other simulations) had to be generated in order to get a single pose that met

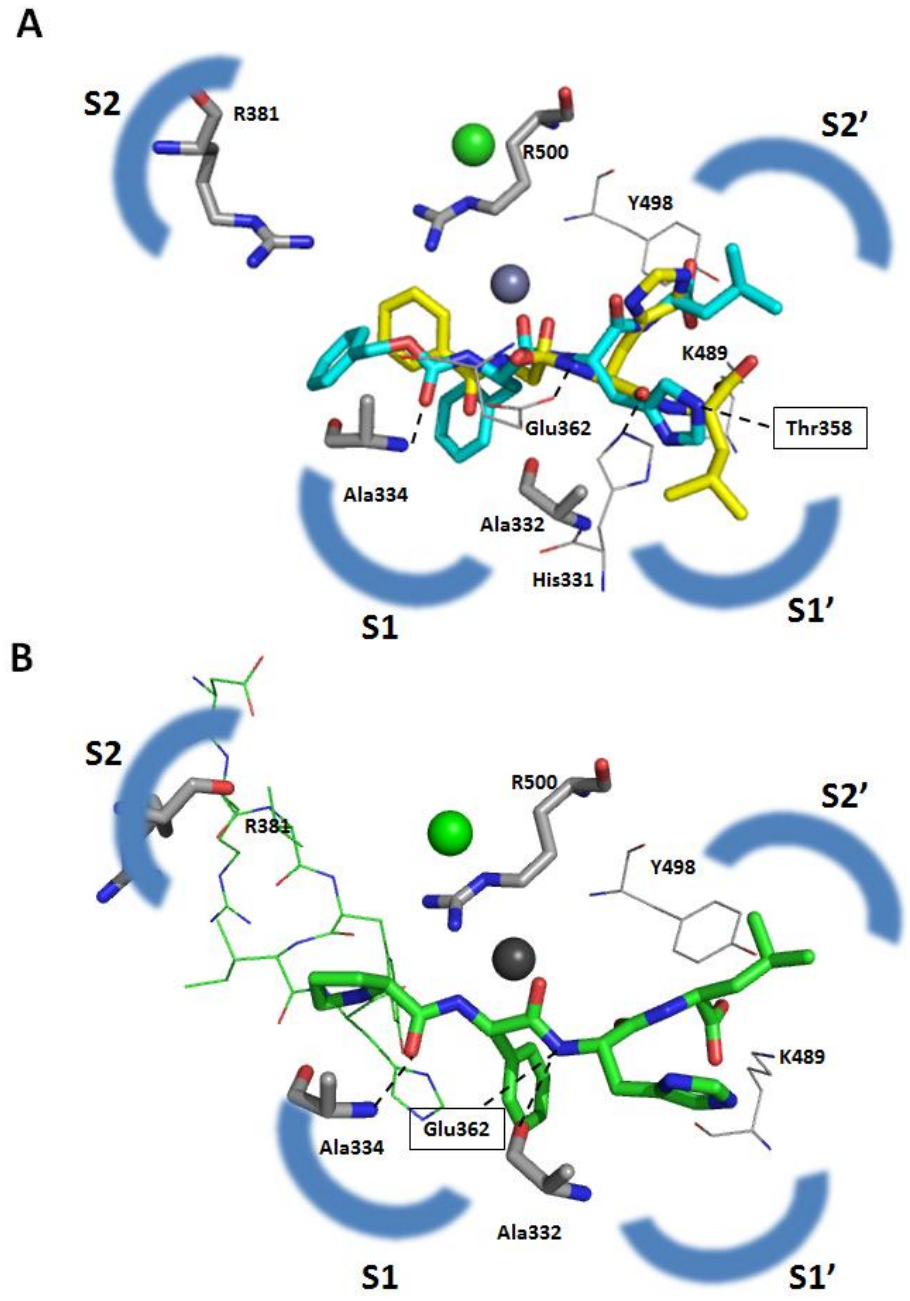

Figure 5.4 Stick representation of HHL, Z-FHL and AngI docked into the N-domain of ACE. A) Best representative overlaid poses for molecular docking of HHL and Z-FHL are shown in yellow and light blue sticks respectively; and B) Lowest energy conformation of AngI (sequence:DRVYIHPFHL) are shown as green sticks (PFHL) and lines (DRVYIH); both in the N-domain of ACE which has key residues displayed as grey sticks and lines of ACE. Active site zinc and chloride 2 pocket chloride ion are represented by the grey and green spheres respectively. Positions of the S2, S1, S1' and S2' sub-sites relative to substrates are indicated by faded blue half-circles. Hydrogen bonds are indicated by dashed black lines. Residues represented by boxes are done so for visualisation purposes. Images were created using PyMOL 0.99 (DeLano Scientific, Palo Alto, CA, U.S.A).

requirements (outlined in 5.2.6). As is evident from Figure 5.3B, there is a significant rotation to the HHL peptide backbone to the C-terminal side of the scissile bond, resulting in the His and Leu swapping pockets. Whilst this is not ideal, the positioning of the gem-diol relative to the active site zinc was almost identical to that of the other docked substrates (HHL & Z-FHL), as well as that of the N-domain-AngI docked structure (not shown). Looking at the composition of the S2' pocket, into which the Leu of HHL should fit, it contains a number of residues that that vary between domains, with the N-domain being generally less hydrophobic. Mutagenic work performed by Kroger et al (2009) where they converted all the variable residues in the tACE S2' pocket to their N-domain counterparts, showed reductions in affinity for RXPA380, which had a bulky hydrophobic tryptophan in this pocket. This would indicate that the S2' pocket is less hospitable for the hydrophobic Leu, and more hospitable to the polar acidic histidine. The S1' pocket shows no major variability in hydrophobicity between domains so it is unlikely that it drives this switch. It could be suggested that the greater number of interactions in the S1 and S2 pockets of the N-domain for Z-FHL and AngI would prevent this rotational swapping of the His and Leu. The only interaction observed in the P1 position for HHL with either domain is a Pi-cation bond between the Hippurate benzene and R500/R522 (N-domain/C-domain), suggesting that this is not a point of major variation between the respective substrate interactions. This further enmeshes the idea that interactions in the P1' and P2' pocket may be key variables in the differing activity towards HHL between domains. The switched orientations in the P1' and P2' residues of HHL could be written off as an artefact of the docking process. However, if one relates it to the considerably lower maximal activity and reduced chloride dependence with HHL observed for the N-domain relative to tACE it may make some sense. Given the lack of interactions of HHL in the S1 and S2 pockets, it can be reasonably suggested that interactions in the S1' and S2' pockets may play an important role in the variable activity observed between domains.

The key summation of this section would be that there is the potential for a degree of rotation around the peptide backbone. This could be mediated by interactions of substrate P' or P residues and represents a potential explanation for the variation in catalytic activity observed not only between domains (for the same substrate) but between substrates for the same domain. This may be a key means by which chloride dependence operates in

affecting the P' and/or P interactions and thereby modulating not only substrate affinity but catalysis as well. These assertions form the basis with which to evaluate the effect that the chloride dependent tACE mutants have on substrate catalysis.

5.3.4 Chloride 1 pocket

The role of the chloride 1 pocket has been suggested to be involved in C-terminal stabilisation of substrates (Guy et al., 2003, Natesh et al., 2003, Sturrock et al., 2004), and initial mutagenic work by Rushworth et al (2008) showed that mutations in this pocket abrogated chloride activation with Angiotensin I. In order to further our understanding of the role of the chloride 1 pocket and how it may affect interactions in the S1' and S2' subpockets, the R186H mutation was evaluated. This mutation involved the coordinating Arg in the C-domain being mutated to a His, the corresponding residue in the N-domain and the only difference in the respective pockets between the two domains. The initial chloride titration evaluation (see 3.3.2.1) showed that R186H produced no significant change to either the overall activity or chloride binding for both HHL and Z-FHL. Thus, chloride activation of AngI was also investigated.

In Figure 5.5A the relative comparison in the overall levels of activity between tACE and R186H for HHL, Z-FHL and AngI is shown. The pattern of overall activity for HHL and Z-FHL correlates fairly well with that reported in 3.3.2.1, differing only in the HHL k_{cat}/K_m at 20mM NaCl for R186H being marginally lower than that for tACE. The AngI k_{cat}/K_m for R186H relative to tACE is 40.38%, which compares extremely favourably with the 42.8% reported by Rushworth et al (2008), suggesting that both mutations are having a similar impact on the chloride 1 pocket. Interestingly these variations in k_{cat}/K_m for AngI are due to the K_m for R186H (0.095mM) being almost 3-fold higher than tACE (0.036mM), with very little change in k_{cat} (7.83.s^{-1} and 7.38.s^{-1} respectively). This is in contrast to Z-FHL where the change is due to an almost 2-fold increase in k_{cat} from tACE (282.0 s^{-1}) to R186H (509.5 s^{-1}), with a concomitant minor increase in K_m (0.120 and 0.150mM respectively). HHL showed a similar pattern to AngI with an increased K_m from tACE to R186H, yet a change in k_{cat} with Z-FHL is observed, suggesting that interactions in the chloride 1 pocket have an appreciable role in substrate catalysis.

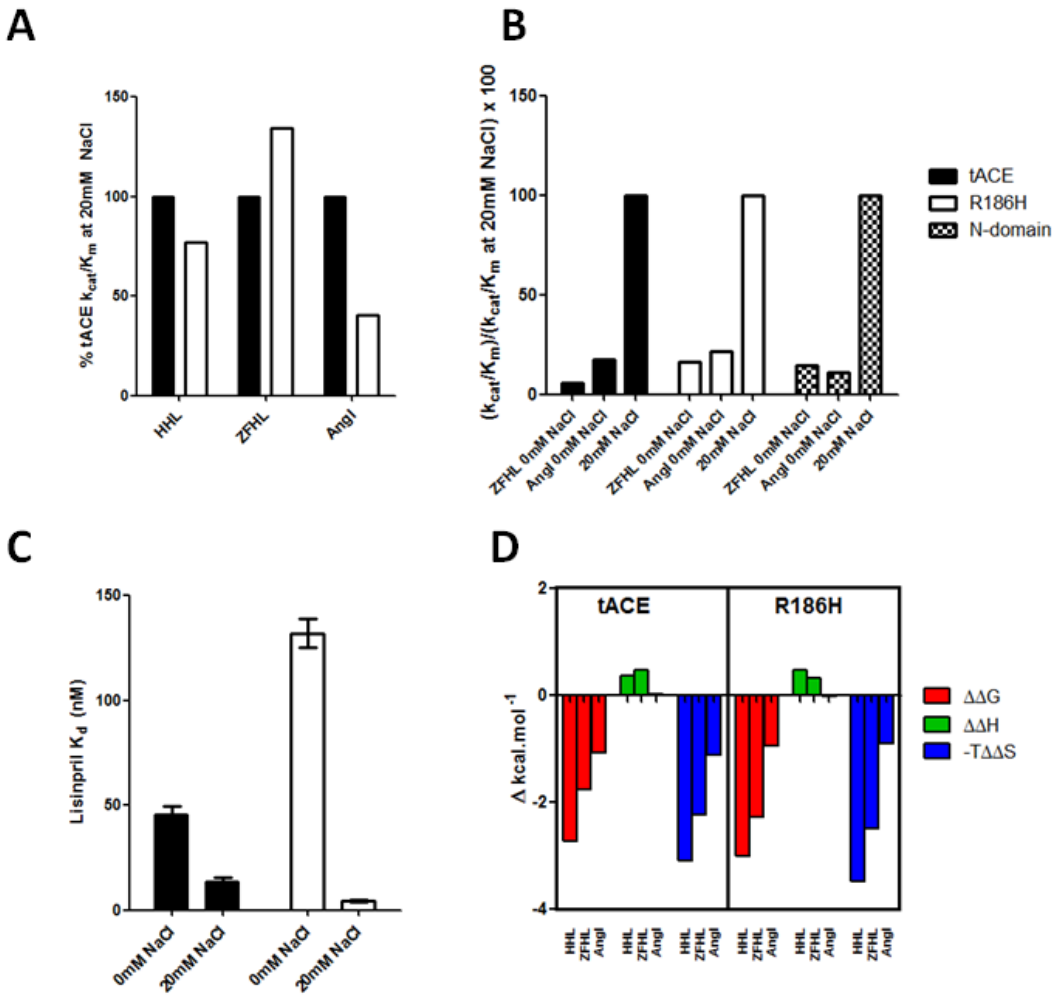

Figure 5.5 Kinetic and thermodynamic comparisons for R186H. A) The k_{cat}/K_m for tACE (black bars) and R186H (white bars) taken as the percentage of the k_{cat}/K_m for tACE. The k_{cat}/K_m values were taken from table 5.1 and are for HHL, Z-FHL and AngI hydrolysis at 20mM NaCl. **B**) The Z-FHL and AngI k_{cat}/K_m means at 0mM NaCl for tACE (black bars), R186H (white bars) and N-domain (chequered) taken as the percentage of their respective k_{cat}/K_m means at 20mM, represented as a single bar of 100% for each construct. **C**) The K_d values (nM) for lisinopril binding to tACE (black bar) and R186H (white bars) at 0mM and 20mM. Values were determined as described in 5.2.4 and error bars indicate the standard deviation calculated by the non-linear regression fitting function provided. **D**) The ΔΔG, ΔΔH and –TΔΔS values for tACE and R186H represent the difference in ΔG, ΔH, -TΔS between 0mM and 20mM NaCl (using values from table 5.2).

However, when the amount of activation between 0 mM and 20 mM NaCl is compared the effect is not the same. R186H maintains a very similar degree of activation for both Z-FHL and AngI relative to tACE and N-domain, with all showing a greater than 5-fold degree of activation (Figure 5.5B). This is contrary to the observed activation for the R186Q mutation,

where Rushworth et al (2008) reported just a 1.2-fold activation when compared to the 8.1-fold activation of the wildtype. A large change in binding affinity with lisinopril for R186H relative to tACE is also observed, with the K_d for R186H (132±6.2 nM) being ~3-fold higher than tACE (45.5±4.24 nM) at 0mM NaCl, as well as ~3-fold lower at 20mM NaCl (4.42±0.5 and 13.5±2.06 respectively) which is displayed in Figure 5.5C. This further indicates that chloride is somehow modulating the conformation via the chloride 1 pocket. This suggests that a Glu in the 186 position of tACE (Rushworth et al., 2008) would be abolishing chloride coordination, given that chloride sensitivity is seemingly abrogated.

Whilst it is tempting to assume that the R186H mutation would also abrogate chloride binding given lack of observed chloride in this pocket for the N-domain crystal structures, it is clear that chloride sensitivity is maintained whilst overall activity is affected. The imidazole ring of histidine carries a positive charge and is potentially capable of coordinating chloride if orientated correctly, thus it is possible that the R186H mutation still binds chloride. When comparing tACE to the R186H mutant, there is some difference (10-50%) in the enthalpic change upon chloride binding (ΔΔH) for the substrates, yet not more than 11% change in the overall ΔH values (Figure 5.5D and Table 5.2), which would suggest that there is no significant variation in interactions allowing for the possibility of chloride still interacting within the pocket. If this were the case, it would suggest that there might be some steric hindrance preventing chloride from accessing the chloride 1 pocket in the N-domain. However, other mutations generated by Rushworth et al (2008), namely W279A and R489Q in tACE, showed similar abrogation of chloride dependence to that of R186Q, indicating that coordination of chloride by R186 is not the only relevant interaction. Tzakos et al (2003) suggested that, in the absence of chloride in the C-domain chloride 1 pocket, any of W279, W485 or W486 may form amino-aromatic interactions with K511, rendering its positive charge unavailable for coordinating the C-terminal carboxylate of the substrate. However, they didn't describe any mechanism whereby binding of chloride, or lack thereof in the N-domain, may moderate this interaction. Further structural inspection was warranted given the additional insights that the mutagenic and kinetic work presented here has provided.

Figure 5.6 shows a schematic representation of the potential interactions observed in the region between the chloride 1 pocket and Lys511 for both tACE and the N-domain. Two

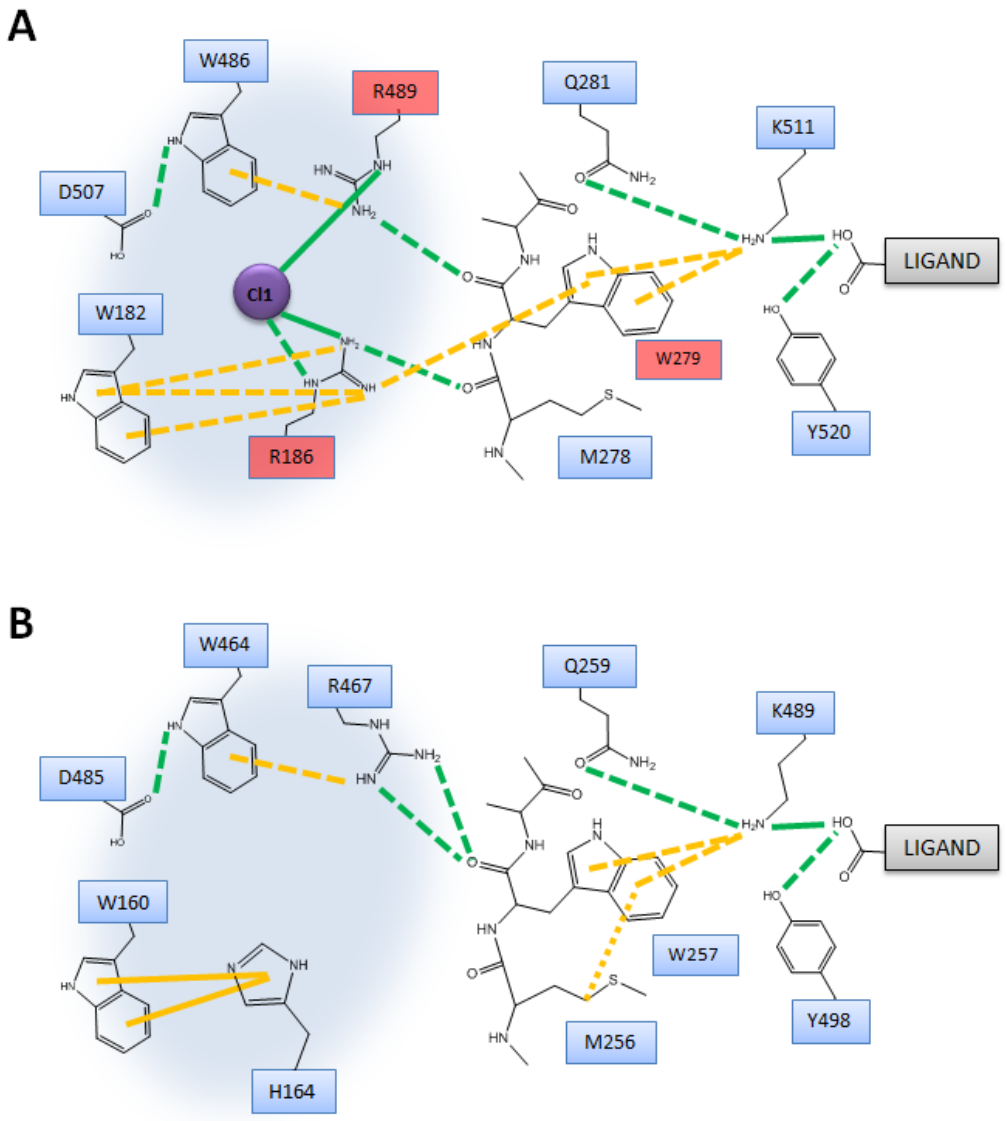

Figure 5.6 Comparative structural interrogation of the Chloride 1 pocket of the C and N-domains of ACE. Interactions in the chloride 1 pocket and region between S2' region were explored for A) C-domain crystal structures tACE-Lisinopril (PDB:1o86) and tACE-RXPA380 (PDB:2OC2), and B) N-domain crystal structures N-domain-Lisinopril (PDB:2C6N) and N-domain389-RXP407 (PDB:3NXQ). Amino acids for both domains are shown in light blue boxes with the 2D side-chain structure attached, except for W279/257 and M278/256 where the protein backbone structure is shown and the boxes are placed next to the 2D sidechain structure. Boxes that are shaded in light red are those that were mutated by Rushworth et al (2008). The grey box labelled ligand represents either a substrate or inhibitor bound in the active site, with the C-terminal carboxylate group structure attached. Chloride ion is represented by the purple sphere. Bonding interactions are: salt bridges (solid green lines), hydrogen bonding (dashed green lines), Pi-cation bonds (dashed yellow lines), Pi-Pi bonds (solid yellow lines) and Pi-Sigma bonds (dotted yellow lines). Light blue haze indicates position of the chloride 1 pocket.

crystal structures were evaluated for each domain; namely, the lisinopril bound crystal structures of both domains as well as those with the domain selective inhibitors RXPA380 (tACE) and RXP407 (N-domain), and found the pattern of interactions to be consistent for each domain. Amino-aromatic (Pi-cation) interactions are formed between W279 and K511 in tACE (Figure 5.6A), a pattern of binding that is also observed in the N-domain between W257 and K489 (Figure 5.6B). Whereas Tzakos et al (2003) suggested that this interaction only forms in the absence of chloride in the C-domain, it is possible that it serves to both stabilize the orientation of K511/489 and that W279/257 acts as its carrier in transmitting effects of interactions in the chloride 1 pocket of both domains. This is based on the idea that the amino group of Lys can form a Pi-cation interaction with W279 and hydrogen bond with the substrate carboxylate simultaneously (Mao et al., 2003). That the W279A mutation (Rushworth et al., 2008) abrogated chloride activation in tACE is indicative of how key this residue is in transmitting effects from the chloride 1 pocket.

Interactions in the chloride 1 pocket were inspected to determine how a structural effect might be transmitted to W279 (W257 in N-domain). As can be seen for both domains in Figure 5.6 A & B, R489 (R467) hydrogen bonds with the primary carbonyl group of W279 (W257). R489 in tACE is also involved in coordinating the chloride ion and hence only one of its amino groups contributes hydrogen bonds to the W279 carbonyl, whereas for the N-domain, due to a lack of chloride coordination, dual hydrogen bonding of the R467 amino groups to the W257 carbonyl can be seen. The R489Q mutation of Rushworth et al (2008) reduced activation with AngI as well, confirming its key role in chloride coordination but also supporting the assertion that it transmits its functional effects via interaction with W279 in tACE. Given that chloride is not observed in the N-domain in this pocket, R467 would not be disrupted and it can be assumed that it's binding of the W257 carbonyl would play a purely stabilizing role. This suggests that, in the absence of chloride in this pocket in tACE, both amino groups of R489 would interact with the W279 carbonyl. Both tACE and the N-domain show W486/464 forming a Pi-cation interaction with R489/467, the relevance of which is most likely that of stabilisation.

The only variable residues between tACE and the N-domain in this pocket are R186 and H164, which occupy the same position within the pocket. As can be seen for tACE in Figure 5.6A, R186 not only coordinates the chloride ion but can possibly interact with a number of

other residues. One of these is W182, where multiple Pi-cation interactions can form between the aromatic rings of the Trp and the amino groups of R186. Interestingly, W160 (W182 in tACE) is the only residue that H164 forms bonds with in the N-domain chloride 1 pocket, which are instead of Pi-Pi interactions between the aromatic rings of both residues. Despite the different types of interactions between R186/H164 and W182/W160, their consistency between domains suggests they may be important in stabilisation. Due to the nature of the arginine sidechain of R186 in tACE, it appears to make more interactions than H164. One of these is the possibility of hydrogen bonding the M278 carbonyl group, which happens to be adjacent to W279 which has been suggested here to be of significance in orientating K511. This represents another direct avenue (apart from R489) through which chloride coordination in the chloride 1 pocket can influence substrate. Of interest in the N-domain is a Pi-sigma interaction between M256 and W257 which was not observed between M278 and W279 in tACE. This may be due to the R186 bonding with the M278 carbonyl and affecting positioning of the M278 side-chain preventing this interaction. Another potential variation between domains is a Pi-cation interaction directly between the chloride coordinating R186 and W279.

Thus far, a number of interactions that vary between the domains have been described; however, this has been with chloride bound in tACE pocket, whereas there is none bound in the N-domain. From these interactions, certain potential mechanisms can be postulated as to what may be occurring in the chloride 1 pocket of tACE in the absence of chloride. Given that the chloride is coordinated by arginines (R489 and R186), which can form multiple electrostatic interactions, there is unlikely to be any major change in their binding pattern apart from the loss of interaction with chloride. R489 would still interact with W486 and the carbonyl of W279, and R186 would still interact with W182, W279 and the carbonyl of M278. What could be suggested is that coordination of the chloride by these two arginines would shift their relative positions and thereby result in subtle shifts propagated via W279 to K511. Where tACE and the N-domain structures are overlaid, subtle differences in the positioning and orientation of all the residues described can be seen, and most markedly in those of R489 and R467 (Figure 5.7). Overall, it is unlikely that there is any significant mechanistic shift in the presence or absence of chloride in tACE, but it would appear that

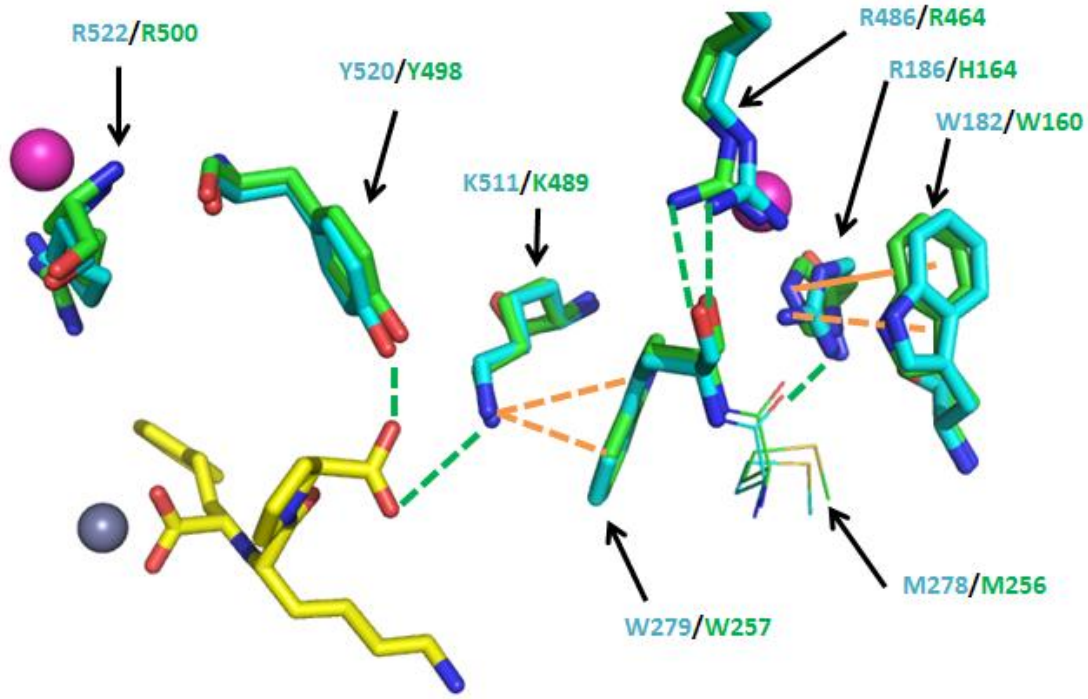

Figure 5.7 Proposed key interactions between chloride 1 pocket and S2' active site pocket. Representative stick overlay of tACE-Lisinopril (PDB:1o86) and N-domain-Lisinopril (PDB:2C6N) showing key interactions indicated in Figure 5.5 in and around the chloride 1 pocket. tACE residues are shown in light blue sticks and N-domain residues are shown in green sticks, with residue labels shown in the same colour for each domain. Lisinopril is shown bound in the active site (yellow sticks), with the active site zinc (grey sphere) and chloride ions (purple spheres) indicated. The position of the chloride 2 pocket is indicated via R522/R500 being adjacent to one of the chloride ions. Bonding interactions are: hydrogen bonding (dashed green lines), Pi-cation bonds (dashed yellow lines), Pi-Pi bonds (solid yellow lines). Images were created using PyMOL 0.99 (DeLano Scientific, Palo Alto, CA, U.S.A).

subtle changes to the positioning of K511 and possibly the conformation of the S2' sub-site are sufficiently large to affect overall ACE activity.

In the absence of a crystal structure of the R186H mutant it is difficult to make any prediction as to what may be occurring and whether chloride would be present in the pocket. In the absence of chloride the histidine of R186H could potentially form Pi-Pi interactions with W182 as H164 does with W160, with R489 showing similar dual coordination of the W279 carbonyl. However, this does not explain the R186Q mutant of Rushworth et al (2008) that abrogated chloride dependence. A glutamate in this position would be capable of coordinating chloride, but not be able to make as many additional

interactions as an arginine, and, given its shorter side-chain length, be unlikely to coordinate the M278 carbonyl. If the glutamate coordinated chloride, its shorter side-chain may force R489 to coordinate the chloride via the more distal ε-amino groups rather than the ε-amino linking the guanidinium group to the side-chain, thus potentially preventing R489 from binding to the W279 carbonyl. This would explain the reduction of activation observed for the R489Q mutation of Rushworth et al (2008), where the differential chloride coordination between the shorter glutamate and R186 might preclude interaction with the W279 carbonyl. The R489Q mutation still showed some activation, and this could be explained via R186 still being able to interact with the M278 carbonyl. In tACE this all serves to indicate that interactions of R489 and R186 with the M278 and W279 carbonyls, respectively, transmit the effects of chloride coordination in the chloride 1 pocket to the substrate coordinating K511. In the N-domain there would be no chloride mediated shift and hence only the R467 to W257 carbonyl interaction would occur.

For the sake of simplicity, the transmitted effects from the chloride 1 pocket to the S2' active site pocket where K511 is situated could be described as resulting in two conformational "states" in tACE (due to chloride binding) and one conformational "state" in the N-domain. In this context, the work done by Liu et al (2001) can be considered, where they evaluated a number of tetrapeptides that differed in their P1' and P2' residue identities. The P2 and P1 residues were an acetylated Ala and a Phe and were consistent across all peptides. What was very clear is that the nature of the prime positioned dipeptide structure greatly affected chloride dependence. The one peptide that shared the same P1' and P2' identity as HHL, Z-FHL and AngI, AcAFHL, displayed a $K_{d,app}$ of 30mM which suggests that it behaves far more like HHL ($K_{d,app}$ = 47mM) than either Z-FHL (1.8mM; table 3.1) or AngI (5.4mM; Wei et al., 1991b). However, tetrapeptides containing a P2'-Arg greatly increased chloride binding affinity (e.g. AcAFHR $K_{d,app}$ = 5mM), and even these were influenced up to 2-4 fold by varying the P1' residues (e.g. AcAFAR $K_{d,app}$ = 1.6mM). These P2'-Arg tetrapeptides also had lower K_m values and had higher activity at 0mM NaCl relative to that at maximal chloride concentration. Conversely, tetrapeptides with P2'-Gly substitutions (AcAFAG & AcAFGG) showed increased $K_{d,app}$ and K_m values relative to AcAFHL. This data shows that interactions in the S1' and S2' pockets are not only important for binding specificity (K_m) but they modulate chloride binding ($K_{d,app}$). It stands to reason that

these interactions would affect the positioning of the C-terminal carboxylate of the substrate. Thus, dependent on the composition of P1' and P2' residues, the C-terminal carboxylate may be positioned either favourably or unfavourably relative to the K511. Taking into consideration that tACE would have two different conformational states (due to chloride binding in the chloride 1 pocket) and the N-domain only one, this may be a way in which chloride further modulates activity in a substrate dependent manner in the C-domain.

5.3.5 Chloride 2 pocket

Whilst the nature of the prime binding dipeptide and interactions within the chloride 1 pocket may help explain the varying levels of overall activity between domains, it does not adequately describe how these interactions affect binding of chloride in the chloride 2 pocket, which has been shown to be the mechanistically important (Liu et al., 2001; section 3.3.2.3). Evidence from the molecular docking simulations (Section 5.2.6) suggested that the orientation of the peptide backbone varied considerably between substrates. Excluding the influence of S1 and S2 interactions for now, this could be determined by the combination of P' dipeptide interactions and the relative orientation of the K511 moderated by the chloride 1 pocket, both affecting how the C-terminal carboxylate could be positioned. The C-terminal carboxylate coordination would determine (at least partially) what orientation the substrate backbone settled in and hence what interactions could be formed. In this regards, there was shown to be variability in the positioning of the scissile bond relative to Y523 in tACE and Y501 in the N-domain, both of which are suggested to be of importance in stabilizing the tetrahedral substrate intermediate. This all suggests that the positioning of this tyrosine relative to the peptide backbone varies between substrates and affects the catalytic efficiency. Thus, the role of Y523/Y501 relative to the chloride 2 pocket was investigated to elucidate the mechanism of action upon chloride ion coordination by R522/R500.

5.3.5.1 Pi-cation interactions between R522/500 and Y523/501

Upon inspection of the various ACE crystal structures, Pi-cation interactions between R522 and Y523 (R500 and Y501 in N-domain) were observed, which were remarkably consistent for both domains irrespective of the inhibitor bound in the active site (Figure 5.8). Liu et al

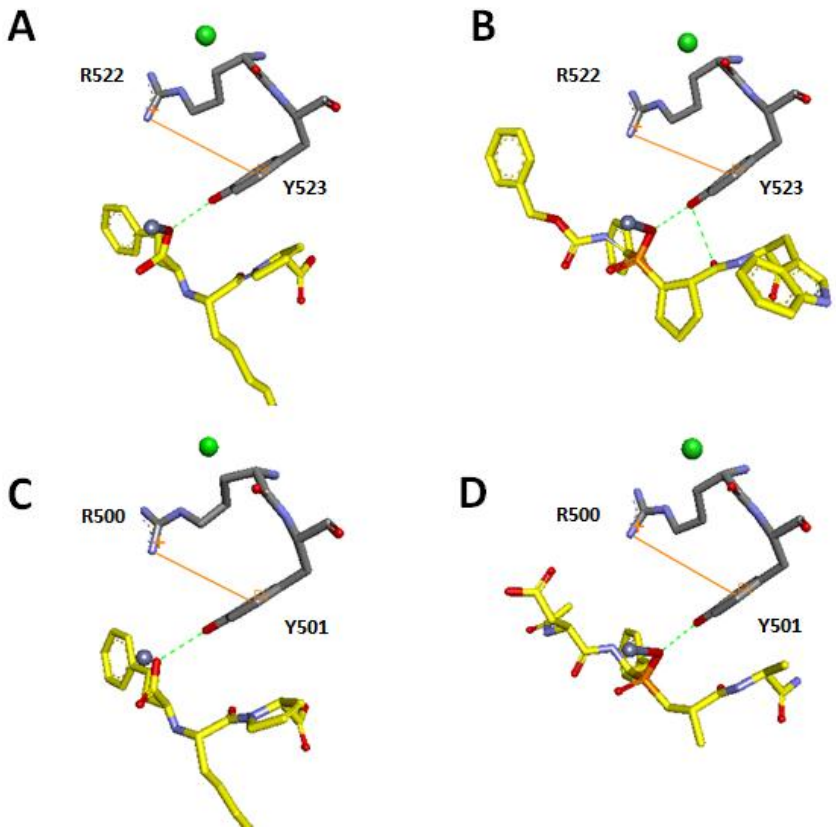

Figure 5.8 Pi-Cation Interactions between R522/500 and Y523/501. Stick representation showing Pi-Cation bonding between R522 and Y523 in tACE (A & B) and R500 and Y501 in the N-domain (C & D) with lisinopril (A & C), RXPA380 (B) and RXP407 (D) inhibitors bound in the active site. Residues are shown as grey sticks, chloride and zinc as green and grey spheres respectively, with inhibitors bound in the active site as yellow sticks. Crystal structures shown are A) tACE-Lisinopril (PDB:1O86), B) tACE-RXPA380 (PDB:2OC2), C) N-domain-Lisinopril (PDB:2C6N) and D) N-domain389-RXP407 (PDB:3NXQ). Images were created using Accelrys Discovery Studio© 3.1 Visualizer.

(1993) describe a similar arrangement found in Glutathione S-Transferase (GST). They found that a Thr on-face hydrogen bonding with the Pi-cloud of a Tyr affected catalysis by "contributing a second-sphere interaction which influences the hydrogen bond between the hydroxyl group of tyrosine 6 and the sulphur of bound glutathione anion (GS^-)". This interaction with the Pi-electron cloud of a Tyr contributed measurably (-4 kJ/mol) to the ability of the hydroxyl group of tyrosine 6 to stabilize the thiolate anion. They also suggest that this effect could translate to Pi-cation interactions, which is what is observed between R522 and Y523 (R500 and Y501 in N-domain). If this is the case, it would likely enhance the ability of Y523/Y501 to stabilize the transition-state intermediate in ACE hydrolysis. This

would also explain the critical nature of chloride coordination by R522 (R500), as this would stabilize the positioning of Y523 (Y501).

5.3.5.2 A structural role for D465/443

The question then is whether this Arg-Tyr interaction occurs in the absence of chloride or is induced by chloride binding, given that all crystal structures of both ACE domains show chloride present in the chloride 2 pocket. One point of evaluation is the potential for the formation of a salt bridge between the R522 (R500) and D465 (D443) as proposed by Tzakos et al (2003). In evaluating the crystal structures of tACE and the N-domain complexed with lisinopril, extensive hydrogen bonding between the D465 (D443) carboxylate and primary amides of both Y520 (Y498) and I521 (I499) is seen (see Figure 5.9A). Y520, I521, R522, Y523 (Y498, I499, R500, Y501 in N-domain) are the first four residues on the C-terminal end of the α23 helix (Y520-A541), with P519 representing the end of the helix and the beginning of a highly variable loop. Tzakos et al (2003) indicate there would have to be some structural rearrangement of this variable loop for a salt bridge to form between R522/500 and D465/443. Figure 5.9B shows the positioning of this variable loop situated between R522/500 and D465/443, indicating that there would have to be some movement of the P519 kink for a salt bridge to form.

However, this region of α23 helix is within subdomain II of both domains, a region predicted to have little major structural variation relative to the proposed hinge region which is part of subdomain I (Watermeyer et al., 2006). This would suggest that there is insufficient structural change in this region to facilitate a salt bridge between D465/443 and R522/500 and would suggest that D465/D443 plays role in stabilization of the end of the variable loop and helix α23. Figure 5.9A indicates the relative positioning of helices α23 and α20, which indicates that the C-terminal end of α23 is the main point of contact with α20, supporting a structural role for D465/443. Further to this, in tACE D465 hydrogen bonds with R468 which interacts strongly with the variable loop via hydrogen bonds with backbone primary carbonyl groups of H513 and V518. In N-domain the D443 doesn't interact with the corresponding R446, but R446 does hydrogen bond with T496 which corresponds to V518 in tACE. Both V518, which lines the S1 active site subpocket, and His513, which interacts with Y523 (Sturrock et al., 2004), are both potentially important

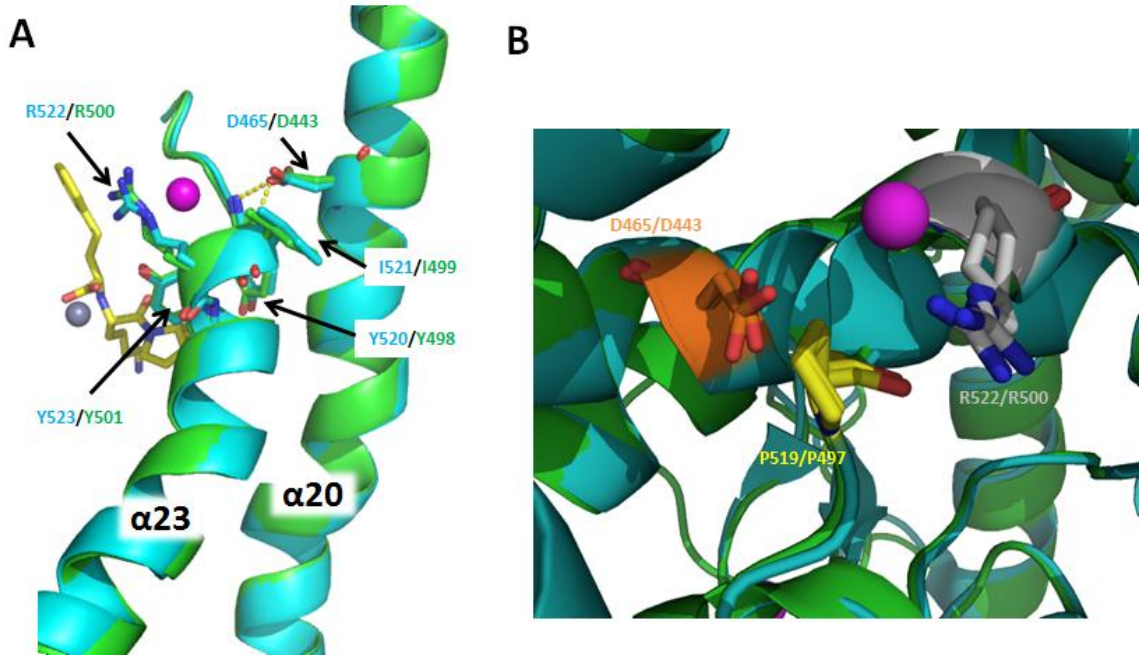

Figure 5.9 Interaction of D465/D443 with the Chloride 2 pocket. A) Representative stick overlay of tACE-Lisinopril (PDB:1o86) and N-domain-Lisinopril (PDB:2C6N) showing positioning of D465/D443 relative to R522/R500 in the chloride 2 pocket. tACE residues are shown in light blue sticks and N-domain residues are shown in green sticks, with residue labels shown in the same colour for each domain. Alpha helices α15 and α17 are labelled. Lisinopril is shown bound in the active site (yellow sticks), with the active site zinc (grey sphere) and chloride ions (purple spheres) indicated. Hydrogen bonding is indicated by dashed yellow lines. Images were created using PyMOL 0.99 (DeLano Scientific, Palo Alto, CA, U.S.A). **B)** Representative stick overlay of tACE-Lisinopril (PDB:1o86) and N-domain-Lisinopril (PDB:2C6N) showing a close-up of the region between R522 (R500) and D465 (D443). D465 (D443), P519 (P497) and R522 (R500) are shown as orange, yellow and grey sticks respectively. Chloride coordinated by R522 is shown as a purple sphere. Images were created using PyMOL 0.99 (DeLano Scientific, Palo Alto, CA, U.S.A).

residues which reside on this variable loop. Suffice to say, given that D465/443 is one of very few contacts between helices α23 and α20, its role is most likely in stabilisation of the C-terminal end of helix α23.

Supporting this assertion is the chloride titration data from Chapter 3 determined for HHL and Z-FHL using the D465T tACE mutant (Table 3.1). The mutation was generated in order that the charge, hence its ability to form a salt bridge, was abolished yet it maintained a similar size and reduced capacity for hydrogen bonding with the single hydroxyl group of threonine. The anticipated result for D465T, if D465 forms a salt bridge with R522, would have been higher $\%SA_{max}$ values compared to tACE as R522 would presumably have allowed

Y523 to swing into the active site. Instead, both the SA_{max} and the $\%SA_{max}$ (activity at 0mM NaCl as percentage of maximal activity) for D465T with both HHL and Z-FHL were lower than that of tACE. An increase in $K_{d,app}$ for Z-FHL and a decrease for HHL with D465Twas also observed which cannot be explained using the salt bridge hypothesis. This also does not correlate with the chloride channel hypothesis where E403 in tACE is supposed to "gate" access, which would presumably mean a fairly constant $K_{d,app}$ for chloride binding. That D465/443 is on the opposite side of the chloride 2 pocket to the proposed channel area precludes any direct interaction. These results make more sense in the context of the suggestion presented here that D465/443 stabilizes the C-terminal end of helix α23 and the variable loop via hydrogen bonding with the primary amides of Y520/498 and I521/499. A Thr in this position would be capable of fewer potential hydrogen bonds, presumably resulting in greater structural movement which could affect the C-terminal carboxylate coordinating Y520/498 (lowering of SA_{max}). Its effect on $\%SA_{max}$ and $K_{d,app}$ would presumably be due to structural destabilization, which suggests that structural rotation or movement around the C-terminal end of helix α23 which contains R522/500 and Y523/501 moderates not only activity, but chloride affinity.

5.3.5.3 R522 mutants and interactions with Y523 and chloride.

The previous section established that there is a low likelihood that D465/443 forms a salt bridge with R522/500 in the absence of chloride in the chloride 2 pocket. This would suggest that the R522/500 sidechain would occupy roughly the same position it does when chloride is not present, obviously though with a fair degree of rotational freedom given the lack of chloride coordination. This begs the question of whether the R522/500 to Y523/501 Pi-cation interaction described earlier is present in the absence of chloride or whether chloride binding induces this interaction.

To probe this interaction, the effect of replacing R522 with a Lys and Gln on the enzyme kinetics constants was investigated. In order to evaluate the data, however, it must be considered how the change in residue identity would

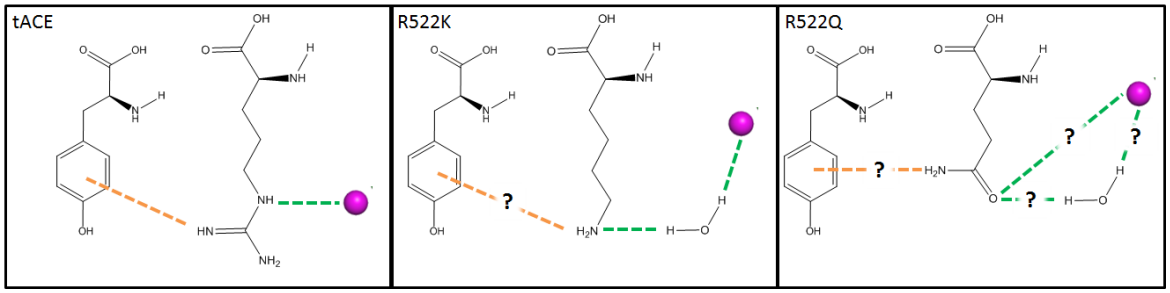

Figure 5.10 Potential interactions with Y523 and chloride for R522K and R522Q mutants. Shown are two dimensional representations of amino acid residues Y523 and either Arg, Lys or Gln in tACE, R522K and R522Q respectively. Chlorides are indicated by purple spheres. Bonding interactions are: hydrogen bonding (dashed green lines), Pi-cation bonds (dashed orange lines). Question marks indicate bonding is unconfirmed.

affect the type of interactions. The potential interactions between Y523, chloride and either the Arg, Lys or Gln residues which are in the 522 position of tACE, R522K and R522Q respectively are depicted in the schematic shown in Figure 5.10. As has been described for tACE, R522 forms a Pi-cation interaction with Y523 (NH1) (5.3.5.1) and coordinates the chloride ion (NE) (Natesh et al., 2003). The change to a Lys in R522K means that there is only one amino group available to form hydrogen bonds. In unpublished work, collaborators (Dr Ravi K. Acharya, University of Bath, UK) have determined the R522K crystal structure and have found that chloride is present in the active site and is being coordinated to the Lys amino group via a water molecule, which is presumably part of its hydration shell. Not having the structure available at time of writing does restrict evaluation of whether the Pi-cation interaction is occurring. The change to Gln in R522Q presents an alternate scenario where the terminal amino group might form Pi-cation bonds with Y523. This can be suggested as the shorter chain length would actually put the amino group closer to the optimal angle (90° to the plane of the Tyr ring structure). Pi-cation interactions are at their strongest when the cation is perpendicular (90°) to the plane of aromatic ring atoms, with variations in this geometry still exhibiting a significant interaction which weakens as the angle approaches 0 degrees (Marshall et al., 2009). Looking back at Figure 5.7, the Pi-cation interaction for R522-Y523 is actually offset from 90°, indicating that a shorter Gln side-chain might result in a more favourable reaction with the amino group closer to 90°. The carbonyl group of Gln is also capable of hydrogen bonding, but whether it directly coordinates

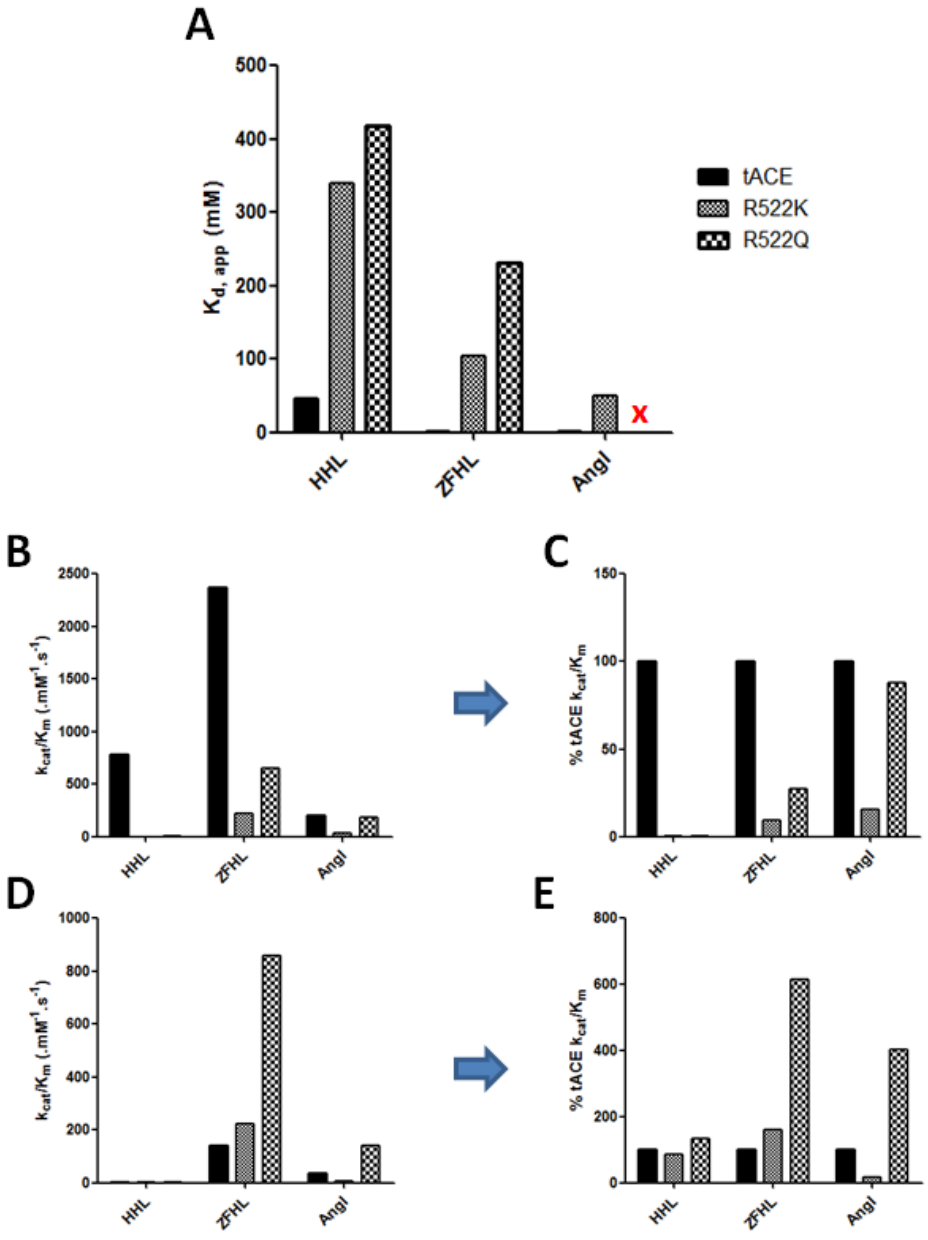

Figure 5.11 Trends in chloride binding and activity for R522Q and R522K. Graphical representation of chloride binding and kinetic values obtained for tACE (black bar), R522K (dotted bars) and R522Q (chequered bars) with HHL, Z-FHL and AngI as substrates. **A)** The $K_{d,app}$ values (mM) for chloride binding. Values for HHL and Z-FHL were taken from Table 3.1, and those for AngI were estimated from the report of Liu et al (2001) (the red "x" indicates no available data) **B)** The maximal k_{cat}/K_m values taken from table 5.1 for HHL, Z-FHL and AngI hydrolysis at 20mM NaCl (except for HHL with tACE which was at 300mM NaCl). C) The k_{cat}/K_m values from B (indicated by blue arrow) taken as the percentage of the k_{cat}/K_m for tACE for each substrate. D) The minimal k_{cat}/K_m values taken from table 5.1 for HHL, Z-FHL and AngI hydrolysis at 0mM NaCl. E) The k_{cat}/K_m values from D (indicated by blue arrow) taken as the percentage of the k_{cat}/K_m for tACE for each substrate.

chloride or does so via the hydration shell like Lys is not readily apparent.

Given these potential interactions, the kinetic data obtained for R522K and R522Q mutants relative to tACE can be assessed. Comparing the $K_{d,app}$ values for HHL and Z-FHL (see 3.3.2.3) with those reported by Liu et al (2001) for AngI (see Figure 5.11A), the largest increases over tACE are seen for HHL with R522K (7-fold) and R522Q (9-fold). These increased $K_{d,app}$ values for HHL correlate with the lack of activation seen when comparing the k_{cat}/K_m values obtained at highest concentration of NaCl and 0mM NaCl (Figure 5.11 B & C). In light of the evidence that R522K interacts with the chloride hydration shell, it can be suggested that, given the similar $K_{d,app}$ values, R522Q might conceivably indirectly interact with chloride in a similar manner via the Gln carbonyl group (see Figure 5.10).

A similar trend is seen with the $K_{d,app}$ values for Z-FHL, though not to the same degree as HHL. A chloride titration protocol was not established for AngI in this study, hence the $K_{d,app}$ values Liu et al (2001) reported for tACE and the R522K mutant have been displayed (they stated that the R522Q $K_{d,app}$ could not be detected). Where Liu et al (2001) saw no change in k_{cat}/K_m for R522Q, an increase in k_{cat}/K_m between 0 and 20mM NaCl (141.75 and 179.5 $.mM^{-1}.s^{-1}$ respectively; table 5.1) is seen indicating that some activation is occurring and that the difference is too small for an accurate detection of $K_{d,app}$. It can be suggested that the $K_{d,app}$ trend for AngI is the same as that for HHL and Z-FHL and estimate the $K_{d,app}$ to be ~100mM. Irrespective of this assertion, it can be seen that R522K and R522Q are reducing the affinity of chloride. What is interesting is that R522K and R522Q are following the same $K_{d,app}$ trend as tACE (AngI<Z-FHL<HHL), though proportionally higher than tACE for each. This would indicate that substrate interactions are somehow moderating access or binding of chloride. Considering that chloride is present in the pocket of R522K, it can be surmised that the effect is on the coordination of chloride and not on access of chloride to the pocket.

Another interaction to consider is whether the Lys or Gln in R522K and R522Q respectively are forming Pi-cation interactions with Y523 (see Figure 5.10). Looking at the maximal k_{cat}/K_m values for HHL, Z-FHL and AngI (Figure 5.11A) confirmation of the varying levels of activity for the three substrates with tACE (Z-FHL>HHL>AngI) can be seen. As would be expected with disruption of a key active site residue, the k_{cat}/K_m values for R522K and R522Q are lower than tACE, with R522K lower than R522Q. To better gauge the relative effects,

the k_{cat}/K_m values for R522K and R522Q are represented as a percentage of the k_{cat}/K_m values for tACE (Figure 5.11B). Here the role that the nature of the substrate plays is clearly evident, where both R522K and R522Q see increases in activity with larger substrates that interact more tightly with the S1 and S2 active site pockets. Whilst R522K shows only a marginal increase over HHL (AngI:15.6% >Z-FHL:9.3%>HHL:0.1%) relative to tACE, there is a marked increase for R522Q (AngI:87.7% >Z-FHL:27.5%>HHL:0.36%) to the point where R522Q activity is almost as high as tACE with AngI. This would indicate at the very least that the bonding pattern is different between R522K and R522Q. A further trend is in regard to the contributions of K_m and k_{cat} to k_{cat}/K_m for R522Q and R522K. For HHL the mechanistic lack of activation is evidence by there being very little variation in K_m but marked differences in the k_{cat} , where values are very similar at 0mM chloride and only tACE shows an increase at 20mM (127.0 s^{-1} vs 4.8 s^{-1} and 2.08 s^{-1} for R522Q and R522K respectively; table 5.1). Interestingly, R522Q shows a 5-fold tighter K_m for Z-FHL at 0mM NaCl than tACE (0.110mM and 0.580mM respectively), yet this trend is reversed at 20mM with R522Q being ~2-fold higher than tACE (0.20mM and 0.12mM respectively). These data show that K_m for R522Q with Z-FHL is higher at 20mM than 0mM, a reversal of the general trend for tACE with all substrates. R522K hydrolysis of Z-FHL also shows a K_m at 20mM (0.880mM) being higher than at 0mM (0.570mM), which shows that this is not a spurious result with R522Q. Both R522Q and R522K show less than 2-fold increases in k_{cat} from 0mM to 20mM NaCl, versus the >3-fold increase observed for tACE. Thus the large decrease in activation for R522Q and R522K with Z-FHL is influenced by the increased K_m as well as the reduced k_{cat} associated with the presence of chloride, in contrast to HHL which is predominantly k_{cat} influenced. Interestingly, a similar lack of variance is seen in K_m values for R522Q and R522K with AngI (though they are 2-fold higher than tACE) and greater variation in k_{cat} which is more similar to the HHL profile. The increases in K_m observed for all substrates with R522K and, to a lesser degree, R522Q indicates that coordination by chloride in this pocket affects substrate affinity as well as catalysis, suggesting some structural movement around helix α23. What is most noticeable between R522K and R522Q is the greater k_{cat} values for R522Q that increase with substrate length and are even higher than tACE for AngI. Taking the $K_{d,app}$ data already described for R522K and R522Q into account where it was ascertained that both residues were interacting with chloride via the hydration shell, it is most likely their ability to form Pi-cation interactions with Y523 that is the point of variation. Thus it can be suggested

that the R522Q Gln is forming Pi-cation interactions with Y523 resulting in more efficient catalysis, and that the greater interactions of Z-FHL and AngI in the S1 and S2 pockets are compensating for the lack of direct chloride coordination, presumably via some structural effect. This would also suggest that the R522K Lys does not form such an interaction as readily, where the structural interactions of Z-FHL and AngI don't sufficiently stabilize Y523 on its own.

The next question would be whether chloride coordination induces R522 to form Pi-cation interactions with Y523, or whether this interaction is present already and chloride coordination merely stabilizes them. This is addressed by referring to the k_{cat}/K_m values for HHL, Z-FHL and AngI at 0mM NaCl (Figure 5.11C) which are also represented as percentages of tACE activity for each substrate (Figure 5.11D). The k_{cat}/K_m values for HHL with all constructs are all extremely low and comparable to each other, yet for Z-FHL and AngI considerable increases in activity are seen for R522Q over both tACE and R522K. Considering the hypothesis that the R522Q Gln doesn't directly coordinate chloride yet Pi-bonds with Y523, and that Z-FHL and AngI interactions in S1/S2 pockets affects their position, then this would indicate that a similar mechanism occurs in the absence of chloride. That tACE activity at 0mM NaCl is substantially lower than R522Q suggests that the Arg does not Pi-bond with Y523 in the absence of chloride, which would indicate that chloride coordination is necessary for this to occur. There were no substantial changes in activity for R522K at 0mM NaCl for any of the substrates indicating that the Lys doesn't Pi-bond with Y523.

The change in thermodynamic profiles upon chloride addition for R522Q and R522K (Figure 5.12), were evaluated. For R522Q a reduced endothermic change in enthalpy is seen for HHL (0.165kcal/mol) and ZHFL (0.105 kcal/mol) relative to tACE (0.36 and 0.48 kcal/mol respectively), which would indicate the loss of an interaction. Presumably this would be loss of the salt bridge/hydrogen bonding interaction with chloride, essentially showing reduced variation with chloride present. That the ΔΔH values don't exceed the minimum hydrogen bonding energy (1kcal/mol) might be due to differing hydration effects associated with the different residue counteracting the enthalpic change.

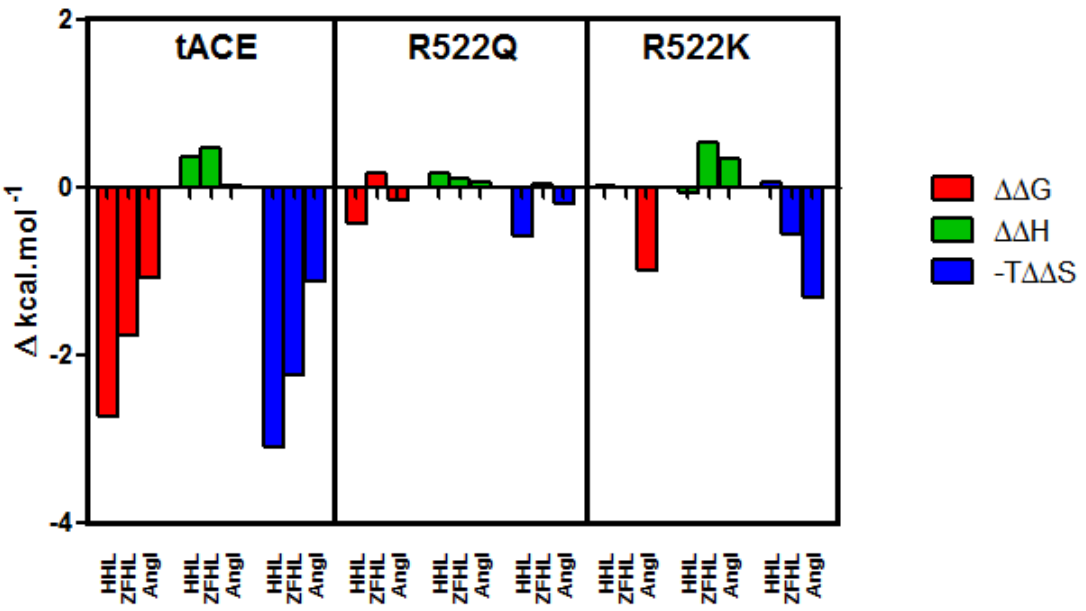

Figure 5.12 Change in thermodynamic parameters for R522Q and R522K. The ΔΔG, ΔΔH and –TΔΔS values for tACE, R522Q and R522K with HHL, Z-FHL and AngI are shown and represent the difference in ΔG, ΔH, -TΔS between 0mM and 20mM NaCl (using values from table 5.2).

For R522K there is a different pattern with the enthalpy changes, with HHL (-0.07kcal/mol) showing an exothermic shift relative to tACE (0.36kcal/mol), AngI (0.35kcal/mol) showing an endothermic shift relative to tACE (0.024kcal/mol), and Z-FHL relatively unchanged. As with R522Q, an exothermic shift would suggest a bond breaking for HHL which would be expected with the lack of direct chloride coordination. The lack of variation in enthalpy with Z-FHL for R522K is interesting seeing that there is no ΔΔG and the k_{cat}/K_m is lower than tACE and R522Q at both 0 and 20mM NaCl. Given the assertions that Lys neither coordinates chloride nor Pi-cation bonds with Y523, the interactions of Z-FHL in the S1 and S2 pockets may be compensating via minor structural shifts. The endothermic shift in enthalpy observed with AngI for R522K is accompanied by a relatively large shift in free energy (-0.989kcal/mol) similar in magnitude to tACE (-1.087kcal/mol), which actually results in a larger –TΔΔS due to the more endothermic enthalpy shift. As can be seen from table 5.1, there is a 5-fold increase in k_{cat}/K_m from 0mM to 20mM resulting in the observed ΔΔG, although these values are considerably lower than tACE. The molecular docking of AngI into tACE (table 5.4) indicates that the P3 His of substrate protrudes into the chloride 2 pocket and interacts with the chloride ion itself. This opens the possibility that the AngI P3 His may

coordinate chloride via the Lys of R522K, which would account for the chloride mediated ΔΔG as well as the lower level of activity overall with AngI.

In summary, chloride coordination is necessary to correctly orientate R522 to Pi-bond with Y523, thereby promoting catalysis of substrate. Substrate interactions within the S1/S2 pockets affect positioning of this complex, presumably via structural effects. Furthermore, this provides a rationale whereby substrate binding modulates chloride affinity and hence its own catalysis, a feature that is explored further in the following sections.

5.3.6 Chloride channel

Thus far, evidence has been provided for a critical interaction between R522 and Y523 that is induced by chloride binding, however it has also been observed that chloride binding was affected by larger substrates which indicated a role for the S1, S2 and other non-prime pockets. The E403R mutation was generated to investigate a proposed chloride channel, where the E403 that was postulated by Tzakos et al (2003) to act as an ionic gate mediating access of chloride to the chloride 2 pocket. The Glu was converted to an Arg, corresponding to R381 in the same position in the N-domain. It was shown in section 3.3.2.2 that the E403R mutation significantly reduced $K_{d,app}$ for chloride binding with HHL and Z-FHL relative to tACE, and that this effect was reversible in the N-domain when R381 was converted to a Glu. It was also suggested that interactions of substrate in the S2 sub-pocket where E403 resides would somehow disrupt its gating function, evidenced by the large discrepancy in $K_{d,app}$ seen between HHL and Z-FHL for tACE which was largely abolished with E403R.

However, not only are $K_{d,app}$ different with different substrates, which would suggest chloride coordination is affected, but changes in overall activity and degrees of activation are also seen which begged further inquiry into whether E403 merely acts as a gate for entry of chloride. Figure 5.13 shows the E403R k_{cat}/K_m relative to tACE (using values from table 5.1) at maximal activity (A & B) and at 0mM NaCl (C &D) for HHL, Z-FHL and AngI. The k_{cat}/K_m values for E403R with all substrates at maximal activity are generally lower relative to tACE, whereas at 0mM NaCl they are all higher. This indicates that E403 affects activity as well as potentially mediating access of chloride to the chloride 2 pocket. It was proposed by Tzakos et al (2003) that E403 forms a potent salt bridge with R522 in the absence of

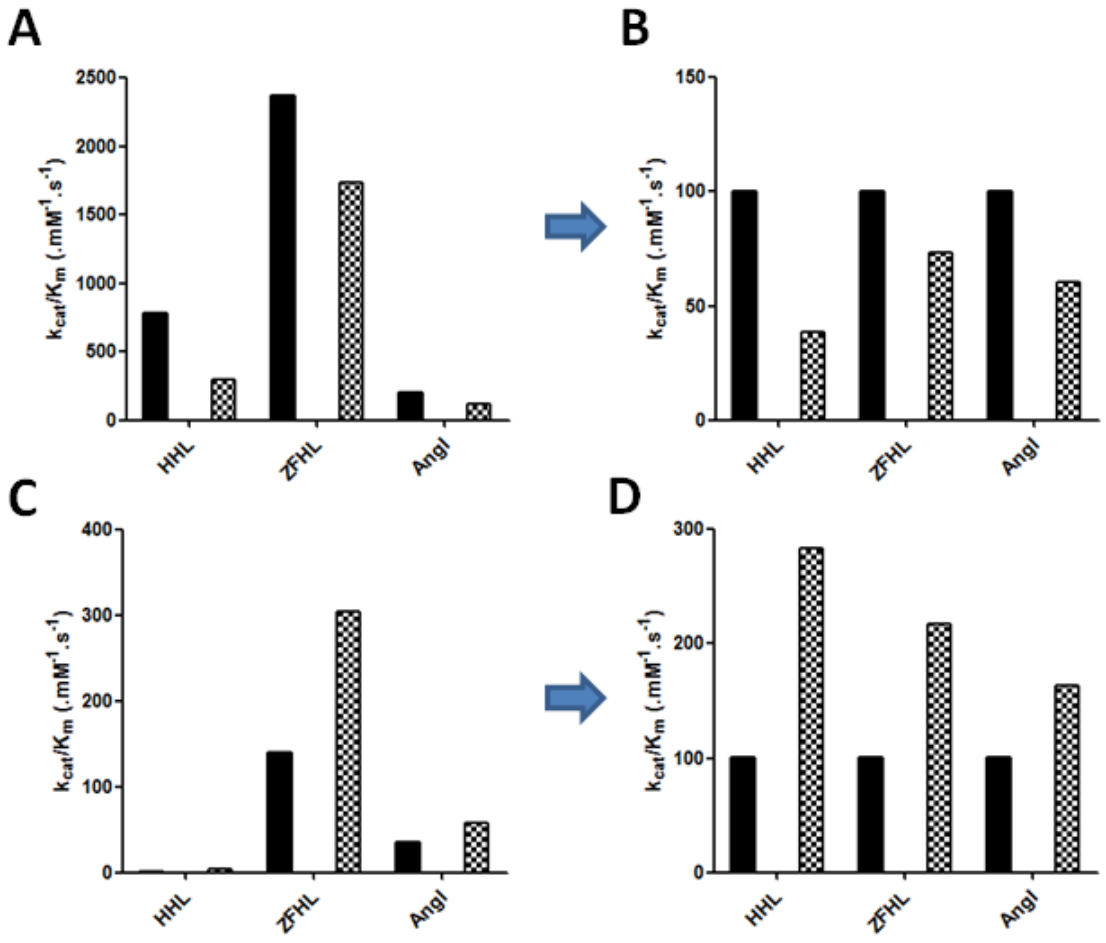

Figure 5.13 Minimal and maximal k_{cat}/K_m for E403R relative to tACE. Graphical representation of k_{cat}/K_m kinetic values obtained for tACE (black bar) and E403R (chequered bars) with HHL, Z-FHL and AngI as substrates. A) The maximal k_{cat}/K_m values taken from table 5.1 for HHL, Z-FHL and AngI hydrolysis at 20mM NaCl (except for HHL with tACE which was at 300mM NaCl). B) The k_{cat}/K_m values from A (indicated by blue arrow) taken as the percentage of the k_{cat}/K_m for tACE for each substrate. C) The minimal k_{cat}/K_m values taken from table 5.1 for HHL, Z-FHL and AngI hydrolysis at 0mM NaCl. D) The k_{cat}/K_m values from C (indicated by blue arrow) taken as the percentage of the k_{cat}/K_m for tACE for each substrate.

chloride, where chloride binding would disrupt this interaction, coordinate R522 and allow Y523 to swing into the active site. Furthermore, K118 residue was proposed to enhance the R522-E403 salt bridge by also forming a salt bridge with E403. Mutation of the K118 corresponding residues, K154 in rabbit testicular ACE (Sen et al., 1993), and K694 of rabbit lung ACE (Chen et al., 1990), drastically reduced chloride sensitivity, thus highlighting its critical role. Looking at Figure 5.14, K118 is 5.13Å away from E403 in the lisinopril bound

structure (PDB:1O86), whereas in the unbound structure (PDB:2IUL, not shown) these form a salt bridge (2.13Å). Of interest, Tzakos et al (2003) claim that these mutations reduce a potent interaction of E403 with R522, suggesting that the E403-R522 salt bridge would still be present. This does not correlate with the reduced chloride sensitivity observed by Sen et al (1993) and Chen et al (1990) for mutation of this residue. Looking at the potential for an R522-E403 salt bridge in the absence of chloride, the distances of 7.9Å and 9.2Å are noted for the lisinopril-bound (PDB:1O86) and open structures (PDB:2UIL). This would require a conformational change resulting in the protein backbone moving at least 5Å in order for a salt bridge to form. This would have to be done either via movement of the 3_{10} helix H5 down towards α17 to bring E403 closer to R522 or from the movement of helix α23 up in order for R522 to move closer to E403 (Figure 5.14). Helix α23 is already in close proximity to helix α17 and significant potential for this movement is not seen as it would affect the position of E411, which is critical to active site zinc coordination, as well as Y520 and Y523 relative to the active site. The H5 movement down also seems unlikely as this would require a shift of helix α15 (not shown) which contains the HEMGH zinc binding motif, also critical to active site zinc coordination. Obviously these conformational changes can occur at the same time and would thus have to move less to bring both residues closer, however, all of these helices mentioned fall within the subdomain II of tACE, which has been shown to have a high degree of structural rigidity and showing little movement relative to neighbouring residues (Watermeyer et al., 2006). Of interest in their work, they highlighted regions containing residues 400-409 (containing E403 and P407) and 98-125 (containing K118) as part of a proposed hinge-bending region mediating access of substrate to the active site (see Figure 5.15). Region 98-125 was suggested to form part of the lid structure and showed a higher temperature factor (thus more flexible) than the 400-409 region that was suggested to be fairly rigid. This also points to the unlikelihood of large structural movements that would be necessary for E403 and R522 to form a salt bridge. Alternatively, the interaction between K118 and E403 could result in stabilization of the flexible 400-409 region in tACE in such a way as to alter the structure of the chloride 2 pocket. As can be seen in Figure 5.14, P407 is on the same flexible loop as E403 and forms Pi-Sigma interactions with Y224 which coordinates chloride within the pocket. Thus movement of this loop would subtly affect the ability of Y224 to coordinate chloride, a potential explanation for the wide range of $K_{d,app}$ values observed. The K118-E403 salt bridge would

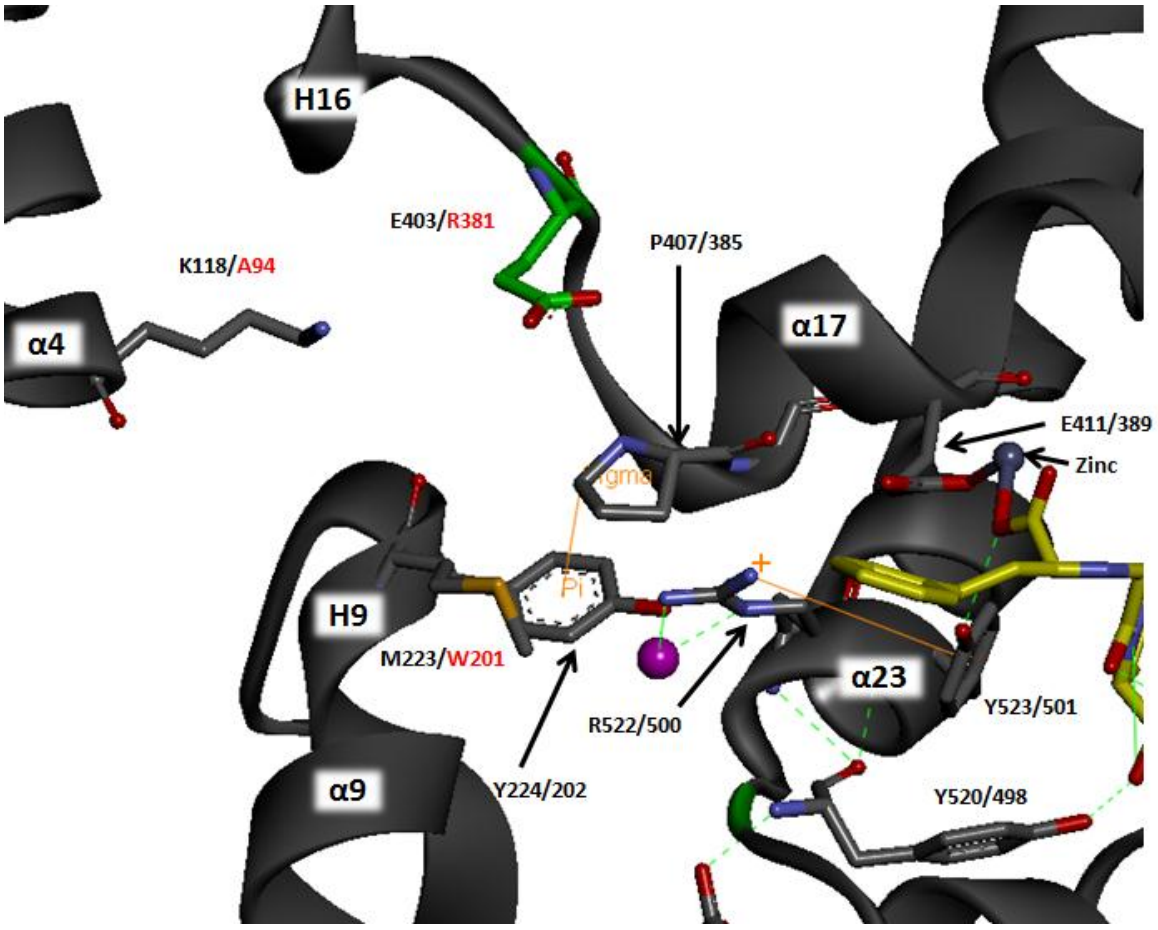

Figure 5.14 Structural features, key residues and interactions in region of chloride 2 pocket and chloride channel. Representative depiction of the region between R522 and D465 in tACE-Lisinopril (PDB:1o86). All residues are shown as sticks, with the colouring indicating atom identity (carbon = grey, nitrogen=blue, oxygen=red), except for E403 residue is in green. Residues are labelled with tACE identity first and corresponding N-domain identity after, which those residues that differ in the N-domain being shown in red. Cartoon depiction of protein backbone is shown, which includes α-helices 4, 9, 17 and 23 and 3_{10} helices H9 and H16. Chloride coordinated by R522 is shown as a purple sphere, zinc is shown as a grey sphere bonded to E411 and the lisinopril (yellow) in the active site. Bonding interactions are: hydrogen bonding (dashed green lines), Pi-cation and Pi-Sigma bonds (solid orange lines). Images were created using Accelrys Discovery Studio© 3.1 Visualizer.

likely occur in the presence or absence of chloride, and excludes the need for chloride disrupting what is a very strong interaction. Whilst it is not observed in the lisinopril-bound structure of tACE (PDB:1O86), a compensatory interaction of K118 with the backbone carbonyl of Ala400 is seen, and the interaction is observed in both the unbound (PDB:2UIL) and RZPA380-bound (PDB:2OC2) tACE structures.

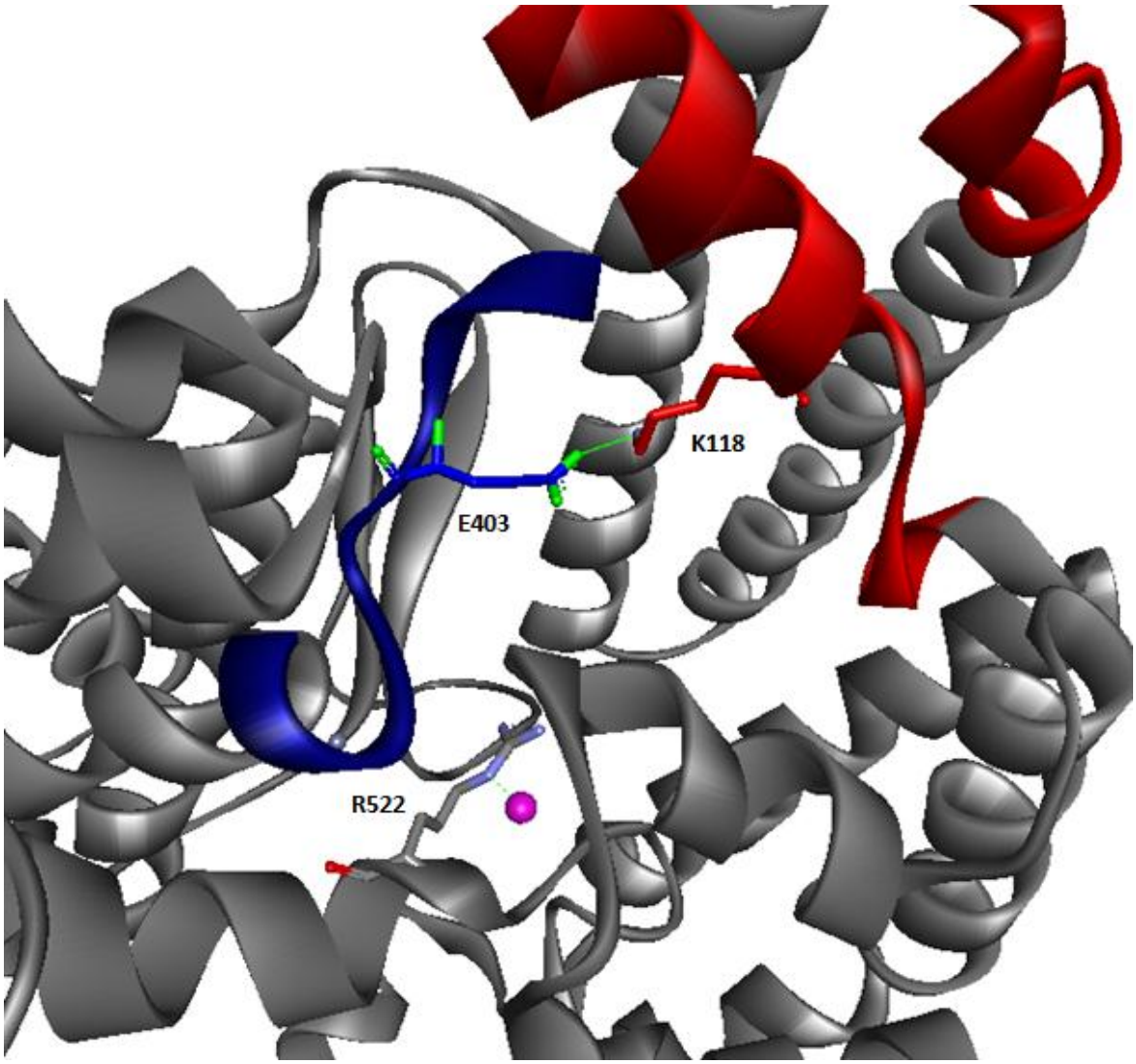

Figure 5.15 Stabilizing interaction between E403 and K118 in tACE. Representative cartoon depiction of tACE-Lisinopril (PDB:1o86) with the high temperature, low sequence conservation region encompassing residues 98-125 (red) and low temperature, high sequence conservation region encompassing 400-409 (blue) highlighted (adapted from Watermeyer et al., 2006). The E403 (blue) and K118 (red) residues are shown as sticks, with chloride (purple sphere) coordinated by R522 (grey stick) also shown to indicate relative position of chloride 2 pocket. A salt bridge interaction between E403 and K118 is shown as a solid green line. Images were created using Accelrys Discovery Studio© 3.1 Visualizer.

Relating this to observed data from section 3.3.2.2, both the E403R mutant and the N-domain would not have this stabilizing interaction, hence the chloride pocket would be in a conformation that more readily coordinates chloride and lower $K_{d,app}$ values are observed for these constructs. The R381E mutant resulted in weaker $K_{d,app}$ values in the N-domain, however the polar charged Glu in position 381 won't interact with the shorter non-polar

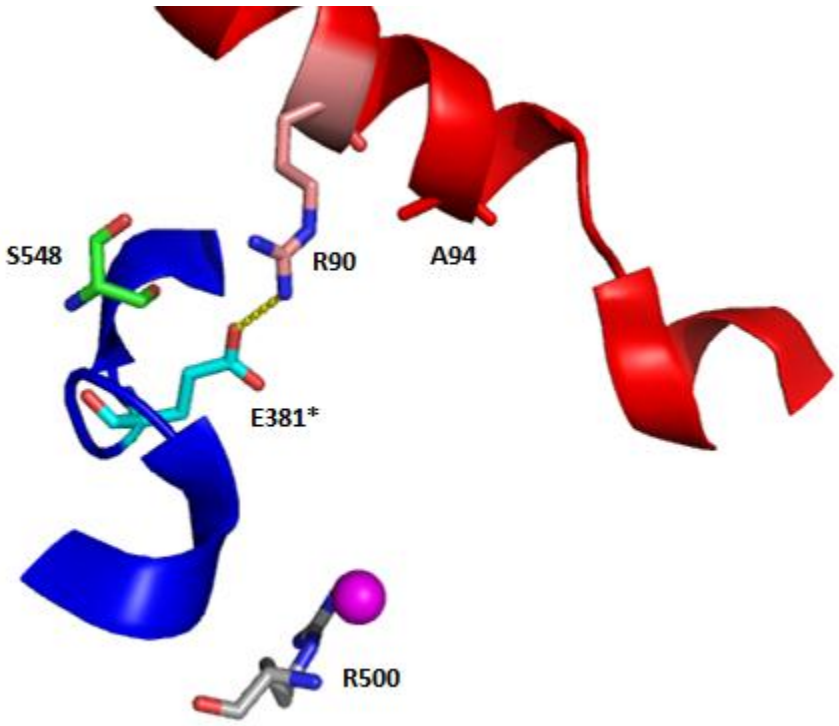

Figure 5.16 Proposed stabilizing interaction between E381 and R90 in the N-domain_R381E mutant. Representative cartoon depiction in N-domain-Lisinopril structure(PDB:2C6N) with the tACE equivalent regions corresponding to residues 98-125 (red) and 400-409 (blue) highlighted in the same manner. Relevant residues are shown as sticks. The R381 residue was mutated (*) using PyMOL to a Glu (E) which is shown in light blue. The residue corresponding to K118 in tACE is A94 (red) and the residue proposed to interact with E381is R90 (light pink). S548 is also indicated in green. Chloride (purple sphere) coordinated by R522 (grey stick) is shown to indicate relative position of chloride 2 pocket. A salt bridge interaction between E381* and R90 is shown as a dashed yellow line. Images were created using PyMOL 0.99 (DeLano Scientific, Palo Alto, CA, U.S.A).

hydrophobic A94, which is 8.9Å distant anyway (Figure 5.16). Instead, it can be suggested that E381 instead interacts with R90 (2.97Å) which is 4 residues away from A94. This would not be possible in tACE as the residue corresponding to S548 is F570, which has a large, bulky hydrophobic side-chain projecting directly between the 381 position and R90 (not shown).

Further evidence of the stabilizing role of the E403-K118 interaction is seen in the change in thermodynamic parameters for E403R relative to tACE (Figure 5.17). The ΔΔG values are reduced for all substrates relative to tACE, which is due to the observed increase in k_{cat}/K_m at 0mM NaCl and decrease at 20mM NaCl (Figure 5.13). That the pattern and magnitude of

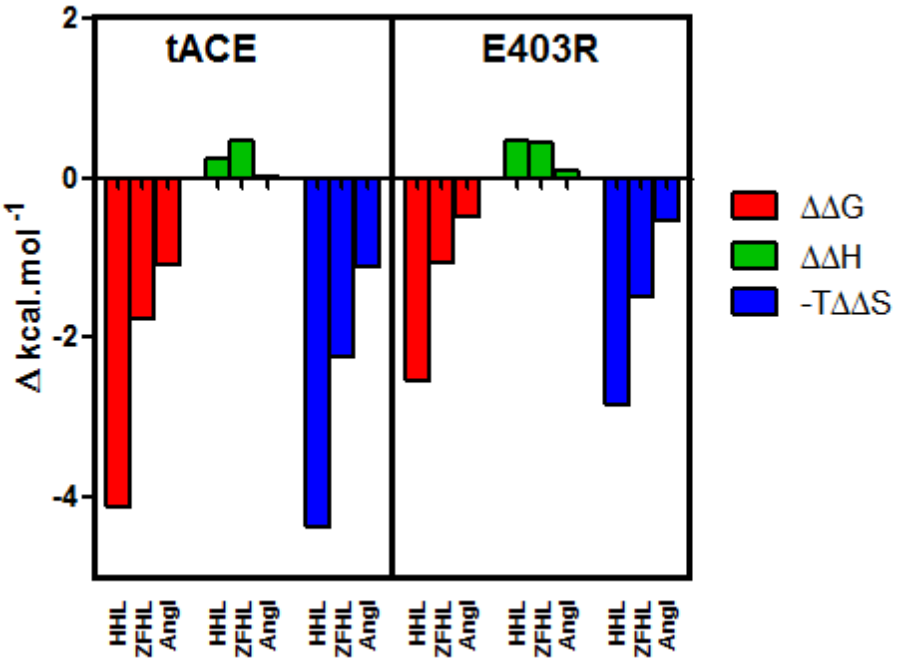

Figure 5.17 Change in thermodynamic parameters for E403R. The ΔΔG, ΔΔH and –TΔΔS values for tACE and E403R are shown and represent the difference in ΔG, ΔH, -TΔS between 0mM and 20mM NaCl (0mM and 300mM for HHL with tACE). Determined using values from table 5.2.

the enthalpies (ΔΔH) for the substrates correlates well with tACE indicates that there should be no major structural rearrangement proposed in the Tzakos et al (2003) model, which would presumably result in large structural shifts and hence enthalpy due to bond rearrangements. The lack of significant enthalpy changes do not discount minor structural differences, which are evidenced by less favourable changes in entropy (-TΔΔS).

These minor structural effects would help explain the K_m and k_{cat} data for E403R relative to tACE (table 5.1). E403R shows increased k_{cat} values at maximal activity for Z-FHL and AngI (929.34 s^{-1} and 9.08 s^{-1}) relative to tACE (282.00 s^{-1} and 7.38 s^{-1}), which is countered by higher K_m values in the presence of chloride for E403R (0.530mM and 0.061mM) over tACE (0.120mM and 0.036mM). These result in lower maximal k_{cat}/K_m values with both substrates for E403R, but serve to confirm that some structural variation is present. The HHL data are not included in this assessment as it doesn't appear to interact strongly within the S2 region (Table 5.4) and it is likely that it's affinity is predominantly affected by S1'/S2' interactions.

In summary this section, for the first time, describes a stabilising role for E403 in tACE via its interaction with K118 within the hinge-bending region, which is contrary to the ion gated channel hypothesis of Tzakos et al (2003). This serves to reduce the affinity of chloride within the chloride 2 pocket of tACE (C-domain) as well as affect the structural architecture of the S2 pocket. Interactions of substrate within this pocket, exemplified by Z-FHL and to a greater extent AngI, appear to disrupt the E403-K118 interaction and allow for improved chloride binding. The lack of this stabilizing interaction in the N-domain (R381 does not bond with A94) means that the chloride 2 pocket would have a higher affinity for chloride, even in the absence of any substrate interaction within the S2 pocket. The size of the substrate, and more importantly how far it extends into the non-prime sub-sites, has been shown to be important where substrate interactions in the S2 pocket modulate chloride affinity directly in the C-domain of ACE. These interactions are likely to be propagated via structural perturbations around the active site rather than any specific interaction, which is consistent with the high degree of variability in ACE substrate identity.

5.3.7 Substrate mediated chloride dependence

Thus far, key interactions and mechanisms within the chloride 1 pocket and chloride 2 pocket have been described and related to substrate composition using structural, mutagenic and kinetic data. In condensing these results, a rationale to account for the relative contributions of prime and non-prime substrate interactions to chloride dependence is suggested below.

Figure 5.18 shows the C-terminal end of the α23 helix along with the variable loop up to part of the 3_{10} H6 helix, but more importantly highlights the number of key residues contained within a 14 residue stretch. As has already been proposed, R522/500 interacts with Y523/501 to position it for its role in stabilizing the enzyme-substrate transition-state intermediate (5.3.5.3). Importantly, the affinity of chloride coordinating R522/500 is moderated by structural constraint via E403-K118 salt bridge in tACE, which is a point of major difference to the N-domain (5.3.6). Two residues down from R522/R500 is Y520/498 which has been suggested to stabilize the C-terminal carboxylate along with K511/489, which, as can be seen in Figure 5.18, is situated on the 3_{10} H6 helix after the variable loop.

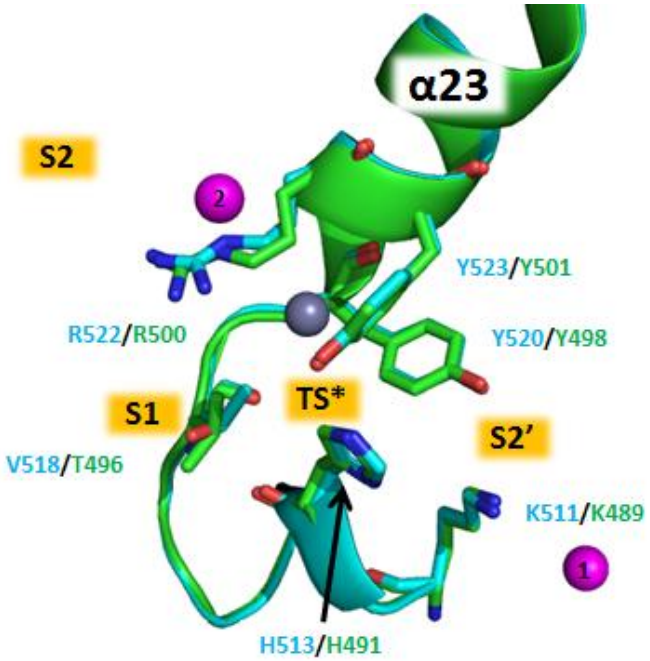

Figure 5.18 Relative orientation and proximity of critical residues to the active site of tACE and N-domain. Representative overlay of tACE-Lisinopril (PDB:1o86) and N-domain-Lisinopril (PDB:2C6N) showing the amino acid region spanning from Y523/501, which is positioned on the C-terminal end of helix α23 , via variable loop region to K511/489 which is on 3_{10} helix H6. tACE residues are shown in light blue sticks and N-domain residues are shown in green sticks, with residue labels shown in the same colour for each domain. The labelled orange squares indicate the proximity to various regions in the active site; Y520/501 and K511/489 are in S2' pocket, V518/T496 lines the S1 pocket, S2 shows position of S2 pocket, and TS* indicates that residues Y523/501 and H513/491 are proposed to be involved with stabilizing the transition-state intermediate. The active site zinc (grey sphere) and numbered chloride ions (purple spheres) indicated. Images were created using PyMOL 0.99 (DeLano Scientific, Palo Alto, CA, U.S.A).

Also on this variable loop are H513/491, which has also been proposed to stabilize the transition-state (Fernandez et al., 2001), and the S1 sub-site positioned V518/T496, for which the V518T mutant was generated and, whilst not found to significantly affect chloride binding did produce an increase in activity (3.3.2). Thus, it is readily apparent that minor structural movement of this area can have a large effect on catalysis and chloride binding, yet more importantly that this can be heavily influenced by substrate interactions. In order to understand the different contributions of various substrates and their role in modulating chloride binding and hence catalysis, a framework was developed that describes different binding modes based on the substrates that have been discussed. Figure 5.19 shows a

schematic depiction of four different binding modes for tACE based on composition of substrate discussed in this chapter.

Scheme A represents the binding mode for the tripeptide HHL, which show a highly chloride dependent profile exemplified by a high $K_{d,app}$. The P1' and P2' residue interactions within their respective pockets have an unfavourable influence on chloride affinity, presumably via interaction or non-interaction with Y523. These assertions are based on the S' tetrapeptides described by Liu et al (2001) and discussed in 5.3.4, some of which are represented by Scheme B which have a similar binding mode. HHL shares its P' composition with AcAFHL, both of which induce poor chloride binding, thus we could extend the same rationale to the other tetrapeptides in Scheme B. The suggestion of a non-interaction of the C-terminal carboxylate with Y523 is based on AcAFAG and AcAFGG where the P' groups would be unlikely to interact with the sub-pockets probably resulting in increased flexibility of the carboxylate. The P' interactions of the remaining tetrapeptides would then result in poor orientation of the carboxylate as well, although it is still highly likely that K511 coordinates the C-terminal carboxylate and that lack of Y523 binding is the only difference. A further implication of the interactions in the S' pockets by peptides in Scheme A and B is the orientation of the peptide backbone around the scissile bond. As was highlighted in 5.3.3, there was some variation in the pattern of interactions either side of the scissile bond for HHL, Z-FHL and AngI, likely a result of some rotation around the backbone, and some difference in the orientation of the P1 residue between HHL and Z-FHL (Figure 5.3). Thus the P' interactions would alter the binding pattern and potentially affect the positioning of the P1 residues, both of which could potentially account for the generally higher K_m values observed for Scheme A and B peptides. Given that V518 is situated within the P1 pocket and is part of the variable loop the orientation of the P1 group may be of significance.

Like Scheme B, the Scheme C tetrapeptides have the same P1 and P2 composition, but show much lower $K_{d,app}$ for chloride binding and generally lower K_m values than Scheme B peptides due entirely to their P' composition. This positive interaction with the S' pockets would presumably orientate the C-terminal carboxylate for optimal interaction with Y523, which would affect positioning of helix α23 and hence chloride affinity within the chloride 2 pocket. As mentioned for Schemes A & B, this might also differentially orientate the peptide

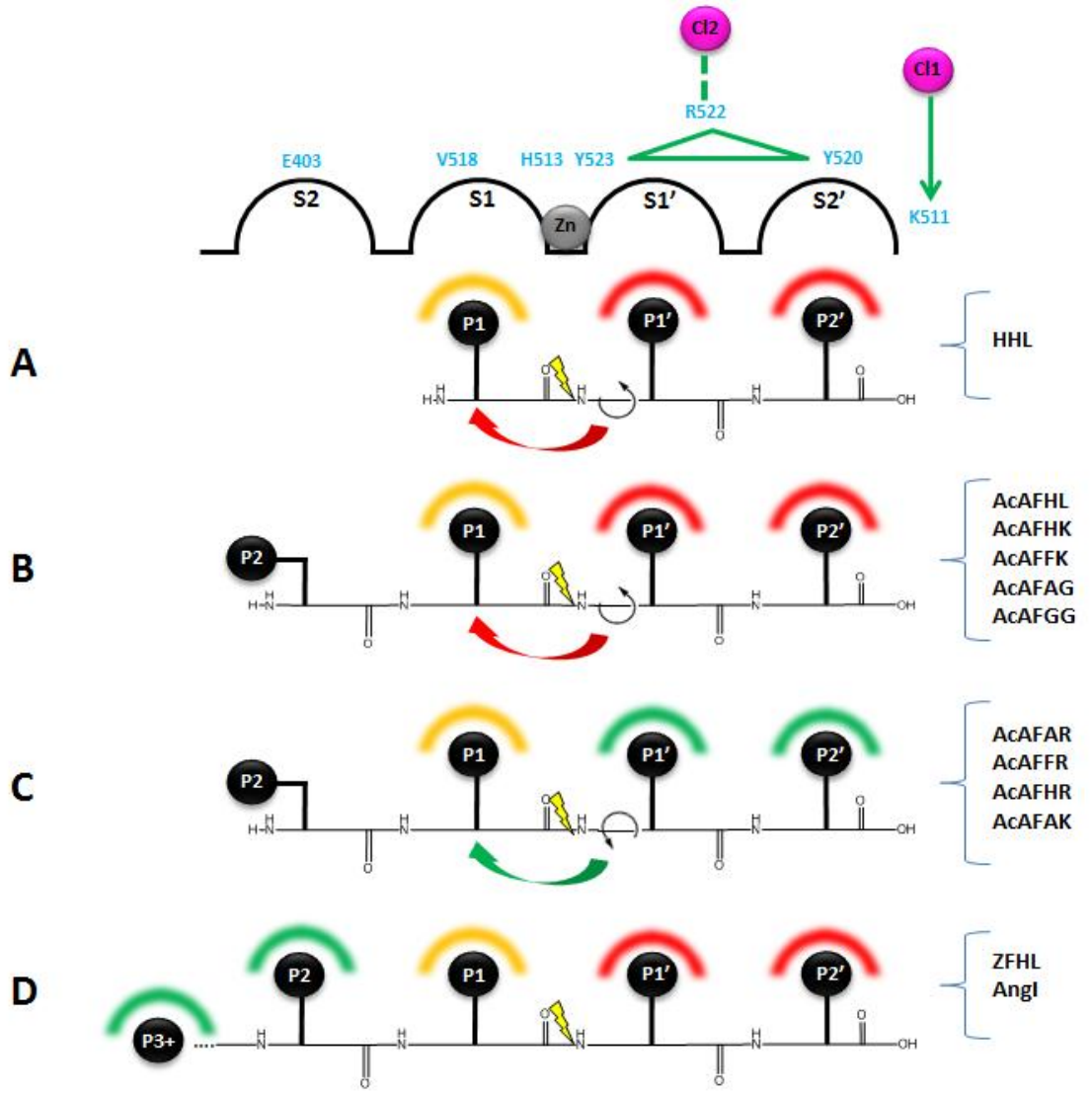

Figure 5.19 Schematic representation of various substrate binding modes in tACE. Binding of substrate to the active site is shown using an adapted Schechter and Berger diagram (Schechter and Berger, 1967), with active site sub pockets (S2, S1, S1' and S2') shown as connect half-spheres and peptides shown with labelled black spheres (P2, P1, P1' and P2', with P3+ indicating residues P3-P10 for AngI). Position of tACE residues highlighted in Figure 5.18 shown (light blue) are shown above relevant sub-sites, with helix α23 containing R522, Y523 and Y520 shown as green triangle between them. Chloride ions (numbered purple spheres) are shown, with chloride coordination to R522 indicated by dashed green line and influence of chloride on K511 by a green arrow. Active site zinc (grey sphere) indicates position of catalytic mechanism between S1 and S1', with yellow lightning showing position of scissile bond for each peptide. Interactions that increase chloride affinity (green shaded semi-circles), those that do not increase chloride affinity (red shaded semi-circles) and interactions that may affect chloride affinity (orange shaded semi-circles) are indicated above each peptide residue. Rotation around the peptide backbone axis (circular arrows) and the potential effect of this rotation (red or green arrows that correspond to influence from P' residues which is either red or green) are shown. The peptides that are characterised by either Scheme A, B, C or D are shown on the right hand side.

backbone resulting in a different pattern of interaction and potentially positioning the P1 residue differently. The tetrapeptides in Schemes B & C have an Acetyl-alanine in the P2 position, however it is unlikely to interact significantly with the S2 pocket due to the smaller size of the alanine (where the larger P2 Cbz group of Z-FHL only just extends into the large S2 pocket) and the similarity in profiles of Scheme B to A which doesn't have a P2 group (HHL).

The peptides in Scheme D are distinguished by the fact that they interact with the S2 pocket (Z-FHL) and S3 and beyond (AngI). What is key to notice here is that they both share the same His-Leu P' composition as HHL (Scheme A) and AcAFHL (Scheme B), which have been shown not to affect chloride binding. Given that both Z-FHL and AngI have much tighter $K_{d,app}$ for chloride binding shows that they moderate chloride affinity via interaction with the S2 pocket. As has been discussed in 5.3.6, this would be mediated by disruption of the E403-K118 salt bridge either directly or via structural interaction. How this affects orientation of the P1 groups is unclear as the peptide is constrained via interactions from S' and S2 sides. Docking simulations for Z-FHL and AngI (5.3.3) do indicate that the backbone rotation might differ which would go some way to explaining the vast differences in k_{cat} between Z-FHL and AngI in presence of chloride (282 s^{-1} and 7.38 s^{-1} respectively). We also showed in 5.3.4.3 that the greater length of AngI had a fairly large structural effect on the chloride pocket, which may also account for the relatively lower k_{cat} values.

The role of the chloride 1 pocket in tACE is less clear as we have no way of determining a $K_{d,app}$ for it, where the measured $K_{d,app}$ values relate to the chloride 2 pocket as confirmed by mutagenic data, and there is no stoichiometric data either. Chloride within this pocket may be present in a structural role and there may not actually be any dynamic movement in this pocket. The other possibility is that proposed by Moiseeva et al (2005) where they suggest chloride binding in this pocket would have an inhibitory role at high chloride concentrations. The latter proposal fits well with our framework, where it would affect C-terminal carboxylate coordination within the S2' pocket and thereby moderate activity via those interactions. This aspect though would require more investigation and was not part of the scope of this investigation. Ultimately though, this framework presents a clear way of evaluating peptide chloride dependence based on either their P' or P residue composition.

5.4 Summary

The tACE mutants that showed marked effects on chloride dependence (R186H, E403R, R522Q and R522K) in Chapter 3 were evaluated further using kinetic and thermodynamic data determined for the hydrolysis of HHL, Z-FHL and AngI under various chloride conditions. The interpretation was supplemented by molecular docking of HHL and Z-FHL, which provided insights into various interactions that these substrates might have with tACE and N-domain in relation to similar work done for AngI. A model of interactions in the chloride 1 pocket was developed in the context of various mutants generated here and in the literature to explain how chloride binding might modulate K511 coordination, and potentially S2' pocket conformation, in tACE. A Pi-cation interaction between R522 and the transition-state stabilizing residue Y523 was observed in multiple crystal structures, the relevance of which was supported by interpretation of the kinetic and thermodynamic effects of the R522Q and R522K mutants. This also suggested that chloride binding was most likely affected by subtle structural effects that could be modulated by differing substrate interactions. Interpretation of the E403R mutant kinetics and thermodynamics allowed refinement of this concept and demonstrated that E403 in tACE plays a role in reducing chloride affinity in the chloride 2 pocket via a salt bridge with K118 through structural constraint, an interaction that is not present in the N-domain. Finally, a framework that describes the different ways that substrate interactions can modulate chloride affinity, via the S' or S2 pockets is presented. The chloride modulation of other substrates could also be evaluated using this model.

Conclusions and Future Directions

This study describes an investigation into the chloride dependence mechanisms of the C-domain of ACE using a mutational approach combined with kinetic, thermodynamic and structural analysis. A series of tACE mutants was generated where specific residues in either the chloride 1 or chloride 2 pockets were replaced with either their corresponding N-domain residues or a residues of differing functionality. These constructs were subsequently characterized using the substrates HHL, Z-FHL and AngI, each of which has varying chloride dependence, activity and domain specificities.

All tACE constructs were initially assessed using chloride titrations with HHL and Z-FHL to determine whether the mutations had an effect on chloride affinity. The chloride 1 pocket R186H mutant showed no major change in chloride affinity ($K_{d,app}$), yet showed modest increases in overall activity for HHL and Z-FHL with no major loss of chloride activation. Previous work by Rushworth et al (2008) showed mutation of R186 to a Gln reduced chloride activation with AngI, suggesting that it resulted in different interactions to those that would be expected with a His in that position. The tACE E403R mutant, along with the R381E reversion in the N-domain, showed that a Glu in that position in either domain increased chloride dependence ($K_{d,app}$) for HHL and Z-FHL, an effect reversed by presence of an Arg. This provided the first clear evidence for the importance of this residue in chloride dependence in tACE. The R522K and R522Q mutations produced large reductions in both chloride affinity and overall activity with HHL and Z-FHL, confirming the critical role of this residue. With the other constructs not showing any appreciable alteration in chloride dependence, the R186H, E403R, R522K and R522Q constructs were chosen for further analysis.

A novel Isothermal Titration Calorimetry-based approach was developed that could be applied to all substrates in order to determine enzyme kinetic constants of tACE constructs. In the development of this methodology, it was established that considerable differences in tACE activity could be attributed to buffer composition, with the Tris and Phosphate buffers shown to disrupt chloride activation, an important consideration to be taken into account when assessing ACE kinetics in future studies. The methodology provides a highly reproducible and efficient alternative to conventional fluorogenic assays, which rely on less than ideal modified substrates, and HPLC-based assays, which can be time consuming and inconsistent. More importantly, it allows for potential evaluation of a wide variety of ACE substrates using the same technique, critical when looking at minor variation in enzyme structure or substrate composition.

This technique also allows the determination of the enthalpy (ΔH) associated with substrate binding and hydrolysis, which, combined with the Gibbs free energy (ΔG) calculated from k_{cat}/K_m, permits determination of the temperature dependent entropy (-TΔS). These values were determined for N-domain and all tACE constructs in the presence and absence of chloride. It was established that substrate binding and hydrolysis for both domains was entropically driven, presumably via substrate desolvation and structural movement of the enzyme which correlates well with the hinge bending hypothesis of Watermeyer et al., (2006). The enthalpy for hydrolysis was also shown to be endothermic, further enforcing the structural movement hypothesis. Critically, chloride binding did not produce any appreciable changes in enthalpy for either domain, suggesting that the chloride dependence mechanisms were not reliant on major salt bridge breakages.

Chloride binding in the chloride 1 pocket of tACE was found to affect positioning of K511 and potentially alter the conformation of the active site. Depending on substrate prime dipeptide identity, this was suggested to affect chloride 2 pocket ion affinity by coordinating Y520 and affecting peptide bond rotation and hence substrate interactions around the scissile bond and potentially in the non-prime sub-sites. Furthermore, my data indicated that the lack of a chloride ion in the chloride 1 pocket in the N-domain was not due to the His residue (H162) instead of an arginine, but more likely to steric hindrances not present in the C-domain that prevented access of the ion.

The R522Q and R522K mutations in the chloride 2 pocket showed kinetic parameters for AngI consistent with previous reports, confirming the critical role of this residue. However, despite both vastly reducing chloride affinities in the chloride 2 pocket, the two mutants exhibited key differences in their overall activities seen with different substrates. Both mutations largely abrogated any chloride activation for all substrates assessed, however, whilst R522K overall activity remained low for all substrates, R522Q showed increases in the overall activity relative to tACE in the order of AngI>Z-FHL>HHL. This indicated that the number of interactions on the non-prime side of the active site was affecting positioning of these residues in the chloride 2 pocket. These analyses, along with structural interpretations, confirmed a key R522-Y523 Pi-cation interaction that is stabilized via chloride coordination of R522. Substrate interactions in the S2 sub-site were shown to affect positioning of this complex as well as chloride affinity in the chloride 2 pocket.

Contrary to the chloride gated channel hypothesis of Tzakos et al (2003), the E403-K118 salt bridge in tACE, which is not present in the N-domain, was shown to stabilize the hinge-bending region and reduce chloride affinity by constraining the chloride 2 pocket. This model accounts for the variability

in $K_{d,app}$ values reported here and in the literature, which can be destabilized via substrate interactions within the S2 pocket.

This work showed that substrate composition to the C-terminal side of the scissile bond, as well as interactions of larger substrates in the S2 sub-site, moderate chloride affinity in the chloride 2 pocket of the ACE C-domain. The shorter the substrate, the greater the influence the prime dipeptide identity has on chloride dependence, a factor that can be largely overridden by larger substrates that interact with the S2 and other non-prime sub-sites. This provides a rationale for the substrate selective nature of chloride dependence in ACE and how this varies between the N and C domains.

Future aspects:

The minimally glycosylated mutants were designed with a view to crystal structure studies and are the focus of ongoing structural studies. Crystals have been obtained for 3 of these mutants using a Pheonix nano-drop robotic system. The structural work will be pursued in an iterative mode so we are able to provide empirical structural data to support the kinetic and thermodynamic findings in this study. A structure for the E403R tACE mutant should reveal whether there is any structural shift in the S2 sub-site and chloride 2 pocket. The R522Q and R522K mutants' crystal structures should provide an indication of any rotation around the C-terminal end of helix α23 and the importance of the proposed Chloride-R522-Y523 Pi-cation interaction in stabilizing Y523 within the active site. A crystal structure for the R186H would reveal whether the interactions in the chloride 1 pocket differ significantly from the N-domain and whether chloride is still being coordinated despite the presence of a His in place of an Arg. The anticipated structural data for these mutants would significantly build on the findings presented in this study and go a long way towards a comprehensive understanding of the mechanism of variability between the C and N domains of ACE.

Further understanding of the role of substrate composition and extension into the non-prime binding sub-sites would be greatly aided by systematically evaluating each residue position of the substrate. This was attempted by Bersanetti et al (2004) where they used positional scanning combinatorial libraries of FRET peptides to determine substrate specificity. However, the presence of large FRET acceptor and donor groups on the termini would no doubt influence substrate selectivity, especially at the C-terminus where large differences in activity and chloride dependencies for short peptides have been described. A similar approach using non-labelled peptides and the ITC-based method described here would allow for a more accurate assessment of substrate selectivity. This methodology would also allow these differential substrates to be considerably

larger, which would aid in delineating the specificity of interactions in the S1, S2 and more distal non-prime binding sites.

It has been reported in the literature that there is a degree of cooperativity between the N and C-domains within the context of somatic ACE (Binevski et al., 2003). This is further evidenced by the findings reported here and by Liu et al (2001) where, individually, the N-domain cleaves AngI at a higher rate than the C-domain, but in vivo the C-domain is the main site of AngI hydrolysis (Fuchs et al., 2008). This avenue of research could be furthered not only by the findings presented here, but also by the ITC-based methodology presented. The importance of the α23 and α17 helices and the hinge-bending region in chloride dependence and activity presented here could be further explored using sACE and single domains, and a range of substrates of differing size and chloride dependence modes (Figure 5.19). Using the ITC-based methodology would yield kinetic and thermodynamic data with which to interpret structural interactions between the domains.

This work has provided unique insights into key interactions and mechanisms of chloride dependence and substrate selectivity in the C-domain of ACE, and has presented a new approach that can be further leveraged in the understanding of ACE activity and its myriad functions in our physiology.

Appendix

Cloning and Mutagenesis

Preparation of E. coli competent cells

Competent cells were prepared using a slightly modified method described previously (Chung & Miller, 1988). E.coli XL1 Blue cells from glycerol stocks were inoculated into 5ml of Luria-Bertani (LB) broth (10g/L tryptone, 5g/L yeast extract, 172mM NaCl) and shaken at 37°C overnight. 1ml of this starter culture was inoculated into 100ml LB and shaken. Absorbance of the culture was monitored until cells reached early log phase (OD_{600} = 0.5 [0.3-0.6]) and then the cells were collected by centrifugation at 4000 rpm, for 5-10 min at 4°C. Supernatant was removed, cells resuspended in 1/10 (10ml) ice-cold TSB (16g/L Peptone, 10g/L Yeast Extract, 86mM NaCl, 29.8mM PEG, 5% DMSO, 10mM $MgCl_2$, 10mM $MgSO_4$) and incubated for 20 min on ice. Glycerol was added to final concentration of 15% and 100µl aliquots were flash frozen in liquid nitrogen and stored at -80°C. To transform, approximately 100ng DNA was mixed with 100µl cells and incubated on ice for 30 min. 900µl TSBG (TSB plus 20mM glucose) was added and mixture incubated for 4h at 37°C, shaking at 225 rpm. Cells were plated out on LB agar plates containing 100µg/ml Ampicillin.

Plasmid Mini-Preparation

Protocol adapted from Sambrook & Russel (2001). Transformed *E.coli* colonies were inoculated into 5ml of LB medium containing 100ug/ml ampicillin and shaken overnight at 37°C. 1.5ml of the culture was harvested by centrifugation at 10000rpm for 2 min, the supernatant removed and the pellet resuspended in 250µl STET buffer (233mM sucrose, 50mg/ml triton X-100, 50mM ethylenediaminetetraacetic acid (EDTA), 50mM Tris-HCl) containing 1mg/ml lysozyme. The suspension was then boiled for exactly 1 min and then centrifuged at 10000rpm for 8 min, with the resultant pellet being removed via sterile toothpick. 250µl of room temperature isopropanol was added to the supernatant and then recentrifuged at 10000rpm for 8min. The supernatant was then carefully discarded and the pellet dried using a vacuum dryer. The pellet was then resuspended via addition of 20µl of

1/10 Tris-EDTA buffer (1mM Tris-HCL, 0.1mM EDTA) and incubation at 60°C for 15min. One microlitre of minipreparation DNA was used in subsequent restriction digests.

Restriction Digestion

Reaction mixture for restriction endonuclease digestion consisted of: 2µl 10x restriction buffer, 0.5-2µl of 1ug/ml plasmid DNA and 5 units of restriction enzyme, made up to a volume of 20µl using sterile dH_2O. The mix was then incubated at 37°C for 1-3 hours. In the case of double digestion reactions, some enzyme combinations required sequential incubation at different temperatures, whereby 2 hours at each temperature was employed. Reactions were stopped via addition of 3ul of STOP loading buffer (8 parts 6x loading buffer (0.25% Bromophenol Blue, 0.25% Xylene Cyanol, 30% glycerol) and 1 part 0.5M EDTA, pH 8.0).

Agarose Gel Electrophoresis

Agarose gels were poured in a 6 x 10cm plate and consisted of 0.8-1.2% agarose in 1x Tris-borate/EDTA (TBE) buffer (0.045M Tris-borate, 0.001M EDTA) containing 0.3ug/ml ethidium bromide. Samples containing 20µl of digestion reaction mixture and 3µl of STOP loading buffer were loaded into the agarose gel along with 7µl of lambda DNA digested with EcoRI and HindIII (40µl 553ug/ml lambda DNA, 16µl 10x restriction buffer, 50 units EcoRI, 50 units HindIII, made up to total volume of 160µl with sterile $dH_2O$and incubated for 4 hours at 37°C) or Fermentas GeneRuler™ DNA Ladder Mix (100-10,000 bp) to serve as a marker for size estimation. Electrophoresis was performed at 80V for approximately 1 hour in 1x TBE buffer with 0.3ug/ml ethidium bromide, with bands visualized via UV exposure and photographed directly using a Syngene InGenius Gel Dock.

References

Acharya, K.R., Sturrock, E.D., Riordan, J.F., and Ehlers, M.R. (2003) Ace revisited: a new target for structure-based drug design. *Nat. Rev. Drug Discov.* 2, 891-902.

Albiston, A.L., McDowall, S.G., Matsacos, D., Sim, P., Clune, E., Mustafa, T., Lee, J., Mendelsohn, F.A., Simpson, R.J., Connolly, L.M., and Chai, S.Y. (2001) Evidence that the angiotensin IV (AT(4)) receptor is the enzyme insulin-regulated aminopeptidase. *J. Biol. Chem.* 276, 48623-48626.

Andrade, M.C., Quinto, B.M., Carmona, A.K., Ribas, O.S., Boim, M.A., Schor, N., Casarini, D.E. (1998) Purification and characterization of angiotensin I-converting enzymes from mesangial cells in culture. *J. Hypertens.* 16(12 Pt 2), 2063-74.

Andujar-Sanchez, M., Jara-Perez, V., and Camara-Artigas, A. (2007) Thermodynamic determination of the binding constants of angiotensin-converting enzyme inhibitors by a displacement method. *FEBS Lett.* 581(18), 3449-54

Anthony, K.S., Corradi, H.R., Schwager, S.L., Redelinghuys, P., Georgiadis, D., Dive, V., Acharya, K.R. and Sturrock, E.D. (2010) The N domain of human angiotensin I-converting enzyme : the role of N-glycosylation and the crystal structure in complex with an N domain specific phosphinic inhibitor RXP407. *J Biol Chem.* 285, 35685–35693.

Araujo, M.C., Melo, R.I., Del Nery, E., Alves, M.F., Juliano, M.A., Casarini, D.E., Juliano, L., and Carmona, A.K. (1999) Internally quenched fluorogenic substrates for angiotensin I-converting enzyme. *J. Hypertens.* 17, 665-672.

Araujo, M.C., Melo, R.L., Cesari, M.H., Juliano, M.A., Juliano, L., and Carmona, A.K. (2000). Peptidase specificity characterization of C- and N-terminal catalytic sites of angiotensin I-converting enzyme. *Biochemistry.* 39, 8519-8525.

Ardaillou, R., and Chansel, D. (1997) Synthesis and effects of active fragments of angiotensin II. *Kidney Int.* 52, 1458-1468.

Azizi, M., Ezan, E., Nicolet, L., Grognet, J.M., and Menard, J. (1997) High plasma level of N-acetyl-seryl-aspartyl-lysyl-proline: a new marker of chronic angiotensin-converting enzyme inhibition. *Hypertension.* 30, 1015–1019.

Azizi, M., Rousseau, A., Ezan, E., Guyene, T-T., Michelet, S., Grognet, J-M., Lenfant, M., Corvol, P., and Me´nard, J. (1996) Acute angiotensin-converting enzyme inhibition increases the plasma level of the natural stem cell regulator N-acetyl-seryl-aspartyl-lysyl-proline. *J. Clin. Invest.* 97, 839–844.

Barnes, K., Matsas, R., Hooper, N.M., Turner, A.J., and Kenny, A.J. (1988) Endopeptidase-24.11 is striosomally ordered in pig brain and, in contrast to aminopeptidase N and peptidyl dipeptidase A ('angiotensin converting enzyme'), is a marker for a set of striatal efferent fibres. *Neuroscience.* 27, 799-817.

Barry, D.A, Parlange, J.Y., Li, L., Prommer, H., Cunningham, C.J., and Stagnitti, F. (2000) Analytical approximations for real values of the Lambert W function. *Math. Comput. Simul.* 53, 95–103.

Baudin, B., and Bénéteau-Burnat, B. (1999) Mixed-Type Inhibition of Pulmonary Angiotensin I-Converting Enzyme by Captopril, Enalaprilat and Ramiprilat. *J. Enzyme. Inhib.* 14 (6), 447-456.

Baudin,B. (2002) New aspects on angiotensin-converting enzyme: from gene to disease. *Clin.Chem.Lab. Med*. 40, 256-265.

Beneteau, B., Baudin, B., Morgant, G., Giboudeau, J., and Baumann, F.C. (1986) Automated kinetic assay of angiotensin-converting enzyme in serum. *Clin. Chem.* 32, 884-886.

Bhoola, K.D., Figueroa, C.D., and Worthy, K. (1992) Bioregulation of kinins: kallikreins, kininogens, and kininases. *Pharmacol.* Rev. 44, 1-80.

Binevski, P.V., Sizova, E.A., Pozdnev, V.F., and Kost, O.A. (2003). Evidence for the negative cooperativity of the two active sites within bovine somatic angiotensin-converting enzyme. *FEBS Lett.* 550, 84-88.

Bissantz, C., Kuhn B., and Stahl, M. (2010) A Medicinal Chemist's Guide to Molecular Interactions. *J. Med. Chem.* 53, 5061–5084.

Bonnet, D., Lemoine, F.M., Pontvert-Delucq, S., Baillou, C., Najman, A., and Guigon, M. (1993) Direct and reversible inhibitory effect of the tetrapeptide acetyl-N-Ser-Asp-Lys-Pro (Seraspenide) on the growth of human CD34+ subpopulations in response to growth factors. *Blood.* 82, 3307–3314.

Cai, L., Cao, A., and Lai, L. (2001) An Isothermal Titration Calorimetric Method to Determine the Kinetic Parameters of Enzyme Catalytic Reaction by Employing the Product Inhibition as Probe. *Anal. Biochem.* 299, 19–23.

Campbell, D.J. (2003) The renin-angiotensin and the kallikrein-kinin systems. *Int. J. Biochem. Cell. Biol.* 35, 784-791.

Chai, S.Y., McKinley, M.J., and Mendelsohn, F.A. (1987) Distribution of angiotensin converting enzyme in sheep hypothalamus and medulla oblongata visualized by in vitro autoradiography. *Clin. Exp. Hypertens.* A. 9, 449-460.

Chen, X., Li, W., Yoshida, H., Tsuchida, S., Nishimura, H., Takemoto, F., Okubo, S., Fogo, A., Matsusaka, T., and Ichikawa, I. (1997) Targeting deletion of angiotensin type 1B receptor gene in the mouse. *Am. J. Physiol.* 272, F299-F304.

Chervenak, M.C. and Toone, E.J. (1994) A direct measure of the contribution of solvent reorganization to the enthalpy of binding. *J. Am. Chem. Soc.* 116, 10533–10539.

Chubb, A.J., Schwager, S.L.U., Woodman, Z.L., Ehlers, M.R.W. and Sturrock, E.D. (2002) Defining the boundaries of the testis angiotensin I-converting enzyme ectodomain. *Bioch. Biophys. Res. Commun.* 297, 1225-1230.

Corless, R.M, Gonnet, G.H., Hare, D.E.G., Jeffrey, D.J., and Knuth, D.E. (1996) On the Lambert W function. *Adv. Comput. Math.* 5, 329–359.

Cornish-Bowden, A. (2004) Fundamentals of Enzyme Kinetics, Portland Press, London.

Corradi R., Acharya, R.K., and Sturrock, E.D. (2006) Structure of Testis ACE Glycosylation Mutants and Evidence for Conserved Domain Movement. *Biochemistry.* 45, 12654-12663

Corradi, H.R., Schwager, S.L., Nchinda, A.T., Sturrock, E.D., and Acharya, K.R. (2006). Crystal structure of the N domain of human somatic angiotensin I-converting enzyme provides a structural basis for domain-specific inhibitor design. *J. Mol. Biol.* 357, 964-974.

Corradi, H.R., Chitapi, I., Sewell, B.T., Georgiadis, D., Dive, V., Sturrock, E.D., and Acharya, K.R. (2007). The structure of testis angiotensin-converting enzyme in complex with the C -domain-specific inhibitor RXPA380. *Biochemistry.* 46, 5473-5478.

Cristovam, P.C., Arnoni, C.P., Andrade, M.C., Casarini, D.E., Pereira, L.G., Schor, N and Boim, M.A. (2008) Glucose-Stimulated Human Mesangial Cells ACE-Dependent and Chymase-Dependent Angiotensin II Generation in Normal. *Exp. Biol. Med.* 233, 1035-1043.

Csikós, T., Chung, O., and Unger, T. (1998) Receptors and their classification: focus on angiotensin II and the AT2 receptor. *J. Hum. Hypertens*. 12, 311-318.

Danilov, S., Jaspard, E., Churakova, T., Towbin, H., Savoie, F., Wei, L., and Alhenc-Gélas, F. (1994) Structure-function analysis of angiotensin I-converting enzyme using monoclonal antibodies. Selective inhibition of the amino-terminal active site. *J. Biol. Chem.* 269, 26806–26814.

Deddish, P.A., Wang, J., Michel, B., Morris, P.W., Davidson, N.O., Skidgel, R.A., and Erdös, E.G. (1994) Naturally occurring active N-domain of human angiotensin I-converting enzyme. *Proc. Natl. Acad. Sci. USA.* 91, 7807-7811.

Defendini, R., Zimmerman, E.A., Weare, J.A., Alhenc-Gelas, F., and Erdös, E.G. (1983) Angiotensin-converting enzyme in epithelial and neuroepithelial cells. *Neuroendocrinology* 37, 32-40.

De Koninck, Y. (2007) Altered chloride homeostasis in neurological disorders: a new target. *Curr Opin Pharmacol.* 7(1), 93-9.

Donoghue, M., Hsieh, F., Baronas, E., Godbout, K., Gosselin, M., Stagliano, N., Donovan, M., Woolf, B., Robison, K., Jeyaseelan, R., Breitbart, R.E., and Acton, S. (2000) A novel angiotensin-converting enzyme-related carboxypeptidase (ACE2) converts angiotensin I to angiotensin 1-9. *Circ. Res.* 87, E1-E9.

Duggleby, R.G. (2001) Quantitative Analysis of the Time Courses of Enzyme-Catalyzed Reactions. *Methods.* 24, 168–174.

Dutzler,R., Campbell, E.B., Cadene, M., Chait, B.T. and MacKinnon, R. (2002) X-ray structure of a ClC chloride channel at 3.0Å reveals the molecular basis of anion selectivity. *Nature.* 415, 287-294.

Dzau, V.J., Bernstein, K., Celermajer, D., Cohen, J., Dahlof, B., Deanfield, J., Diez, J., Drexler, H., Ferrari, R., Van Gilst, W., Hansson, L., Hornig, B., Husain, A., Johnston, C., Lazar, H., Lonn, E., Luscher, T., Mancini, J., Mimran, A., Pepine, C., Rabelink, T., Remme, W., Ruilope, L., Ruzicka, M., Schunkert, H., Swedberg, K., Unger, T., Vaughan, D. and Weber, M. (2001) The relevance of tissue angiotensin-converting enzyme: manifestations in mechanistic and endpoint data. *Am. J. Cardiol.* 88, 1L-20L.

Eftink, M.R., Johnson, R.E., and Biltonen, R.L. (1981) The application of flow microcalorimetry to the study of enzyme kinetics. *Anal. Biochem.* 111, 305–320.

Ehlers, M.R. and Riordan, J.F. (1989) Angiotensin-converting enzyme: new concepts concerning its biological role. *Biochemistry.* 28, 5311-5318.

Ehlers, M.R., Fox, E.A., Strydom, D.J. and Riordan, J.F. (1989) Molecular cloning of human testicular angiotensin-converting enzyme: the testis isozyme is identical to the C-terminal half of endothelial angiotensin-converting enzyme. *Proc. Natl. Acad. Sci. U.S.A.* 86, 7741-7745.

Ehlers, M.R., and Riordan, J.F. (1991). Angiotensin-converting enzyme: zinc- and inhibitor-binding stoichiometries of the somatic and testis isozymes. *Biochemistry.* 30, 7118-7126.

Ehlers, M.R., Chen, Y.N. and Riordan, J.F. (1991) Purification and characterization of recombinant human testis angiotensin-converting enzyme expressed in Chinese hamster ovary cells. *Protein. Expr. Purif.* 2, 1-9.

Ehlers, M.R., Chen, Y.N. and Riordan, J.F. (1992) The unique N-terminal sequence of testis angiotensin-converting enzyme is heavily O-glycosylated and unessential for activity or stability. *Biochem. Biophys. Res. Commun.* 183, 199-205.

Ehlers, M.R., Schwager, S.L., Scholle, R.R., Manji, G.A., Brandt, W.F. and Riordan, J.F. (1996) Proteolytic release of membrane-bound angiotensin-converting enzyme: role of the juxtamembrane stalk sequence. *Biochemistry.* 35, 9549-9559.

Eisenthal, R. and Danson, M.J. (1992) Enzyme Assays: A Practical Approach, IRL Press, Oxford, UK.

Elkins, J.S., Douglas, V.C., and Johnston, S.C. (2004) Alzheimer disease risk and genetic variation in ACE: a meta-analysis. *Neurology.* 62(3), 363-368

Erdos, E.G., and Yang, H.Y. (1967) An enzyme in microsomal fraction of kidney that inactivates bradykinin. *Life Sci.* 6, 569-574.

Eriksson, U., Danilczyk, U. and Penninger, J.M. (2002) Just the beginning: novel functions for angiotensin-converting enzymes. *Curr.Biol.* 12, R745-R752.

Esther, C.R., Howard, T.E., Marino, E.M., Goddard, J.M., Capecchi, M.R., and Bernstein, K.E. (1996). Mice lacking angiotensin-converting enzyme have low blood pressure, renal pathology, and reduced male fertility. *Lab. Invest.* 74, 953-965.

Fernandez, M., Liu, X., Wouters, M.A., Heyberger, S., and Husain, A. (2001). Angiotensin I-converting enzyme transition state stabilization by HIS1089: evidence for a catalytic mechanism distinct from other gluzincin metalloproteinases. *J. Biol. Chem.* 276, 4998-5004.

Freire, E. (2004) Isothermal titration calorimetry: controlling binding forces in lead optimization. *Drug Discovery Today.* 1(3), 295‑299.

Freire, E. (2008) Do enthalpy and entropy distinguish first in class from best in class? *Drug Discovery Today.* 13, 869–874.

Friedland, J. and Silverstein, E. (1976) A sensitive fluorimetric assay for serum angiotensin-converting enzyme. *Am. J. Clin. Pathol.* 66, 416-424.

Fuchs, S., Frenzel, K., Hubert, C., Lyng, R., Muller, L., Michaud, A., Xiao, H.D., Adams, J.W., Capecchi, M.R., Corvol, P., Shur, B.D. & Bernstein, K.E. (2005) Male fertility is dependent on dipeptidase activity of testis ACE. *Nature Medicine.* 11, 1140 - 1142

Fuchs, S., Xiao, H.D., Hubert, C., Michaud, A., Campbell, D.J., Adams, J.W., Capecchi, M.R., Corvol, P., and Bernstein, K.E. (2008) Angiotensin-converting enzyme C-terminal catalytic domain is the main site of angiotensin I cleavage in vivo. *Hypertension.* 51, 267-274.

Gallivan, J.P. and Dougherty, D.A. (2000) A computational study of cation-pi interactions vs salt bridges in aqueous media: implications for protein engineering. *J. Am. Chem. Soc.* 122, 870–874.

Gasparo, M., Husain, A., Alexander, W., Catt, K.J., Chiu, A.T., Drew, M., Goodfriend, T., Harding, J.W., Inagami, T., and Timmermans, P.B. (1995) Proposed update of angiotensin receptor nomenclature. *Hypertension* 25, 924-927

Gavish, B., and Werber, M.M. (1979) Viscosity-dependent structural fluctuations in enzyme catalysis. *Biochemistry.* 18(7), 1269–1275.

Gill, S.C. & Von Hippel, P.H. (1989) Calculation of Protein Extinction Coefficients from amino acid sequence data. Anal. *Biochem.* 182, 319-326.

Gilson, M.K. and Zhou, H. (2007) Calculation of protein-ligand binding affinities. *Annu. Rev. Biophys. Biomol. Struct.* 36, 21–42.

Goldblatt, H., Lynch, J., Hanzal, R.F., and Summerville, W.N. (1934) Studies on experimental hypertension.I. The production of persistent elevation of systolic blood pressure by means of renal ischemia. *J. Exp. Med.* 59, 347-379.

Gordon, K., Redelinghuys, P., Schwager, S.L., Ehlers, M.R., Papageorgiou, A.C., Natesh, R., Acharya, K.R. and Sturrock E.D. (2003) Deglycosylation, processing and crystallization of human testis angiotensin-converting enzyme. *Biochem J.* 371(2), 437-42.

Golicnik M. (2010) Explicit reformulations of time-dependent solution for a Michaelis–Menten enzyme reaction model. *Anal. Biochem.* 406, 94–96.

Golicnik M. (2011a) Evaluation of enzyme kinetic parameters using explicit analytic approximations to the solution of the Michaelis–Menten equation. *Biochemical Engineering Journal* 53, 234–238.

Golicnik M. (2011b) Explicit analytic approximations for time-dependent solutions of the generalized integrated Michaelis–Menten equation. *Anal. Biochem.* 411, 303–305.

Golicnik M. (2011c) Exact and Approximate Solutions for the Decades-old Michaelis-Menten Equation: Progress-curve analysis through integrated rate equations. *Biochemistry and Molecular Biology Education.* 39(2), 117–125.

Goudar, C.T., Sonnad, J.R. and Duggleby, R.G. (1999) Parameter estimation using a direct solution of the integrated Michaelis–Menten equation. *Biochim. Biophys. Acta* 1429, 377–383.

Goudar, C.T., Harris, S.K., McInerney, M.J. and Suflita, J.M. (2004) Progress curve analysis for enzyme and microbial kinetic reactions using explicit solutions based on the Lambert W function, *J. Microbiol. Methods.* 59, 317–326.

Guimarães P.B., Alvarenga, É.C., Siqueira, P.D., Paredes-Gamero, E.J., Sabatini, R.A., Morais, R.L., Reis, R.I., Santos, E.L., Teixeira, L.G., Casarini, D.E., Martin, R.P., Shimuta, S.I., Carmona, A.K., Nakaie, C.R., Jasiulionis, M.G., Ferreira, A.T., Pesquero, J.L., Oliveira, S.M., Bader, M., Costa-Neto, C.M. and Pesquero, J.B. (2011) Angiotensin II binding to angiotensin I-converting enzyme triggers calcium signaling. *Hypertension.* 57(5), 965-72.

Guy, J.L., Jackson, R.M., Acharya, K.R., Sturrock, E.D., Hooper, N.M. and Turner, A.J. (2003) Angiotensin-converting enzyme-2 (ACE2): comparative modeling of the active site, specificity requirements, and chloride dependence. *Biochemistry.* 42, 13185–13192.

Guy, J.L., Jackson, R.M., Jensen, H.A., Hooper, N.M. and Turner, A.J. (2005) Identification of critical active-site residues in angiotensin-converting enzyme-2 (ACE2) by site-directed mutagenesis. *FEBS J.* 272, 3512-3520.

Hagaman, J.R., Moyer, J.S., Bachman, E.S., Sibony, M., Magyar, P.L., Welch, J.E., Smithies, O., Krege, J.H., and O'Brien, D.A. (1998). Angiotensin-converting enzyme and male fertility. *Proc. Natl. Acad. Sci. USA.* 95, 2552-2557.

Hammond, C., Braakman, I. and Helenius, A. (1994). Role of Nlinked oligosaccharide recognition, glucose trimming, and calnexin in glycoprotein folding and quality control. *Proc. Natl. Acad. Sci. USA* 91, 913–917.

Hanesworth, J.M., Sardinia, M.F., Krebs, L.T., Hall, K.L., and Harding, J.W. (1993) Elucidation of a specific binding site for angiotensin II(3–8), angiotensin IV, in mammalian heart membranes. *J. Pharmacol. Exp. Ther.* 266, 1036–1042.

Hangauer, D.G., Monzingo, A.F. and Matthews, B.W. (1984) An interactive computer graphics study of thermolysin-catalyzed peptide cleavage and inhibition by N-carboxymethyl dipeptides. *Biochemistry.* 23, 5730–5741.

Haq, I., Jenkins, T.C., Chowdhry, B.Z., Ren, J. & Chaires, J.B. (2000) Parsing free energies of drug-DNA interactions. *Meth. Enzymol.* 323, 373-405.

Haq, I., Chowdhry, B.Z. and Jenkins, T.C. (2001) Calorimetric techniques in the study of high-order DNA-drug interactions. *Meth. Enzymol.* 340, 109-149.

Helenius, A., and Aebi, M. (2004) Roles of N-linked glycans in the endoplasmic reticulum. *Annu. Rev. Biochem.* 73, 1019–1049.

Hemming, M.L. and Selkoe, D.J. (2005) Amyloid beta-protein is degraded by cellular angiotensin-converting enzyme (ACE) and elevated by an ACE inhibitor. *J Biol Chem.* 280(45), 37644-50.

Hille, B. (1992) Ionic channels of excitable membranes. Sunderland, Mass.: Sinauer Associates, p. xiii, 607.

Holmquist, B., Bünning, P. and Riordan, J.F. (1979) A continuous spectrophotometric assay for angiotensin converting enzyme. *Anal. Biochem.* 95, 540-548.

Horiuchi, M. (1996) Functional aspects of angiotensin type 2 receptor. *Adv. Exp. Med. Biol.* 396, 217-224

Houssay., B.A., and Fasciolo, J.C. (1937) Secretion hipertensora del rinon isquemaido. *Rev. Soc. Argent. Biol.* 13, 284-294.

Howard, T.E., Shai, S.Y., Langford, K.G., Martin, B.M., and Bernstein, K.E. (1990) Transcription of testicular angiotensin-converting enzyme (ACE) is initiated within the 12th intron of the somatic ACE gene. *Mol. Cell Biol.* 10, 4294-4302.

Hu, J., Igarashi, A., Kamata, M. and Nakagawa, H. (2001) Angiotensin-converting enzyme degrades Alzheimer amyloid beta-peptide (A beta); retards A beta aggregation, deposition, fibril formation; and inhibits cytotoxicity. *J Biol Chem.* 276(51), 47863-8.

Hubert, C., Houot, A.M., Corvol, P. and Soubrier, F. (1991) Structure of the angiotensin I-converting enzyme gene. Two alternate promoters correspond to evolutionary steps of a duplicated gene. *J.Biol.Chem.* 266, 15377-15383.

Inagami, T. (1994). The renin-angiotensin system. *Essays Biochem.* 28, 147-164.

Inoue, H., Mori, S., Morishima, S. and Okada, Y. (2005) Volume-sensitive chloride channels in mouse cortical neurons: characterization and role in volume regulation. *Eur. J. Neurosci.* 21, 1648–1658.

Ito, M., Oliverio, M.I., Mannon, P.J., Best, C.F., Maeda, N., Smithies, O., and Coffman, T.M. (1995) Regulation of blood pressure by the type 1A angiotensin II receptor gene. *Proc. Natl. Acad. Sci. U S A* 92, 3521-3525.

Iyer, S.N., Averill, D.B., Chappell, M.C., Yamada, K., Allred, A.J., and Ferrario, C.M. (2000) Contribution of angiotensin-(1-7) to blood pressure regulation in salt-depleted hypertensive rats. *Hypertension* 36, 417-422.

Jaspard, E., Wei, L. and Alhenc-Gelas, F. (1993) Differences in the properties and enzymatic specificities of the two active sites of angiotensin I-converting enzyme (kininase II). Studies with bradykinin and other natural peptides. *J.Biol.Chem.* 268, 9496-9503.

Jelesarov, I. and Bosshard, H.R. (1999) Isothermal titration calorimetry and differential scanning calorimetry as complementary tools to investigate the energetics of biomolecular recognition. *J. Mol. Recognit.* 12, 3-18.

Jenkins, T.A., Mendelsohn, F.A. and Chai, S.Y. (1997) Angiotensin-converting enzyme modulates dopamine turnover in the striatum. *J Neurochem.* 68(3), 1304-11.

Jeyendran, R.S., Van der Ven, H.H., Rosecrans, R., Perez-Pelaez, M., Al-Hasani, S., Zaneveld, L.J.D. (1989) Chemical constituents of human seminal plasma: relationship to fertility. *Andrologia.* 21, 423–428.

Junot, C., Gonzales, M.F., Ezan, E., Cotton, J., Vazeux, G., Michaud, A., Azizi, M., Vassiliou, S., Yiotakis, A., Corvol, P., and Dive, V. (2001) RXP 407, a selective inhibitor of the N-domain of angiotensin I-converting enzyme, blocks in vivo the degradation of hemoregulatory peptide acetyl-Ser-Asp-Lys-Pro with no effect on angiotensin I hydrolysis. *J. Pharmacol. Exp. Ther.* 297, 606-611.

Karim, N., Okada, H. and Kidokoro, S. (2005) Calorimetric evaluation of the activity and the mechanism of cellulases for the hydrolysis of cello-oligosaccharides accompanied by the mutarotation reaction of the hydrolyzed products. *Thermochimica Acta.* 431, 9–20.

Kehoe, P.G., Russ, C., McIlory, S., Williams, H., Holmans, P., Holmes, C., Liolitsa, D., Vahidassr, D., Powell, J., McGleenon, B., Liddell, M., Plomin, R., Dynan, K., Williams, N., Neal, J., Cairns, N. J., Wilcock, G., Passmore, P., Lovestone, S., Williams, J., and Owen, M. J. (1999) Variation in DCP1, encoding ACE, is associated with susceptibility to Alzheimer disease. *Nat. Genet.* 21(1), 71-72.

Kim, H.S., Krege, J.H., Kluckman, K.D., Hagaman, J.R., Hodgin, J.B., Best, C.F., Jennette, J.C., Coffman, T.M., Maeda, N., and Smithies, O. (1995) Genetic control of blood pressure and the angiotensinogen locus. *Proc. Natl. Acad. Sci. U S A*. 92, 2735-2739.

Klebe, G., Dullweber, F., and Boehm, H-J. (2001) Thermodynamic Models of Drug-Receptor Interactions: A General Introduction. In Drug-Receptor Thermodynamics: Introduction and Applications; Raffa, R. B., Ed.; Wiley: Chichester, U.K., 83-103.

Knight, C.G. (1995). Active-site titration of peptidases. *Methods Enzymol.* 248, 85-101.

Krege, J.H., John, S.W., Langenbach, L.L., Hodgin, J.B., Hagaman, J.R., Bachman, E.S., Jennette, J.C., O'Brien, D.A. and Smithies, O. (1995). Male-female differences in fertility and blood pressure in ACE-deficient mice. *Nature.* 375, 146-148.

Kroeger, D., Tamburri, A., Amzica, F., Sík, A. (2010) Activity-dependent layer-specific changes in the extracellular chloride concentration and chloride driving force in the rat hippocampus. *J Neurophysiol.* 103(4), 1905-14.

Kroger, W. L., Douglas, R. G., O'Neill, H. G., Dive, V. and Sturrock, E. D. (2009) Investigating the domain specificity of phosphinic inhibitors RXPA380 and RXP407 in angiotensin-converting enzyme. *Biochemistry.* 48, 8405–8412.

Ladbury, J. E. (1995) Counting the calories to stay in the groove. *Structure.* 3, 635-639.

Lazard, D., Briend-Sutren, M.M., Villageois, P., Mattei, M.G., Strosberg, A.D., and Nahmias, C. (1994) Molecular characterization and chromosome localization of a human angiotensin I AT2 receptor gene highly expressed in fetal tissues. *Receptors Channels.* 2, 271-280.

Lenfant, M., Wdzieczak-Bakala, J., Guittet, E., Prome, J.C., Sotty, D., and Frindel, E. (1989) Inhibitor of hematopoietic pluripotent stem cell proliferation: purification and determination of its structure. *Proc. Natl. Acad. Sci. USA.* 86, 779–782.

Lehmann, D. J., Cortina-Borja, M., Warden, D. R., Smith, A. D., Sleegers, K., Prince, J. A., van Duijn, C. M., and Kehoe, P. G. (2005) Large meta-analysis establishes the ACE insertion-deletion polymorphism as a marker of Alzheimer's disease. *Am. J. Epidemiol.* 162(4), 305-17

Lodish, H.F. (1999). Molecular cell biology. New York: Scientific American Books.

Liu, X., Fernandez, M., Wouters, M.A., Heyberger, S. and Husain, A. (2001) Arg(1098) is critical for the chloride dependence of human angiotensin I-converting enzyme C-domain catalytic activity. *J. Biol. Chem.* 276, 33518-33525.

Liu, S., Ji, X., Gilliland, G.L., Stevens, W.J., Armstrong, R.N. (1993) Second-Sphere Electrostatic Effects in the Active Site of Glutathione S-Transferase. Observation of an On-Face Hydrogen Bond between the Side Chain of Threonine 13 and the π-Cloud of Tyrosine 6 and Its Influence on Catalysis. J. Am. Chem. SOC. 115, 7910-7911.

Lonhienne, T., Baise, E., Feller, G., Bouriotis, V. and Gerday, C.. (2000) Enzyme activity determination on macromolecular substrates by isothermal titration calorimetry: Application to mesophilic and psychrophilic chitinases. *Biochim. et. Biophys. Acta.* 1545, 349-356.

Mao, L., Wang, Y., Liu, Y. and Hu, X. (2003) Multiple Intermolecular Interaction Modes of Positively Charged Residues with Adenine in ATP-Binding Proteins. *J.Am. Chem.*Soc. 125(47), 14216–14217.

Marshall, M.S., Steele, R.P., Thanthiriwatte, K.S. and Sherrill, C.D. (2009) Potential Energy Curves for Cation−π Interactions: Off-Axis Configurations Are Also Attractive. *J. Phys. Chem. A.* 113(48), 13628–32.

Matsas, R., Kenny, A.J., and Turner, A.J. (1984) The metabolism of neuropeptides. The hydrolysis of peptides, including enkephalins, tachykinins and their analogues, by endopeptidase-24.11. *Biochem. J.* 223, 433-440.

Matthews, B.W. (1988) Structural basis of the action of thermolysin and related zinc peptidases. *Acc. Chem. Res.* 21, 333-340.

McKinley, M.J., Albiston, A.L., Allen, A.M., Mathai, M.L., May, C.N., McAllen, R.M, Oldfield, B.J., Mendelsohn, F.A. and Chai, S.Y. (2003) The brain renin-angiotensin system: location and physiological roles. *Int. J. Biochem. Cell Biol.* 35(6), 901-18.

Michaelis, L. & Menten, M.L. (1913) Die Kinetik der Invertinwirkung. *Biochemische Zeitschrift.* 49, 333.

Michaud, A., Williams T.A., Chauvet, M.T. and Corvol, P. (1997) Substrate Dependence of Angiotensin I-Converting Enzyme Inhibition: Captopril Displays a Partial Selectivity for Inhibition of N-Acetyl-Seryl-Aspartyl-Lysyl-Proline Hydrolysis Compared with That of Angiotensin. *Mol. Pharmacol.* 51, 1070–1076.

Michaud, A., Chauvet, M.T. and Corvol, P. (1999) N-domain selectivity of angiotensin I-converting enzyme as assessed by structure-function studies of its highly selective substrate, N-acetyl-seryl-aspartyl-lysyl-proline. *Biochem.Pharmacol.* 57, 611-618.

Moiseeva, N.A., Binevski, P.V., Baskin, I.I., Palyulin, V.A. and Kost, O.A. (2005) Role of two chloride-binding sites in functioning of testicular angiotensin-converting enzyme. *Biochemistry (Mosc).* 70(10), 1167-72.

Morin, P.E. and Freire, E. (1991) Direct calorimetric analysis of the enzymatic activity of yeast cytochrome c oxidase. *Biochemistry.* 30, 8494-8500.

Nakamoto, H., Ferrario, C.M., Fuller, S.B., Robaczewski, D.L., Winicov, E., and Dean, R.H. (1995). Angiotensin-(1-7) and nitric oxide interaction in renovascular hypertension. *Hypertension*. 25, 796-802.

Nakamura, S., Averill, D.B., Chappell, M.C., Diz, D.I., Brosnihan, K.B., and Ferrario, C.M. (2003) Angiotensin receptors contribute to blood pressure homeostasis in salt-depleted SHR. *Am. J. Physiol. Regul. Integr. Comp. Physiol.* 284, R164-R173.

Natesh, R., Schwager, S.L.U., Sturrock, E.D. and Acharya, K.R. (2003) Crystal structure of the human angiotensin-converting enzyme-lisinopril complex. *Nature.* 421, 551-554.

Natesh, R., Schwager, S.L., Evans, H.R., Sturrock, E.D., and Acharya, K.R. (2004) Structural details on the binding of antihypertensive drugs captopril and enalaprilat to human testicular angiotensin I-converting enzyme. *Biochemistry.* 43, 8718-8724.

Oba, R., Igarashi, A., Kamata, M., Nagata, K., Takano, S., and Nakagawa, H. (2005) The N-terminal active centre of human angiotensin-converting enzyme degrades Alzheimer amyloid beta-peptide. *Eur J Neurosci.* 21(3), 733-740.

Oblin, A., Danse, M.J., and Zivkovic, B. (1988) Degradation of substance P by membrane peptidases in the rat substantia nigra: effect of selective inhibitors. *Neurosci. Lett.* 84, 91-96.

Ohtaka, H., Velazquez-Campoy, A., Xie, D., Freire, E. (2002) Overcoming drug resistance in HIV-1 chemotherapy: The binding thermodynamics of amprenavir and TMC-126 to wild-type and drug-resistant mutants of the HIV-1 protease. *Protein. Sci.* 11, 1908-1916.

Okwan-Duodu, D., Datta, V., Shen, X.Z., Goodridge, H.S., Bernstein, E.A., Fuchs, S., Liu, G.Y. and Bernstein, K.E. (2010) Angiotensin-converting enzyme overexpression in mouse myelomonocytic cells augments resistance to Listeria and methicillin-resistant Staphylococcus aureus. *J Biol Chem.* 285(50), 39051-60.

O'Neill, H.G., Redelinghuys, P., Schwager, S.L., and Sturrock, E.D. (2008) The role of glycosylation and domain interactions in the thermal stability of human angiotensin-converting enzyme. *Biol. Chem.* 389, 1153–1161

Oliverio, M.I., Kim, H.S., Ito, M., Le, T., Audoly, L., Best, C.F., Hiller, S., Kluckman, K., Maeda, N., Smithies, O., and Coffman, T.M. (1998) Reduced growth, abnormal kidney structure, and type 2 (AT2) angiotensin receptor-mediated blood pressure regulation in mice lacking both AT1A and AT1B receptors for angiotensin II. *Proc. Natl. Acad. Sci. U S A* 95, 15496-15501.

Olsson, T.S. G., Williams, M.A., Pitt, W.R. and Ladbury, J.E. (2008) The thermodynamics of protein-ligand interaction and solvation: insights for ligand design. *J. Mol. Biol*. 384, 1002–1017.

Ortiz-Salmerón, E., Barón, C. and García-Fuentes, L. (1998) Enthalpy of captopril-angiotensin I-converting enzyme binding. *FEBS Lett*. 435(2-3), 219-224

Papworth, C., Braman, J., and Wright, D.A. (1996). Site-directed mutagenesis in One Day with 80 % efficiency. *Strategies*. 9, 3-4.

Page, I.H., and Helmer, O.M. (1940) A crystalline pressor substance (angiotonin) resulting from the interaction between renin and renin activator. *J. Exp. Med.* 71, 29.

Peng, H., Carretero, O.A., Peterson, E.L. and Rhaleb, N-E. (2010) Ac-SDKP inhibits transforming growth factor-β 1-induced differentiation of human cardiac fibroblasts into myofibroblasts. *Am. J. Physiol. Heart. Circ. Physiol.* 298, H1357-H1364

Rasoul, S., Carretero, O.A., Peng, H., Cavasin, M.A., Zhuo, J., Sanchez-Mendoza, A., Brigstock, D.R. and Rhaleb, N.E. (2004) Antifibrotic effect of Ac-SDKP and angiotensin-converting enzyme inhibition in hypertension. *J. Hypertens.* 22(3), 593-603.

Regoli, D., Rhaleb, N.E., Drapeau, G., Dion, S., Tousignant, C., D'Orléans-Juste, P., and Devillier, P. (1989) Basic pharmacology of kinins: pharmacologic receptors and other mechanisms. *Adv. Exp. Med. Biol.* 247A, 399-407.

Rice, G.I., Thomas, D.A., Grant, P.J., Turner, A.J. and Hooper, N.M. (2004) Evaluation of angiotensin converting enzyme (ACE), its homologue ACE2 and neprilysin in angiotensin peptide metabolism. *Biochem. J.* 383 (1), 45-51.

Rigat, B., Hubert, C., Alhenc-Gelas, F., Cambien, F., Corvol, P., and Soubrier, F. (1990) An insertion/deletion polymorphism in the angiotensin I-converting enzyme gene accounting for half the variance of serum enzyme levels. *J. Clin. Invest.* 86(4), 1343-1346.

Rosecrans, R.R., Jeyendran, R.S., Perez-Pelaez, M. and Kennedy W.P. (1987) Comparison of biochemical parameters of human blood serum and seminal plasma. *Andrologia.* 19:625–628.

Rousseau, A., Michaud, A., Chauvet, M.T and Corvol, P. (1995) The hemoregulatory peptide N-acetyl-Ser-Asp-Lys-Pro is a natural and specific substrate of the N-terminal active site of human angiotensin-converting enzyme. *J. Biol. Chem.* 270, 3656-3661.

Rousseau-Plasse, A., Lenfant, M., and Potier, P. (1996) Catabolism of the hemoregulatory peptide N-Acetyl-Ser-Asp-Lys-Pro: a new insight into the physiological role of the angiotensin-I-converting enzyme N-active site. *Bioorg. Med. Chem.* 4(7), 1113-1119.

Rushworth, C.A., Guy, J.L., and Turner, A.J. (2008) Residues affecting the chloride regulation and substrate selectivity of the angiotensin-converting enzymes (ACE and ACE2) identified by site-directed mutagenesis. *FEBS J.* 275, 6033-6042.

Sadhukhan, R., and Sen, I. (1996) Different glycosylation requirements for the synthesis of enzymatically active angiotensin-converting enzyme in mammalian cells and yeast. *J. Biol. Chem.* 271, 6429–6434.

Santos, R.A., Simoes e Silva, A.C., Maric, C., Silva, D.M., Machado, R.P., de Buhr, I., Heringer-Walther, S., Pinheiro, S.V., Lopes, M.T., Bader, M., Mendes, E.P., Lemos, V.S., Campagnole-Santos, M.J., Schultheiss, H.P., Speth, R., and Walther, T. (2003) Angiotensin-(1-7) is an endogenous ligand for the G protein-coupled receptor Mas. *Proc. Natl. Acad. Sci. U S A.* 100, 8258-8263.

Sasaguri, M., Ideishi, M., Ogata, S., Miura, S., Ikeda, M., and Arakawa, K. (1995) Human urinary kallikrein can generate angiotensin II from homologous renin substrates. Hypertens. Res. 18, 33-37.

Savaskan,E. (2005) The role of the brain renin-angiotensin system in neurodegenerative disorders. *Curr. Alzheimer Res.* 2, 29-35.

Schechter, I., and Berger, A. (1967). On the size of the active site in proteases. I. Papain. *Biochem. Biophys. Res. Commun*. 27, 157-162.

Schnell, S. and Mendoza, C. (1997) Closed form solution for time-dependent enzyme kinetics. *J. Theor. Biol.* 187, 207–212.

Schnell, S., and Maini, P.K. (2000) Enzyme kinetics at high enzyme concentration. *Bull.Math. Bio.* 62, 483-499.

Schnell, S., and P. K. Maini (2003). A century of enzyme kinetics: Reliability of the K_M and v_{max} estimates. *Comments on Theoretical Biology.* 8, 169-187.

Schon, A. and Velazquez-Campoy, A. (2005) Methods for the structural Analysis of Protein Pharmaceuticals (Jiskoot, W. and Crommelin, D.J.A., Eds) Arlington, VA, AAPS Press; 573-589.

Schulleck, J. R. & Wilson, I. B. (1989) Angiotensin Converting Enzyme: Substrate Inhibition. *Peptides.* 10, 431-434.

Sealey, J.E., Atlas, S.A., Laragh, J.H., Silverberg, M., and Kaplan, A.P. (1979) Initiation of plasma prorenin activation by Hageman factor-dependent conversion of plasma prekallikrein to kallikrein. *Proc. Natl. Acad. Sci. U S A.* 76, 5914-5918.

Shanmugam, S., and Sandberg, K. (1996). Ontogeny of angiotensin II receptors. *Cell Biol. Int.* 20, 169-176.

Shapiro,R., Holmquist,B. and Riordan,J.F. (1983) Anion activation of angiotensin converting enzyme: dependence on nature of substrate. *Biochemistry.* 22, 3850-3857.

Shapiro, R. and Riordan J.F. (1984) Inhibition of angiotensin converting enzyme: mechanism and substrate dependence. *Biochemistry.* 23(22), 5225–5233.

Shen, X.Z., Li, P., Weiss, D., Fuchs, S., Xiao, H.D., Adams, J.A., Williams, I.R., Capecchi, M.R., Taylor, W.R. and Bernstein, K.E. (2007) Mice with enhanced macrophage angiotensin-converting enzyme are resistant to melanoma. *Am J Pathol.* 170(6), 2122-34.

Shen, X.Z., Lukacher, A.E., Billet, S., Williams, I.R. and Bernstein, K.E. (2008) Expression of angiotensin-converting enzyme changes major histocompatibility complex class I peptide presentation by modifying C termini of peptide precursors. *J Biol Chem.* 283(15), 9957-65.

Sibony, M., Gasc, J.M., Soubrier, F., Alhenc-Gelas, F., and Corvol, P. (1993). Gene expression and tissue localization of the two isoforms of angiotensin I converting enzyme. *Hypertension.* 21, 827-835.

Skeggs, L.T., Kahn, J.R., and Shumway, N.P. (1956) The preparation and function of the hypertensin-converting enzyme. *J. Exp. Med.* 103, 295-299.

Skeggs, L.T., Marsh, W.H., Kahn, J.R., and Shumway, N.P. (1954) The purification of hypertensin I. *J. Exp. Med.* 100, 363-370.

Skidgel, R.A., Defendini, R., and Erdos, E.G. (1987) in Neuropeptides and their Neurope tidases (Turner, A. J., ed) pp. 165-182, V. C. H. Ellis- Horwood, Chichester, U. K.

Skidgel,R.A. and Erdos,E.G. (1985) Novel activity of human angiotensin I converting enzyme: release of the NH2- and COOH-terminal tripeptides from the luteinizing hormone-releasing hormone. *Proc. Natl. Acad. Sci. U S A.* 82, 1025-1029.

Skidgel, R.A. and Erdös, E.G. (2004) Angiotensin converting enzyme (ACE) and neprilysin hydrolyze neuropeptides: a brief history, the beginning and follow-ups to early studies. *Peptides.* 25(3), 521-5.

Soubrier, F., Alhenc-Gelas, F., Hubert, C., Allegrini, J., John, M., Tregear, G. and Corvol, P. (1988) Two putative active centers in human angiotensin I-converting enzyme revealed by molecular cloning. *Proc. Natl. Acad. Sci. U S A.* 85, 9386-9390.

Spink, C. & Wadso, I. (1976) Calorimetry as an analytical tool in biochemistry. *Meth. Biochem. Anal.* 23, 1-159.

Spolar, R.S. and Record Jr., M.T. (1994) Coupling of local folding to site-specific binding of proteins to DNA. *Science.* 263, 777–784.

Strittmatter, S.M., Lo, M.M., Javitch, J.A., and Snyder, S.H. (1984). Autoradiographic visualization of angiotensin-converting enzyme in rat brain with [3H]captopril: localization to a striatonigral pathway. *Proc. Natl. Acad. Sci. USA.* 81, 1599-1603.

Sturrock, E.D., Natesh, R., van Rooyen, J.M. and Acharya, K.R. (2004) Structure of angiotensin I-converting enzyme. *Cell Mol. Life Sci.* 61, 2677-2686.

Swanson, G.N., Hanesworth, J.M., Sardinia, M.F., Coleman, J.K., Wright, J.W., Hall, K.L., Miller-Wing, A.V., Stobb, J.W., Cook, V.I., and Harding, E.C. (1992) Discovery of a distinct binding site for angiotensin II (3-8), a putative angiotensin IV receptor. *Regul. Pept.* 40, 409-419.

Takada, Y., Hiwada, K., Akutsu, H., Hashimoto, A., and Kokubu, T. (1984) The immunocytochemical detection of angiotensin-converting enzyme in alveolar macrophages from patients with sarcoidosis. *Lung.* 162, 317-323.

Takeda, S., Sato, N., Takeuchi, D., Kurinami, H., Shinohara, M., Niisato, K., Kano, M., Ogihara, T., Rakugi, H. and Morishita, R. (2009) Angiotensin Receptor Blocker Prevented β-Amyloid–Induced Cognitive Impairment Associated With Recovery of Neurovascular Coupling. *Hypertension.* 54, 00-00.

Timmermans, P.B., Benfield, P., Chiu, A.T., Herblin, W.F., Wong, P.C., and Smith, R.D. (1992) Angiotensin II receptors and functional correlates. *Am. J. Hypertens.* 5, 221S-235S.

Timmermans, P.B., Wong, P.C., Chiu, A.T., Herblin, W.F., Benfield, P., Carini, D.J., Lee, R.J., Wexler, R.R., Saye, J.A., and Smith, R.D. (1993) Angiotensin II receptors and angiotensin II receptor antagonists. *Pharmacol. Rev.* 45, 205-251.

Tsai B-S., and Peach M.J. (1976) Angiotensin Homologs and Analogs as Inhibitors of Rabbit Pulmonary Angiotensin-converting Enzyme. *J. Biol. Chem.* 252(19), 4674-4681.

Tsuchida, S., Matsusaka, T., Chen, X., Okubo, S., Niimura, F., Nishimura, H., Fogo, A., Utsunomiya, H., Inagami, T., and Ichikawa, I. (1998) Murine double nullizygotes of the angiotensin type 1A and 1B receptor genes duplicate severe abnormal phenotypes of angiotensinogen nullizygotes. *J. Clin. Invest.* 101, 755-760.

Turner, A.J. and Hooper, N.M. (2002) The angiotensin-converting enzyme gene family: genomics and pharmacology. *Trends Pharmacol. Sci.* 23, 177-183.

Tzakos, A.G., Galanis, A.S., Spyroulias, G.A., Cordopatis, P., Manessi-Zoupa, E. and Gerothanassis, I.P. (2003) Structure-function discrimination of the N- and C- catalytic domains of human angiotensin-converting enzyme: implications for Cl- activation and peptide hydrolysis mechanisms. *Protein Eng.* 16, 993-1003.

van den Buuse, M., Zheng, T.W., Walker, L.L. and Denton, D.A. (2005) Angiotensin-converting enzyme (ACE) interacts with dopaminergic mechanisms in the brain to modulate prepulse inhibition in mice. *Neurosci Lett.* 380(1-2), 6-11.

Velazquez-Campoy, A., Todd, M.J. and Freire, E. (2000) HIV-1 protease inhibitors: Enthalpic versus entropic optimization of the binding affinity. *Biochemistry.* 39, 2201-2207.

Velazquez-Campoy, A., Kiso, Y. and Freire, E. (2001) The binding energetics of first- and second-generation HIV-1 protease inhibitors: Implications for drug design. *Arch. Biochem. Biophys.* 390, 169-175.

Voronov, S., Zueva, N., Orlov, V., Arutyunyan, A., and Kost, O. (2002). Temperature-induced selective death of the C-domain within angiotensin-converting enzyme molecule. *FEBS Lett.* 522, 77-82.

Wang, D., Carretero, O.A., Yang, X.Y, Rhaleb, N-E., Liu, Y-H., Liao, T-D., and Yang, X-P. (2004) N-acetyl-seryl-aspartyl-lysyl-proline stimulates angiogenesis in vitro and in vivo. *Am. J. Physiol. Heart. Circ. Physiol.* 287, H2099–H2105.

Watermeyer, J.M., Sewell, B.T., Schwager, S.L., Natesh, R., Corradi, H.R., Acharya, K.R., and Strurrock, E.D. (2006) Structure of Testis ACE Glycosylation Mutants and Evidence for Conserved Domain Movement. *Biochemistry.* 45, 12654 12663.

Watt, G.D. (1990) A microcalorimetric procedure for evaluating the kinetic parameters of enzyme-catalyzed reactions: kinetic measurements of the nitrogenase system. *Anal. Biochem.* 187, 141-146.

Wei, L., Alhenc-Gelas, F., Soubrier, F., Michaud, A., Corvol, P. and Clauser, E. (1991a) Expression and characterization of recombinant human angiotensin I-converting enzyme. Evidence for a C-terminal transmembrane anchor and for a proteolytic processing of the secreted recombinant and plasma enzymes. *J. Biol. Chem.* 266, 5540-5546.

Wei, L., Alhenc-Gelas, F., Corvol, P. and Clauser, E. (1991b) The two homologous domains of human angiotensin I-converting enzyme are both catalytically active. *J. Biol. Chem.* 266, 9002-9008.

Wei, L., Clauser, E., Alhenc-Gelas, F. and Corvol, P. (1992) The two homologous domains of human angiotensin I-converting enzyme interact differently with competitive inhibitors. *J.Biol.Chem.* 267, 13398-13405.

Wiseman, T., Williston, S., Brandts, J.F. & Lin, L-N. (1989) Rapid measurement of binding constants and heats of binding using a new titration calorimeter. *Anal. Biochem.* 179, 131-137.

Williams, B.A. and Toone, E.J. (1993) Calorimetric evaluation of enzyme kinetics parameters. *J. Org. Chem.* 58, 3507-3510.

Woodman, Z.L., Oppong, S.Y., Cook, S., Hooper, N.M., Schwager, S.L.U., Brandt, W.F., Ehlers, M.R.W. and Sturrock, E.D. (2000) Shedding of somatic angiotensin-converting enzyme (ACE) is inefficient compared with testis ACE despite cleavage at identical stalk sites. *Biochemical J*. 347, 711-718.

Wright, J.W., and Harding, J.W. (1997) Important role for angiotensin III and IV in the brain renin-angiotensin system. *Brain Res. Brain Res. Rev.* 25, 96-124.

Wright, J.W. and Harding, J,W. (2004) The brain angiotensin system and extracellular matrix molecules in neural plasticity, learning, and memory. *Progress in Neurobiology* 72, 263–293

Wu, G., Robertson, D.H., Brooks, C.L. and Vieth, M. (2003) Detailed Analysis of Grid-Based Molecular Docking: A Case Study of CDOCKER - A CHARMm-Based MD Docking Algorithm. *J. Comp. Chem.* 24, 1549.

Yanai, K., Saito, T., Kakinuma, Y., Kon, Y., Hirota, K., Taniguchi-Yanai, K., Nishijo, N., Shigematsu, Y., Horiguchi, H., Kasuya, Y., Sugiyama, F., Yagami, K., Murakami, K., and Fukamizu, A. (2000) Renin-dependent cardiovascular functions and renin-independent blood-brain barrier functions revealed by renin-deficient mice. *J. Biol. Chem.* 275, 5-8.

Yang, H.Y., Erdös, E.G., and Levin, Y. (1970) A dipeptidyl carboxypeptidase that converts angiotensin I and inactivates bradykinin. *Biochim Biophys Acta* 214, 374-376

Yang, H.Y., Erdös, E.G., and Levin, Y. (1971) Characterization of a dipeptide hydrolase (kininase II: angiotensin I converting enzyme). *J. Pharmacol. Exp. Ther.* 177, 291-300.

Yamada, K., Uchida, S., Takahashi, S., Takayama, M., Nagata, Y., Suzuki, N., Shirakura, S. and Kanda, T. (2010) Effect of a centrally active angiotensin-converting enzyme inhibitor,

perindopril, on cognitive performance in a mouse model of Alzheimer's disease. *Brain Res.* 1352, 176-186

Yamaguchi, T., Carretero, O.A., and Scicli, A.G. (1991) A novel serine protease with vasoconstrictor activity coded by the kallikrein gene S3. *J. Biol. Chem.* 266, 5011-5017.

Yu, X.C., Sturrock, E.D., Wu, Z.C., Biemann, K., Ehlers, M.R.W. and Riordan, J.F. (1997) Identification of N-linked glycosylation sites in human testis angiotensin-converting enzyme and expression of an active deglycosylated forms. *J. Biol. Chem.* 272, 3511-3519.

Zou, K., Yamaguchi, H., Akatsu, H., Sakamoto, T., Ko, M., Mizoguchi, K., Gong, J.S., Yu, W., Yamamoto, T., Kosaka, K., Yanagisawa, K. and Michikawa M. (2007) Angiotensin-converting enzyme converts amyloid beta-protein 1-42 (Abeta(1-42)) to Abeta(1-40), and its inhibition enhances brain Abeta deposition. *J. Neurosci.* 27, 8628-8635.